Properties of rare earth phosphate glasses and rare-earth halide liquids

Martin, Richard Alan

Award date:
2002

Awarding institution:
University of Bath

PROPERTIES OF RARE EARTH PHOSPHATE GLASSES AND RARE - EARTH HALIDE LIQUIDS.

Submitted by

Richard Alan Martin

for the degree of PhD of the University of Bath

ProQuest LLC
789 East Eisenhower Parkway
P.O. Box 1346
Ann Arbor, MI 48106-1346

ACKNOWLEDGEMENTS

I would like to thanks my supervisor Dr. Phil Salmon for his help with the diffraction studies and proof reading my thesis. I would also like to thank: Dr. Chris Bennmore for the lanthanum/ cerium diffraction data, Dr. Henry Fischer and Dr. Gabriel Cuello for help with the rare earth phosphate diffraction data and Dr. Adrian Barnes for the $TbCl_3$ diffraction data. I would also like to thank: Professor Jonathon Knight for help with optical studies, Professor John Davies for proof reading my thesis and suggestions on up-conversion techniques, resulting in up-conversion being demonstrated in rare earth phosphate glasses manufactured at the University of Bath for the first time (results not presented here), Dr. Daniel Wolverson for help with the Raman studies and optical fluorescence results (results not presented here).

I would also like to thank both the physics and material science technical staff at the University of Bath for their help during the course of these studies: Harry Bone, Barry Chapman, Bob Draper, Dr. Peter Ford, Adrian Hooper, Frank Hammett, Mike Harriman, Eddie Lambson, Wendy Lambson, Dr. Glyn Love, Hugh Perrot, Miklos Tatar, Pete Taylor and Ian Trussler.

I would like to thank my office mates and fellow postgraduates; Greg Chance, Pete Clegg, Graham Cook, Simon Dodd, Jim Gregory, Dave Lawton, Auturo Ortigosa, Jim Partridge, Will Reeves, Dejan Uzer and Emma Williams for their friendship over the past few years. I would also like to thank my friends studying within the physics department including, Shaffiq Armed, Maria Box and of course Jamie Cara-Southey (I dread to think how dull life would have been without his constant stream of Kamikaze accidents) and my other friends throughout the university including Helen Mansfield and Andy Wylie all who have had to put up with constant up dates on the state of my thesis as well as the occasional moan or two.

Finally, I would like to thank my parents and my fiancé for their support during the past few years.

ABSTRACT

A method for preparing rare earth phosphate glasses in alumina crucibles was refined and the resultant glasses were found to be of good optical quality, free from visible stresses or bubbles, and resistant to shatter and moisture contamination. A compositional analysis highlighted the presence of aluminium impurities and revealed that the glass compositions could be made much closer than previously found possible.

The Faraday effect for a series of rare earth phosphate glasses was studied as a function of wavelength (450 – 520 nm) and rare earth concentration and the magneto-optical Figure-of-Merit $F \equiv V/\alpha$, where V is the Verdet constant and α the optical absorption coefficient, was measured. The optimum F value was obtained for glassy $TbP_{2.94}O_{9.18}Al_{0.26}$.

The structure of La^{3+} / Ce^{3+} and Dy^{3+} / Ho^{3+} phosphate glasses was measured by applying the method of isomorphic substitution in neutron diffraction. The use of difference function methods and an explicit modelling of the Al correlations allowed unprecedented information to be obtained, thus allowing the O-O and R-O correlations to be resolved unambiguously. The partial pair distribution function, $g_{RR}(r)$, was also measured for the smaller ions (Dy^{3+} / Ho^{3+}) and gave an R-R coordination number of 8.0(2) at a mean nearest neighbour distance of $\approx$ 5.5 Å.

A neutron diffraction experiment on molten $TbCl_3$ at 617 °C was undertaken and the data showed that significant discrepancies occur between experiment and recent polarisable ion model molecular dynamics simulations.

Silica clad optical fibres were drawn from bulk rare earth phosphate glasses. Lasing of these rare earth phosphate glass fibres was demonstrated through the construction of a tuneable fibre laser cavity.

CONTENTS

CHAPTER 1
INTRODUCTION

1.1 INTRODUCTION

Glasses doped with rare earth elements (represented by R) have received much attention owing to their desirable optical properties which have led to many applications in the laser and optoelectronics industry (Marion and Weber 1991). Rare earth ions possess strong fluorescence bands throughout the visible and infra-red spectrum such that their incorporation into glass networks results in the energy level structures necessary to produce lasers and up-conversion lasers (Marion and Weber 1991). The spontaneous radiative lifetime of a lasing ion must be sufficiently long to enable a population inversion to be established and maintained. The spontaneous lifetime (and fluorescence lifetime) is dependent upon the separation of the lasing ions (Wagener *et al* 1992) i.e. the larger the distance between lasing ions the longer the spontaneous lifetime.

There has been considerable interest in rare earth phosphate glasses. For example, these materials have large Faraday rotations which give them potential for application in optical isolators (Berger *et al* 1964); they have suitable fluorescence bands and fluorescence lifetimes to make commercial laser glasses (Marion and Weber 1991); they can be used to make up-conversion lasers (Hutchinson and Allik 1992); and they have interesting magnetic properties at low temperatures (Brennan *et al* 1999).

Knowledge of the structure of rare earth phosphate glasses is important for understanding their opto-electronic and physico-chemical properties. In this context, the R-R separation is of interest as it has a strong influence on the fluorescence lifetime (Brennan 1998), on the cross-relaxation terms in up-conversion amplifiers (Blixt *et al* 1991) and will presumably have a strong bearing on the magnetic properties (Brennan *et al* 1999). The R-R separation also provides information on the connectivity of the rare earth coordination polyhedra e.g. edge sharing of polyhedra will give rise to shorter R-R distances than corner sharing.

1.2 DISORDERED MATERIALS

When a liquid is cooled it will either crystallise at the melting temperature, T_m, or if the cooling rate is sufficiently large it will super-cool for temperatures below T_m, becoming more viscous with decreasing temperature until a glass is formed (Figure 1.1). Glasses are a subset of amorphous materials that undergo a glass transition at temperature, T_g, whose precise value depends on the cooling rate. The structure of glasses thus lacks translational symmetry and cannot be described in terms of unit cells in the way a crystal can. Instead glasses retain features of the structural disorder of the liquid state and are described statistically in terms of nearest neighbours, co-ordination numbers and bond lengths.

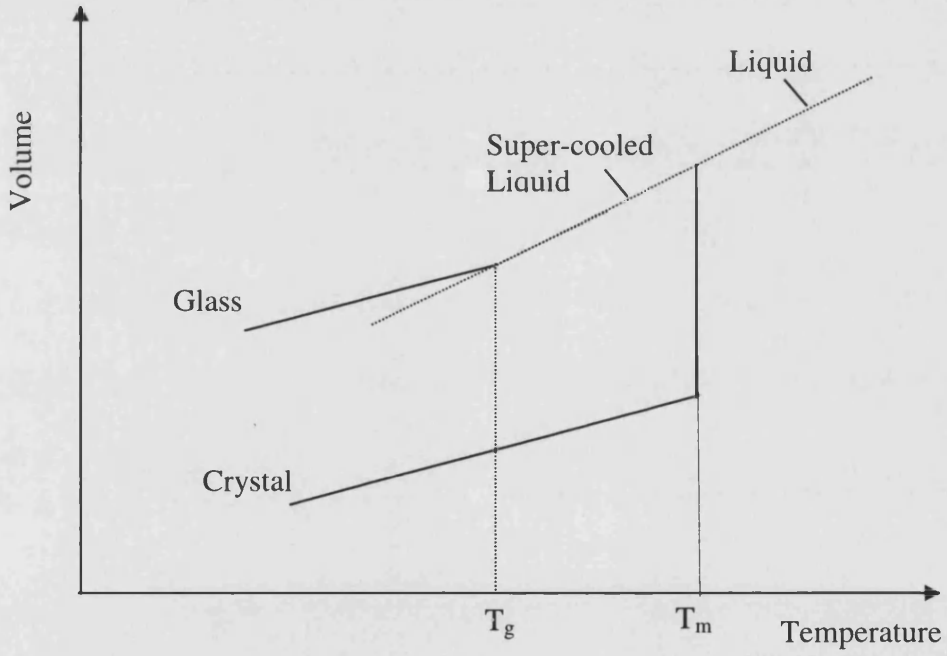

Figure 1.1. The volume-temperature transformation from a liquid to a crystalline or glassy state.

1.3 STRUCTURAL PROBES

The structure of disordered materials can be investigated using a variety of experimental probes including neutron and x-ray diffraction, extended x-ray absorption fine structure spectroscopy (EXAFS), anomalous x-ray scattering and vibrational spectroscopy (e.g. Raman spectroscopy and infra-red spectroscopy).

Neutron diffraction has an advantage, compared to x-ray diffraction, in that it can usually distinguish between elements of similar atomic weight, it can detect light atomic nuclei and the intensity in a neutron diffraction pattern (neglecting magnetic scattering) does not diminish with increasing scattering vector Q. Another advantage of neutron diffraction is the ability to use isotopic substitution methods to separate out the partial structure factors. Furthermore, the method of isomorphic substitution can be applied to chemically similar elements, for example the rare earths, that are adjacent to each other in the periodic table. A central theme of this thesis is therefore to investigate the structure of disordered (glassy and liquid) materials by using the method of isomorphic substitution in neutron diffraction.

1.4 PHOSPHATE NETWORK

In phosphate compounds phosphorus atoms exhibit sp^3 bonding which gives a four-fold co-ordination number and tetrahedral symmetry. Four oxygen atoms arranged at the corners of a tetrahedron surround each phosphorus cation.

In condensed phosphates these PO_4 tetrahedra usually link to give corner sharing configurations and there is no evidence of edge or face sharing. Isolated PO_4 tetrahedra are also known e.g. in rare earth ortho-phosphates.

The rotational flexibility of the P-O-P linking allows four arrangements to occur where 0, 1, 2 or 3 oxygen atoms of a tetrahedron are shared thus allowing chains, rings and branching polymers to be formed. A PO_4 group in which three oxygen atoms are shared with its neighbouring PO_4 groups is called a 'branching

group' Figure 1.2(a). A PO_4 group in which two oxygen atoms are shared with neighbouring PO_4 groups and one oxygen is negatively charged (counterbalanced by a cation) is called a 'middle PO_4 group' Figure 1.2(b). A PO_4 group in which one oxygen atom is shared with a neighbouring PO_4 group and two oxygens are negatively charged is called a 'PO_4 end group' Figure 1.2(c). The last type of group in which there are no bridging oxygen atoms and three negatively charged oxygen atoms is an ortho-phosphate group Figure 1.3.

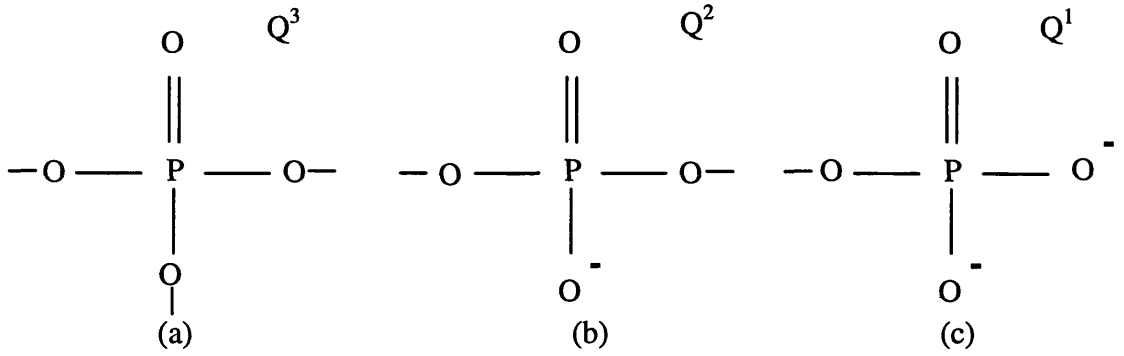

Figure 1.2. The basic PO_4 tetrahedral linking structures:
(a) branching group, (b) middle PO_4 group, (c) PO_4 end group.

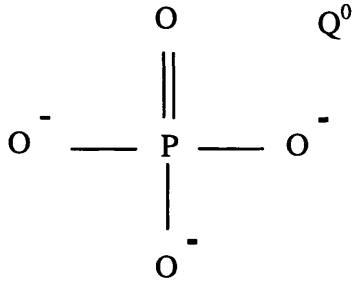

Figure 1.3. The simplest PO_4 tetrahedral group without any bridging oxygen atoms.

The phosphate building blocks are often labelled Q^0 to Q^3 as shown in Figures 1.2 and 1.3. Diffraction studies have confirmed that Q^3 tetrahedra are the basic building blocks of P_2O_5 (Hoppe *et al* 1998). With the addition of network modifiers (metal oxides) these Q^3 units are progressively replaced by twofold–linked tetrahedral Q^2 units. Ultra-phosphates, RP_5O_{14} (where R represents a 3+ rare earth ion), have networks based on a mixture of Q^2 and Q^3 units. Meta-phosphate glasses, RP_3O_9, have

networks based entirely on Q^2 tetrahedra (Brow 2000). The network is completely dissociated for ortho-phosphates, RPO_4, which comprises entirely Q^0 units.

An additional structural unit, called the 'four-way-branching-unit', can exist in mixed phosphates-aluminates, Figure 1.4 (Van Waser 1958). Aluminium acts as an electron pair acceptor for the neutral phosphorus structure and Al is four-fold coordinated by oxygen in a four-way-branching-unit (Figure 1.4). However, Al can also be six-fold coordinated by oxygen as in AlP_3O_9 (Van der Meer 1973) as shown in Figure 1.5. Recent NMR studies suggest that Al can be 4, 5 or 6 fold coordinated in phosphate glasses (Cole *et al* 1999, Karabulut *et al* 2001, Metwalli and Brow 2001).

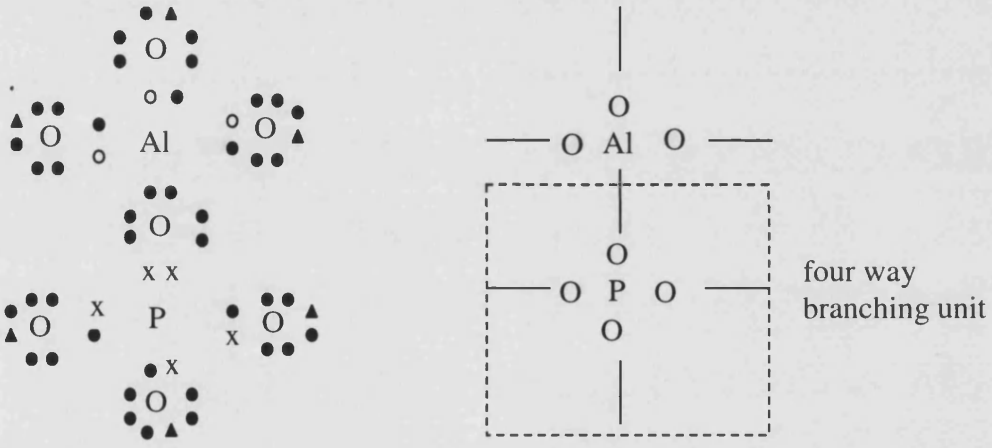

Figure 1.4. Four way branching unit (Van Waser 1958). The P, O and Al electrons are represented by x, • and o respectively and ▲ represents the electrons from atoms not shown.

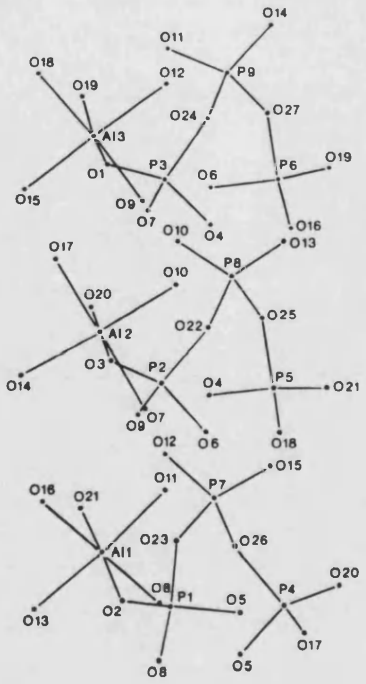

Figure 1.5. Six fold coordinated Al in AlP_3O_9 (Van der Meer 1973).

1.5 LANTHANIDE CONTRACTION

The rare earth elements, or lanthanides, consist of 14 elements from cerium (atomic number 58) to lutetium (atomic number 71). All the lanthanides contain a xenon inner core ($1s^2$ $2s^2$ $2p^6$ $3s^2$ $3p^6$ $3d^{10}$ $4s^2$ $4p^6$ $4d^{10}$ $5s^2$ $5p^6$) with a $6s^2$ level. For the lanthanide series there is a systematic filling of the 4f shell as given in Table 1.1 (Moeller 1973) and there is an associated reduction of the crystal radii (Figure 1.6), a reduction which is often called the 'lanthanide contraction'.

Strictly speaking lanthanum is not a lanthanide due to its lack of 4f electrons; however, the series is often extended to include lanthanum $4f^0$. Lanthanum is often used as a dummy dopant as its properties enable it to be interchanged with the rare earth ions whilst still preserving the overall structure.

Atomic No.	Symbol	Configuration		Hund state		Atomic radius (Å)	Ionic radius (Å)		
		R^0	R^{3+}	R^0	R^{3+}		R^{2+}	R^{3+}	R^{4+}
57	La	$5d^16s^2$	$4f^0$	$^2D_{3/2}$	$^1S_0$	1.877	-	1.061	-
58	Ce	$4f^15d^16s^2$	$4f^1$	$^1G_4$	$^2F_{5/2}$	1.824	-	1.034	0.92
59	Pr	$4f^36s^2$	$4f^2$	$^4I_{9/2}$	$^3H_4$	1.828	-	1.013	0.90
60	Nd	$4f^46s^2$	$4f^3$	$^5I_4$	$^4I_{9/2}$	1.821	-	0.995	-
61	Pm	$4f^56s^2$	$4f^4$	$^6H_{5/2}$	$^5I_4$	1.810^{est}	-	0.979^{est}	-
62	Sm	$4f^66s^2$	$4f^5$	$^7F_0$	$^6H_{5/2}$	1.802	1.11	0.964	-
63	Eu	$4f^76s^2$	$4f^6$	$^8S_{7/2}$	$^7F_0$	2.042	1.09	0.950	-
64	Gd	$4f^75d^16s^2$	$4f^7$	$^9D_2$	$^8S_{7/2}$	1.802	-	0.938	-
65	Tb	$4f^96s^2$	$4f^8$	$^6H_{15/2}$	$^7F_6$	1.782	-	0.923	0.84
66	Dy	$4f^{10}6s^2$	$4f^9$	$^5I_8$	$^6H_{15/2}$	1.773	-	0.908	-
67	Ho	$4f^{11}6s^2$	$4f^{10}$	$^4I_{15/2}$	$^5I_8$	1.766	-	0.894	-
68	Er	$4f^{12}6s^2$	$4f^{11}$	$^3H_6$	$^4I_{15/2}$	1.757	-	0.881	-
69	Tm	$4f^{13}6s^2$	$4f^{12}$	$^2F_{7/2}$	$^3H_6$	1.746	0.94	0.869	-
70	Yb	$4f^{14}6s^2$	$4f^{13}$	$^1S_0$	$^2F_{7/2}$	1.940	0.93	0.858	-
71	Lu	$4f^{14}5d^16s^2$	$4f^{14}$	$^2D_{3/2}$	$^1S_0$	1.734	-	0.848	-

Table 1.1. The electronic configuration, atomic and ionic radii and the spectroscopic notation ($^{2S+1}L_J$) for the rare earth ions (Moeller 1973).

The chemical properties of the rare earth elements are remarkably similar. The valency of the rare earths is usually 3+, although occasionally they exist in a 2+ or 4+ state in order to achieve an empty, half full or full shell, see Table 1.1. The Hund notation, described in many texts e.g. Kittel (1986), is given by $^{2S+1}L_J$ where S is the total spin, L is the total orbital angular momentum and J is the total angular momentum quantum numbers.

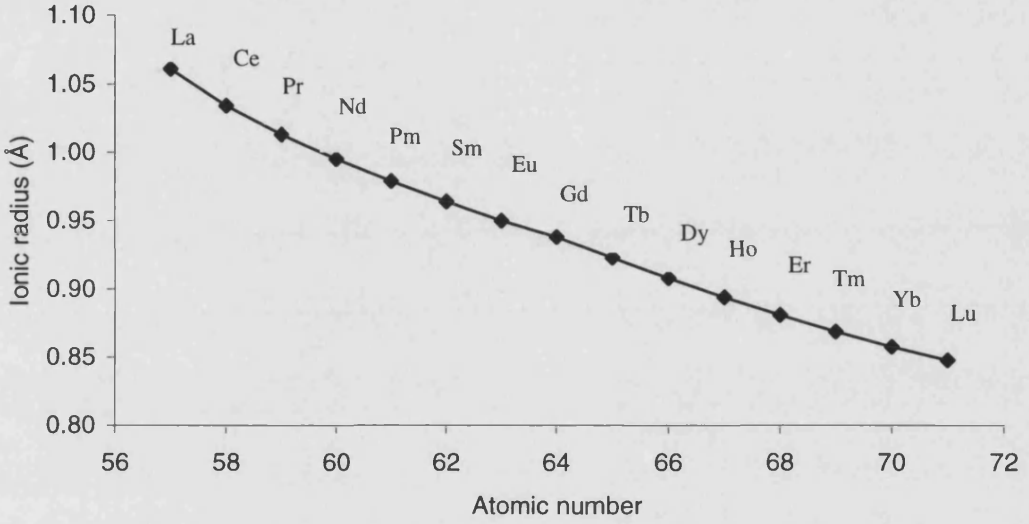

Figure 1.6. Variation of the ionic radii for the rare earth R^{3+} ions (Moeller 1973).

1.6 OUTLINE OF THE PRESENT WORK

In Chapter 2 the preparation and characterisation of rare earth phosphate glasses is described in detail. In Chapter 3 results are presented for the Faraday rotation, optical absorption and the magneto-optical Figure-of-Merit for a series of rare earth phosphate glasses.

In Chapter 4 the theory of neutron diffraction relevant to the present work is summarised and the method of isomorphic substitution is introduced. In Chapter 5 details are given of the neutron diffraction instruments used. The data analysis

procedure required to extract the total structure factors from the measured data is also outlined.

In Chapter 6 the structure of rare earth phosphate glasses containing the larger rare earth ions La^{3+} and / or Ce^{3+} is studied using the method of isomorphic substitution in neutron diffraction and the complexity of the correlations associated with a single diffraction experiment is reduced by using difference function methods.

In Chapter 7 the structure of rare earth phosphate glasses containing the small rare earth ions Dy^{3+} and / or Ho^{3+} is studied using the method of isomorphic substitution in neutron diffraction. Specifically, the pair correlation function describing the R-R correlations is measured for the first time and unprecedented information on the structure of rare earth phosphate glasses is therefore obtained.

In Chapter 8 the structure of molten $TbCl_3$ is studied using neutron diffraction and the effect that truncation of a measured diffraction pattern has on the corresponding real space information is considered. The results are compared to molecular dynamic simulations and discussed by reference to the structure of other rare earth trivalent metal halides.

In Chapter 9 details on the fabrication of rare earth phosphate glass fibres and provisional studies on the lasing properties of these glasses are presented.

In Chapter 10 a summary of the results obtained in this work is given and ideas for future work arising from this thesis are discussed.

REFERENCES

Berger S.B, Rubinstein C.B, Kurkjian C.R and Treptow A.W. 1964. *Physical Review.* **133** (3A) A723.

Blixt P, Nilsson J, Carlnas T and Jaskorzynska B. 1991. *IEEE Transactions Photonics Technology Letter.* **3**. No. 11. p. 996.

Brennan T. 1998. *Structure and Properties of Rare Earth Metaphosphate Glasses.* PhD. Thesis, University of Bath. UK.

Brennan T. Saunders G.A. Rainford B.D.R, Eccleston R, Carini G, D'Angelo and Tripodo G. 1999. *Philosophical Magazine B.* **79.** No. 11/12. p. 2121.

Brow R.K. 2000. *Journal of Non-Crystalline Solids.* **263&264**. p. 1.

Cole J.M, van Eck E.R.H, Mountjoy G, Newport R.J, Brennan T and Saunders G.A. 1999. *Journal of Physics: Condensed Matter.* **11**. p. 9165.

Hutchinson J.A and Allik T.H. 1992. *Applied Physics Letters.* **60**. No. 12. p. 1424.

Hoppe U, Walter G, Barz A, Stachel D and Hannon A.C. 1998. *Journal of Physics: Condensed Matter.* **10**. p. 261.

Karabulut M, Metwalli E and Brow R.K. 2001. *Journal of Non-Crystalline Solids.* **283**. p. 211.

Kittel C. 1986. *Introduction to Solid State Physics.* John Wiley & Sons. Chichester. UK.

Marion J.E and Weber M.J. 1991. *European Journal Solid State Inorganic Chemistry.* **28**. p. 271.

Metwalli E and Brow R.K. 2001. *Journal of Non-Crystalline Solids.* **289**. p. 113.

Moeller T. 1973. *The Chemistry of THE LANTHANIDES.* Pergamon Press. Oxford UK.

Van der Meer. 1973. *Acta Crystallographic.* **B32**. p. 2423.

Van Waser J.R. 1958. *Phosphorus and its compounds. Volume I Chemistry.* Interscience Publishers, London. UK.

Wagener J.L, Wysocki P.F, Digonnet M.J.F, Shaw H.J, Edward L and DiGiovanni D.J. 1992. *Proc. SPIE Fibre Laser Sources and Amplifiers IV.* **1789**. p. 80.

CHAPTER 2
PREPARATION AND CHARACTERISATION OF RARE-EARTH PHOSPHATE GLASSES.

2.1 INTRODUCTION

In recent years numerous groups using a variety of manufacturing techniques have prepared rare earth phosphate glasses. For example, the materials can be prepared by melting the crystalline $R(PO_3)_3$ form and rapidly quenching (Hoppe *et al* 1988). They can also be formed by melting appropriate quantities of ammonium dihydrogen orthophosphate, Al_2O_3 and rare earth oxide (Shikerkar *et al* 2000). Another method involves melting P_2O_5 and R_2O_3 in sealed silica ampoules (Hoppe *et al* 2002). Rare earth phosphate glasses prepared at the University of Bath use rare earth oxides, typically R_2O_3 (with the notable exceptions of CeO_2 and Pr_6O_{11}) and phosphorous pentoxide, P_2O_5, heated in alumina crucibles.

Different parts of the procedure, which include the initial moisture level of the P_2O_5, crucible type, atmosphere and heating and quenching process, all contribute to the exact composition and structure of the resultant glasses. Moisture present during the heating process may act as a catalyst allowing intermediate phases to form, such as phosphoric acids, resulting in different PO_4 groups. Impurities from crucibles, e.g. silicon or aluminium, can leach into the resultant glasses. Much of the work conducted on rare earth glasses looks at effects that different rare earth ions across the lanthanide series have on a given property and any comparison must therefore rely on the glasses being identical in every other aspect. It is with this in mind that a careful approach has been adopted to ensure that the samples used within this work were all made in an identical self-consistent manner.

It is only recently that the compositions of the glasses made in Bath have been fully characterised using X-ray analysis. In the earliest work (Mierzejewski *et al* 1988) it was assumed that the resultant glasses would be determined simply by the ratio of R_2O_3 and P_2O_5 used in the starting mix placed in the crucibles. It has since been discovered that excess P_2O_5 sublimes and the glass always tends to the stable

metaphosphate composition. It has also recently been discovered using an Electron Probe Microanalyser (EPMA) (by the author) and independently through NMR measurements (Cole *et al* 1999) that these glasses contain a significant amount of aluminium contamination emanating from the crucible. Such contaminants can have a significant effect on the overall structure and network properties of a given glass. Aluminium impurities can incorporate themselves into the PO_4 network, providing additional bridging sites (section 1.4), which strengthen the network and therefore alter the hardness and elastic properties of the material. It has been shown that glasses containing aluminium are much less brittle than those containing no aluminium (Cole, private communication). Even small amounts of aluminium as low as 0.2 – 0.5 mole percent have been shown to increase the fluorescence intensity and transition probabilities considerably in rare earth ions (Patra *et al* 1998).

2.2 THE FORMATION OF PHOSPHORIC ACIDS

In an initial attempt to control the glass composition the rare earth oxide and phosphorous pentoxide were weighed and mixed in a dry glove box environment before being instantly transferred into a pre-heated furnace. Attempts to pour glasses prepared in this way, however, proved to be unsuccessful. It was found that mixing the chemicals for six or seven minutes in air whilst allowing small amounts of water to be absorbed from the atmosphere made fabrication of the glasses far easier. It has also been shown that by adding small amounts of water and leaving the mixture exposed to the atmosphere over night allows glasses to be heated and poured from much lower temperatures (Cole, private communication). It is therefore assumed that water acts as a catalyst in the first stage of the reaction allowing the formation of phosphoric acid. With the addition of water the reaction with the oxide is initiated prior to heating, thus enabling the reaction to occur more easily. Figure 2.1 illustrates the formation of different forms of phosphoric acid dependent on the amount of water present and the activation temperature.

The different reactions are given in equations 2.1-2.6. Water absorbed from the atmosphere reacts with the phosphorus pentoxide to form meta-phosphoric acid. Upon heating with excess water the metaphosphoric acid forms a pyro-phosphoric and then a ortho-phosphoric acid as given in equations 2.2 and 2.3 respectively. Continued heating to 220 °C and 330 °C reverses equations 2.2 and 2.3 resulting in metaphosphoric acid as given by equations 2.5 and 2.6.

$$P_4O_{10} + 2H_2O \xrightarrow{\text{cold}} 4HPO_3 \quad [2.1]$$

$$2HPO_3 + H_2O \xrightarrow{\text{boiling}} H_4P_2O_7 \quad [2.2]$$

$$H_4P_2O_7 + H_2O \xrightarrow{\text{boiling}} 2H_3PO_4 \quad [2.3]$$

$$P_4O_{10} + 6H_2O \xrightarrow{\text{hot}} 4H_3PO_4 \quad [2.4]$$

$$2H_3PO_4 \xrightarrow{220°C} H_4P_2O_7 + H_2O\uparrow \quad [2.5]$$

$$H_4P_2O_7 \xrightarrow{320°C} 2HPO_3 + H_2O\uparrow \quad [2.6]$$

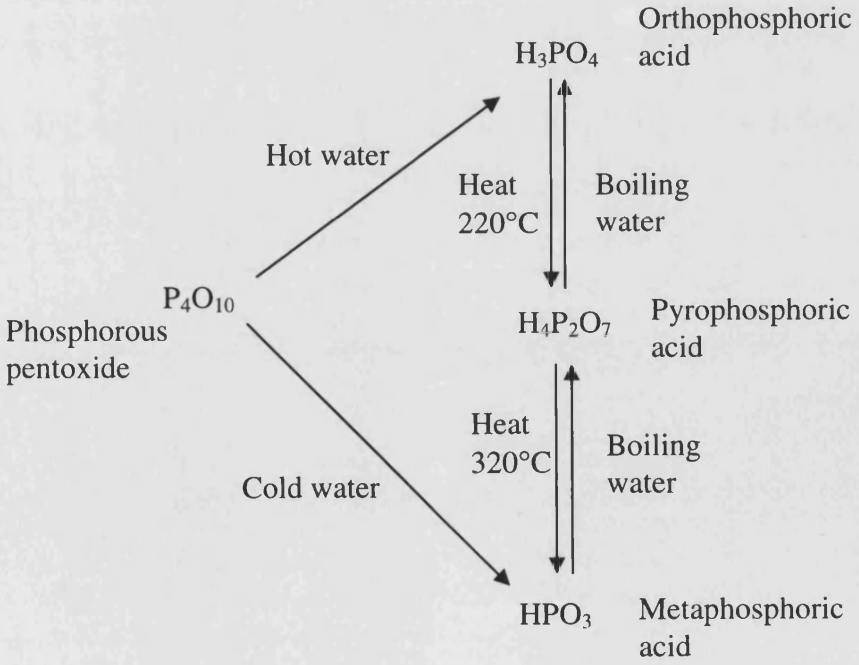

Figure 2.1. Formation of phosphoric acids upon addition of water and heating (Hicks 1971).

2.3 PHOSPHATE UNITS

There are four distinct PO_4 units, termed orthophosphate, branching, middle and end units, as described in section 1.4. During the heating process these structural units are free to combine with other structural units as illustrated below in Figures 2.2 – 2.5 (Van Waser 1958) where M represents a monovalent cation or one third of a triply ionised rare earth ion. Note that a rare earth ion can bind to more than one phosphate unit.

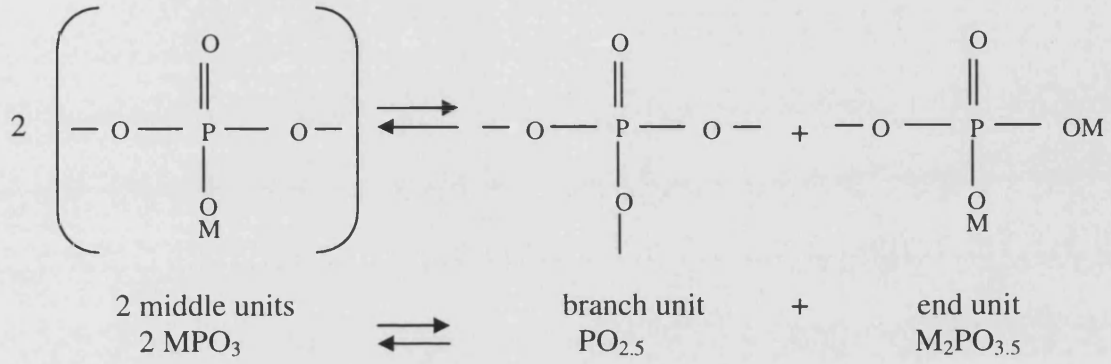

Figure 2.2 Recombination of two middle units to form a branch and an end unit.

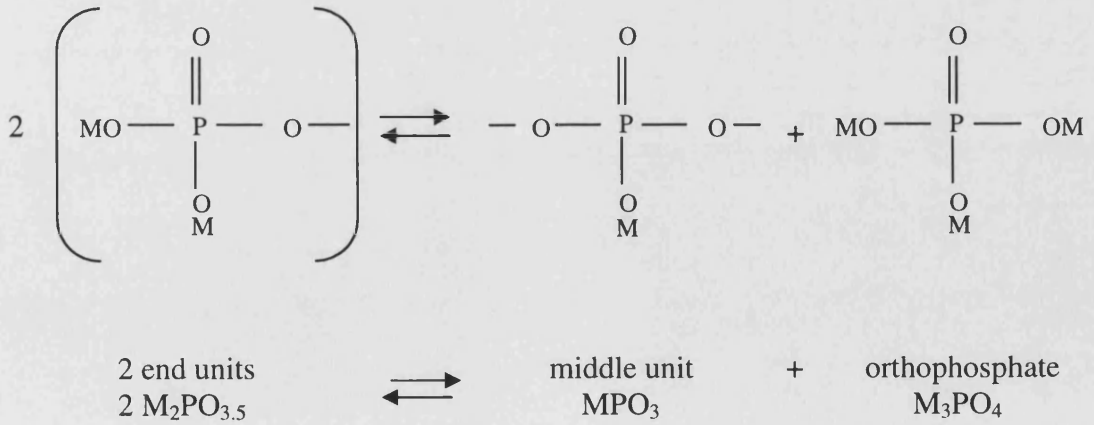

Figure 2.3. Recombination of two end units to form a middle unit and an orthophosphate unit.

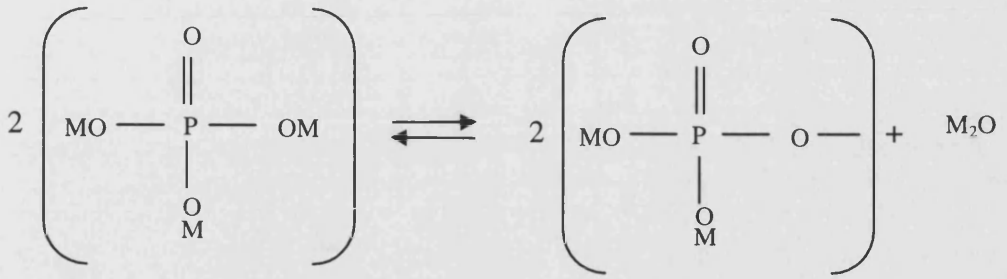

2 ortho units
2 M_3PO_4

2 end units
$M_2PO_{3.5}$

+ M_2O

Figure 2.4. Recombination of two orthophosphate units to form two end units and M_2O.

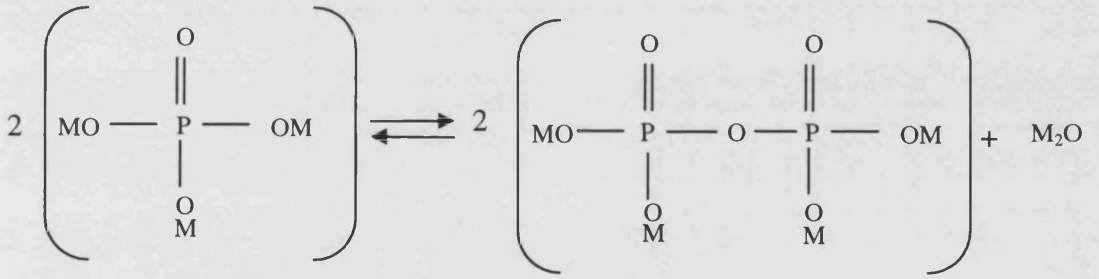

2 orthophosphates
2 M_3PO_4

2 pyro units
$M_4P_2O_7$

+ M_2O

Figure 2.5. Recombination of two orthophosphate units to form a pyro unit and M_2O.

Due to the degrees of freedom exhibited by the PO_4 units it is important that the glasses are prepared in as near identical conditions as possible. This will hopefully ensure that the PO_4 groups in the resultant glasses occur in a similar ratio.

2.4 MANUFACTURING PROCESS

Glasses discussed in this work have been prepared using two slightly different methods. The first method, to be described in detail, is that originally employed at the University of Bath (Senin 1994, Brennan 1998). A refined version of the original method was also employed, in order to reduce the number of variables between different glasses.

The following safety precautions were observed when preparing the samples. Gloves and a dust mask were worn whilst handling chemicals. When transferring crucibles between furnaces, a high temperature reflective jacket and gloves were worn and the crucible was manipulated using long handled tongs (0.5m). A protective face shield with darkened welding visor was worn allowing the crucible to be viewed for the pouring process.

In the original method of preparation the glassware and crucibles were rinsed with acetone and dried. The proportions of P_2O_5 (99 %) and rare earth oxide (99.9%) required to produce 25 g of glass of metaphosphate composition were then calculated. The phosphorus pentoxide was placed in a beaker and covered with the rare earth oxide to reduce the absorption of water from the atmosphere. At this stage approximately 2-3 g of excess phosphorus pentoxide was added to cover losses during the heating process. The chemicals were then stirred, whilst exposed to the atmosphere, for 6-7 minutes to ensure a uniform mix and were then transferred into an alumina crucible, covered with a lid and placed in a furnace at 500 °C. It has been shown that excess P_2O_5 sublimes to produce a glass of approximately metaphosphate composition provided there is sufficient P_2O_5 present (Senin 1994). Since phosphorus pentoxide has a low melting point (580 °C) and sublimes at 395 °C under atmospheric pressure, the chemicals were heated in three stages. The chemicals were left in the first furnace at 500 °C for a minimum of 30 minutes. The crucible was transferred into a second furnace preheated to 1000 °C and allowed to react for a minimum of 30 minutes. The crucible was then transferred into a third furnace preheated to approximately 1600 °C. The chemicals were left to react and become molten for approximately 30 minutes before being poured into a graphite mould preheated to 500

°C. The glass was then left to anneal at 500 °C for 24 hours. Preheating the graphite mould and annealing the glass help to reduce thermal stresses. After 24 hours the furnace was switched off and the glass was allowed to cool slowly down to room temperature at a rate of about 1 degree per minute.

In the present work the above method was refined to reduce variables in the procedure. Firstly, the glassware used during the weighing process was cleaned using chromic acid and then rinsed thoroughly using distilled water. Spatulas were rinsed thoroughly using micro-solution followed by distilled water. The alumina crucibles were cleaned using distilled water and then dried in an oven at 150 °C for three or four hours. Due to the hydroscopic nature of phosphorous pentoxide the container was only opened in a dry glove box, containing less than 10 ppm water where weighing took place. Chemicals were weighed out in the ratio 0.85 mol % P_2O_5 and 0.15 mol % R_2O_3 using an electronic balance accurate to 0.1 mg. Rare earth oxides not in the form R_2O_3 were weighed out such that the rare earth content was equal to 0.15 mol % and there was an excess of oxygen. Although excess P_2O_5 is known to sublime, resulting in a glass of approximately metaphosphate composition, care was taken to ensure accurate weighing to reduce variation between samples. This is in contrast to the original method where P_2O_5 was weighed in air and an arbitrary excess added. The total weights of the rare earth oxide and phosphorus pentoxide were combined to give 25 g, allowing a suitable sized ingot to be made.

Once the chemicals had been weighed they were removed from the glove box and placed on a balance exposed to the atmosphere and stirred for six or seven minutes whilst allowing the P_2O_5 to absorb approximately 100 mg of water. Allowing the phosphorous pentoxide to absorb a small amount of water from the atmosphere will result in the formation of metaphosphoric acid as given in equation 2.1.

After mixing the chemicals were placed into a closed alumina crucible and transferred into a preheated furnace at 500 °C for one hour, allowing the P_2O_5 to react with the rare earth oxide. The rapid heating coupled with the lack of excess water reduces the probability of the metaphosphoric acid reacting via equations 2.2 and 2.3 thus ensuring that the reaction is mainly a metaphosphoric one. This is consistent with

the compositional analysis (section 2.5) which shows the glasses cannot be predominantly $R_4(P_2O_7)_3$ or RPO_4 but are predominantly $R(PO_3)_3$. After an hour the crucible was transferred to a second preheated furnace at 1000 °C and left for 30 minutes. The crucible was then transferred into a third furnace preheated to 1620 °C for the low atomic weight rare earths and 1680 °C for the higher atomic weight rare earths. After 30 minutes the glass was then poured into a preheated graphite mould and annealed at 500 °C as before. Each of the heating stages was carefully timed to ensure consistency; this is again in contrast to previously made glasses where the times were only approximate. Indeed, in certain instances the chemicals were left for several days at 500 °C until the other furnaces became available. Whilst this has not been proven to have any detrimental effect on the formation of these glasses it was felt that since aluminium impurities are known to emanate from the crucibles a fixed heating schedule would be more suitable.

The resulting glasses are transparent, free of stresses and bubbles. The glasses are coloured according to the rare earth dopant present as given by Table 2.1. No evidence for crystalline impurities could be found from neutron diffraction experiments as indicated by the absence of sharp Bragg peaks in Figure 2.6.

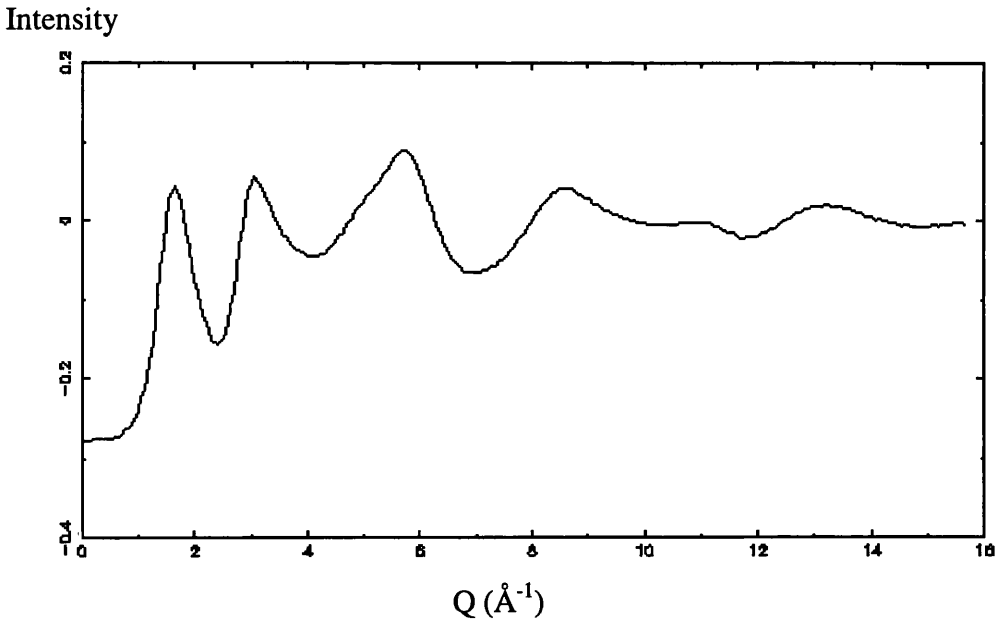

Figure 2.6. A neutron diffraction pattern of $HoP_{2.77}O_{9.39}Al_{0.25}$ illustrating the absence of Bragg peaks.

Rare Earth Dopant	Glass colour	Standard
Y	Colourless	Y
La	Colourless	LaP_5O_{14}
Ce	Yellow	Ce coil
Pr	Green	PrP_5O_{14}
Nd	Purple	$NdAl_2$
Sm	Yellow	SmS
Eu	Pale pink	EuS
Gd	Colourless	$GdAl_2$
Tb	Colourless	$Tb_3Fe_5O_{12}$
Dy	Colourless	DyF_3
Ho	Orange/pink	HoF_3
Er	Pink	ErF_3
Tm	Pale green	TmF_3
Yb	Colourless	YbF_3

Table 2.1 Rare earth glass colour and standard used during the EPMA compositional analysis.

2.5 COMPOSITIONAL ANALYSIS.

A small amount of each glass was analysed using a JEOL JXA 8600 M electron-probe micro analyser (EPMA). A brief explanation of the operation of an EMPA will be given here but for a more detailed review see Goodhew and Humphreys (1988). An electron probe micro analyser bombards the material with a finely focused beam of high-energy electrons. This results in the emission of characteristic X-rays whose wavelengths depend on the nature of the atoms being probed. Measuring the wavelength (or energy) of these characteristic X-rays provides qualitative information on the atoms present as shown in Figure 2.7. Quantitative information is obtained by monitoring the number of each X-ray emitted per second.

The electron probe microanalyser is fitted with four wavelength dispersive crystals, which filter the incoming X-ray radiation such that only the wavelengths of interest can propagate through to the detector. These crystals are placed in selected orientations allowing different energy ranges to be monitored for each of the elements present.

The sample surface must be flat and polished before it can be probed using the EPMA. A small fragment of glass is mounted in resin, which is then pumped down to low pressure encouraging air bubbles to escape from the resin. Any air bubbles at the surface would impede the polishing process. Once the resin has been allowed to cure the samples are polished. Epoxy resin is used to ensure that the resin and sample are of similar hardness and are worn and polished at the same rate. The edges of the sample are first smoothed to stop tearing or excessive wear of the polishing/ grinding papers. Initially a coarse 200-grit paper rotating at 150 rpm with a load of 5 lb per sample is used to remove any large variations in surface height and remove the resin so the sample surface is exposed. Once the resin has been worn sufficiently and the glass surface exposed, finer 1000 and 2500 grit papers are used. After each polishing stage the samples are rinsed using distilled water since tap water has particles sufficiently large to impair the polishing process. The samples are sprayed with methylated spirit and gently dried with a hair dryer to avoid smear marks appearing on the sample. Once the sample has been polished using the 2500 grit paper a metlap

10 plate with a 9 micron oil base diamond paste are used to polish the sample. The sample is then polished using a 3-micron diamond paste on a metlap 4 plate rotating at 220 rpm with a load of 5 lb per sample. The final polish uses 0.06 micron colodial silica on a tex met cloth. After polishing the sample was placed in an ultrasonic water tank to remove the remaining silicon carbide. The samples are now ready to be mounted and analysed.

To avoid the unwanted build up of charge on the sample surface, non-conducting samples and standards are coated in a thin layer of carbon. The coated samples and standards were carefully positioned at the same height and as tilt free as possible into a mounting plate and a conducting coat applied to ensure that the sample and mounting plate are at a constant potential. The mounting plate is placed into the outer housing of the EPMA, which is then evacuated before the samples are transferred into the main chamber. A stable 15 kV beam is used with a current of 5 x 10^{-8} A. The beam is allowed to stabilise for an hour prior to analysing the samples. Standards (Table 2.1) of known composition are analysed first to provide concentration reference levels. The sample was scanned and a suitable area, free from defects, located. Firstly a qualitative spectrum such as Figure 2.7 is measured. By comparing the wavelengths with those of the known standards, the elements present are identified. Peaks that do not correspond to those of the standards, therefore arise from unwanted impurities. It was using this qualitative spectrum that the aluminium impurities were first identified.

The electron beam uses a finely focused beam and therefore only probes a few square microns per scan. Therefore it is important to probe several areas across the sample surface, typically eight per sample, to check for uniformity. An example of the composition analysis data given by the EPMA is shown Table 2.2.

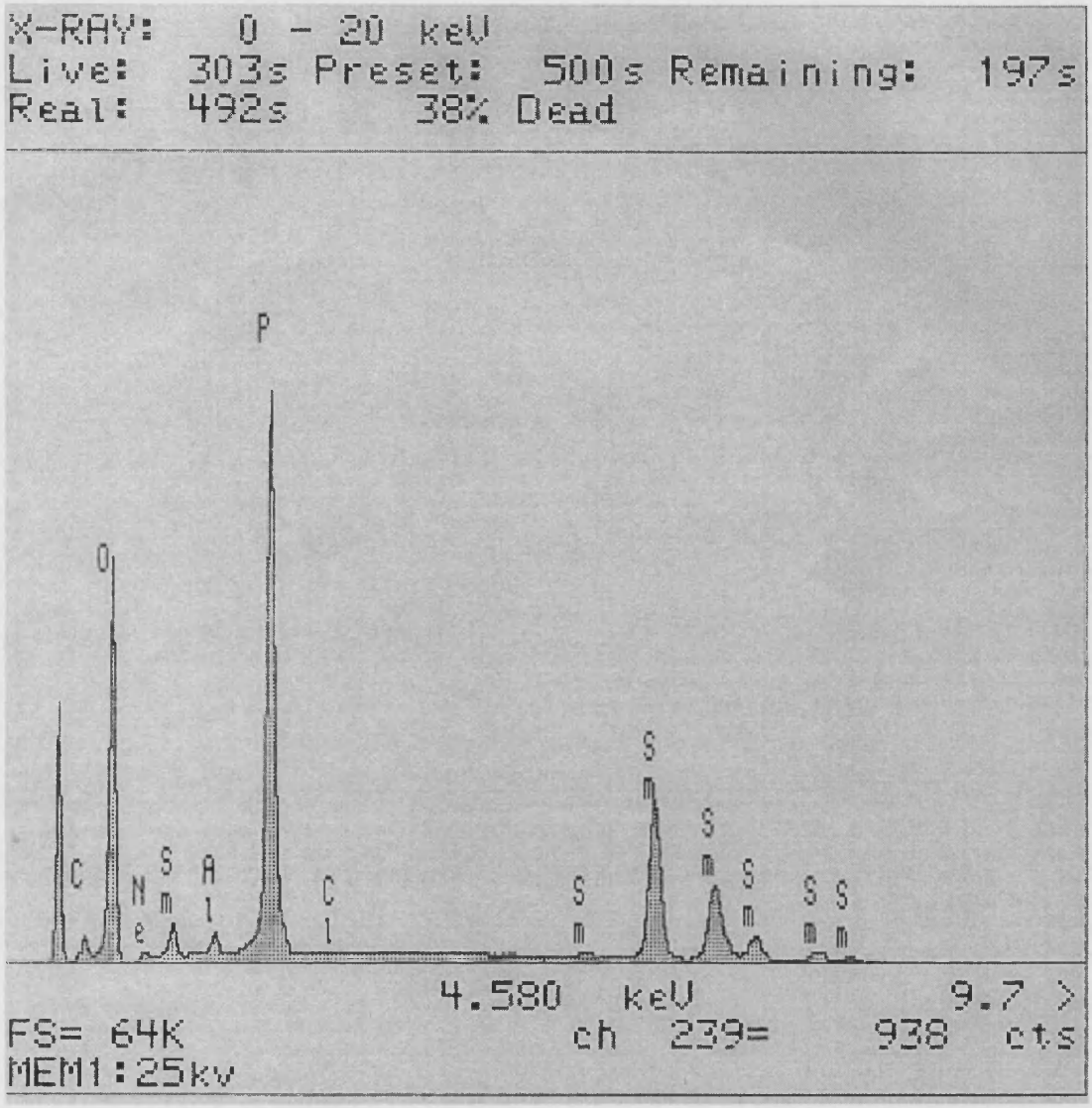

Figure 2.7. Qualitative spectra of a samarium rare earth phosphate glass.

Accelerator Voltage: 15.0 (kV)

	Mean atomic %	Standard deviation %
Dy	7.232	0.093
P	20.826	0.194
O	70.133	0.071
Al	1.809	0.108
Total	100	

Table 2.2. The composition and standard deviation determined using EPMA analysis. Measurements are an average of six points measured across the sample surface.

In previous work (Senin 1994, Brennan 1998) the aluminium content was not quantified and the data presented in Table 2.2 was always written in the form $(R_2O_3)_x(P_2O_5)_{1-x}$ where x is the mole fraction. The metaphosphate composition corresponds to x = 0.25 and the ultra-phosphate corresponds to x = 0.167. It was therefore considered appropriate to describe glasses in this form. The sum of the mean atomic %s for R and P were normalised to give one and the ratio of R:P then gave x:1-x respectively. For example, the glass presented in Table 2.2 would be written as $(R_2O_3)_{0.258}(P_2O_5)_{0.742}$ giving 63 atomic % oxygen. However, the data of Table 2.2 shows that the oxygen content is 70 atomic %. Trying to force the glass composition into the form $(R_2O_3)_x(P_2O_5)_{1-x}$ is therefore unacceptable and can result in large errors (10% or greater) in the oxygen content. Hence, in the present work, the atomic fraction of each element was normalised with respect to the rare earth component such that the dysprosium glass given in Table 2.2 is written as $RP_{2.88}O_{9.70}Al_{0.25}$. The ideal metaphosphate composition is given by RP_3O_9, whilst the orthophosphate and ultra-phosphates are represented by RPO_4 and RP_5O_{14} respectively. Therefore it is concluded that these glasses tend towards the metaphosphate composition and cannot be predominately orthophosphate or ultra-phosphate in composition. The errors on the composition were determined from the standard deviation of the measurements made at different parts of the glass in the EPMA analysis.

The composition of glasses prepared using the refined method and the original method are presented in Table 2.3. The aluminium and exact oxygen content of glasses prepared and analysed by Senin (1994) is not known since the composition

	Atomic %	average	Standard deviation	Standard deviation as %	% difference between extremes
		Glasses made recently by author			
La	0.231 0.239 0.244	0.238	0.006	2.64	5.36
Ce	0.256 0.265 0.271	0.264	0.007	2.74	5.61
Dy	0.254 0.258 0.261	0.257	0.004	1.41	2.86
Ho	0.266 0.283 0.286	0.278	0.011	3.98	7.73
		Glasses made by Senin (1994)			
Ce	0.226 0.235 0.245 0.254 0.257	0.243	0.013	5.33	13.72
Pr	0.216 0.254 0.256	0.242	0.023	9.31	18.52
Nd	0.191 0.194 0.196 0.234 0.254	0.214	0.029	13.34	32.98
Eu	0.186 0.200 0.208 0.218 0.252	0.213	0.025	11.67	35.48
Tb	0.226 0.247 0.263 0.271	0.252	0.020	7.89	19.91
Ho	0.208 0.220 0.231	0.220	0.012	5.24	11.06

Table 2.3. Composition and deviation between rare earth phosphate glasses made in the present work and by Senin (1994).

was forced into the form $(R_2O_3)_x(P_2O_5)_{1-x}$. Therefore the glasses recently prepared have also been written in the $(R_2O_3)_x(P_2O_5)_{1-x}$ form to allow a direct comparison to be made. It can be seen that the glasses made using the refined method are closer in composition.

As shown in Table 2.4 it is also possible to make a series of glasses containing different concentrations of rare earth ions such as cerium and erbium with very similar overall compositions. Glasses can also be made containing very small quantities of a given rare earth ion, using lanthanum or yttrium as a dummy dopant. This enables glasses to be made that are suitable for lasing or up-conversion.

Ideal composition	Actual composition
CeP_3O_9	$CeP_{2.90}O_{9.03}Al_{0.39}$
$Ce_{0.200}Er_{0.800}P_3O_9$	$Ce_{0.200}Er_{0.800}P_{2.82}O_{9.63}Al_{0.40}$
$Ce_{0.400}Er_{0.600}P_3O_9$	$Ce_{0.407}Er_{0.593}P_{3.00}O_{10.20}Al_{0.48}$
$Ce_{0.500}Er_{0.500}P_3O_9$	$Ce_{0.507}Er_{0.493}P_{3.11}O_{10.58}Al_{0.46}$
$Ce_{0.600}Er_{0.400}P_3O_9$	$Ce_{0.607}Er_{0.393}P_{2.94}O_{9.79}Al_{0..30}$
$Ce_{0.800}Er_{0.200}P_3O_9$	$Ce_{0.806}Er_{0.194}P_{3.08}O_{10.15}Al_{0.46}$
ErP_3O_9	$ErP_{3.20}O_{10.16}Al_{0.16}$

Table 2.4. Series of cerium and erbium rare earth phosphate glasses.

2.6 MEASURING THE DENSITY OF RARE EARTH PHOSPHATE GLASSES

The densities of rare earth phosphate glasses were determined using Archimedes principle. The glasses were weighed using an electronic balance, accurate to 0.1 mg, in air, distilled water and acetone. Each measurement was repeated several times to give an average reading. The temperature of the distilled water and acetone were recorded allowing an accurate density to be obtained. The density of the sample was then calculated using equation 2.7

$$D_s = D_f \frac{W_a}{W_a - W_f}. \qquad [2.7]$$

D_s and D_f are the mass density of the sample and fluid respectively. W_a and W_f are the weight of the sample in air and fluid respectively. Densities measured in acetone and distilled water were in agreement within 0.5 %.

2.7 PREPARATION OF SAMPLES

Glassy samples were prepared according to the type of experiment to be conducted. Split graphite moulds were used to form cylindrical ingots, approximately 10 mm in diameter and 20 mm long, for use in ultrasonic measurements or for drawing fibres. Alternatively, large area plates were formed (Figure 2.8) by pouring onto a flat graphite plate for diffraction experiments. For ultrasonic and optical experiments the samples had be cut and polished to produce flat parallel sides. Samples were mounted onto a cutting platform and a peripheral diamond saw (660 rpm) was applied allowing parallel faces to be cut. Coarse 600-grit carborundum was used to grind the sample before using progressively smaller pastes until a 6-micron diamond paste was used for the final polish. Once prepared the samples were stored in desiccators containing silica gel.

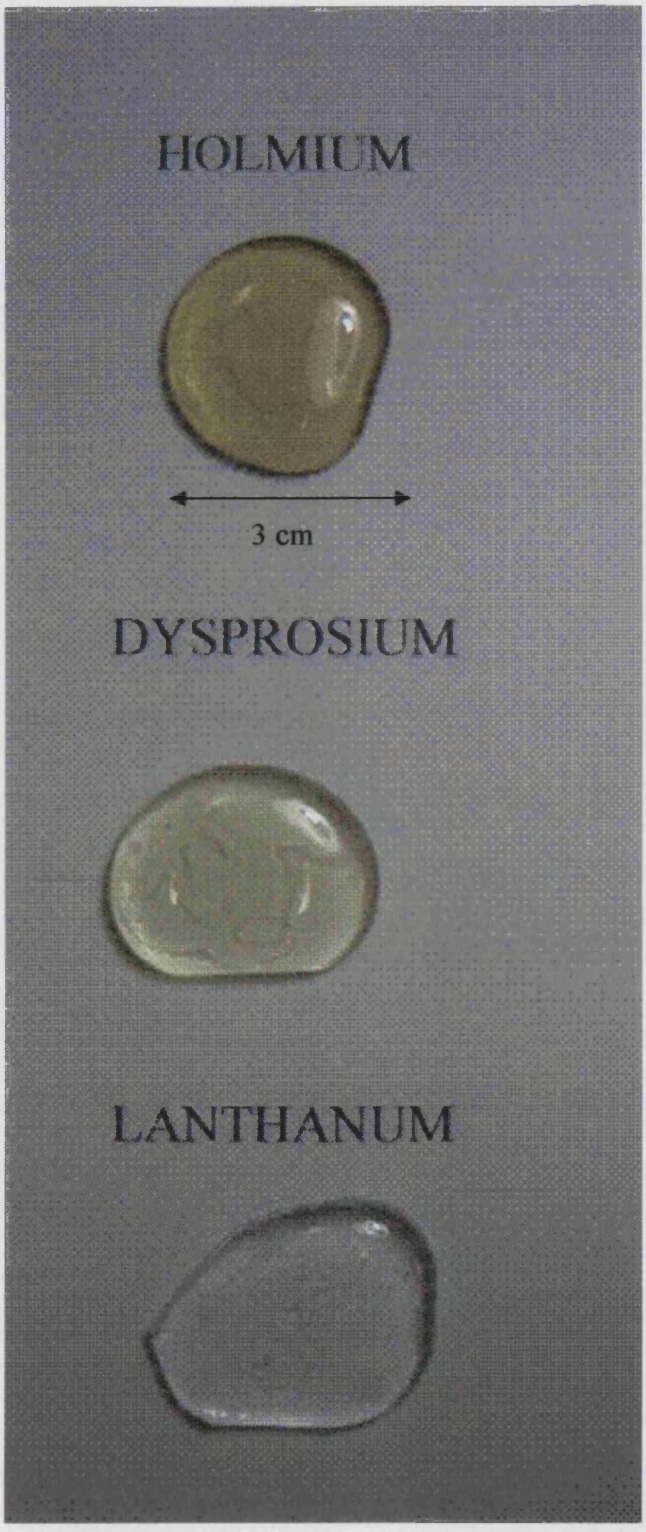

Figure 2.8. Rare earth phosphate glasses.

2.8 PHYSICAL AND MECHANICAL PROPERTIES

In order to cut and polish glasses and for other practical purposes they must posses appropriate mechanical properties. For example, phosphate glasses prepared using platinum crucibles were found to shatter when handled which would seriously limit their practical applications. However glasses prepared using alumina crucibles, as outlined in section 2.4, were found to be very hard and shatter resistant. The glasses were also found to be very resistant to temperature changes allowing Faraday and ultrasonic measurements to be conducted down to 20 K with no obvious detrimental effect to the glass. Susceptibility to moisture, which is often a problem in phosphate glasses, is not believed to be a problem for samples prepared using alumina crucibles (Bowron *et al* 1996). The glasses can also withstand pressures of up to 1200 atmospheres as used in ultrasonic measurements. In an attempt to quantify the hardness of these glasses Vickers hardness measurements were conducted.

A Zwick hardness tester, operating under varying loads, with an impact velocity of 0.3 mm s^{-1} was used to carry out Vickers indentation tests on several samples. The sample surface was mounted and polished as described in section 2.5. A very small diamond pyramid with a 136° angle is forced into the surface of each glass using a variable load. The diagonals of the resulting impression, Figure 2.9, were measured under a microscope and an average value calculated. The Vickers hardness is equal to the force applied divided by the area of indentation and can be related to the applied mass and the diagonal length of indentation as described using equation 2.8 (Callister 1997)

$$\text{Vickers hardness (kg mm}^{-2}) = 1.854 \frac{\text{mass (kg)}}{[\text{diagonal (mm)}]^2}. \qquad [2.8]$$

Measurements were conducted for different applied loads and for glasses doped with different rare earth ions. The hardness was found to be dependent upon the applied mass as shown in Figure 2.10. The dependence of hardness on load is one of the most controversial aspects of indentation hardness and will not be discussed here. Several different mechanisms have been proposed to explain load dependence

involving flow, the movement of dislocations and deformation (for example see Salama and El-Batal 1994). Increasing the applied load resulted in a decrease of the order 10% in the Vickers hardness value for the glasses in the present work. Measurements were also conducted for a constant load of 1 kg on glasses doped with different rare earth ions. The hardness was found to be similar for glasses doped with different rare earth ions as shown in Figure 2.11.

The rare earth phosphate glasses were found to have acceptable mechanical properties and compared well with other phosphate glasses doped with sodium, lithium and potassium which have been reported to have a Vickers hardness between 347-401, 407-464 and 336-386 kg mm^{-2} respectively depending on applied load (Salama and El-Batal 1994).

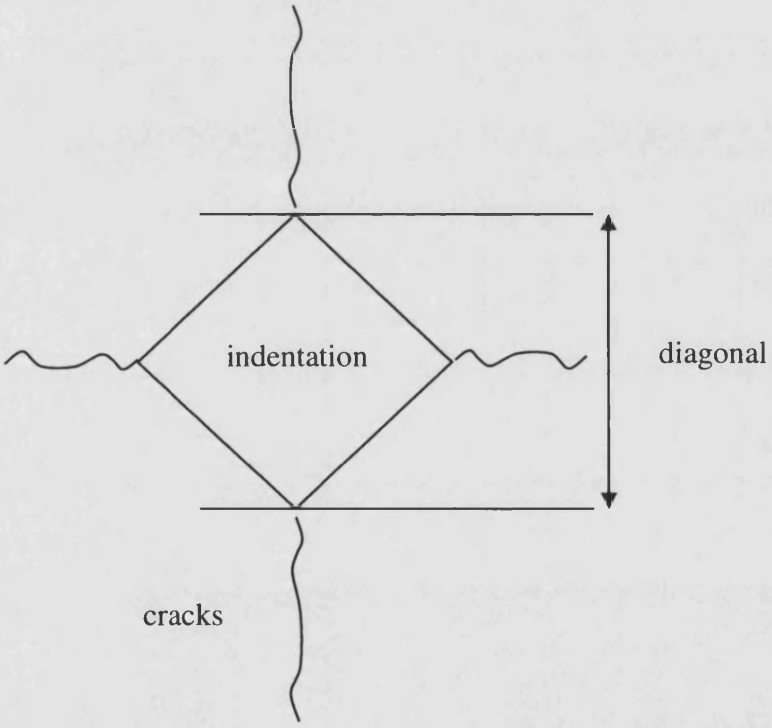

Figure 2.9. Indentation produced by a Zwick hardness tester.

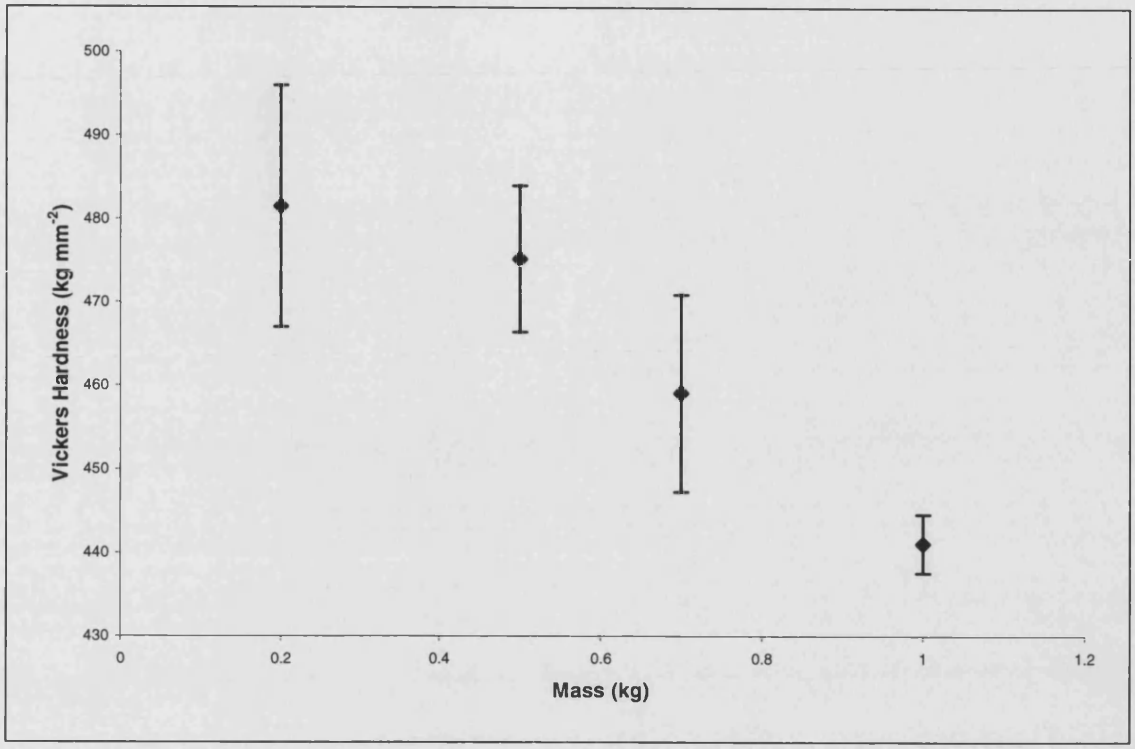

Figure 2.10. Vickers hardness as a function of applied load for $HoP_{3.10}O_{9.70}Al_{0.31}$.

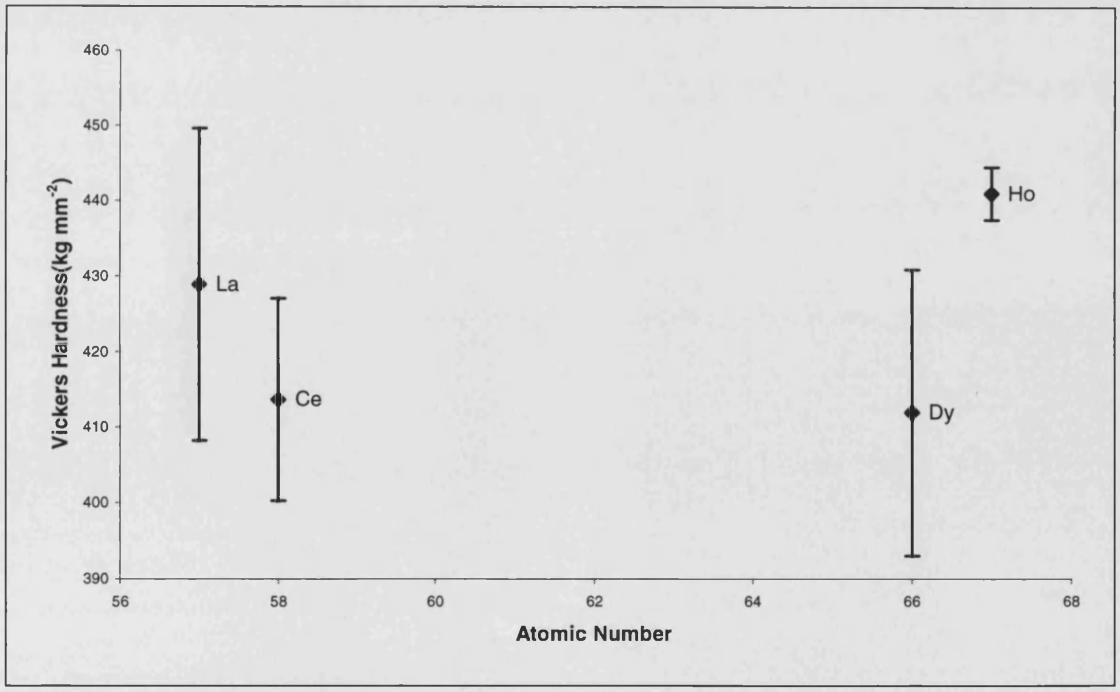

Figure 2.10. The Vickers hardness of $LaP_{3.10}O_{9.70}Al_{0.31}$, $CeP_{2.69}O_{8.92}Al_{0.44}$, $DyP_{2.94}O_{9.63}Al_{0.26}$ and $HoP_{2.50}O_{8.80}Al_{0.30}$ under a constant load of 1.0 kg.

2.9 CONCLUSIONS

Rare earth phosphate glasses have been successfully prepared using a refined version of the methods previously employed at the University of Bath. Attempts have been made to understand the chemical steps involved when forming these glasses and great care has been taken to eliminate variations in sample environment. The resultant glasses formed are of good optical quality, free from visible stresses or bubbles, shatter resistant and resistant to moisture contamination. A thulium phosphate glass has been prepared for the first time at the University of Bath, and glasses have also been successfully made containing ytterbium. Compositional analysis has confirmed that use of a self-consistent procedure results in glasses of closer composition than previously found possible. A quantitative analysis has highlighted the presence of aluminium impurities within these glasses, which originate from the alumina crucibles.

REFERENCES

Bowron D.T, Bushell-Wye G, Newport R.J, Rainford B.D and Saunders G.A. 1996. *Journal of Physics: Condensed Matter.* **8** p. 3337.

Brennan T. 1998. PhD. *University of Bath. UK.*

Callister W.D. Jr. 1997. *Materials Science and Engineering an Introduction. 4th - Edition.* John Wiley and Sons. Chichester. UK.

Cole J.M, van Eck E.R.H, Mountjoy G, Newport R.J, Brennan T and Saunders G.A. 1999. *Journal of Physics: Condensed Matter.* **11** p. 9165.

Goodhew P.J and Humphreys F.J. 1988. *Electron microscopy and analysis. 2nd Ed.* Taylor and Francis. London. UK.

Hicks J. 1971. *Comprehensive Chemistry.* Macmillan; London. UK.

Hoppe U, Kranold R, Stachel D, Barz A and Hannon A.C. 1998. *Journal of Non-Crystalline Solids.* **232-234** p. 44.

Hoppe U, Metwalli E, Brow R.K and Neuefeind J. 2002. *Journal of Non-Crystalline Solids.* **263-274** p. 297.

Mierzejewski A, Saunders G.A, Sidek H.A.A and Bridge B. 1988. *Journal of Non-Crystalline Solids.* **104** p. 323.

Patra A, Reisfeld R and Minti H. 1998. *Materials Letters.* **37** p. 325.

Slama S.N and El-Batal H.A. 1994. *Journal of Non-Crystalline Solids.* **168** p. 179.

Senin H.B. 1994. PhD. *University of Bath. UK.*

Shikerkar A.G, Desa J.A.E, Krishna P.S.R and Chitra R. 2000. *Journal of Non-Crystalline Solids.* **270** p. 234.

Van Wazer J.R. 1958. *Phosphorus and its Compounds. Vol 1.* Interscience Publishers, Inc., New York. USA.

CHAPTER 3

MAGNETIC PROPERTIES. THE FARADAY ROTATION OF RARE EARTH PHOSPHATE GLASSES.

3.1. INTRODUCTION

A magneto-optical property of rare earth oxide glasses that has attracted considerable attention, both theoretical and experimental, since the original works of Berger *et al* (1964), Rubinstein *et al* (1964) and Borrelli (1964), is the Faraday effect. Faraday (1845) discovered that when a beam of plane polarised light passes through a substance its plane of polarisation is observed to rotate by an angle (θ) proportional to the magnetic field strength parallel to the direction of propagation (H) and the path length (l). The constant of proportionality (V) is known as the Verdet constant:

$$\theta = VHl. \qquad [3.1]$$

By convention V has a positive value for polarisations rotated clockwise when looking along the direction of the magnetic field. Therefore θ is in the direction of rotation of a current which would give a field in the direction of H i.e. the rotation of the plane of polarisation can be described using Maxwell's corkscrew rule.

Table 3.1 gives a conversion chart between different units in which the Verdet constant is given in the literature and also gives the Verdet constants for typical materials. In the present work all of the results are given in units of rad T^{-1} m^{-1}.

	rad T^{-1} m^{-1}	min Oe^{-1} cm^{-1} ≡ min $G^{-1}cm^{-1}$	min T^{-1} m^{-1}
Conversion factor	1	3.438×10^{-3}	3438
Water	3.8	0.0131	1.31×10^4
Quartz (⊥ to axis)	4.8	0.0166	1.66×10^4
Glass (light flint)	9.2	0.0317	3.17×10^4
NaCl	10.4	0.0359	3.59×10^4
$TbP_{2.94}O_{9.18}Al_{0.26}$*	-113	- 0.3885	-38.85×10^4

* Current work

Table 3.1. Typical room temperature values of Verdet constants in standard units (Hecht 1987).

The largest Faraday rotation is typically observed in glasses containing Ce^{3+}, Pr^{3+}, Dy^{3+} and Tb^{3+} ions (Berger *et al* 1964, Rubinstein *et al* 1964 and Borrelli 1964). Consequently much of the work in the literature has concentrated on these four rare earth ions and attention has been paid to glass hosts that allow large quantities of rare earth ions to be incorporated such as fluorophosphates (Letellier *et al* 1989), aluminosilicates (Kohli and Shelby 1991) and silico-phosphates, alumino-borates, boro-silicates and barium-borates (Petrovskii *et al* 1991). More recently there has been interest in aluminosilicates (Ballato and Snitzer 1995), fluorozirconates (MacFarlane *et al* 1997) and fluorides (Qiu *et al* 1997b). Amorphous materials are of interest for optical applications because they can be easily fabricated and formed into complex shapes such as lenses and optical fibres.

The Verdet constant has been shown to increase linearly with rare earth concentration (Berger *et al* 1964) and its value also depends on the host glass matrix (Borrelli 1964). Phosphate glasses are therefore advantageous since they have high rare earth solubilities. However, in previous work on these materials (Berger *et al* 1964) the method of preparation and the mechanical properties of the glasses were not discussed. The rare earth phosphate glasses prepared in Bath contain substantial aluminium impurities, which affect the glass matrix and yields favourable mechanical properties (e.g. the impurities give less brittle materials). Unlike many other phosphate glasses, these materials are resistant to moisture contamination (Bowron *et al* 1996). A series of measurements on the Verdet constant for these materials was therefore made and the results compared with other rare earth glasses.

The trend towards miniaturisation drives the continual demand towards materials containing larger Verdet constants, thus enabling magneto-optical devices such as optical isolators, switches and magnetic field sensors to be further reduced in size. Rare earth ions are some of the most magnetic materials known and produce some of the largest Faraday rotations. Many attempts have been made to increase the Faraday rotation in rare earth glasses. Although large Verdet constants can be obtained for diamagnetic glasses (e.g. As_2S_3), paramagnetic glasses that contain high concentrations of rare earth ions are preferred because of their greater durability and lower absorption in the visible and infrared regions (Ballato and Snitzer 1995). For

practical applications the magneto-optical figure of merit, F, is an important value, where F is the ratio of Verdet constant, V, to the optical absorption coeffiecent, α, as given in equation 3.2. Large values of F are desirable since they correspond to large rotations with small losses.

$$F = \left| \frac{V}{\alpha} \right| \qquad [3.2]$$

To assess their suitability for practical applications, the attenuation coefficient of a series of rare earth phosphate glasses was therefore measured, allowing a value for the magneto-optical figure of merit to be calculated.

3.1.1 OPTICAL ISOLATORS

Faraday rotators can be used for a number of applications including optical switches, modulators, field sensors and optical isolators (Kohli and Shelby 1991). A Faraday medium used in conjunction with a pair of polarisers acts as an optical isolator as shown in Figure 3.1. An optical isolator is analogous to an electronic diode, allowing light to propagate in one direction only.

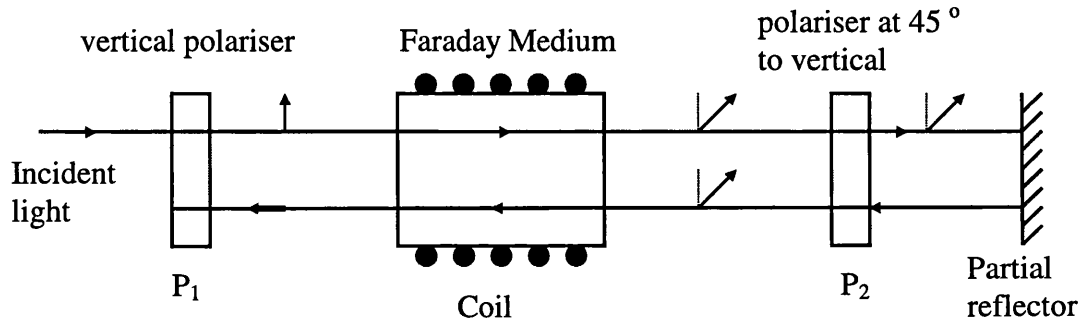

Figure 3.1. An optical isolator.

Light entering the isolator is vertically polarised by the first polariser P_1. The magnetic field and the length of the Faraday rotator are adjusted such that the rotation, θ, is 45 degrees in a clockwise sense. The second polariser, P_2, at 45 degrees transmits light emerging from the Faraday-rotating medium. Thus light travelling through an isolator in the forward biased direction (left to right) is unaffected. A partial mirror (note this is not part of the isolator) is used to represent back reflections occurring in the external optical system. Those back reflected waves, travelling right to left, with suitable polarisations will pass through the second polariser. As the light travels back through the Faraday rotator the light is rotated a further 45 degrees clockwise relative to the field, such that the light emerging from the rotator is entirely in the horizontal plane. The light incident on the second polariser is therefore absorbed and none is allowed to propagate through the isolator i.e. light can only pass through the optical isolator in a single direction. Isolators can be used in laser amplifying chains to eliminate any reflected waves travelling back through the system which could cause damage.

An important difference between Faraday rotators and other optically active mediums is that the sense of rotation is dependent on the direction of the magnetic field and independent of the direction of propagation of the incident light. Consequently when light is passed back and forth through a Faraday rotating medium the rotations continues to increase with each pass. This is not true for a simple birefringent material where the rotation of light travelling through the material is independent of magnetic field and dependent on the direction of propagation (Hecht 1987). It would therefore be impossible to construct an isolator from a simple birefringent material, since multiple passes through the optically active medium would cancel with each other.

3.1.2 WAVELENGTH DEPENDENCE OF V

Linearly polarised light emitted from lasers consists of two circularly polarised components with an opposite sense of rotation. Half of the light is left-handed

polarised and half right-handed polarised. The speed of rotation is determined by the refractive index of the material, which can be thought of as having two components n_l and n_r for left and right circularly polarised light. Applying a magnetic field to the sample induces a change in refractive index. Therefore as the light propagates through a sample one sense rotates faster than the other, resulting in a net rotation and a phase change. The microscopic origin of the rotation of polarisation of light is the inequality in the refractive indices as given by

$$\theta = \frac{2\pi}{\lambda}(n_r - n_l)l \qquad [3.3]$$

where λ is the wavelength and l the optical path length (Wilson and Hawkes 1983). The inequality arises from the magnetically induced splitting of the energy levels associated with the rare earth ions.

The Verdet constant may also be described *empirically* in terms of the incident wavelength, λ, and absorption transition wavelength, λ_t, as given by (Berger *et al* 1964)

$$V = \frac{K}{\lambda^2 - \lambda_t^2} \qquad [3.4]$$

where K is a parameter independent of λ but a function of temperature and concentration. λ_t corresponds to the weighted average of the ultraviolet absorption bands in the material and the proximity to the measurement wavelength.

3.1.3 CONCENTRATION DEPENDENCE OF V

The Verdet constant of glassy $(CeP_3O_9)_a$ $(NdP_3O_9)_{1-a}$, $(0 \leq a \leq 1)$ has been reported to show a linear relationship with concentration of rare earth ion (Berger *et al* 1964). For a mixed rare earth phosphate glass of nominal composition $^1R_x{}^2R_{1-x}P_3O_9Al_{0.2}$ it is anticipated that the total Verdet constant, V, can also be expressed in terms of the rare earth concentration using

$$V = \sum_{n}^{\infty} N_n v_n \qquad [3.5]$$

where v_n represents the Verdet constant of the rare earth ion ^nR divided by the number density N_n of those ions. Linearity is anticipated due to the isolated nature of the rare earth 4f electrons and the relatively large distance between rare earth ions (Chapters 6 and 7).

3.1.4 EXPERIMENTAL METHOD

The Faraday rotation and Verdet constant were investigated in rare earth phosphate glasses of nominal composition $RP_3O_9Al_{0.2}$. Samples were cut and polished to give flat parallel opposite sides. Samples varied in thickness between 3 and 10 mm. Larger samples were preferable since these result in larger rotations, but some of the glasses absorbed strongly in the spectral region of interest. Thus a trade off between the rotation of polarisation and optical absorption dictated sample dimensions. The glasses were placed in a uniform magnetic field as shown in Figure 3.2 between two polarisers, the first of which was adjusted to give maximum transmission of the laser light. A silicon photodiode was used as the detector.

The Verdet constant was measured at six wavelengths: 457.9, 476.5, 488.0, 496.5, 501.7 and 514.5 nm emitted by an argon laser and the magnetic field, measured using a Gauss meter, was varied between 0.1 and 1.4 T in 0.1 T steps. The second polariser was rotated to find the minimum transmission and the angle recorded. The magnetic field was varied and the second polariser rotated until the transmission was again a minimum and the angle of the polariser was recorded. The difference between the two angles corresponds to the rotation induced due to the change in magnetic field.

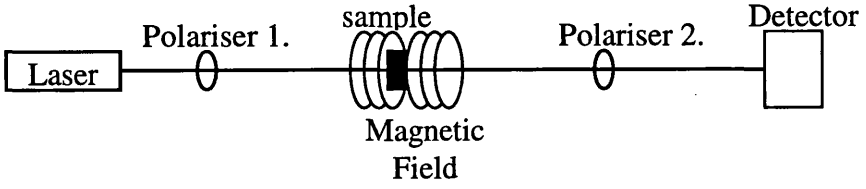

Figure 3.2. The experimental set-up to measure the Faraday rotation.

3.2 RESULTS AND DISCUSSION OF FARADAY ROTATION EXPERIMENTS

3.2.1 RARE EARTH ION AND WAVELENGTH DEPENDENCE

The rare earth ion and wavelength dependence of eight rare earth phosphate glasses were investigated. The rare earth phosphate glasses studied, their density and R^{3+} ion concentrations are presented in Table 3.2. Using linear regression the Verdet constants at each of the six wavelengths were obtained from equation 3.1 from the plots shown in Figures 3.3 – 3.10 and the results are summarised in Table 3.3. As expected the intercepts were all equal to zero within the experimental errors.

Figures 3.11- 3.17 show λ^2 verses 1/V which give, via equation 3.4, the transition wavelength, λ_t, and parameter K. Through a least squares linear regression fit these parameters could be deduced for the four largest rotators Ce, Pr, Tb and Dy, but equation 3.4 did not hold for Nd, Ho and Er in the wavelength region of interest as illustrated in Figures 3.13, 3.16 and 3.17 respectively. The breakdown of equation 3.4 was attributed to absorption bands, which will be discussed in section 3.2.3. However the measured Verdet constants, v, for Nd, Ho and Er were in good overall agreement with those measured by Berger *et al* (1964) as shown in Figures 3.18 – 3.20.

Rare earth element	Density (kg m^{-3}) $\pm$ 20 kg m^{-3}	R^{3+} concentration (10^{27} ions per m^3) $\pm 0.05 \times 10^{27}$	Composition $\pm$ 0.03
La	3210	4.65	$LaP_{3.43}O_{10.45}Al_{0.10}$
Ce	3250	4.55	$CeP_{3.57}O_{10.73}Al_{0.21}$
Pr	3310	5.15	$PrP_{3.13}O_{9.24}Al_{0.09}$
Nd	3120	3.75	$NdP_{4.31}O_{13.40}Al_{0.23}$
Tb	3530	5.25	$TbP_{2.94}O_{9.18}Al_{0.26}$
Dy	3370	4.60	$DyP_{3.34}O_{10.55}Al_{0.20}$
Ho	3380	4.30	$HoP_{3.43}O_{10.55}Al_{0.55}$
Er	3480	4.85	$ErP_{3.20}O_{10.16}Al_{0.16}$

Table 3.2. Details of the rare earth phosphate glasses studied.

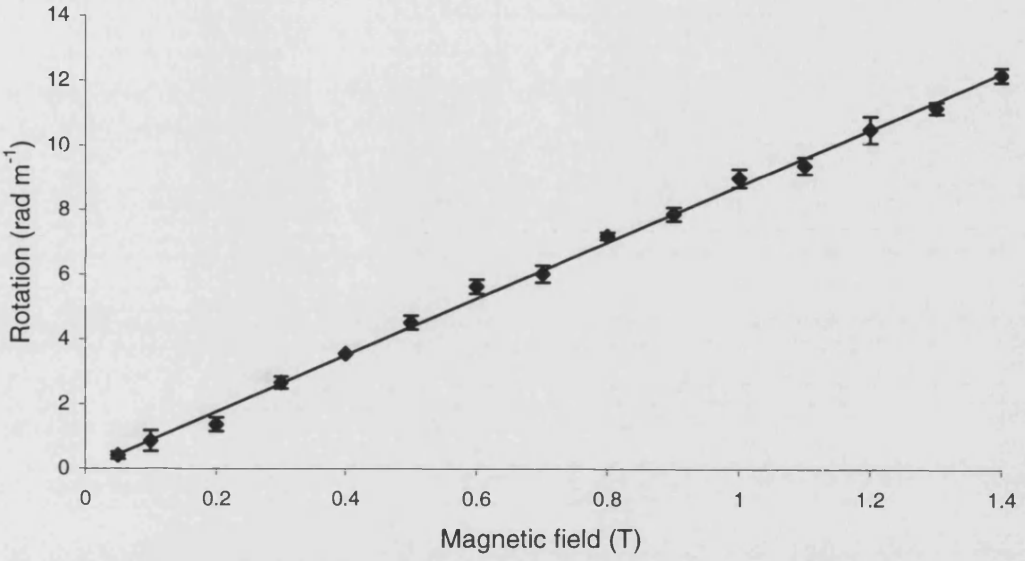

Figure 3.3. The Faraday rotation of La phosphate glass

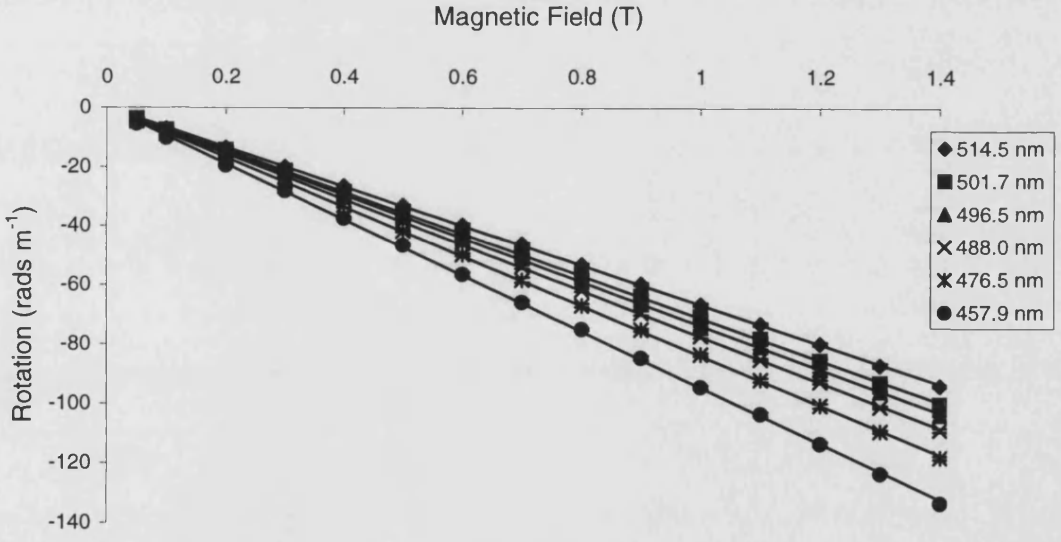

Figure 3.4. The Faraday rotation of Ce phosphate glass

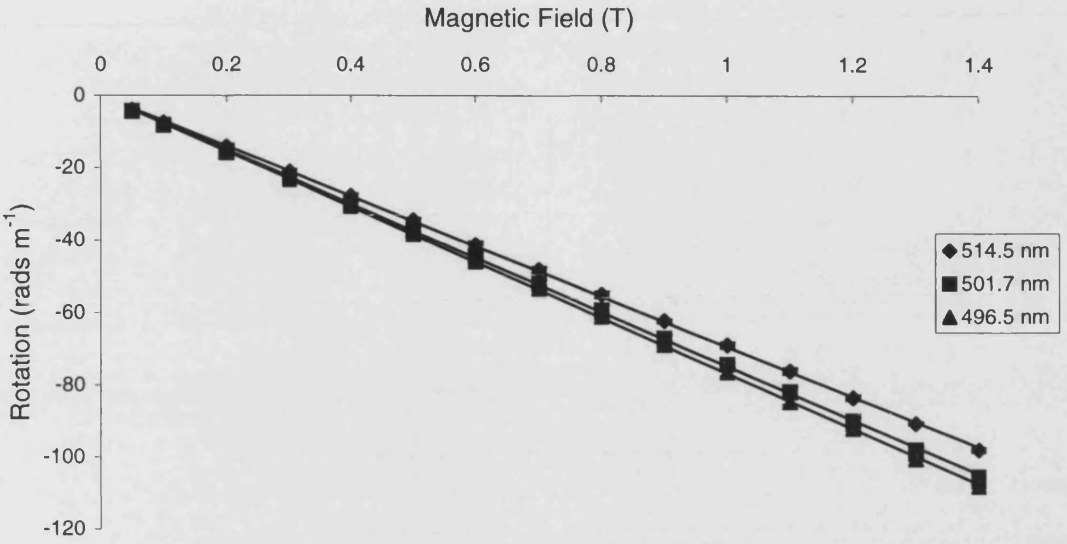

Figure 3.5. The Faraday rotation of Pr phosphate glass.

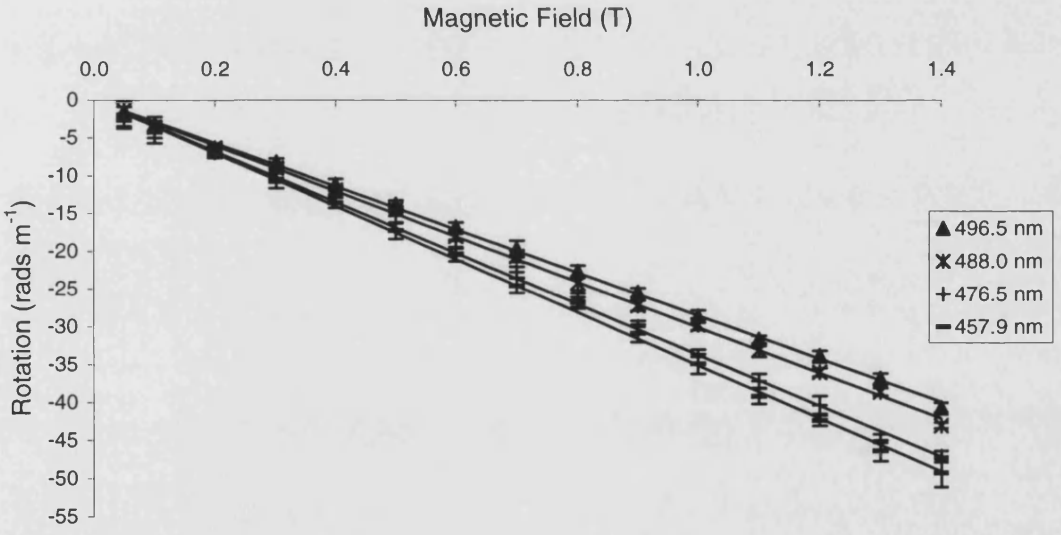

Figure 3.6. The Faraday rotation of Nd phosphate glass.

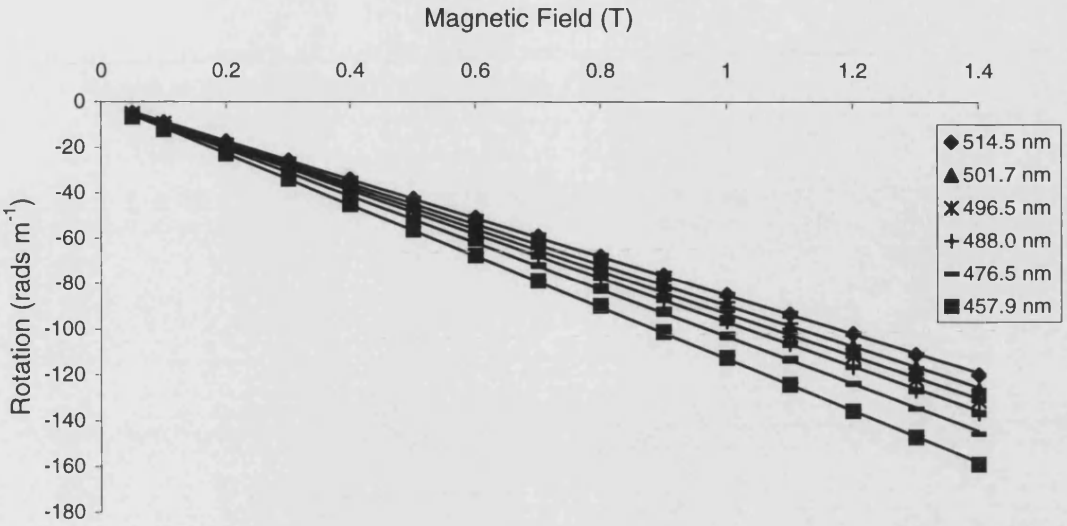

Figure 3.7. Faraday rotation of Tb phosphate glass.

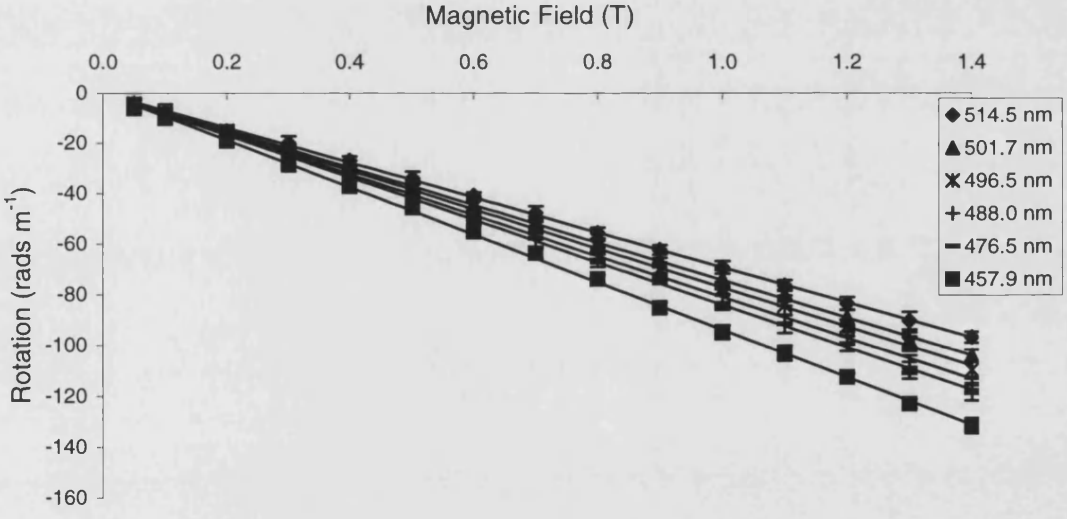

Figure 3.8. Faraday rotation of Dy phosphate glass.

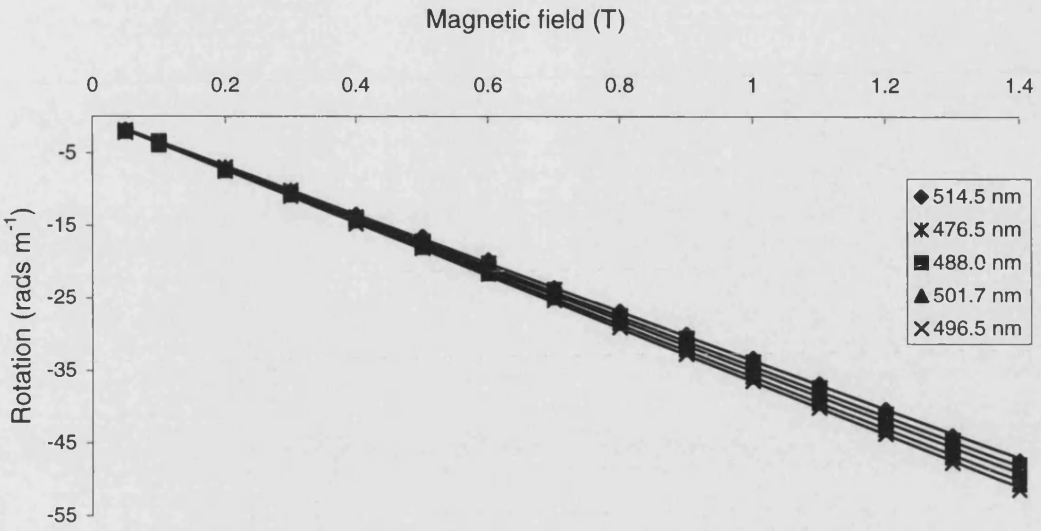

Figure 3.9. Faraday rotation of Ho phosphate glass.

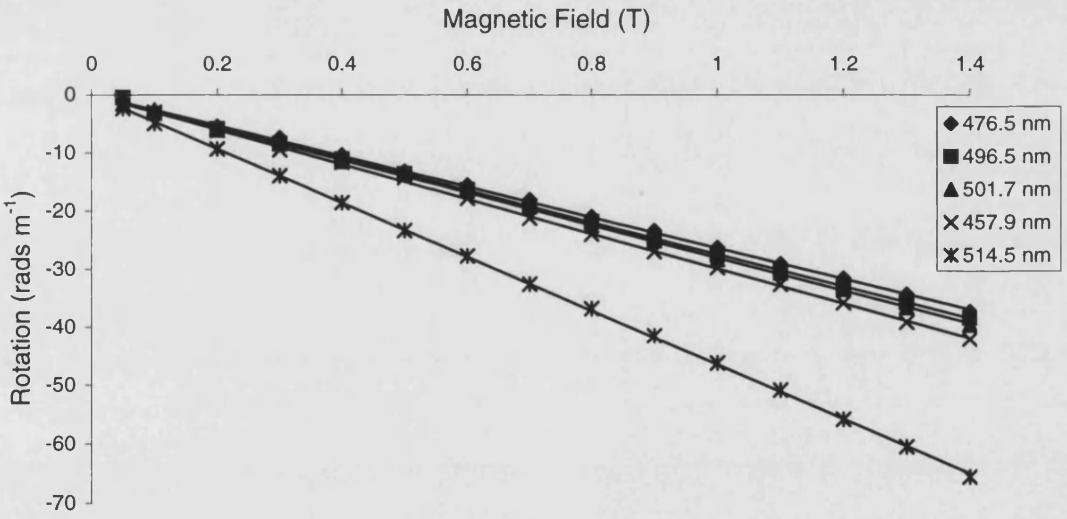

Figure 3.10. Faraday rotation of Er phosphate glass.

	Wavelength (nm)					
	457.9	476.5	488.0	496.5	501.7	514.5
La	8.8 ± 0.1	-	-	-	-	-
Ce	-94.6 ± 0.4	-83.8 ± 0.3	-77.3 ± 0.2	-73.6 ± 0.2	-71.2 ± 0.2	-66.7 ± 0.2
Pr	*	*	*	-77.0 ± 0.3	-74.9 ± 0.3	-69.6 ± 0.3
Nd	-35.1 ± 0.4	-33.7 ± 0.4	-30.1 ± 0.2	-28.5 ± 0.3	*	*
Tb	-113.1 ± 0.3	-103.3 ± 0.3	-97.1 ± 0.3	-93.3 ± 0.2	-89.8 ± 0.3	-85.2 ± 0.3
Dy	-93.9 ± 0.7	-84.0 ± 0.6	-81.0 ± 0.6	-77.3 ± 0.4	-74.3 ± 0.5	-69.3 ± 0.4
Ho	*	-34.5 ± 0.1	-35.1 ± 0.1	-36.5 ± 0.1	-35.9 ± 0.1	-33.7 ± 0.2
Er	-29.9 ± 0.2	-26.3 ± 0.2	*	-27.4 ± 0.2	-28.0 ± 0.2	-46.4 ± 0.2

* Due to absorption bands it was not possible to measure the Verdet constant at these wavelength.

Table 3.3. The Verdet constant, V, (rad T^{-1} m^{-1}) as a function of wavelength for each of the rare earth ions.

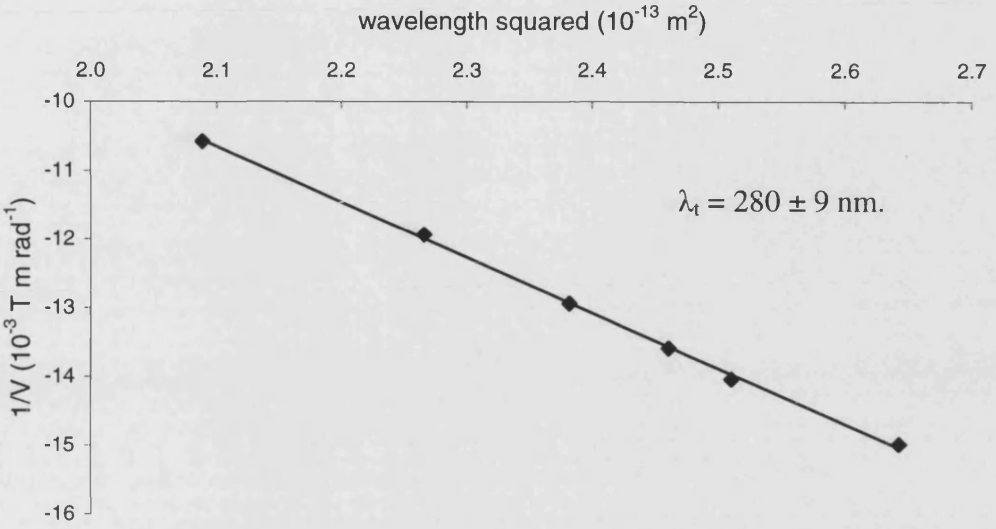

Figure 3.11. Inverse Verdet constant of Ce phosphate glass as a function of wavelength squared.

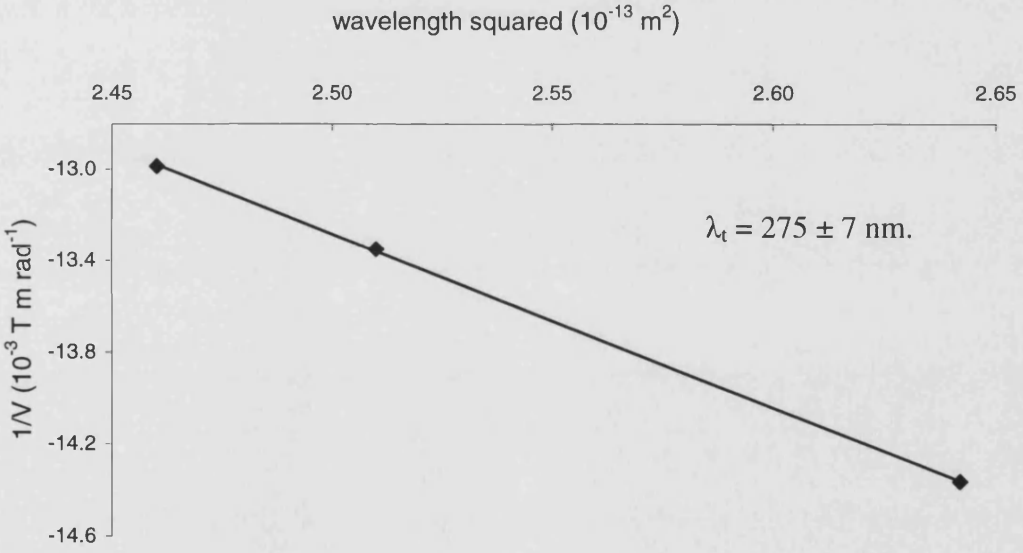

Figure 3.12. Inverse Verdet constant of Pr phosphate glass as a function of wavelength squared.

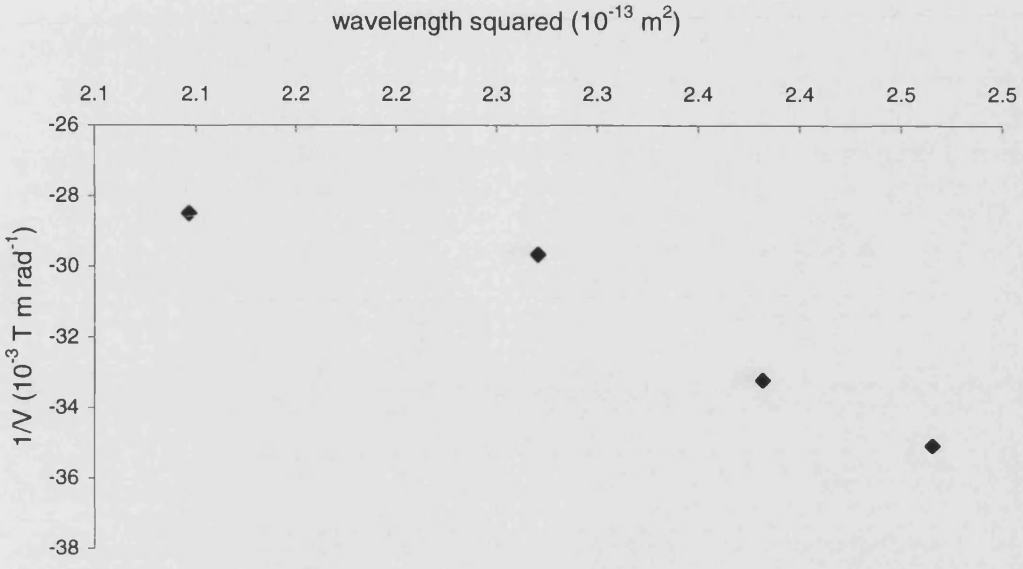

Figure 3.13. Inverse Verdet constant of Nd phosphate glass as a function of wavelength squared.

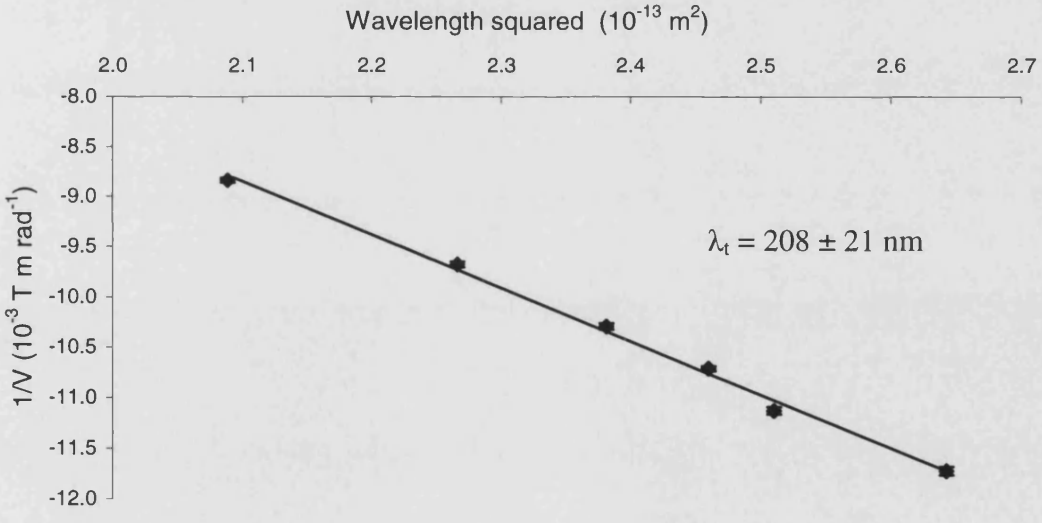

Figure 3.14. Inverse Verdet constant of Tb phosphate glass. as a function of wavelength squared.

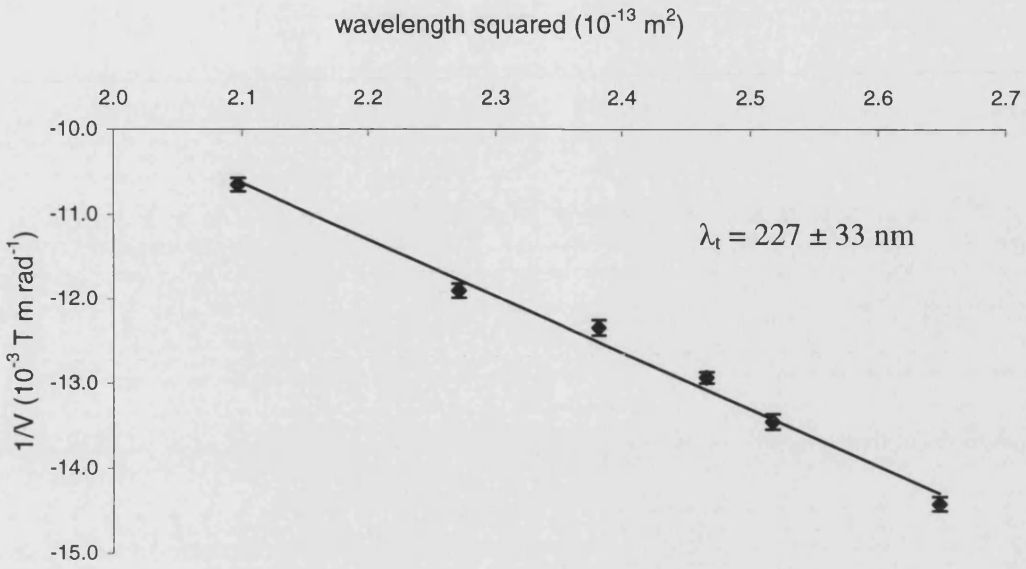

Figure 3.15. Inverse Verdet constant of Dy phosphate glass as a function of wavelength squared.

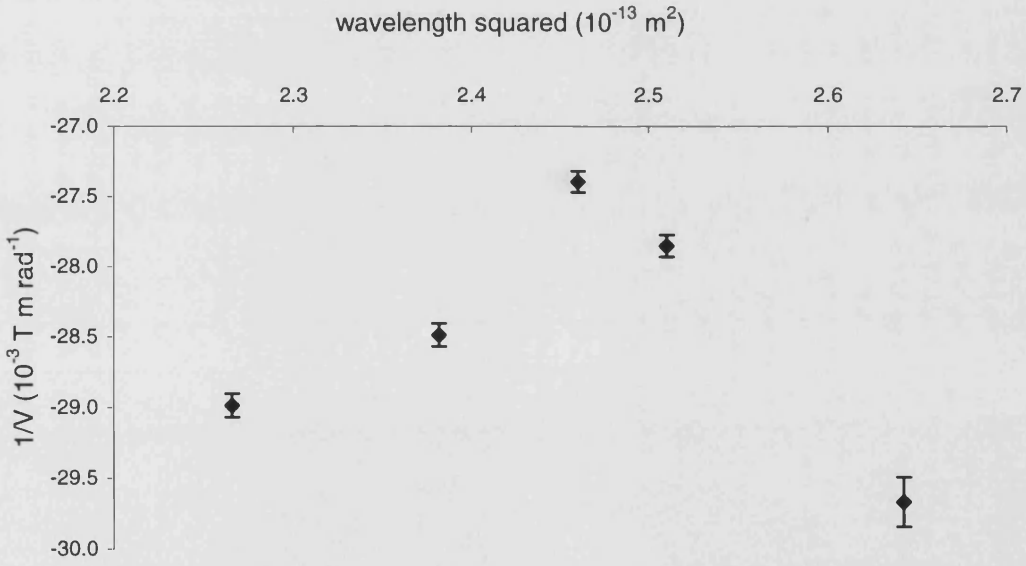

Figure 3.16. Inverse Verdet constant of Ho phosphate glass as a function of wavelength squared.

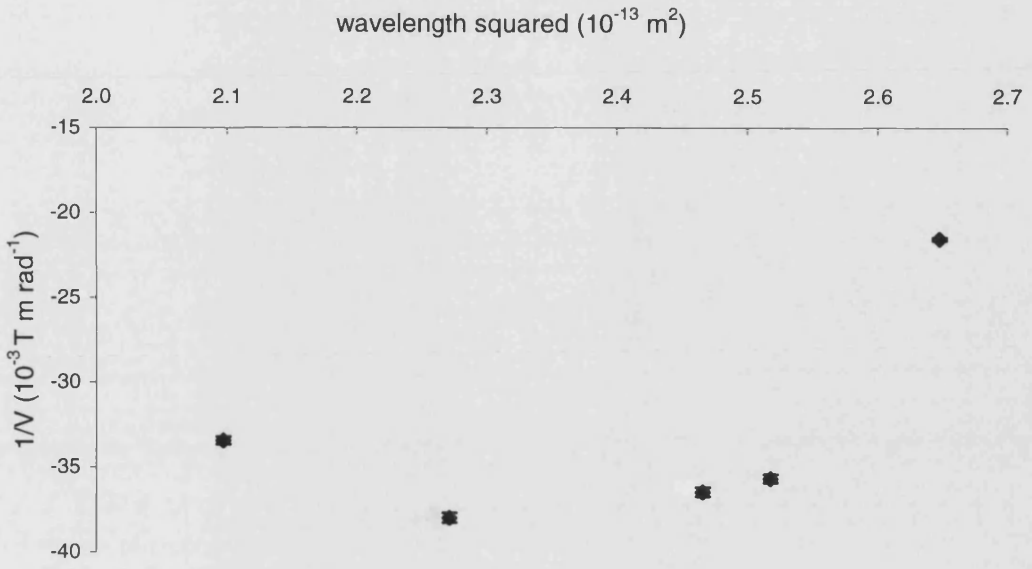

Figure 3.17. Inverse Verdet constant of Er phosphate glass as a function of wavelength squared.

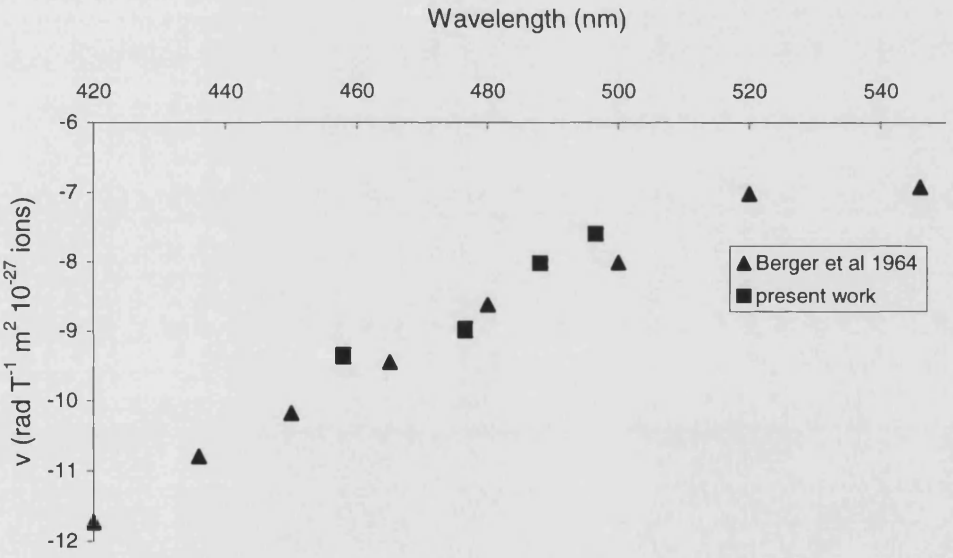

Figure 3.18.Verdet constant, v, of $NdP_{4.31}O_{13.40}Al_{0.23}$ compared to Nd phosphate glass (Berger *et al* 1964).

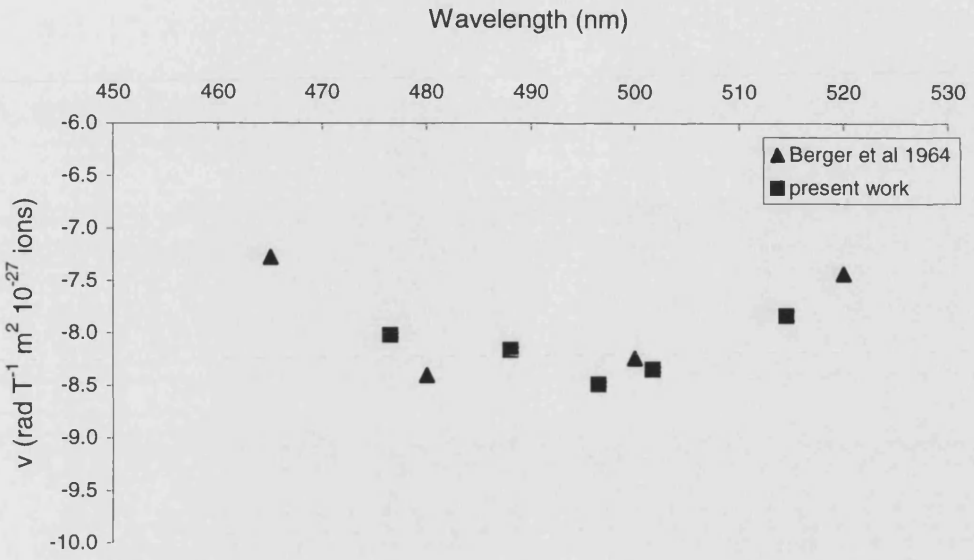

Figure 3.19. Verdet constant, v, of $HoP_{3.43}O_{10.55}Al_{0.55}$ compared to Ho phosphate glass (Berger *et al* 1964).

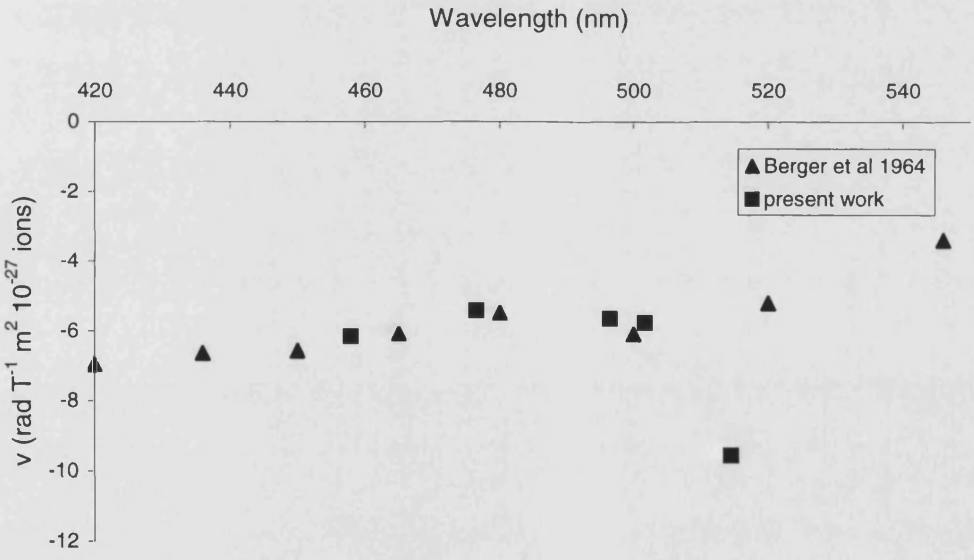

Figure 3.20. Verdet constant, v, of $ErP_{3.20}O_{10.16}Al_{0.16}$ compared to Er phosphate glass (Berger *et al* 1964).

Tables 3.4 – 3.7 give a summary of the Verdet constant parameters for the Ce, Pr, Tb and Dy glasses respectively and a comparison is made with other rare earth based glasses. Values of the Verdet constant presented in the literature are typically given for a range of wavelengths at which the measurements were recorded together with the transition wavelength λ_t. In these cases K can be calculated using equation 3.4 and this formula was subsequently used to find V at two commonly used wavelengths namely 633 nm and 1.06 μm which correspond to the lasing lines of HeNe and Ti-Sapphire.

The rotation caused by the glasses used in the current work compares favourably with other glasses reported in the literature. The largest Verdet constant v is found in glasses of the form $50GaS_{3/2}20GeS_220LaS_{3/2}10RS_{3/2}$ for R = Ce, Pr, Tb and Dy. However the low solubility of rare earth ions limits the total Verdet constant V. Fluorozirconates are characterised by both low Verdet constants v and low rare earth solubilities.

The transition wavelength, λ_t, and Verdet constant v of the Ce based glass in the present work are very similar to those of other phosphate and silico phosphate glasses. The phosphate glasses have a high rare earth solubility compred to the non-phosphate based glasses (Table 3.4). By comparison, those for the Pr glass in the present work deviate slightly from those of other phosphate and silico phosphate glasses. In particular λ_t is between 65 – 75 nm longer which results in a larger Verdet constant at shorter wavelengths as the transition wavelength is approached (see equation 3.4). The phosphate glasses again have a high solubility of rare earth ions.

The λ_t and Verdet constant v of the Tb glass in the present work are very similar to those of other phosphate and fluorophosphate glasses although the solubility is much higher than the fluorophosphates. Crystalline terbium gallium garnet, a commercially available Faraday rotator, has a rotation of just over twice that of the phosphate glasses at 1.06 μm. However glasses have many practical advantages over crystals as discussed in section 3.1. Two other glasses, which have large rare earth solubilities and large Verdet constants, are the aluminosilicates and the borates (see Table 3.6).

The Verdet constant, v, of the Dy glass in the present work is similar to that of other phosphate and silico-phosphate glasses. However, the transition wavelength, λ_t, is slightly longer, which will result in a larger Verdet constant at shorter wavelength as the transition wavelength is approached. The phosphate glasses again have high rare earth solubility.

Glass	N 10^{27} ions m^{-3}	λ_t nm	K rad m T^{-1} $\times 10^{-11}$	V rad $T^{-1}m^{-1}$ 633 nm	 1060 nm	v 10^{-27} rad T^{-1} m^2 633 nm	Reference
$CeP_{3.57}O_{10.73}Al_{0.21}$	4.55	280 ± 9	-1.23	-38.5	-11.9	8.5	Present work
$(Ce_2O_3)_{0.272}(P_2O_5)_{0.728}$	6.0	289	-2.11	-49.8	-15.2	8.3	Berger *et al* 1964
Ce silico-phosphate	3.8	280	-1.02	-31.7	-9.8	8.3	Petrovskii *et al* 1991
$60ZrF_4.30BaF_2.10CeF_3$	1.63	262	-0.41	-12.5	-3.9	7.7	Qiu *et al* 1997 (a)
$50GaS_{3/2}20GeS_220LaS_{3/2}10CeS_{3/2}$	1.62	416	-0.78	-34.2	-8.2	21.1	Qiu *et al* 1996
Ce fluorozirconate	1.73	250 ± 8		-10.5	-	6.1	MacFarlane *et al* 1997

Table 3.4. Comparison of Verdet constant parameters for several Ce based glasses.

Glass	N 10^{27} ions m^{-3}	λ_t nm	K rad m T^{-1} $\times 10^{-11}$	V rad $T^{-1}m^{-1}$ 633 nm	 1060 nm	v 10^{-27} rad T^{-1} m^2 633 nm	Reference
$PrP_{3.13}O_{9.24}Al_{0.09}$	5.15	275 ± 7	-1.31	-40.4	-12.5	7.8	Present work
$(Pr_2O_3)_{0.244}(P_2O_5)_{0.756}$	5.3	210	-1.95	-54.8	-18.1	10.3	Berger *et al* 1964
Pr Silicates	3.79	188.6	-0.95	-26.1	-8.7	6.9	Borrelli 1964
Pr silico-phosphate	3.76	220	-1.07	-30.4	-10.0	10.3	Petrovskii *et al* 1991
Pr Lanthanum borate	5.0	210	-1.3	-36.9	-12.2	7.4	Rubinstein *et al* 1964
$60ZrF_4.30BaF_2.10PrF_3$	1.63	207	-0.48	-13.4	-4.4	8.2	Qiu *et al* 1997 (a)
$50GaS_{3/2}20GeS_2 20LaS_{3/2}10PrS_{3/2}$	1.63	328	-0.83	-28.4	-8.2	17.4	Qiu *et al* 1996
Pr fluorozirconate	1.43	190 ± 8	-0.32	-8.9	-3.0	6.4	MacFarlane *et al* 1997

Table 3.5. Comparison of Verdet constant parameters for several Pr based glasses.

Glass	N 10^{27} ions m^{-3}	λ_t nm	K (rad m T^{-1}) $\times 10^{-11}$	V (rad $T^{-1}m^{-1}$) 633 nm	1060 nm	v (10^{-27} rad T^{-1} m^2) 633 nm	Reference
$TbP_{2.94}O_{9.18}Al_{0.26}$	5.25	208 ± 21	-1.88	-52.5	-17.4	10.0	Present work
$(Tb_2O_3)_{0.254}(P_2O_5)_{0.746}$	5.4	215	-1.91	-54.0	-17.8	10.0	Berger *et al* 1964
$20BaF_2 39TbF_3 41NaPO_3$	6.52	216.8	-2.11	-57.3	-18.8	9.1	Letellier *et al* 1989
Tb Silicates	3.37	126.5	-0.99	-25.8	-9.0	7.7	Borrelli 1964
Tb Aluminosilicate	6.6	385	-1.97	-73.7	-20.0	11.2	Ballato and Snitzer 1995
$20Tb_2O_3 20Al_2O_3 60SiO_2$	10.3	-		-102	-	9.9	Kohli and Shelby 1991
Tb Borosilicate	3.8	250	-0.74	-21.8	-6.9	5.7	Petrovskii *et al* 1991
Tb Lanthanum borate	5.5	225	-1.67	-47.7	-15.6	8.7	Rubinstein *et al* 1964
$30Tb_2O_3 70B_2O_3$	11.2	255	-3.40	-102.7	-32.6	9.2	Tanaka et al 1995
$60ZrF_4.30BaF_2.10TbF_3$	1.64	242	-0.46	-13.4	-4.3	8.2	Qiu *et al* 1997 (a)
$50GaS_{3/2} 20GeS_2 20LaS_{3/2} 10TbS_{3/2}$	1.64	277	-1.20	-37.7	-11.7	23	Qiu *et al* 1996
Tb fluoride (AF)	1.1	218	-0.34	-9.6	-3.1	8.7	Qiu *et al* 1997(b)
Tb zircona fluoride (AZF)	1.07	219	-0.33	-9.4	-3.1	8.8	Qiu *et al* 1997(b)
Tb borate (BO)	1.95	220	-0.29	-15.9	-5.2	8.2	Qiu *et al* 1997(b)
Tb fluorophosphates (POF)	0.806	234	-0.30	-8.6	-2.8	10.6	Qiu *et al* 1997(b)
Tb fluorozirconate	1.04	283	-0.27	-7.5[d]	-	7.2	MacFarlane *et al* 1997
Crystalline terbium gallium garnet	-	-		-136.3	-38.9	-	Ballato and Snitzer 1995

Table 3.6. Comparison of Verdet constant parameters for several Tb based glasses

Glass	N 10^{27} ions m^{-3}	λ_t nm	K rad m T^{-1} $\times 10^{-11}$	V rad $T^{-1}m^{-1}$ 633 nm	 1060 nm	v 10^{-27} rad T^{-1} m^2 633 nm	Reference
$DyP_{3.34}O_{10.55}Al_{0.20}$	4.60	227 ± 33	-1.49	-42.5	-13.9	9.2	Present work
$(Dy_2O_3)_{0.285}(P_2O_5)_{0.715}$	6.2	175	-2.11	-57.1	-19.3	9.2	Berger *et al* 1964
$20BaF_2 30DyF_3 50NaPO_3$	4.6	173.2		-47.2		10.3	Letellier *et al* 1989
Dy Silicates	3.46	119	-0.93	-24.0	-8.4	6.9	Borrelli 1964
Gd/Tb aluminosilicates	7.9	-		-67.6	-	8.6	Kohli and Shelby 1991
Dy silico-phosphate	3.55	190	-1.3	-36.6	-12.3	10.3	Petrovskii *et al* 1991
Dy Lanthanum borate	5.8	180	-1.73	-46.9	-15.8	8.1	Rubinstein *et al* 1964
$60ZrF_4.30BaF_2.10DyF_3$	1.64	195		-15.4		9.4	Qiu *et al* 1997 (a)
$50GaS_{3/2}20GeS_2 20LaS_{3/2}10DyS_{3/2}$	1.64	253		-31.4		19.1	Qiu *et al* 1996
Dy fluorozirconate	1.2	165 ± 28		-4.9	-	4.1	MacFarlane *et al* 1997

Table 3.7. Comparison of Verdet constant parameters for several Dy based glasses.

3.2.2 CONCENTRATION DEPENDENCE OF V

The Faraday rotation work has so far focussed on glasses of the nominal composition $RP_3O_9Al_{0.2}$ that contain only one rare earth species. The objective of the next section is to investigate whether glasses of the form $^1R_x{}^2R_{1-x}P_3O_9Al_{0.35}$ obey equation 3.5. A series of mixed cerium and erbium rare earth phosphate glasses was prepared (according to Chapter 2) and their details are presented in Table 3.8. These ions were chosen since cerium has one of the largest Faraday rotations of the rare earths and erbium has a smaller but easily measurable rotation (approximately one third that of Ce). This will result in large rotations thus reducing errors accordingly.

There has been much interest in whether clustering of rare earth ions occur in these glasses (Hoppe *et al* 1998, Cole *et al* 1999 and Cole *et al* 2001). Even though the outer electrons shield the 4 f electrons, which gives rise to the isolated nature of rare earth ions, the Verdet constant is known to be dependent on the host environment, as shown in Tables 3.3 – 3.7. It is therefore questioned whether the structure of the glass network will affect the rotation. The two rare earths chosen are from opposite ends of the lanthanide series, cerium having a large atomic radius whilst erbium has a much smaller atomic radius due to the lanthanide contraction. In the crystalline phase large and small R^{3+} meta-phosphates have different structures (Hong 1974a,b). Large R^{3+} ions (e.g. Ce) are surrounded by 8 oxygens at $\approx$ 2.33 – 2.67 Å and the closest R-R distance is $\approx$ 4.234 Å, while smaller R^{3+} ions (e.g. Er) are surrounded by 6 oxygens at $\approx$ 2.07 – 2.31 Å and the closest R-R distance is $\approx$ 5.610 Å. If clustering of rare earth ions was to occur in the glassy phase the R-R distance may become short enough for interactions to occur and this might be indicated by a deviation in the Verdet constant from equation 3.5 which assumes independent ions.

Composition	Ce^{3} (10^{27} ions m^{-3})	Er^{3+} (10^{27} ions m^{-3})	Ratio Ce^{3+} / Er^{3+}	$V_{experimental}$ (10^{-27} rad T^{-1} m^{-1})	$V_{calculated}$ (10^{-27} rad T^{-1} m^{-1})
$CeP_{3.57}O_{10.73}$ $Al_{0.21}$	4.55	0.00	1.000 : 0.000	-73.6 ± 0.2	-70.7 ± 2.1
$Ce_{0.81}Er_{0.19}P_{3.08}O_{10.15}Al_{0.46}$	3.90	0.95	0.805 : 0.195	-65.3 ± 0.2	-65.8 ± 2.0
$Ce_{0.61}Er_{0.39}P_{2.94}O_{9.79}Al_{0.30}$	3.10	2.00	0.610 : 0.390	*	-59.2 ± 1.8
$Ce_{0.51}Er_{0.49}P_{3.11}O_{10.58}Al_{0.46}$	2.40	2.30	0.505 : 0.495	-49.2 ± 0.2	-49.9 ± 1.5
$Ce_{0.41}Er_{0.59}P_{3.00}O_{10.20}Al_{0.48}$	2.00	2.90	0.405 : 0.595	-46.6 ± 0.1	-47.0 ± 1.4
$Ce_{0.20}Er_{0.80}P_{2.82}O_{9.63}Al_{0.40}$	1.00	4.05	0.200 : 0.800	*	-37.8 ± 1.2
$ErP_{3.20}O_{10.16}Al_{0.16}$	0.00	4.85	0.000 : 1.000	-27.4 ± 0.2	-26.7 ± 0.9

* Due to bubbles and defects the optical quality of these glasses was not suitable for optical transmission experiments and therefore the Faraday rotation of these glasses could not be measured.

Table 3.8. Parameters describing the Faraday rotation of mixed Ce/Er glasses at 496.5 nm.

The Faraday rotation of the glasses was measured at room temperature at a wavelength of 496.5 nm and the results are presented in Table 3.8. The Verdet constant, v, for Ce and Er in the mixed glasses were found using equation 3.5 by solving the simultaneous equations and the results are presented in Table 3.9.

	v (10^{-27} rad T^{-1} m^2)
Ce	15.5 ± 0.5
Er	5.5 ± 0.2

Table 3.9. Mean Verdet constant v of the Ce^{3+} and Er^{3+} ions in $Ce_xEr_{1-x}P_3O_9Al_{0.35}$.

The experimental data and calculated results using equation 3.5 are plotted in Figure 3.21. As shown in this figure, the Verdet constant is a linear function of rare earth ion number density at room temperature in the wavelength region studied. This is consistent with the isolated nature of the 4 f electrons, and presumably a relatively large distance between rare earth ions (see Chapter 6 and 7).

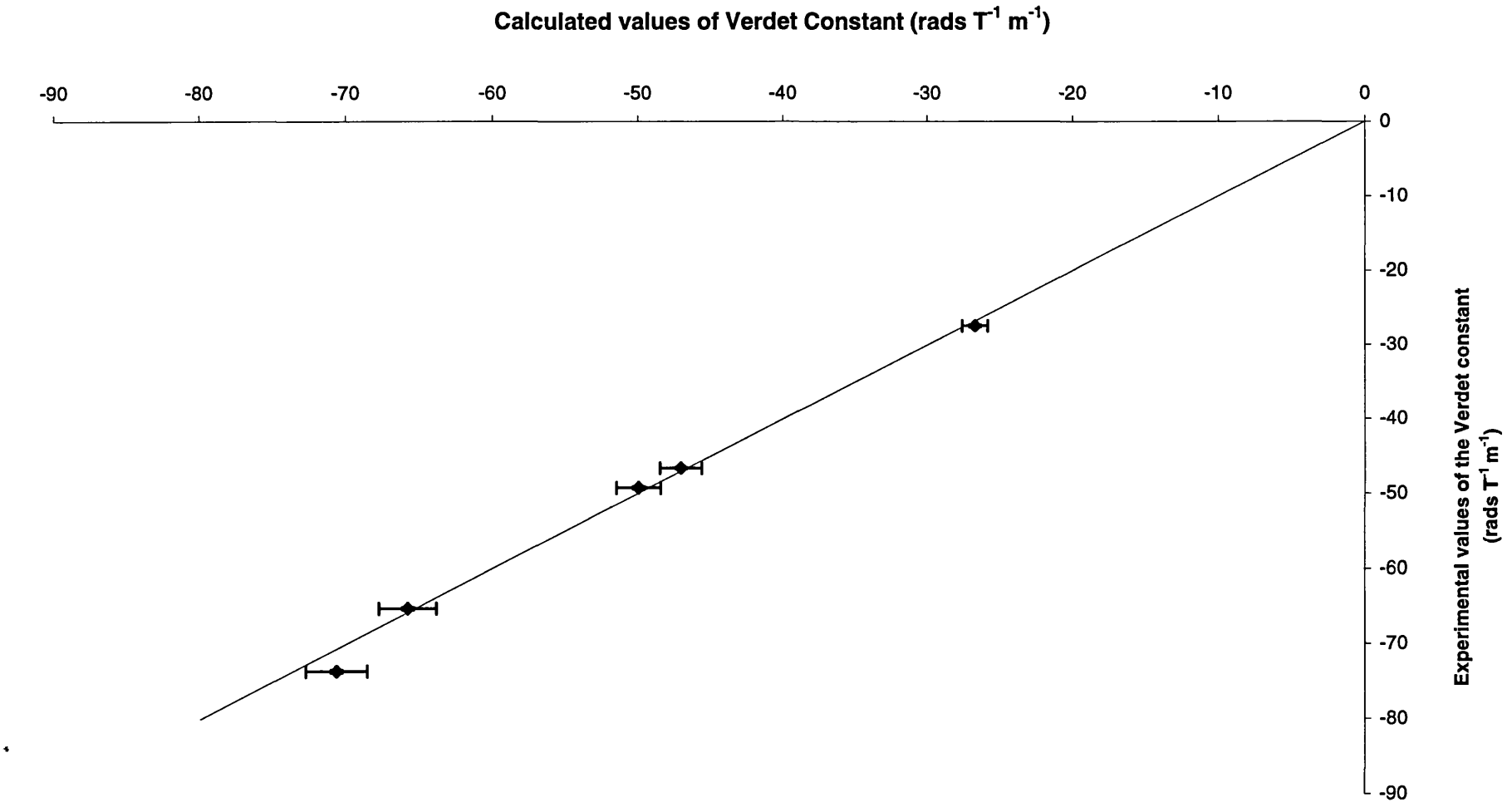

Figure 3.21. Concentration dependence of the Verdet constant for mixed Ce/Er phosphate glasses. The points give the experimental data while the line gives the vaules calculated using equation 3.5.

3.2.3 ABSORPTION COEFFICIENT AND FIGURE OF MERIT

In order to calculate the magneto optical figure of merit, F, described by equation 3.2 the optical absorption coefficient of the glasses was measured. The absorption was measured over the wavelength region 450 – 520 nm with a resolution of 1 nm.

The propagation of light through a slab-like sample of thickness x is represented in Figure 3.22. Light incident on the first air-sample interface with intensity ${}^1I_0$ can be either reflected with intensity ${}^1I_r$ or transmitted with intensity ${}^1I_t$ such that

$$ {}^1I_0 = {}^1I_r + {}^1I_t \qquad [3.6] $$

This transmitted intensity is then diminished by scattering and absorption, on propagating through the sample such that the intensity on the second sample-air interface is

$$ {}^2I_0 = {}^1I_t e^{-\alpha x} \qquad [3.7] $$

where α is the attenuation coefficient. The light at the second interface can then be reflected with intensity ${}^2I_r$ or transmitted with intensity ${}^2I_t$ such that

$$ {}^2I_0 = {}^2I_r + {}^2I_t \qquad [3.8] $$

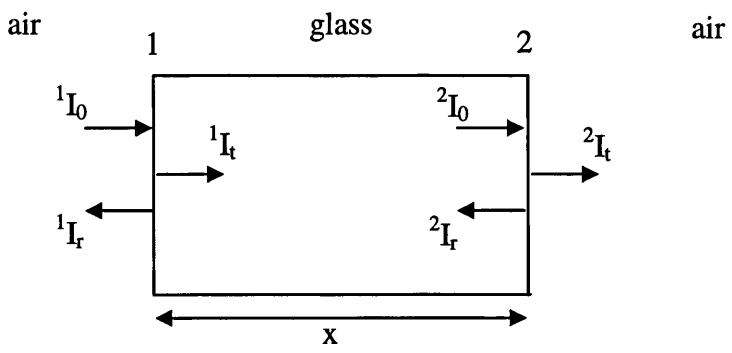

Figure 3.22. The reflection and transmission of light through a parallel-sided sample. Provided $I_t >> I_r$ subsequent reflections are negligible and can be ignored.

The reflectance, R, and transmission, T, are related to the incident, reflected and transmitted intensities by

$$^1R = \frac{^1I_r}{^1I_0} \qquad [3.9]$$

and

$$^2R = \frac{^2I_r}{^2I_0} \qquad [3.10]$$

where the transmission is given by

$$^iR + ^iT = 1 \qquad [3.11]$$

where i = 1 or 2.

Hence the measured intensities $^1I_0$ and ^2I_t, ignoring multiple reflections, can be related by

$$^2I_t = {}^1I_0\,{}^1T\,{}^2T\,e^{-\alpha x} \quad . \qquad [3.12]$$

The rare earth phosphate glasses measured were of good optical quality, being free from defects and air bubbles, such that scattering from within the sample was assumed to be negligible. Hence the attenuation coefficient, α, is equivalent to the optical absorption coefficient.

Reflection losses were calculated using the Fresnel equations. For light with an electric field vector perpendicular to the plane of incidence the amplitude reflection coefficient $r_\perp$ is given by

$$r_\perp = -\frac{\sin(\theta_i - \theta_t)}{\sin(\theta_i + \theta_t)} \qquad [3.13]$$

where θ_i and θ_t are the angles of incidence and transmission and n_i and n_t are the refractive indices of the incident and transmitted mediums (Hecht 1987). Expanding

equation 3.14 using $\sin(\theta_i-\theta_t) = \sin\theta_i\cos\theta_t - \cos\theta_i\sin\theta_t$ and $\sin(\theta_i+\theta_t) = \sin\theta_i\cos\theta_t + \cos\theta_i\sin\theta_t$ and substituting Snell's law $n_i\sin\theta_i = n_t\sin\theta_t$ gives

$$r_{\perp} = \frac{n_i \cos\theta_i - n_t \cos\theta_t}{n_i \cos\theta_i + n_t \cos\theta_t}. \qquad [3.14]$$

If the incident wave is perpendicular to the interface, such that $\theta_i \approx 0$, then in this limiting case $\cos\theta_i$ and $\cos\theta_t$ approach unity. Equation 3.14 therefore simplifies to give

$$r_{\perp} = \frac{n_i - n_t}{n_i + n_t} \qquad [3.15]$$

The reflectance, R, is defined as the ratio of the reflected power to the incident power and is therefore given by

$$R = r_{\perp}^{\,2} = \left(\frac{n_t - n_i}{n_t + n_i}\right)^2 \qquad [3.16]$$

therefore ${}^1R = {}^2R$ when $\theta = 0$. The refractive index of a rare earth phosphate glass prepared at the University of Bath has been measured (Brennan 1998) and was found to be 1.56 ± 0.02. This falls in the middle of the range for phosphate glasses and is assumed to be similar for rare earth glasses doped with different ions. The refractive index of air is ≈ 1. Using equation 3.16 the reflectance is calculated to be 0.048.

Figure 3.23 shows the set-up for the optical absorption measurements. A white light source is collimated using a single lens placed one focal length away. The collimated beam is incident on an aperture and onto an optical spectrum analyser (O.S.A). The incident intensity I_0 of the white light source was recorded with the sample absent. The sample was then placed between the aperture and the detector to record its transmission. The measurements were repeated a minimum of four times, the sample being translated in the y, z plane where x is the plane of the incident light.

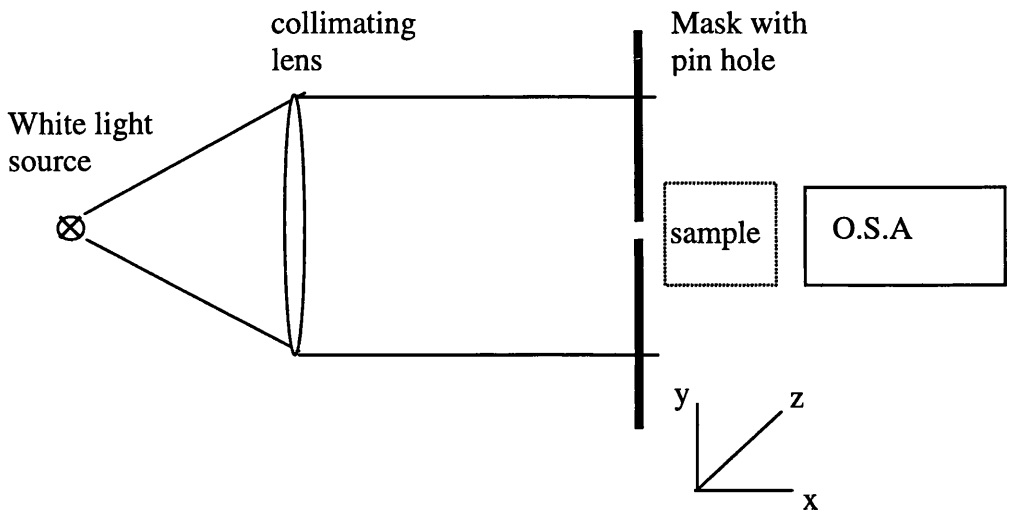

Figure 3.23. Optical absorption set-up.

The negative absorption coefficient (-α) is plotted as a function of wavelength for each of the rare earth phosphate glasses as shown in Figures 3.24 – 3.31. The absorption peaks are assigned using the data of Carnall *et al* (1968 a,b) for rare earth ions in aqueous solution. The transitions are described by Hund notation $^{2S+1}L_J$, where S is the total spin, J the total angular momentum of the electrons and L is the total orbital angular momentum (Kittel 1986) and given in Tables 3.10 – 3.15. La and Ce do not have any absorption bands in the measured wavelength range.

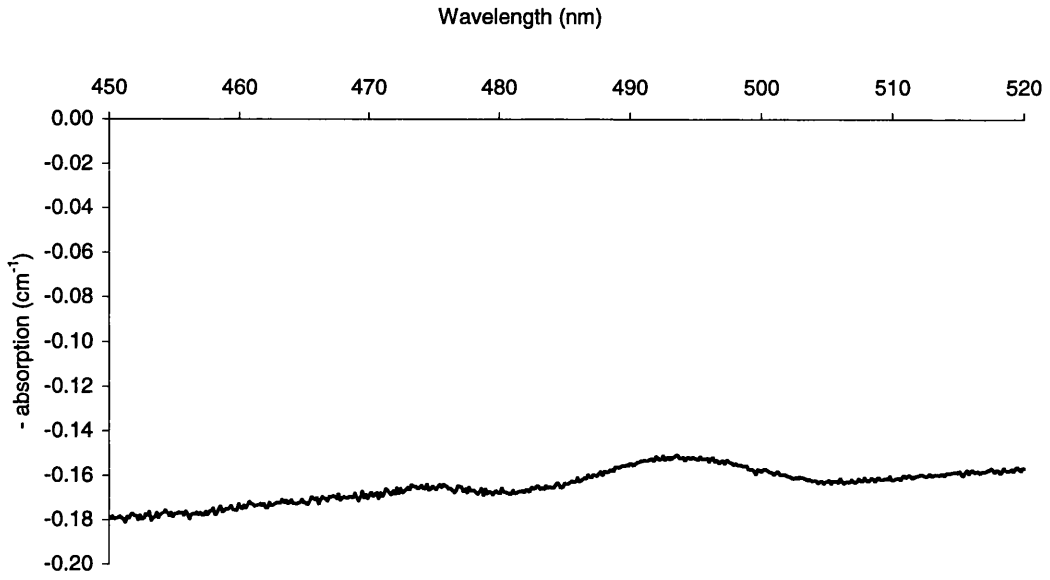

Figure 3.24. The absorption coefficient of glassy $LaP_{3.43}O_{10.45}Al_{0.10}$

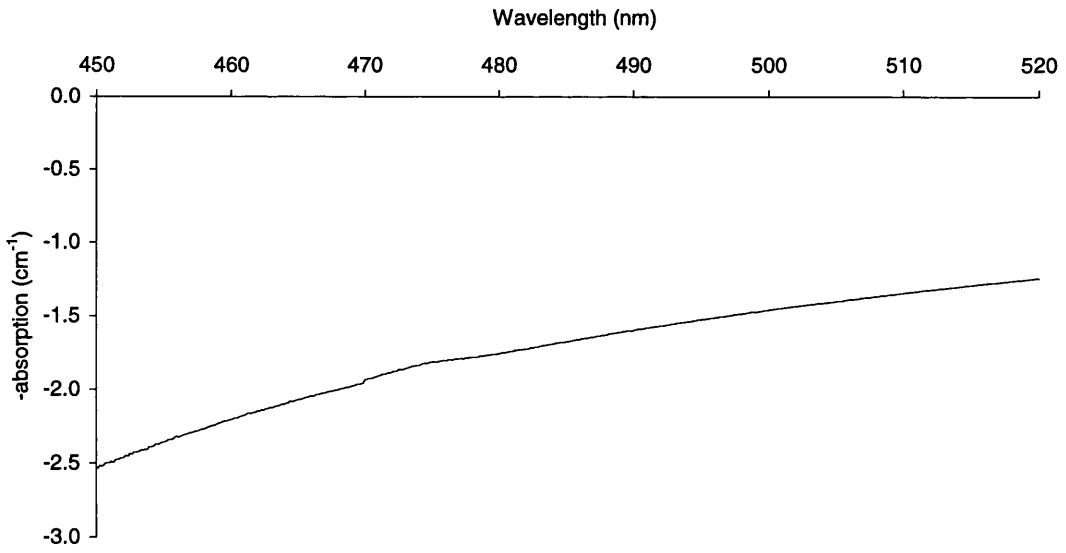

Figure 3.25. The absorption coefficient of glassy $CeP_{3.57}O_{10.73}Al_{0.21}$.

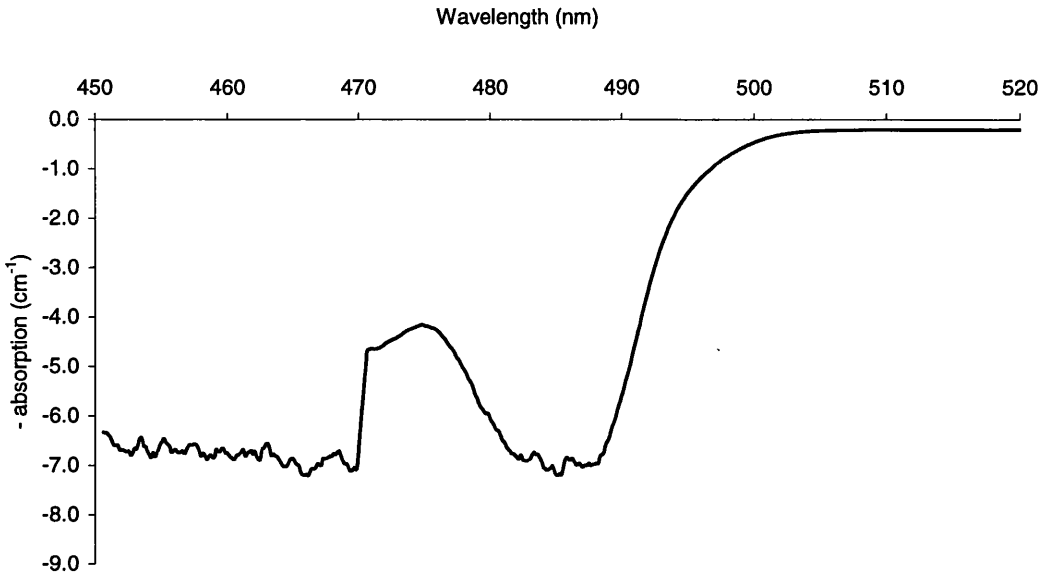

Figure 3.26. The absorption coefficient of glassy $PrP_{3.13}O_{9.24}Al_{0.09}$.

Wavelength (nm) Pr	Wavelength (nm) (Carnall *et al* 1968a)	Assigned transition (Carnall *et al* 1968a)
450-470	448.9	$^3H_4 - {}^3P_2$
	470.5	$^3H_4 - {}^1I_6$
	474.9	$^3H_4 - {}^3P_1$
480-490	487.7	$^3H_4 - {}^3P_0$

Table 3.10. The measured absorption bands of $PrP_{3.13}O_{9.24}Al_{0.09}$ compared to those for Pr^{3+} ions in aqueous solution Carnall *et al* (1968a).

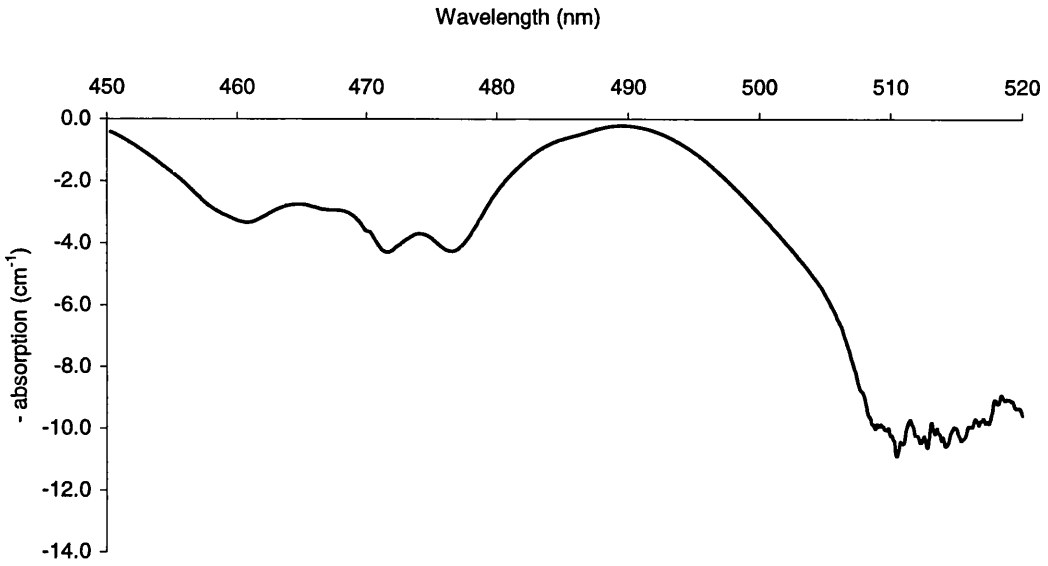

Figure 3.27. The absorption coefficient of glassy $NdP_{4.31}O_{13.40}Al_{0.23}$.

Wavelength (nm) Nd	Wavelength (nm) (Carnall *et al* 1968a)	Assigned transition (Carnall *et al* 1968a)
460	465.0	$^4I_{9/2}$ - $^4G_{11/2}$
472	472.7	$^4I_{9/2}$ - $^2G_{9/2}$, $^2D_{3/2}$, $^2P_{3/2}$
476	479.5	$^4I_{9/2}$ - $^2K_{15/2}$
505 - 520	515.4	$^4I_{9/2}$ - $^4G_{9/2}$
	525.9	$^4I_{9/2}$ - $^4G_{7/2}$

Table 3.11. The measured absorption bands of $NdP_{4.31}O_{13.40}Al_{0.23}$ compared to those for Nd^{3+} ions in aqueous solution Carnall *et al* (1968a).

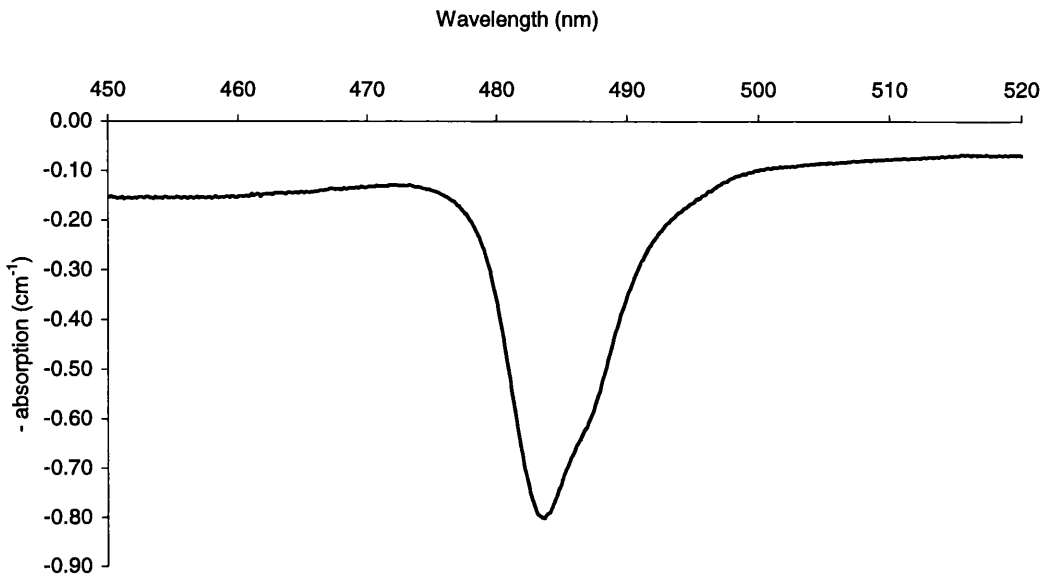

Figure 3.28. The absorption coefficient of glassy $TbP_{2.94}O_{9.18}Al_{0.26}$.

Wavelength (nm) Tb	Wavelength (nm) (Carnall *et al* 1968b)	Assigned transition (Carnall *et al* 1968b)
484	489.8	$^7F_6 - {}^5D_4$

Table 3.12. The measured absorption of $TbP_{2.94}O_{9.18}Al_{0.26}$ compared to those for Tb^{3+} ions in aqueous solution Carnall *et al* (1968b).

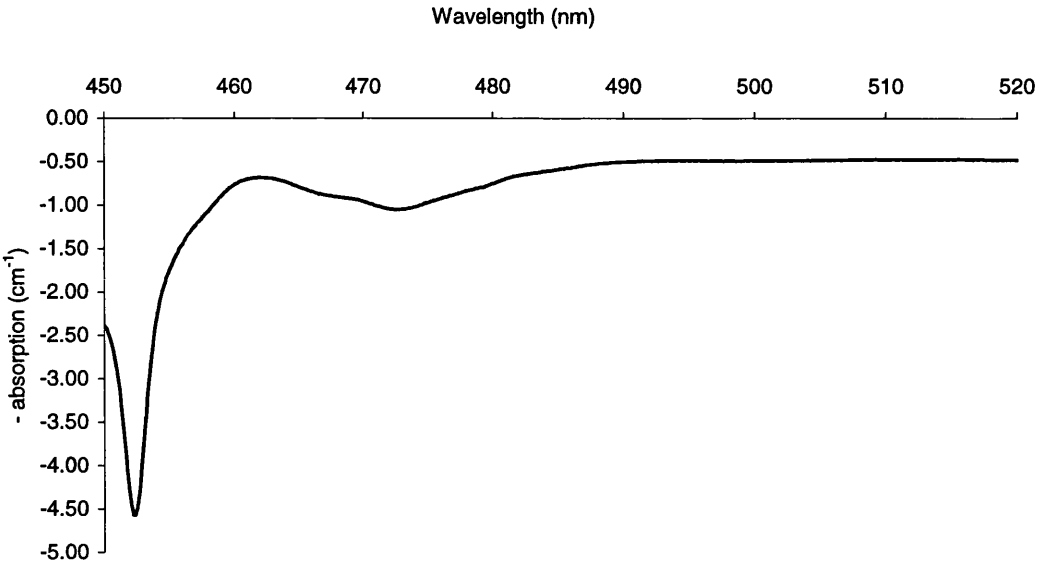

Figure 3.29. The absorption of coefficient glassy $DyP_{3.34}O_{10.55}Al_{0.20}$.

Wavelength (nm) Dy	Wavelength (nm) (Carnall *et al* 1968a)	Assigned transition (Carnall *et al* 1968a)
452.5	453.6	$^4H_{15/2} - {}^4I_{15/2}$
469-477	475.1	$^4H_{15/2} - {}^4F_{9/2}$

Table 3.13. The measured absorption of $DyP_{3.34}O_{10.55}Al_{0.20}$ compared to those for Dy^{3+} ions in aqueous solution Carnall *et al* (1968a).

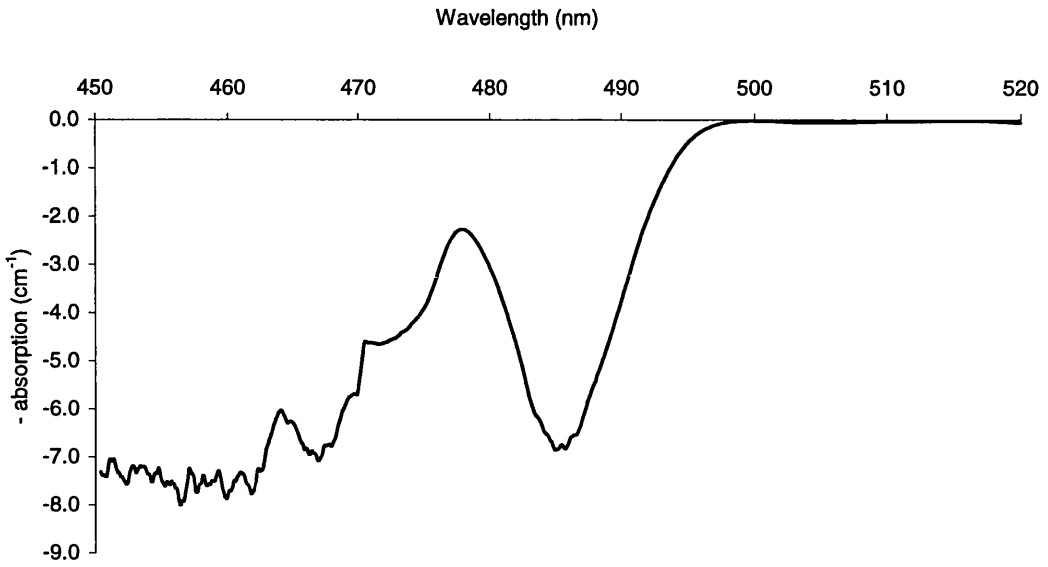

Figure 3.30. The absorption coefficient of glassy $HoP_{3.43}O_{10.55}Al_{0.55}$.

Wavelength (nm) Ho	Wavelength (nm) (Carnall *et al* 1968a)	Assigned transition (Carnall *et al* 1968a)
450-460	454.7	$^5I_8 - {}^5G_6$
465-470	470.3	$^5I_8 - {}^3K_8$
470-475	476.4	$^5I_8 - {}^5F_2$
484-488	488.0	$^5I_8 - {}^5F_3$

Table 3.14. The measured absorption of $HoP_{3.43}O_{10.55}Al_{0.55}$ compared to those for Ho^{3+} ions in aqueous solution Carnall *et al* (1968a).

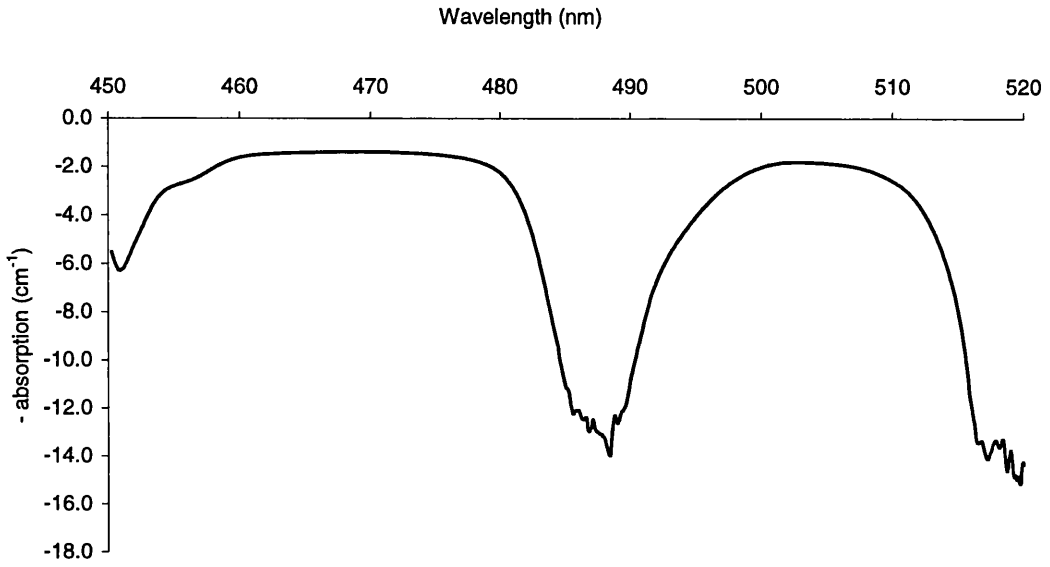

Figure 3.31. The absorption coefficient of glassy $ErP_{3.20}O_{10.16}Al_{0.16}$.

Wavelength (nm) Er	Wavelength (nm) (Carnall *et al* 1968a)	Assigned transition (Carnall *et al* 1968a)
450 - 452	446.6	$^4I_{15/2} - {}^4F_{3/2}$
	454.7	$^4I_{15/2} - {}^4F_{5/2}$
485-490	491.6	$^4I_{15/2} - {}^4F_{7/2}$
515-520	525.2	$^4I_{15/2} - {}^2H_{11/2}$

Table 3.15. The measured absorption of $ErP_{3.20}O_{10.16}Al_{0.16}$ compared to those for Er^{3+} ions in aqueous solution Carnall *et al* (1968a).

The four largest rotators Ce, Pr, Tb and Dy all obey equation 3.4 as shown by the straight-line graphs of Figures 3.11, 3.12, 3.14 and 3.15 respectively. Using the calculated values of K and λ_t it is therefore possible to interpolate the Verdet constant over the wavelength region 450 – 520 nm. The corresponding figure of merit for the Ce, Pr, Tb and Dy phosphate glasses are given in Figures 3.32 – 3.35 respectively. Equation 3.4 does not hold very close to strong absorption peaks such that interpolated values of the Verdet constant are not reliable in these regions. Therefore the figure of merit is only valid between 503 – 520 nm for $PrP_{3.13}O_{9.24}Al_{0.09}$, between 450 - 474 and 497 – 520 nm for $TbP_{2.94}O_{9.18}Al_{0.26}$ and between 488 – 520 nm for $DyP_{3.34}O_{10.55}Al_{0.20}$. For the absorbing rare earth glasses the figure of merit can only be calculated at the wavelengths used to measure the Verdet constant. A summary of the Verdet constant, V, absorption coefficient, α, and figure of merit, F, at these wavelengths is given in Table 3.16.

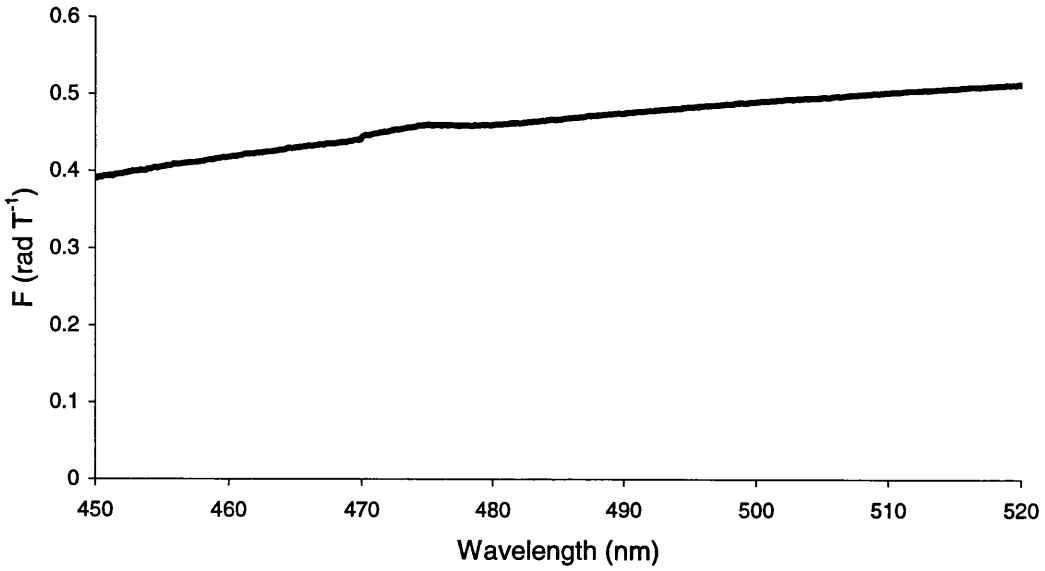

Figure 3.32. Figure of Merit for glassy $CeP_{3.57}O_{10.73}Al_{0.21}$.

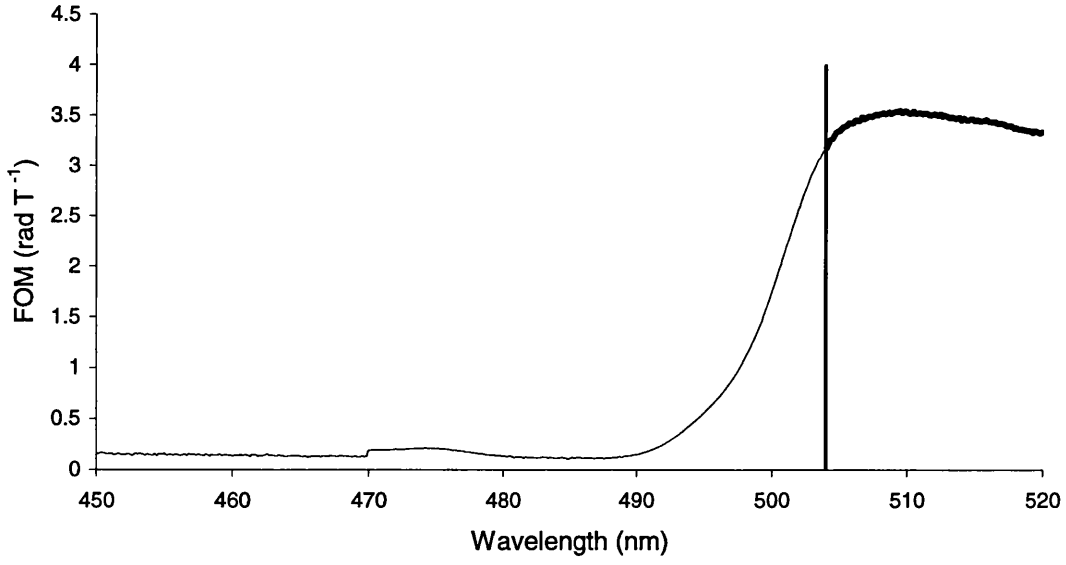

Figure 3.33. Figure of Merit for glassy $PrP_{3.13}O_{9.24}Al_{0.09}$. The thin line represents the F-O-M close to an absorption band whilst the solid line represents the F-O-M sufficiently far away from the absorption band. The vertical line indicates the region sufficiently far away from the absorption band.

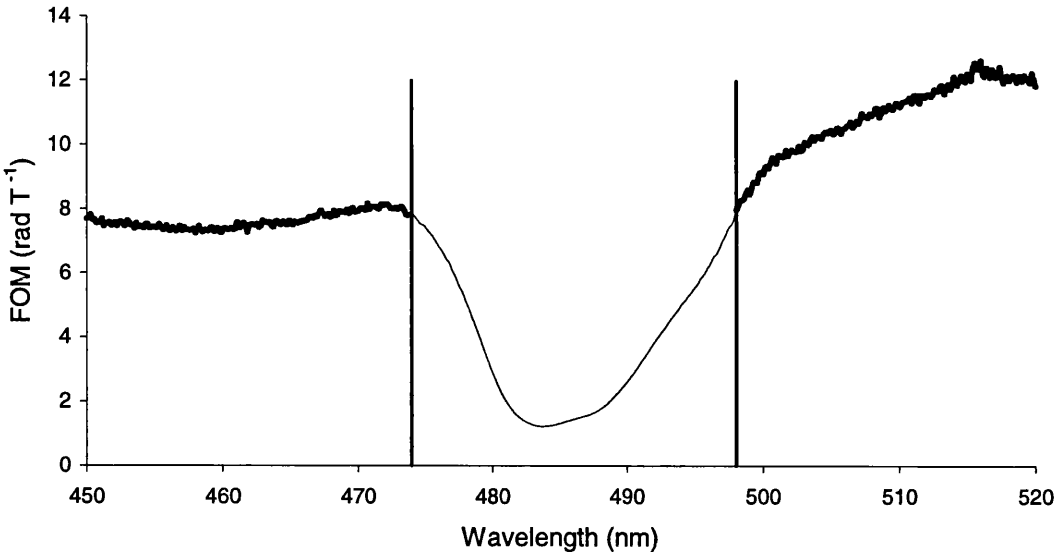

Figure 3.34. Figure of Merit for glassy $TbP_{2.94}O_{9.18}Al_{0.26}$. The thin line represents the F-O-M close to an absorption band whilst the solid line represents the F-O-M sufficiently far away from the absorption band. The vertical line indicates the region sufficiently far away from the absorption band.

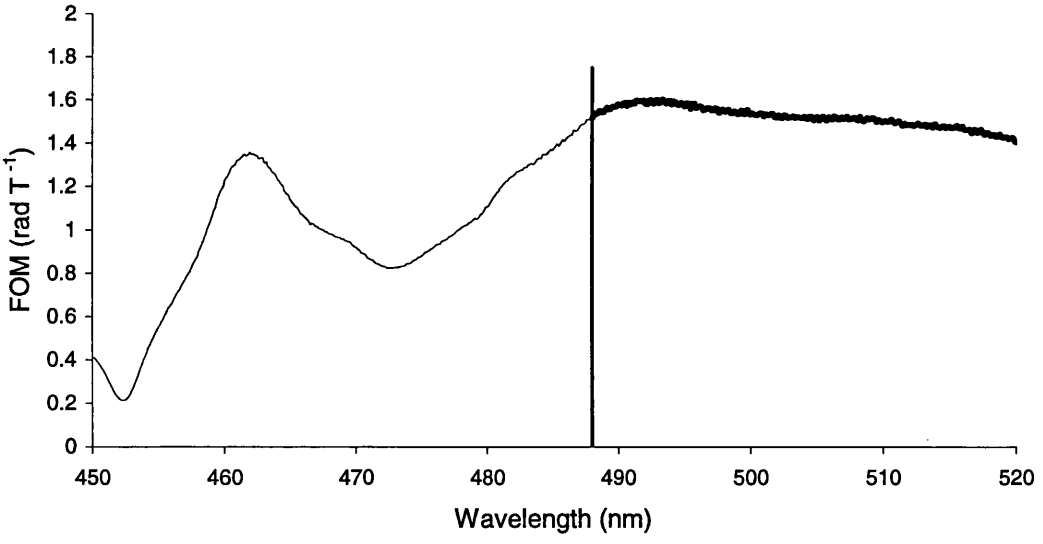

Figure 3.35. Figure of Merit for glassy $DyP_{3.34}O_{10.55}Al_{0.20}$. The thin line represents the F-O-M close to an absorption band whilst the solid line represents the F-O-M sufficiently far away from the absorption band. The vertical line indicates the region sufficiently far away from the absorption band.

Ion		Wavelength (nm)					
		457.9	476.5	488.0	496.5	501.7	514.5
La	V	8.8	-	-	-	-	-
	α	17.6	16.8	15.8	15.4	16.0	15.9
	F	0.50	-	-	-	-	-
Ce	V	-94.6	-83.8	-77.4	-73.6	-71.2	-66.7
	α	227	180	163	150	144	130
	F	0.42	0.47	0.47	0.49	0.49	0.51
Pr	V	-	-	-	-77.0	-74.9	-69.6
	α	700	459	688	98	30	20
	F	-	-	-	0.8	2.5	3.5
Nd	V	-35.1	-33.7	-30.1	-28.5	-	-
	α	287	426	28	164	395	1010
	F	0.12	0.08	1.08	0.17	-	-
Tb	V	-113.1	-103.3	-97.1	-93.3	-89.8	-85.2
	α	15.4	16.1	53.4	13.9	9.2	7.0
	F	7.3	6.4	1.8	6.7	9.8	12.2
Dy	V	-93.9	-84.0	-81.0	-77.3	-74.3	-69.3
	α	108	90	53	49	49	47
	F	0.87	0.93	1.53	1.58	1.52	1.47
Ho	V	-	-34.5	-35.1	-36.6	-35.9	-33.7
	α	730	262	531	14	3.4	1.2
	F	-	0.13	0.07	2.61	10.56	28.08
Er	V	-26.3	-27.4	-	-28.0	-29.9	-46.4
	α	206	160	132	313	190	709
	F	0.13	0.17	-	0.09	0.16	0.07

Table 3.16. V (rad T^{-1} m^{-1}), α (m^{-1}) and F (rad T^{-1}) for the phosphate glasses studied.

3.3 CONCLUSIONS.

The wavelength dependence of the Verdet constant for a series of rare earth phosphate glasses has been successfully measured. The rotation was found to be a linear function of the applied magnetic field as described by equation 3.1. The larger rotating glasses, containing Ce, Pr, Tb or Dy, were found to obey equation 3.4 allowing values of the transition wavelength, λ_t, and constant, K, to be determined. Although more complex glasses have a larger rotation per unit concentration the limited solubility of the rare earth means that the total Verdet constant, V, of the Ce and Pr samples is largest for the phosphate glasses - see Tables 3.4 – 3.5 (Berger *et al* 1964 and present work). By comparison with the results of Berger *et al* (1964) for phosphate glasses, the addition of aluminium into the glass host appears to have a negligible effect on the Verdet parameters; this is in contrast with silicate glasses whose properties depend heavily on the addition of aluminium (see e.g. Table 3.6).

Of the rare earth phosphate glasses studied, $TbP_{2.94}O_{9.18}Al_{0.26}$ was found to have the largest rare earth ion concentration and the highest Verdet constant, v, resulting in the largest total Verdet constant V. At 1060 nm, V is similar to that recently reported for other Tb glasses and is $\approx$ 50% that of terbium gallium garnet crystals (TGG) used in current isolator systems (see Table 3.6). Current Faraday isolators operating between 1.0 – 1.1 μm have an optical path length of rotating medium of about 40 mm for TGG and 60 mm for Tb glass (EOT). Sm-Co permanent magnets provide the required magnetic field. Due to commercial sensitivity values of the magnetic field strength and Verdet constant are not available. However it is estimated that a TGG isolator of path length 40 mm requires a magnetic field of 0.5 T to produce the required 45-degree rotation and Sm-Co permanent magnets are capable of producing field strengths greater than 1 T (MMC). A magnetic field of 0.75 T would be required to produce a 45-degree rotation though a path length of 60 mm in the $TbP_{2.94}O_{9.18}Al_{0.26}$ glass studied. For commercial use other factors like the thermal stability, absorption at 1.06 μm and maximum power density damage threshold must be considered. However, on the basis of the current results the rotational properties of $TbP_{2.94}O_{9.18}Al_{0.26}$ would be large enough for commercial isolators to be produced.

The absorption coefficient of bulk glasses was measured as a function of wavelength for each of the rare earth phosphate glasses. Absorption peaks were measured and the transitions assigned. The absorption measurements were then used to calculate the magneto optical figure of merit, F, for each of the glasses. For the Ce, Pr, Tb and Dy based glasses it was possible to interpolate values of the Verdet constant, V, allowing F to be calculated over the wavelength range 450-520 Å (excluding regions close to the absorption bands).

REFERENCES

Ballato J and Snitzer E. 1995. *Applied Optics.* **34** (30) p. 6848.

Berger S.B, Rubinstein C.B, Kurkjian C.R and Treptow A.W. 1964. *Physical Review.* **133** (3A) p. A723.

Borrelli N.F. *The Journal of Chemical Physics.* 1964. **41** (11) p. 3289.

Bowron D.T. Bushnell-Wye G. Newport R.J. Rainford B.D and Saunders G.A.1996. *Journal of Physics: Condensed Matter.* **8** p. 3337.

Brennan T. 1998. PhD. *University of Bath.*_ UK.

Carnall W.T, Fields P.R and Rajnak K.1968 (a). *Journal of Chemical Physics.* **49** (10) p. 4424.

Carnall W.T, Fields P.R and Rajnak K.1968 (b). *Journal of Chemical Physics.* **49** (10) p. 4447.

Cole J.M, van Eck E.R.H, Mountjoy G, Newport R.J, Brennan T and Saunders G.A. 1999. *Journal of Physics: Condensed Matter.* **11** p. 9165.

Cole J.M, van Eck E.R.H, Mountjoy G, Anderson R, Brennan T, Bushnell-Wye, Newport R.J, and Saunders G.A. 2001. *Journal of Physics: Condensed Matter.* **13** p. 4105.

EOT. Electro-Optics Technology, Inc.1030 Hastings Street, Ste 140, Traverse City MI 49686. US.http://www.eotech.com/

Faraday M. 1845. Philos Trans Royal Society London **1** p. 104.

Hecht E. 1987. *Optics.* Addison-Wesley. Wokingham. UK.

Hong H.Y.P. 1974 (a) Acta Cryst. **B 30.** p. 468.

Hong H.Y.P. 1974 (b) Acta Cryst. **B 30.** p. 1857.

Hoppe A, Kranold R, Stachel D, Barz A and Hannon A. 1998. *Journal of Non-Crystalline Solids.* **232-234.** p. 44.

Kittel C. 1986. *Introduction to Solid State Physics.* Wiley. Chichester. UK.

Kohli J.T and Shelby J.E. 1991. *Physics and Chemistry of Glasses.* **32.** (3) p.109.

Letellier V, Seignac A, Le Floch A and Matecki M. 1989. *Journal of Non-Crystalline Solids.* **111.** p. 55.

MacFarlane D.R, Bradbury C.R, Newman P.J and Javorniczky J. 1997. *Journal of Non-Crystalline Solids.* **213&214.** p. 199.

MMC. Magnetic Materials & Components.500 N Broadway,Jericho, NY,11753-2119, US. http://www.mmcmagnetics.com/ourproducts/main_SmCo.htm

Petrovskii G.T, Edelman I.S, Zarubina T.V, Malakhovskii A.V, Zabluda V.N and Ivanov M. Yu. 1991. *Journal of Non-Crystalline Solids.* **130.** p. 35.

Qui J, Higuchi H and Kawamoto Y. 1996. *Journal of Applied Physics.* **80** (9) p. 5297.

Qui J, Kawamoto Y and Hirao K. 1997 (a). *Japanese Journal of Applied Physics.* **36.** p. 1091.

Qui J, Tanaka K, Sugimoto N and Hirao K. 1997 (b). *Journal of Non-Crystalline Solids.* **213&214.** p. 193.

Rubinstein C.B, Berger S.B, Van Uitert L.G, and Bonner W.A. 1964. *Journal of Applied Physics.* **35.** (8) p. 2338.

Tanaka K, Hirao K and Soga N. 1995. *Japanese Journal of Applied Physics.* **34.** p. 4825.

Wilson J and Hawkes J.F.B. 1983. *Optoelectronics: An Introduction.* Prentice-Hall. London. UK.

CHAPTER 4

THE THEORY OF THERMAL NEUTRON SCATTERING

The theory of neutron scattering has been described in many texts e.g. Squires (1978), Lovesey (1984). This chapter will only give a brief outline of the basic theory relating to the results presented in the following chapters.

4.1 INTRODUCTION

The neutron is a subatomic particle with mass m = 1.675×10^{-27} kg, zero charge, spin = ½ and magnetic dipole moment $\mu_n = -1.913\ \mu_N$ where μ_N is the nuclear magneton. The de Broglie wavelength of a neutron with velocity v is given by

$$\lambda = \frac{h}{mv} \qquad [4.1]$$

where h is Planck's constant. The wavevector **k** has a magnitude

$$k = \frac{2\pi}{\lambda} \qquad [4.2]$$

in the direction of **v**. The momentum **p** of the neutron is

$$\mathbf{p} = \hbar\mathbf{k} \qquad [4.3]$$

where $\hbar = h/2\pi$. A neutron with an energy E corresponding to a temperature T and wavelength λ is therefore expressed as

$$E = k_B T = \frac{1}{2}mv^2 = \frac{h^2}{2m\lambda^2} = \frac{\hbar^2 k^2}{2m} \qquad [4.4]$$

where k_B is the Boltzmann constant.

The standard parameters for the thermal neutron are T = 293 K, v = 2.2 km s^{-1}, E = 25.3 meV and λ = 1.798 Å. Neutrons produced by reactor sources have a wide range of energies as described by the Maxwellian distribution and neutrons with temperatures between 60 – 1000 K are described as thermal neutrons.

The following basic properties of the thermal neutron make it an important tool for investigating the microscopic structure and dynamics of condensed matter:

(a) The mass and speed of the neutron results in a de Broglie wavelength of the same order as inter-atomic distances in solids and liquids. Therefore diffraction occurs resulting in important information on the structure of the scattering system.

(b) The neutron has zero charge and therefore has no Coulomb barrier to overcome, allowing the neutron to penetrate deep into a target. Neutrons are scattered by nuclear forces, by contrast with x-rays which are scattering by electrons, such that the cross section scales with atomic number. Neutrons can detect light nuclei such as hydrogen that are virtually transparent to x-rays. Also there can be a large contrast in the scattering length between isotopes of the same element or between neighbouring elements which allows techniques such as isotopic and isomorphic substitution to be applied.

(c) The energy of thermal neutrons is comparable to many excitations in condensed matter. Inelastically scattered neutrons can therefore provide information on the energies of these excitations and hence the inter-atomic forces.

(d) The neutron has a magnetic moment and can therefore interact with unpaired electrons in magnetic atoms thus providing information on the magnetic properties of matter.

4.2 DEFINITIONS OF SCATTERING CROSS SECTIONS

Consider a monochromatic beam of thermal neutrons, with energy E_0 incident on a target as shown in Figure 4.1.

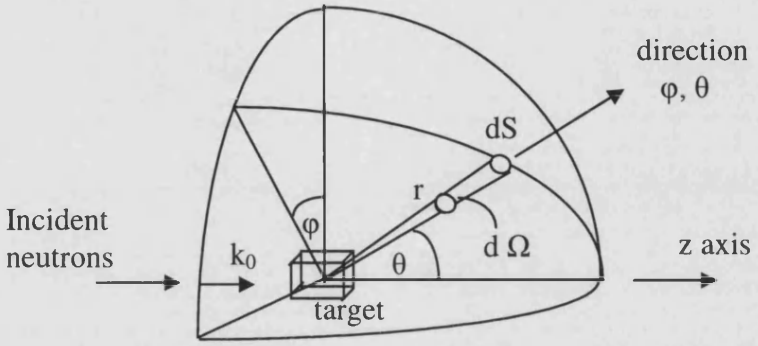

Figure 4.1 The geometry for a scattering experiment.

The target is a collection of atoms and shall be referred to as the scattering system. Provided the distance between the target and the detector is large compared to the dimensions of the target then the small solid angle $d\Omega$ will be well defined. There are various measurements that can be made on the scattering system. If the detector counts neutrons of energies between E_1 and $E_1 + dE_1$ into the solid angle $d\Omega$ in the direction of φ, θ then the double differential cross section, defined by equation 4.5, is measured

$$\frac{d^2\sigma}{d\Omega\, dE_1} = \frac{\text{(number of neutrons scattered per second into a solid angle } d\Omega \text{ in the direction } \theta, \varphi \text{ with final energy between } E_1 \text{ and } E_1 + dE_1)}{\Phi\, d\Omega\, dE_1}$$

where Φ denotes the incident flux.

If the energy of the neutrons is not analysed and the detector counts all of the neutrons scattered into the solid angle in the direction φ, θ the differential cross section

$$\frac{d\sigma}{d\Omega} = \frac{\text{(number of neutrons scattered per second into a solid angle } d\Omega \text{ in the direction } \theta, \varphi)}{\Phi\, d\Omega} \qquad [4.6]$$

is measured. The total scattering cross section is defined by

$$\sigma_{tot} = \text{(total number of neutrons scattered per second)} / \Phi \qquad [4.7]$$

where σ_{tot} is the total number of neutrons scattered in all directions. The cross sections are the quantities actually measured in the scattering experiments. The experimental cross sections are usually quoted per atom or per molecule.

In a neutron scattering experiment the measured intensity $I(\boldsymbol{Q}, \omega)$ can be expressed in terms of the double differential cross section by

$$I(\mathbf{Q}, \omega) = \frac{d^2\sigma}{d\Omega\, dE_1} \Phi\, d\Omega\, dE_1. \qquad [4.8]$$

The momentum transfer is simply $\mathbf{Q} = \mathbf{k}_0 - \mathbf{k}_1$ in units of $\hbar$ (see Figure 4.2) and the energy transfer is denoted by $\hbar\omega = E_0 - E_1$, where E_0 and E_1 are the energies of the incident and scattered neutrons respectively.

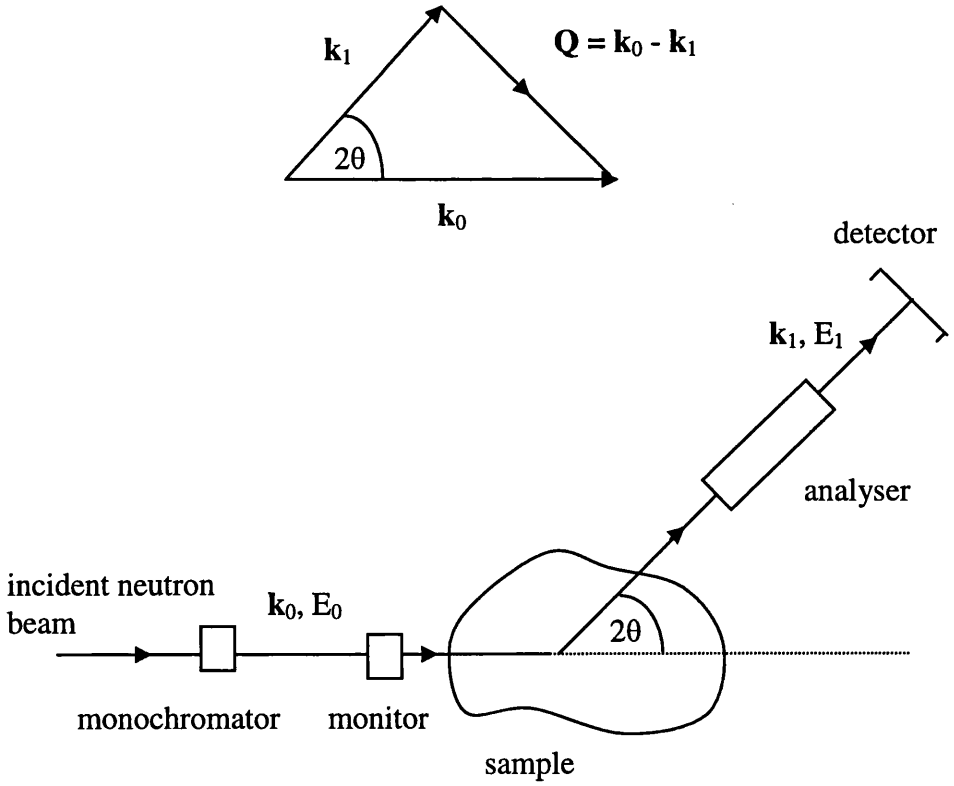

Figure 4.2. The scattering triangle and a schematic representation of a neutron scattering experiment.

4.3 EXPRESSIONS FOR SCATTERING CROSS SECTIONS.

The simple case of nuclear scattering by a single nucleus in a fixed position shall now be considered. From basic diffraction theory it is known that if waves are scattered by an object much smaller than the wavelength then the scattered wave is spherically symmetric. This is the case for neutron scattering since the nuclear forces, which cause the scattering, have a range of about 10^{-14} to 10^{-15} m and the wavelength of thermal neutrons is of the order 10^{-10} m. In this case the scattered waves are entirely S waves (l=0) and the angular distribution is symmetric.

If we take the origin to be at the scattering nucleus, and the z axis to be along the direction of $\mathbf{k_0}$, as shown in Figure 4.1, then the incident neutrons can be represented by the wavefunction

$$\psi_{inc} = e^{ik_0 z}. \qquad [4.9]$$

As the scattering is spherically symmetric, the wavefunction of the scattered neutrons at a point r can be written in the form

$$\psi_{sc} = -\frac{b}{r} e^{ik_0 r} \qquad [4.10]$$

where b is a constant independent of the angles θ, φ. The minus sign is conventional and corresponds to a positive value of the scattering length, b, for a repulsive potential. The scattering length is complex and the imaginary part corresponds to absorption. The real and imaginary parts can vary rapidly with the incident neutron energy when it is close to a resonance but sufficiently far from a resonance the energy dependence of the real part can be neglected. The scattering lengths are determined experimentally and have been well documented (Sears 1992).

The cross-section $d\sigma/d\Omega$ for scattering from a single bound nucleus can be calculated using ψ_{sc} and ψ_{inc}. If v is the velocity of the neutrons then the number of neutrons passing through an area dS per second is

$$v\, dS\, |\psi_{sc}|^2 = v\, dS\, \frac{b^2}{r^2} = vb^2\, d\Omega . \qquad [4.11]$$

The flux of the incident neutrons is

$$\Phi = v\,|\psi_{inc}|^2 = v\,. \qquad [4.12]$$

It then follows from the definition of the differential cross section that

$$\frac{d\sigma}{d\Omega} = \frac{v b^2\, d\Omega}{\Phi\, d\Omega} = b^2 \qquad [4.13]$$

and in this simple case

$$\sigma_{tot} = 4\pi b^2. \qquad [4.14]$$

In a more sophisticated treatment of neutron scattering it can be shown (Squires 1978, Lovesey 1984) that the double differential cross section of an isotropic scattering system comprising N particles can be written as

$$\frac{d^2\sigma}{d\Omega\, dE_1} = \left.\frac{d^2\sigma}{d\Omega\, dE_1}\right|_{coh} + \left.\frac{d^2\sigma}{d\Omega\, dE_1}\right|_{inc} \qquad [4.15]$$

where the coherent term is given by

$$\left.\frac{d^2\sigma}{d\Omega\, dE_1}\right|_{coh} = \frac{\sigma_{coh}}{4\pi}\frac{k_1}{k_0} NS(Q,\omega) \qquad [4.16]$$

and the incoherent term by

$$\left.\frac{d^2\sigma}{d\Omega\, dE_1}\right|_{inc} = \frac{\sigma_{inc}}{4\pi}\frac{k_1}{k_0} NS_{inc}(Q,\omega) \qquad [4.17]$$

where

$$\sigma_{coh} = 4\pi b_{coh}^2 \qquad [4.18]$$

and

$$\sigma_{inc} = 4\pi b_{inc}^2 \qquad [4.19]$$

and the total scattering cross section is

$$\sigma_{total} = \sigma_{coh} + \sigma_{inc}. \qquad [4.20]$$

$S(Q,\omega)$ and $S_{inc}(Q,\omega)$ are real observable functions and are usually referred to as the coherent and incoherent scattering laws or dynamic structure factors. These factors contain information on the structure and dynamics of the scattering system and are independent of the nature of the neutron –nucleus interaction.

Physically the incoherent scattering arises from the random distribution of the deviations of the scattering lengths from their mean value. The scattering lengths are quoted in units of femtometers fm (1 fm = 10^{-15} m) and the cross sections are usually measured in barns (1 barn = 10^{-28} m^2).

4.4 THE STATIC APPROXIMATION AND PLACZEK CORRECTIONS.

In a diffraction experiment an effective differential scattering cross section is measured where its coherent part is given by

$$\left(\frac{d\sigma_{coh}}{d\Omega}\right)_{eff} = N\frac{\sigma_{coh}}{4\pi}\int_{-\infty}^{E_0/\hbar}\eta(k_1)\frac{k_1}{k_0}S(Q,\omega)\,d\omega \qquad [4.21]$$

and its incoherent part is given by

$$\left(\frac{d\sigma_{inc}}{d\Omega}\right)_{eff} = N\frac{\sigma_{inc}}{4\pi}\int_{-\infty}^{E_0/\hbar}\eta(k_1)\frac{k_1}{k_0}S(Q,\omega)\,d\omega \qquad [4.22]$$

where E_0 is the energy of the incident neutrons and $\eta(k_1)$ is the detector efficiency. The upper limit $E_0/\hbar$ in the integral implies that the maximum energy that a neutron can transfer to the system is its incident energy.

In the static approximation it is assumed that the incident energy of the neutron is much greater than the energy transfers involved in the neutron-nucleus

interaction, i.e. $E_0 >> \hbar\omega$ such that $k_1 \approx k_0$. The scattering triangle (Figure 4.2) expressed as

$$Q^2 = k_1^2 + k_0^2 - 2k_0k_1\cos(2\theta) \qquad [4.23]$$

then reduces to

$$Q^2 \approx 2k_0^2\,(1-\cos 2\theta)$$

such that

$$Q = (4\pi/\lambda)\sin\theta \qquad [4.24]$$

and the differential cross section becomes

$$\left(\frac{d\sigma_{coh}}{d\Omega}\right)_{eff}^{static} = N\frac{\sigma_{coh}}{4\pi}\eta_0 \int_{-\infty}^{\infty} S(Q,\omega)\,d\omega$$

$$= N\frac{\sigma_{coh}}{4\pi}\eta_0\, S(Q)\ . \qquad [4.25]$$

In this equation η_0 is the detector efficiency for the elastically scattered neutrons and S(Q) is the static structure factor which is related to the pair distribution function g(r) by the Fourier transform relation

$$S(Q) = 1+\frac{4\pi n_0}{Q}\int_0^{\infty}\left[g_{\alpha\beta}(r)-1\right]r\sin(Qr)\,dr\,. \qquad [4.26]$$

g(r) gives a measure of the probability of finding a nucleus in a volume element $d^3\mathbf{r}$ at r away from another placed at the origin of coordinates.

Provided deviations from the static approximation are small they can be corrected for by using the method outlined by Placzek which is described in full for reactor experiments by Yarnell *et al* (1973). The coherent part of the effective differential scattering cross section is then given by

$$\left(\frac{d\sigma_{coh}}{d\Omega}\right)_{eff} = N\eta_0\frac{\sigma_{coh}}{4\pi}\{\ [S(Q)-1]+[1+P(Q)]\ \} \qquad [4.27]$$

where

$$P(Q) = -C_1\left(\frac{E_{rec}}{E_0}\right)+C_2\left(\frac{E_{rec}}{E_0}\right)^2-C_3\left(\frac{E_{rec}k_BT}{E_0^2}\right)+\frac{m}{2M}\left(\frac{E_{rec}}{E_0}+\frac{k_BT}{E_0}\right), \qquad [4.28]$$

m is the mass of the neutron, M the mass of the nucleus, E_0 is the incident neutron energy given by

$$E_0 = \frac{h^2}{2m\lambda^2} \quad , \qquad [4.29]$$

and E_{rec} is the recoil energy of the scattering nucleus given by

$$E_{rec} = \frac{\hbar^2Q^2}{2M} = \frac{h^2(1-\cos 2\theta)}{M\lambda^2} \quad . \qquad [4.30]$$

C_1, C_2 and C_3 are constants depending on the detector efficiency which is given by

$$\eta(k_1) = 1 - \exp\left(\frac{-ak_0}{k_1}\right) \qquad [4.31]$$

where a is positive constant whose value depends on the pressure, temperature and type of gas in the detectors. By using equations 4.29 and 4.30 the ratios given in equation 4.28 can be expressed as

$$\frac{E_{rec}}{E_0} = \frac{2(1-\cos 2\theta)m}{M} \qquad [4.32]$$

and

$$\frac{k_BT}{E_0} = \frac{2mk_B}{h^2}T\lambda^2 . \qquad [4.33]$$

The inelasticity corrections are therefore angular dependent (equation 4.32) and are largest for nuclei of low mass and low incident neutron energies.

4.5 MULTICOMPONENT SYSTEMS

For a disordered material containing more than one element, the total effective differential cross section becomes

$$\left(\frac{d\sigma}{d\Omega}\right)_{eff} = N\eta_0 \{ F(Q) + \sum_{\alpha} c_\alpha \left[b_\alpha^2 + b_{inc,\alpha}^2\right] [1 + P_\alpha(Q)] \} \qquad [4.34]$$

$$\equiv N \eta_0 F_S(Q)$$

where F(Q) is the total structure factor

$$F(Q) = \sum_{\alpha=1}^{x} \sum_{\beta=1}^{x} b_\alpha b_\beta c_\alpha c_\beta [S_{\alpha\beta}(Q) - 1] \qquad [4.35]$$

and $S_{\alpha\beta}(Q)$ is a so-called Faber-Ziman (1964) partial structure factor. $P_\alpha(Q)$ is the Placzek correction for chemical species α and c_α is the atomic fraction of species α

$$c_\alpha = \frac{N_\alpha}{N} \qquad [4.36]$$

where N_α is the number of atoms of species α. N is the total number of atoms in the system, $N = \sum_{\alpha=1}^{x} N_\alpha$, and x is the number of different chemical species. b_α is the scattering length of chemical species α and $b_{inc,\alpha}$ is the incoherent scattering length of chemical species α.

The corresponding real-space information is contained in the total pair correlation function

$$G(r) = \frac{1}{2\pi^2 n_0 r} \int_0^\infty F(Q) \sin(Qr) Q \, dQ$$

$$= \sum_{\alpha=1}^{x} \sum_{\beta=1}^{x} c_\alpha c_\beta b_\alpha b_\beta [g_{\alpha\beta}(r) - 1] \qquad [4.37]$$

where $g_{\alpha\beta}(r)$ is a partial pair distribution function.

The co-ordination number $\bar{n}_{\alpha}^{\beta}$ is defined as the average number of atoms of type β surrounding an atom of type α between radii r_1 and r_2 and is given by

$$\bar{n}_{\alpha}^{\beta} = \int_{r_1}^{r_2} 4\pi r^2 c_{\beta} n_0 g_{\alpha\beta}(r) dr . \qquad [4.38]$$

4.6 MAGNETIC SCATTERING

For systems containing rare earth paramagnetic ions the total effective differential cross section can be written as

$$\left(\frac{d\sigma}{d\Omega}\right)_{tot} = \left(\frac{d\sigma}{d\Omega}\right)_{nucl} + \left(\frac{d\sigma}{d\Omega}\right)_{mag} \qquad [4.39]$$

where $\left(\frac{d\sigma}{d\Omega}\right)_{nucl}$ is given by equation 4.34. The paramagnetic differential cross section, in the free ion approximation, is given by (Balcar and Lovesey 1989, Wasse and Salmon 1999)

$$\left(\frac{d\sigma}{d\Omega}\right)_{mag} = N\eta_0 c_R (\gamma r_e)^2 \frac{1}{6} J(J+1) g_J^2 f^2(Q) \qquad [4.40]$$

where c_R is the atomic fraction of the paramagnetic ion, $\gamma = 1.91$ is the magnitude of the neutron magnetic moment in units of the nuclear magneton, r_e is the classical radius of an electron such that $(\gamma r_e)^2 = 0.291$ barn, J is the total angular momentum quantum number and g_J is the Landé splitting factor (Bleaney and Bleaney 1976). The magnetic form factor, $f(Q)$, is obtained from the expression

$$f^2(Q) = \langle j_0(Q)\rangle^2 + C_{02}\langle j_0(Q)\rangle\langle j_2(Q)\rangle + C_{22}\langle j_2(Q)\rangle^2 + C_{24}\langle j_2(Q)\rangle\langle j_4(Q)\rangle + C_{44}\langle j_4(Q)\rangle^2 + C_{46}\langle j_4(Q)\rangle\langle j_6(Q)\rangle + C_{66}\langle j_6(Q)\rangle^2 \quad [4.41]$$

where the radial integrals $\langle j_X(Q)\rangle$ for X = 0, 2, 4 and 6 are given by Brown (1995) and the C_{ij}'s are given in appendix E.3 of Balcar and Lovesey (1989). The expression for the total structure factor $F_S(Q)$ given by equation 4.34 is then generalised in the presence of the paramagnetic ions to give

$$F_S(Q) = \left\{\left(\frac{d\sigma}{d\Omega}\right)_{eff} + \left(\frac{d\sigma}{d\Omega}\right)_{mag}\right\} \Big/ N\eta_0 \,. \quad [4.42]$$

4.7 THE METHOD OF ISOMORPHIC SUBSTITUTION IN NEUTRON DIFFRACTION.

Isomorphic substitution can be used to extract some or even all of the partial structure factors, $S_{\alpha\beta}(Q)$, which contribute to the total structure factor F(Q) (Wasse and Salmon 1999). The method of isomorphic substitution is analogous to that of isotopic substitution. The technique is based on substituting one of the elements in the system by a neighbouring element in the periodic table that forms the same structure and has a similar ion size; the substituted atom is assumed to be identical in every other respect apart from the scattering length. As the scattering length for the substituted species is different, the weighting factors for individual $S_{\alpha\beta}(Q)$ in the total structure factors are changed. The technique relies on the fact that the neutron scattering length for neighbouring elements in the periodic table can vary considerably unlike the case of x-ray scattering where the atomic form factor simply scales with atomic number. The technique is limited to the availability of isomorphic pairs, e.g. La and Ce or Dy and Ho, as will be discussed in Chapters 6 and 7.

4.8 FIRST AND SECOND ORDER DIFFERENCE METHODS APPLIED TO R-P-O-Al SYSTEMS

Consider the four-component glassy system R-P-O-Al, where R represents a rare earth ion (e.g. La, Ce, Dy or Ho) and P, O and Al form the glass matrix. The latter shall be referred to collectively as matrix μ elements.

By performing three diffraction experiments on samples that are identical in every aspect, except for the scattering lengths of the isomorphically substituted atoms, three total structure factors $F^{(1)}(Q)$, $F^{(2)}(Q)$ and $F^{(3)}(Q)$ are measured corresponding to bound coherent scattering lengths $b_{1,R}$, $b_{2,R}$ and $b_{3,R}$ respectively where $b_{1,R} > b_{2,R} > b_{3,R}$. In matrix notation

$$[F] = [A]\,[S] \qquad [4.43]$$

where

$$[F] = \begin{vmatrix} F^{(1)}(Q) \\ F^{(2)}(Q) \\ F^{(3)}(Q) \end{vmatrix}, \qquad [S] = \begin{vmatrix} S_{RR}(Q) - 1 \\ S_{PP}(Q) - 1 \\ S_{OO}(Q) - 1 \\ S_{AlAl}(Q) - 1 \\ S_{RP}(Q) - 1 \\ S_{RO}(Q) - 1 \\ S_{RAl}(Q) - 1 \\ S_{PO}(Q) - 1 \\ S_{PAl}(Q) - 1 \\ S_{OAl}(Q) - 1 \end{vmatrix}$$

and

$$[A] = \begin{vmatrix} c_R^2 b_{1,R}^2 & c_P^2 b_P^2 & c_O^2 b_O^2 & c_{Al}^2 b_{Al}^2 & 2c_R c_P b_{1,R} b_P & 2c_R c_O b_{1,R} b_O & 2c_R c_{Al} b_{1,R} b_{Al} & 2c_P c_O b_P b_O & 2c_P c_{Al} b_P b_{Al} & 2c_O c_{Al} b_O b_{Al} \\ c_R^2 b_{2,R}^2 & c_P^2 b_P^2 & c_O^2 b_O^2 & c_{Al}^2 b_{Al}^2 & 2c_R c_P b_{2,R} b_P & 2c_R c_O b_{2,R} b_O & 2c_R c_{Al} b_{2,R} b_{Al} & 2c_P c_O b_P b_O & 2c_P c_{Al} b_P b_{Al} & 2c_O c_{Al} b_O b_{Al} \\ c_R^2 b_{3,R}^2 & c_P^2 b_P^2 & c_O^2 b_O^2 & c_{Al}^2 b_{Al}^2 & 2c_R c_P b_{3,R} b_P & 2c_R c_O b_{3,R} b_O & 2c_R c_{Al} b_{3,R} b_{Al} & 2c_P c_O b_P b_O & 2c_P c_{Al} b_P b_{Al} & 2c_O c_{Al} b_O b_{Al} \end{vmatrix}$$

The individual total structure factors can be written explicitly as

$$F^{(1)}(Q) = c_R^2 b_{1,R}^2 [S_{RR}(Q) - 1] + c_P^2 b_P^2 [S_{PP}(Q) - 1] + c_O^2 b_O^2 [S_{OO}(Q) - 1] + c_{Al}^2 b_{Al}^2 [S_{AlAl}(Q) - 1] + 2c_R c_P b_{1,R} b_P [S_{RP}(Q) - 1] + 2c_R c_O b_{1,R} b_O [S_{RO}(Q) - 1] + 2c_R c_{Al} b_{1,R} b_{Al} [S_{RAl}(Q) - 1] + 2c_P c_O b_P b_O [S_{PO}(Q) - 1] + 2c_P c_{Al} b_P b_{Al} [S_{PAl}(Q) - 1] + 2c_O c_{Al} b_O b_{Al} [S_{OAl}(Q) - 1] \quad [4.44]$$

$$F^{(2)}(Q) = c_R^2 b_{2,R}^2 [S_{RR}(Q) - 1] + c_P^2 b_P^2 [S_{PP}(Q) - 1] + c_O^2 b_O^2 [S_{OO}(Q) - 1] + c_{Al}^2 b_{Al}^2 [S_{AlAl}(Q) - 1] + 2c_R c_P b_{2,R} b_P [S_{RP}(Q) - 1] + 2c_R c_O b_{2,R} b_O [S_{RO}(Q) - 1] + 2c_R c_{Al} b_{2,R} b_{Al} [S_{RAl}(Q) - 1] + 2c_P c_O b_P b_O [S_{PO}(Q) - 1] + 2c_P c_{Al} b_P b_{Al} [S_{PAl}(Q) - 1] + 2c_O c_{Al} b_O b_{Al} [S_{OAl}(Q) - 1] \quad [4.45]$$

$$F^{(3)}(Q) = c_R^2 b_{3,R}^2 [S_{RR}(Q) - 1] + c_P^2 b_P^2 [S_{PP}(Q) - 1] + c_O^2 b_O^2 [S_{OO}(Q) - 1] + c_{Al}^2 b_{Al}^2 [S_{AlAl}(Q) - 1] + 2c_R c_P b_{3,R} b_P [S_{RP}(Q) - 1] + 2c_R c_O b_{3,R} b_O [S_{RO}(Q) - 1] + 2c_R c_{Al} b_{3,R} b_{Al} [S_{RAl}(Q) - 1] + 2c_P c_O b_P b_O [S_{PO}(Q) - 1] + 2c_P c_{Al} b_P b_{Al} [S_{PAl}(Q) - 1] + 2c_O c_{Al} b_O b_{Al} [S_{OAl}(Q) - 1] \quad . \quad [4.46]$$

Those correlations involving only the rare earth atom R can be extracted by forming the first order difference functions

$$\Delta_R^{(1)}(Q) = F^{(1)}(Q) - F^{(3)}(Q)$$

$$= c_R^2 [b_{1,R}^2 - b_{3,R}^2] [S_{RR}(Q) - 1] + 2c_R c_P b_P [b_{1,R} - b_{3,R}] [S_{RP}(Q) - 1] + 2c_R c_O b_O [b_{1,R} - b_{3,R}] [S_{RO}(Q) - 1] + 2c_R c_{Al} b_{Al} [b_{1,R} - b_{3,R}] [S_{RAl}(Q) - 1], \quad [4.47]$$

$$\Delta_R^{(2)}(Q) = F^{(1)}(Q) - F^{(2)}(Q)$$

$$= c_R^2 [b_{1,R}^2 - b_{2,R}^2] [S_{RR}(Q) - 1] + 2c_R c_P b_P [b_{1,R} - b_{2,R}] [S_{RP}(Q) - 1] + 2c_R c_O b_O [b_{1,R} - b_{2,R}] [S_{RO}(Q) - 1] + 2c_R c_{Al} b_{Al} [b_{1,R} - b_{2,R}] [S_{RAl}(Q) - 1], \quad [4.48]$$

$$\Delta_R^{(3)}(Q) = F^{(2)}Q) - F^{(3)}(Q)$$

$$= c_R^2 [b_{2,R}^2 - b_{3,R}^2] [S_{RR}(Q) -1] + 2c_R c_P b_P [b_{2,R}-b_{3,R}] [S_{RP}(Q) -1]$$
$$+ 2c_R c_O b_O [b_{2,R}-b_{3,R}] [S_{RO}(Q) -1] + 2c_R c_{Al} b_{Al} [b_{2,R}-b_{3,R}] [S_{RAl}(Q) -1] . \quad [4.49]$$

A first order difference function can be extracted using only two total structure factors. This is very beneficial when modelling the rare earth environment since the matrix-matrix correlations cancel and the number of partial structure factors is reduced from ten to four, thus leading to a clearer interpretation of the data. By using a first order difference function it is also possible to eliminate the rare earth-matrix correlations by forming a total minus weighted function

$$\Delta_F^{(1)}(Q) = F^{(1)}(Q) - b_{1,R} \Delta_R^{(1)}(Q) / (b_{1,R} - b_{3,R}) . \quad [4.50]$$

Substituting for $\Delta_R^{(1)}(Q)$ and rearranging gives

$$\Delta_F^{(1)}(Q) = F^{(1)}(Q) - b_{1,R} [F^{(1)}(Q) - F^{(3)}(Q)]/ (b_{1,R} - b_{3,R})$$

$$= [b_{1,R} F^{(3)}(Q) - b_{3,R}F^{(1)}(Q)] / (b_{1,R} - b_{3,R}). \quad [4.51]$$

Substituting $F^{(1)}(Q)$ and $F^{(3)}(Q)$ in equation 4.51 then gives

$$\Delta_F^{(1)}(Q) = - c_R^2 b_{1,R} b_{3,R} [S_{RR}(Q) -1] + c_P^2 b_P^2 [S_{PP}(Q) -1] + c_O^2 b_O^2 [S_{OO}(Q) -1]$$
$$+ c_{Al}^2 b_{Al}^2 [S_{AlAl}(Q) -1] + 2c_P c_O b_P b_O [S_{PO}(Q) -1]$$
$$+ 2c_P c_{Al} b_P b_{Al} [S_{PAl}(Q) -1] + 2c_O c_{Al} b_O b_{Al} [S_{OAl}(Q) -1] . \quad [4.52]$$

The other total minus weighted difference functions are defined in an analogous fashion as

$$\Delta_F^{(2)}(Q) = F^{(1)}(Q) - b_{1,R} \Delta_R^{(2)}(Q) / (b_{1,R} - b_{2,R})$$

$$= -c_R^2 b_{1,R} b_{2,R} [S_{RR}(Q) - 1] + c_P^2 b_P^2 [S_{PP}(Q) - 1] + c_O^2 b_O^2 [S_{OO}(Q) - 1]$$
$$+ c_{Al}^2 b_{Al}^2 [S_{AlAl}(Q) - 1] + 2c_P c_O b_P b_O [S_{PO}(Q) - 1]$$
$$+ 2c_P c_{Al} b_P b_{Al} [S_{PAl}(Q) - 1] + 2c_O c_{Al} b_O b_{Al} [S_{OAl}(Q) - 1] \quad [4.53]$$

and

$\Delta_F^{(3)}(Q) = F^{(2)}(Q) - b_{2,R}\, \Delta_R^{(3)}(Q) / (b_{2,R} - b_{3,R})$

$$= - c_R^2 b_{2,R} b_{3,R} [S_{RR}(Q) - 1] + c_P^2 b_P^2 [S_{PP}(Q) - 1] + c_O^2 b_O^2 [S_{OO}(Q) - 1]$$
$$+ c_{Al}^2 b_{Al}^2 [S_{AlAl}(Q) - 1] + 2c_P c_O b_P b_O [S_{PO}(Q) - 1]$$
$$+ 2c_P c_{Al} b_P b_{Al} [S_{PAl}(Q) - 1] + 2c_O c_{Al} b_O b_{Al} [S_{OAl}(Q) - 1] \; . \quad [4.54]$$

The total minus weighted function can also be formed from only two total structure factors and again reduces the number of partials from ten to seven. The total minus weighted function can be thought of as being the matrix-matrix function with a small negative R-R contribution. This is useful in many cases since often the R-R spacing is large and can be ignored when modelling the short range matrix-matrix real space correlations.

Measuring a third total structure factor allows the partial structure factor $S_{RR}(Q)$ to be extracted, where $S_{RR}(Q)$ is given by

$$[S_{RR}(Q) - 1] = \frac{\Delta_R^{(2)}(Q) - \gamma\, \Delta_R^{(1)}(Q)}{c_R^2\, \gamma (1-\gamma) (b_{1,R} - b_{3,R})^2} \quad [4.55]$$

and γ is given by

$$\gamma = \frac{b_{1,R} - b_{2,R}}{b_{1,R} - b_{3,R}} . \quad [4.56]$$

Once the second order difference function has been extracted it can be subtracted from the first order difference function to remove the R-R correlations, to give the rare earth-matrix difference function $\Delta_{R\mu}(Q)$ that consists entirely of the rare earth matrix (R-P, R-O and R-Al) correlations. These functions are given by

$$\Delta_{R\mu}^{(1)}(Q) = \Delta_R^{(1)}(Q) - c_R^2 [b_{1,R}^2 - b_{3,R}^2] [S_{RR}(Q) - 1]$$

$$= 2c_R c_P b_P [b_{1,R} - b_{3,R}] [S_{RP}(Q) - 1] + 2c_R c_O b_O [b_{1,R} - b_{3,R}] [S_{RO}(Q) - 1]$$
$$+ 2c_R c_{Al} b_{Al} [b_{1,R} - b_{3,R}] [S_{RAl}(Q) - 1], \qquad [4.57]$$

$$\Delta_{R\mu}^{(2)}(Q) = \Delta_R^{(2)}(Q) - c_R^2 [b_{1,R}^2 - b_{2,R}^2] [S_{RR}(Q) - 1]$$
$$= 2c_R c_P b_P [b_{1,R} - b_{2,R}] [S_{RP}(Q) - 1] + 2c_R c_O b_O [b_{1,R} - b_{2,R}] [S_{RO}(Q) - 1]$$
$$+ 2c_R c_{Al} b_{Al} [b_{1,R} - b_{2,R}] [S_{RAl}(Q) - 1] \qquad [4.58]$$

and

$$\Delta_{R\mu}^{(3)}(Q) = \Delta_R^{(3)}(Q) - c_R^2 [b_{2,R}^2 - b_{3,R}^2] [S_{RR}(Q) - 1]$$

$$= 2c_R c_P b_P [b_{2,R} - b_{3,R}] [S_{RP}(Q) - 1] + 2c_R c_O b_O [b_{2,R} - b_{3,R}] [S_{RO}(Q) - 1]$$
$$+ 2c_R c_{Al} b_{Al} [b_{2,R} - b_{3,R}] [S_{RAl}(Q) - 1]. \qquad [4.59]$$

The second order difference function can also be added to the total minus weighted function to remove the R-R correlations, resulting in a function $\Delta_{\mu\mu}(Q)$ that consists entirely of the matrix-matrix correlations. These functions are given by

$$\Delta_{\mu\mu}^{(1)}(Q) = \Delta_F^{(1)}(Q) + c_R^2 b_{1,R} b_{3,R} [S_{RR}(Q) - 1]$$
$$= c_P^2 b_P^2 [S_{PP}(Q) - 1] + c_O^2 b_O^2 [S_{OO}(Q) - 1] + c_{Al}^2 b_{Al}^2 [S_{AlAl}(Q) - 1]$$
$$+ 2c_P c_O b_P b_O [S_{PO}(Q) - 1] + 2c_P c_{Al} b_P b_{Al} [S_{PAl}(Q) - 1] + 2c_O c_{Al} b_O b_{Al} [S_{OAl}(Q) - 1]$$
[4.60]

$$\Delta_{\mu\mu}^{(2)}(Q) = \Delta_F^{(2)}(Q) + c_R^2 b_{1,R} b_{2,R} [S_{RR}(Q) - 1]$$
$$= c_P^2 b_P^2 [S_{PP}(Q) - 1] + c_O^2 b_O^2 [S_{OO}(Q) - 1] + c_{Al}^2 b_{Al}^2 [S_{AlAl}(Q) - 1]$$
$$+ 2c_P c_O b_P b_O [S_{PO}(Q) - 1] + 2c_P c_{Al} b_P b_{Al} [S_{PAl}(Q) - 1] + 2c_O c_{Al} b_O b_{Al} [S_{OAl}(Q) - 1]$$
[4.61]

and

$$\Delta_{\mu\mu}^{(3)}(Q) = \Delta_F^{(3)}(Q) + c_R^2 b_{2,R} b_{3,R} [S_{RR}(Q) - 1]$$
$$= c_P^2 b_P^2 [S_{PP}(Q) - 1] + c_O^2 b_O^2 [S_{OO}(Q) - 1] + c_{Al}^2 b_{Al}^2 [S_{AlAl}(Q) - 1]$$
$$+ 2c_P c_O b_P b_O [S_{PO}(Q) - 1] + 2c_P c_{Al} b_P b_{Al} [S_{PAl}(Q) - 1] + 2c_O c_{Al} b_O b_{Al} [S_{OAl}(Q) - 1].$$
[4.62]

The three matrix-matrix functions are identical as shown by equations 4.60-4.62 which serves as a useful consistency check.

A summary of the functions and notation used in the following chapters is presented in Table 4.1. It can be seen that the use of difference functions methods leads to a reduction in the overall complexity of correlations associated with a single total structure factor. For example

$$F^{(1)}(Q) = \frac{b_{1,R}}{b_{1,R} - b_{3,R}} \Delta_R^{(1)}(Q) + \Delta_F^{(1)}(Q)$$

$$= c_R^2 b_{1,R}^2 [S_{RR}(Q)-1] + \frac{b_{1,R}}{b_{1,R} - b_{3,R}} \Delta_{R\mu}^{(1)}(Q) + \Delta_{\mu\mu}^{(1)}(Q). \qquad [4.63]$$

Also it can be shown that the use of difference methods leads to a cancellation of many of the systematic errors (Salmon *et al* 1998) associated with the data correction procedure which is described in Chapter 5.

Function	Q-space function	r space function	Contributing pair correlation functions
Measured total structure factor	F(Q)	G(r)	R-R, R-P, R-O, R-Al P-P, P-O, P-Al, O-O, O-Al, Al-Al
First order difference	$\Delta_R(Q)$	$\Delta G_R(r)$	R-R, R-P, R-O, R-Al
Total minus weighted	$\Delta_F(Q)$	$\Delta G_F(r)$	P-P, P-O, P-Al, O-O, O-Al, Al-Al, -(R-R)
Second order difference	$S_{RR}(Q)$	$g_{RR}(r)$	R-R
Rare earth-matrix	$\Delta_{R\mu}(Q)$	$\Delta G_{R\mu}(r)$	R-P, R-O, R-Al
Matrix-matrix	$\Delta_{\mu\mu}(Q)$	$\Delta G_{\mu\mu}(r)$	P-P, P-O, P-Al, O-O, O-Al, Al-Al

Table 4.1. The functions and contributing partial structure factors.

4.9 DATA MODELLING

The real space information corresponding to a total structure factor F(Q) can also be represented by the function

$$D(r) = \frac{2}{\pi}\frac{1}{|G(0)|}\int_0^\infty Q\,F(Q)\sin(Qr)\,dQ$$

$$= \frac{4\pi n_0 r}{|G(0)|}G(r) \qquad [4.64]$$

where

$$G(0) = -\sum_{\alpha=1}^{x}\sum_{\beta=1}^{x} b_\alpha b_\beta\, c_\alpha c_\beta . \qquad [4.65]$$

In a diffraction experiment this function is seldom obtained directly from the measured F(Q) because of the finite measurement window of the diffractometer M($Q \leq Q_{max}$) = 1, M($Q > Q_{max}$) = 0 which is represented in real space by

$$M(r) = \frac{1}{\pi}\int_0^{Q_{max}}\cos(Qr)\,dQ = \frac{Q_{max}}{\pi}\,\mathrm{sinc}\,(Q_{max}r) \qquad [4.66]$$

where sinc(x) ≡ sin(x)/x. Instead the function D′(r) is obtained where

$$D'(r) = \frac{2}{\pi}\frac{1}{|G(0)|}\int_0^\infty Q\,F(Q)\,M(Q)\sin(Qr)\,dQ = D(r)\otimes M(r) \qquad [4.67]$$

and ⊗ denotes the one-dimensional convolution operator i.e.

$$D(r)\otimes M(r) = \int_{-\infty}^{\infty} D(r')\,M(r-r')\,dr'$$

$$= \int_0^\infty D(r')[M(r-r') - M(r+r')]\,dr' . \qquad [4.68]$$

The real space function corresponding to the first order difference is given by

$$\Delta D'_{R}{}^{(1)}(r) = \frac{4\pi n_0 r}{\left|\Delta G_{R}{}^{(1)}(0)\right|} \Delta G_{R}{}^{(1)}(r) \otimes M(r) \qquad [4.69]$$

where

$\Delta G_R^{(1)}(r) = G^{(1)}(r) - G^{(3)}(r)$

$$= c_R^2 \left(b_{1,R}^2 - b_{3,R}^2\right)[g_{RR}(r) - 1] + \sum_{\alpha(\neq R)} 2c_R c_\alpha b_\alpha \left(b_{1,R} - b_{3,R}\right)[g_{R\alpha}(r) - 1] \qquad [4.70]$$

and $\Delta G_R^{(1)}(0)$ is obtained by setting the $g_{\alpha\beta}(r)$ equal to their low r limit of zero.

The real space function corresponding to the total minus weighted difference is given by

$$\Delta D'_{F}{}^{(1)}(r) = \frac{4\pi n_0 r}{\left|\Delta G_{F}{}^{(1)}(0)\right|} \Delta G_{F}{}^{(1)}(r) \otimes M(r) \qquad [4.71]$$

where

$$\Delta G_F^{(1)}(r) = G^{(1)}(r) - b_{1,R} G^{(3)}(r) \,/\, (b_{1,R} - b_{3,R}). \qquad [4.72]$$

$$= -c_R^2 b_{1,R}^2 b_{3,R}^2 [g_{RR}(r) - 1] + \sum_{\alpha\neq R}\sum_{\beta\neq R} c_\alpha c_\beta b_\alpha b_\beta [g_{\alpha\beta}(r) - 1]. \qquad [4.73]$$

The second order difference function is given by

$$D'_{RR}(r) = 4\pi n_0 r\, g_{RR}(r) \otimes M(r). \qquad [4.74]$$

The metal-matrix function is given by

$$\Delta D'_{R\mu}{}^{(1)}(r) = \frac{4\pi n_0 r}{\left|\Delta G_{R\mu}{}^{(1)}(0)\right|} \Delta G_{R\mu}{}^{(1)}(r) \otimes M(r) \qquad [4.75]$$

where

$$\Delta G_{R\mu}^{(1)}(r) = \Delta G_R^{(1)}(r) - c_R{}^2 (b_{1,R}{}^2 - b_{3,R}{}^2)\, [g_{R\alpha}(r) - 1] \qquad [4.76]$$

$$= \sum_{\alpha(\neq R)} 2c_R c_\alpha b_\alpha (b_{1,R} - b_{3,R})[g_{R\alpha}(r) - 1]. \qquad [4.77]$$

The matrix-matrix function is given by

$$\Delta D'^{(1)}_{\mu\mu}(r) = \frac{4\pi n_0 r}{\left|\Delta G^{(1)}_{\mu\mu}(0)\right|} \Delta G^{(1)}_{\mu\mu}(r) \otimes M(r) \qquad [4.78]$$

where

$$\Delta G^{(1)}_{\mu\mu}(r) = \Delta G^{(1)}_F(r) + c_R^2 b_{1,R}^2 b_{3,R}^2 [g_{R\alpha}(r) - 1] \qquad [4.79]$$

$$= \sum_{\alpha\neq R}\sum_{\beta\neq R} c_\alpha c_\beta b_\alpha b_\beta [g_{\alpha\beta}(r) - 1] \qquad [4.80]$$

To enable those features in D'(r), $\Delta D'_R(r)$, $\Delta D'_F(r)$, $\Delta D'_{R\mu}(r)$ and $\Delta D'_{\mu\mu}(r)$ that are artefacts of M(r) to be distinguished, each peak i in $rg_{\alpha\beta}(r)$ can be represented by a Gaussian centred at $r_{\alpha\beta}(i)$ with standard deviation $\sigma_{\alpha\beta}(i)$ and area corresponding to a coordination number of species β around α of $\bar{n}^{\beta}_{\alpha}(i)$

$$rg_{\alpha\beta}(r,i) = \frac{\bar{n}^{\beta}_{\alpha}(i)}{4\pi\, n_0\, c_\beta(i) r_{\alpha\beta}(i)} \frac{1}{\sqrt{2\pi}\,\sigma_{\alpha\beta}(i)} \exp\left(\frac{-(r - r_{\alpha\beta}(i))^2}{2\sigma^2_{\alpha\beta}(i)}\right) . \qquad [4.81]$$

In the case of the total pair distribution function, the measured D'(r) can then be fitted by least squares to a sum of these Gaussians convoluted with M(r) such that

$$D'(r) = \left[\sum_i 4\pi n_0\, W_{\alpha\beta}(i) rg_{\alpha\beta}(r,i)\right] \otimes M(r) - 4\pi n_0 r \qquad [4.82]$$

where $W_{\alpha\beta}(i) = 2c_\alpha c_\beta b_\alpha b_\beta \,/\, |G(0)|$ if $\alpha \neq \beta$ and $W_{\alpha\beta}(i) = c_\alpha^2 b_\alpha^2 \,/\, |G(0)|$ if $\alpha = \beta$.

The reason for choosing to fit the D'(r) function is that the modification function M(r) used in the convolution procedure is symmetric. The choice of weighting functions $W_{\alpha\beta}(i)$ ensures that the fitted function sits on a 'background' slope of $4\pi n_0 r$. Equivalent expressions hold for the other real space function. For

example, in the case of the first order difference function D′(r) is replaced by $\Delta D'_R{}^{(1)}(r)$ and $W_{\alpha\beta}(i) = c_R{}^2(b_{1,R}{}^2 - b_{3,R}{}^2) / \left|\Delta G_R{}^{(1)}(0)\right|$ if $\alpha = \beta = R$ and $W_{\alpha\beta}(i) = 2c_R c_\alpha b_\alpha (b_{1,R} - b_{3,R}) / \left|\Delta G_R{}^{(1)}(0)\right|$ if $\alpha \neq R$ and $\beta = R$. For the total minus weighted difference function D′(r) is replaced by $\Delta D'_F{}^{(1)}(r)$ and $W_{\alpha\beta}(i) = -c_R{}^2 b_{1,R} b_{3,R} / \left|\Delta G_F{}^{(1)}(0)\right|$ if $\alpha = \beta = R$ and $W_{\alpha\beta}(i) = 2c_\alpha c_\beta b_\alpha b_\beta / \left|\Delta G_F{}^{(1)}(0)\right|$ if $\alpha \neq \beta \neq R$ and $W_{\alpha\beta}(i) = c_\alpha{}^2 b_\alpha{}^2 / \left|\Delta G_F{}^{(1)}(0)\right|$ if $\alpha = \beta \neq R$. For the metal-matrix function D′(r) is replaced by $\Delta D'_{R\mu}{}^{(1)}(r)$ and $W_{\alpha\beta}(i) = 2c_R c_\alpha b_\alpha (b_{1,R} - b_{3,R}) / \left|\Delta G_{R\mu}{}^{(1)}(0)\right|$. For the matrix-matrix difference function D′(r) is replaced by $\Delta D'_{\mu\mu}{}^{(1)}(r)$ and $W_{\alpha\beta}(i) = 2c_\alpha c_\beta b_\alpha b_\beta / \left|\Delta G_{\mu\mu}{}^{(1)}(0)\right|$ if $\alpha \neq \beta$ and $W_{\alpha\beta}(i) = c_\alpha^2 b_\alpha^2 / \left|\Delta G_{\mu\mu}{}^{(1)}(0)\right|$ if $\alpha = \beta$.

In many neutron scattering studies of disordered materials the real space functions G(r), $\Delta G_R(r)$, $\Delta G_F(r)$, $g_{RR}(r)$, $\Delta G_{R\mu}(r)$ and $\Delta G_{\mu\mu}(r)$, given in Table 4.1 are presented. In practice, these functions are also modified by the finite measurement window of the diffractometer M(Q). For example, the modified total pair distribution function G′(r) is given by (Etherington *et al* 1982)

$$
\begin{aligned}
rG'(r) &= \frac{1}{2\pi^2 n_0} \int_0^\infty F(Q)\, Q\, M(Q) \sin(Qr)\, dQ \\
&= \int_{-\infty}^{\infty} r'\, G(r')\, M(r - r')\, dr' \\
&= \int_0^\infty r'\, G(r') \left[M(r - r') - M(r + r')\right] dr' . \qquad [4.83]
\end{aligned}
$$

Likewise

$$
r\Delta G'_R(r) = \frac{1}{2\pi^2 n_0} \int_0^\infty \Delta_R(Q)\, Q\, M(Q) \sin(Qr)\, dQ \qquad [4.84]
$$

and equivalent expressions hold for $r\Delta G'_F(r)$, $rg'_{RR}(r)$, $r\Delta G'_{R\mu}(r)$ and $r\Delta G'_{\mu\mu}(r)$.

REFERENCES

Balcar E and Lovesey S. W. 1989. *Theory of Magnetic Neutron and Phonon Scattering.* Oxford Science Publications. UK.

Bleaney B.I and Bleaney B. 1976. *Electricity and Magnetism.* 3rd edition. Clarendon Press. Oxford. UK.

Brown P.J. 1995. *International Tables for Crystallography* Vol. C, ed Wilson A.J.C (Dordrecht: Kluwer) p. 391.

Etherington G, Wright A.C, Wenzel J.T, Dore J.C, Clarke J.H and Sinclair R.N. 1982. *Journal of Non-Crystalline Solids.* **48.** p. 265.

Faber T.E and Ziman J.M. 1964. *Philosophical Magazine.* **11.** p.153.

Lovesey S.W. 1984. *Theory of Neutron Scattering from Condensed Matter.* Claranden Press. Oxford. UK.

Salmon P.S, Xin S and Fischer H.E. 1998. *Physical ReviewB.* **58.** No. 10. p. 6115.

Sears V.F. 1992. *Neutron News.* **3** No. 3. p. 26.

Squires G.L. 1978. *Introduction to the theory of thermal neutron scattering.* Cambridge University Press. UK.

Wasse J.C. and Salmon P.S. 1999. *Journal of Physics: Condensed Matter.* **11.** p.1381.

Yarnell J.L, Katz M.J, Wenzel R.G and Koeing S.H. 1973. *Physical Review A.* **7.** no.6. p. 2130.

CHAPTER 5
THE DIFFRACTION EXPERIMENTS AND DATA ANALYSIS

The instrumentation, experimental measurements and the data analysis procedure will be described in this chapter.

5.1 NEUTRON SOURCES.

In a diffraction experiment the scattered intensity is measured as a function of momentum transfer Q, where $Q = 4\pi\sin(\theta)/\lambda$. In reactor source experiments the incident wavelength is kept constant and the scattering angle 2θ is varied. Conversely the scattering angle is fixed for pulsed neutron source experiments and the incident wavelength is varied. The results presented in chapters 6-8 were conducted using the instruments D4C at the Institut Laue Langevin (ILL), Grenoble, France and GLAD at the Intense Pulsed Neutron Source (IPNS), Argonne National Laboratory, USA. The author did not conduct the experiments at the IPNS and the instrumentation will not be discussed here. A brief outline of the D4C set-up is given in section 5.2. The reactor source at the ILL operates at a power of 57 MW producing high-energy neutrons from fission of uranium fuel.

5.2 THE D4C DIFFRACTOMETER

The D4C diffractometer, which is optimised for the structural investigation of liquid and amorphous materials, is shown in Figure 5.1. This instrument is capable of operating at three wavelengths 0.7, 0.5 or 0.35 Å. The short wavelengths allow a large Q_{max} to be measured, which is required for a good Fourier transform of S(Q). The standard operation is at 0.7 Å, which corresponds to a Q range of 0.196 to 16.6 $Å^{-1}$, where the incident flux is a maximum. A Cu(200) monochromator composed of small single crystals is used to select this wavelength. It works in reflection mode, has a surface of 20 cm height by 18 cm width and is self-focusing vertically. After the monochromator the neutrons pass through a virtually transparent ^3He (monitor) detector, which allows the flux of incoming neutrons to be measured. The monitor

count allows the measurements to be properly normalised. The beam is then collimated by two sets of slits before being incident on the sample. The sample inside its container, possibly inside a vanadium furnace, is placed in the sample chamber, which is the evacuated to reduce air scattering. After scattering from the sample the neutrons pass through the detector collimators and onto the detectors. The detector collimators ensure that the detectors only see the solid angle corresponding to the sample position, thus reducing background scattering. There are nine ^{3}He detector arrays consisting of 64 cells covering $2\theta = 0.125°$, such that each detector array covers $2\theta = 8°$. The detectors are separated by a fixed angle of 7.5° and therefore several positions are required to cover the whole angular range ($2\theta = 140°$) with no gaps. The detectors are a radial distance of 1145.92 mm from the sample position and have a high detection efficiency of about 90% at 0.7 Å.

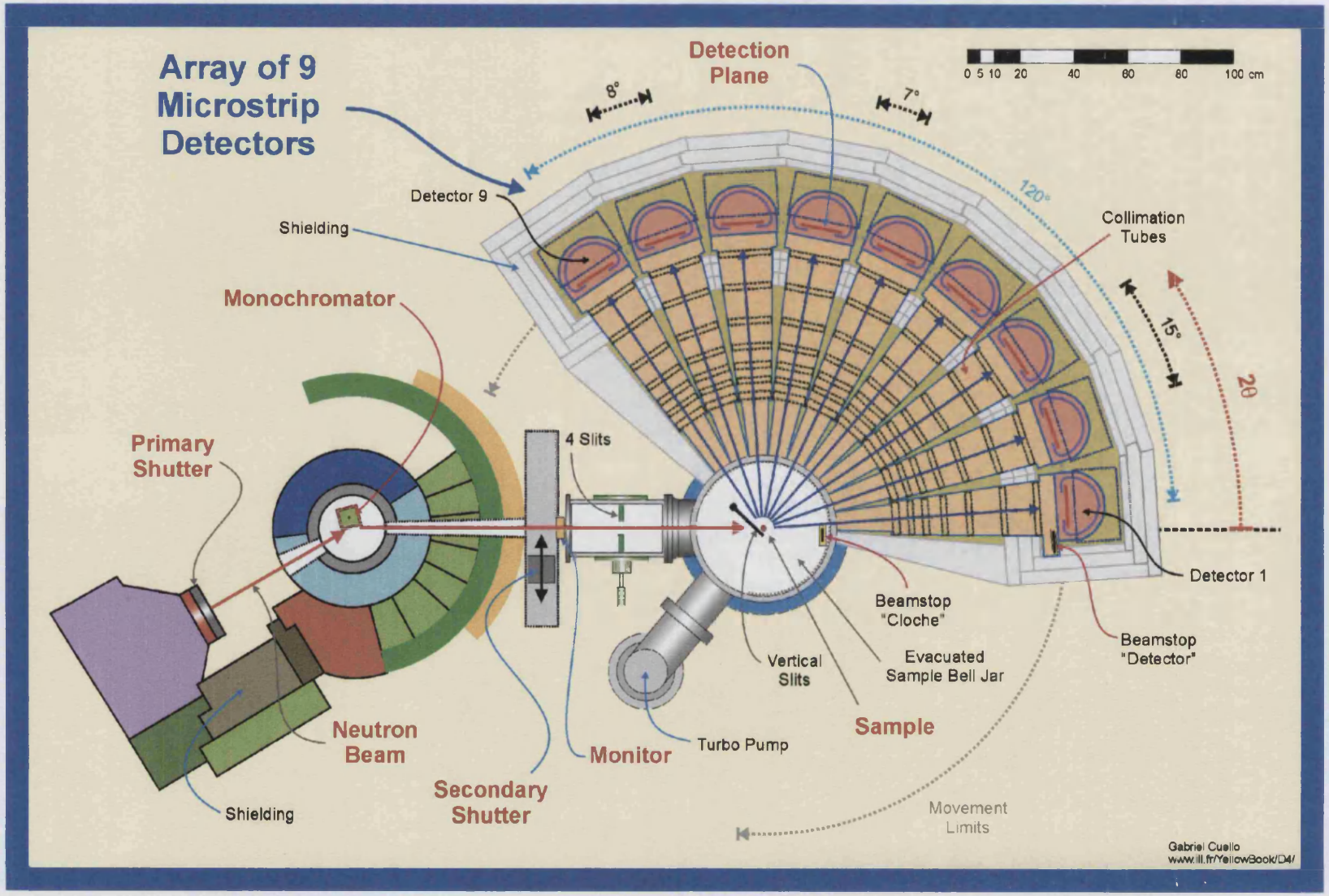

Figure 5.1. The D4C diffractometer.

5.3 DIFFRACTION FROM A REAL SAMPLE

If we consider a small sample with no container or heater present and negligible attenuation and multiple scattering then the experimentally observed intensity is given by

$$I^{E}_{S,back}(\theta) \propto \left(\frac{d\sigma}{d\Omega}\right)_{eff} \qquad [5.1]$$

where $(d\sigma/d\Omega)_{eff}$ is defined by equation [4.34]. In reality the instrument background count, sample attenuation and multiple scattering terms are not negligible and must be corrected for. Also the sample is usually placed inside a container and sometimes inside a furnace, such that the furnace and/ or container must also be corrected for. A diffraction pattern of a vanadium rod of similar dimensions to the sample is required for normalisation of the data. For a finite sized sample the experimentally observed intensity is given by

$$I^{E}_{S,back}(\theta) = \alpha(\theta)\,[F_S(Q) + \beta(\theta)] \qquad [5.2]$$

where $F_S(Q)$ is the single scattering from the sample and is given by equation 4.34, $Q = \frac{4\pi}{\lambda}\sin(\theta)$, $\beta(\theta)$ is an additional factor resulting from the multiple scattering, background and container (or container plus heater) scattering, while $\alpha(\theta)$ depends on the attenuation of the beam by the sample and contains the normalisation term.

5.4 DIFFRACTION PATTERNS

In order to extract the scattering from the sample a series of diffraction patterns must be measured:

[1] Sample in the container

[2] Empty container

[3] Vanadium rod of similar dimensions to the sample

[4] Background with no sample or container present

[5] Cadmium rod of similar dimensions to the sample.

If the sample is enclosed in a furnace during the experiment then [1] becomes a sample in the container in the furnace, [2] becomes a container in the furnace and an additional empty furnace diffraction pattern will be required. The sample/ container are always placed in exactly the same position (~0.1 mm) since the diffractometer is sensitive to small changes in position.

5.5 BACKGROUND CORRECTIONS

The measured intensity at a given angle can be divided into four different contributions as represented in Figure 5.2.

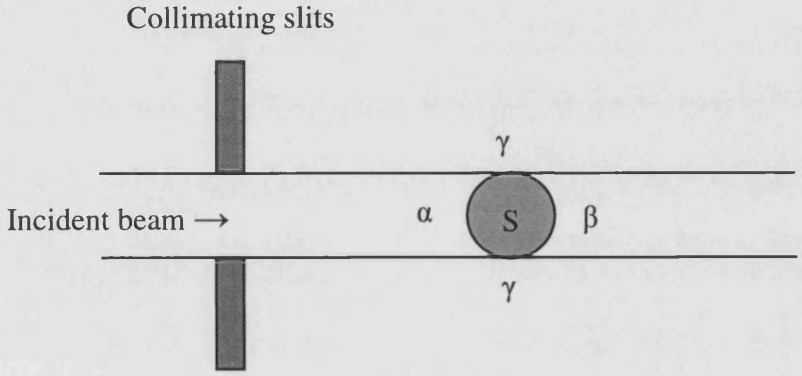

Figure 5.2. The background scattering.

In Figure 5.2, α denotes the scattering region in the direct incident beam before it reaches the sample, γ the scattering region out of the direct beam to the sides of the sample, β the scattering region in the direct beam behind the sample and S the scattering region of the sample. The background intensity (no sample present) is therefore given by

$$I^{E}_{back}(\theta) = I_{\alpha}(\theta) + I_{\gamma}(\theta) + I_{\beta}(\theta) \qquad [5.3]$$

where $I_{\alpha}(\theta)$, $I_{\gamma}(\theta)$ and $I_{\beta}(\theta)$ are the scattered intensities from the regions α, γ and β respectively. If a sample is placed in the beam as shown then the experimentally measured scattering intensity can be described by

$$I^{E}_{S,back}(\theta) = I_{\alpha}(\theta) + I_{\gamma}(\theta) + I^{E}_{S}(\theta) + T_{S}(\theta)\, I_{\beta}(\theta) \qquad [5.4]$$

where $T_S(\theta)$ is the transmission coefficient of the sample. The scattering from regions α and γ remain constant whilst the scattering from β is attenuated due to the scattering and absorption by the sample. $I_S^E(\theta)$ is the scattering from the sample corrected only for background.

At high angles ($2\theta > 12$ ° on D4C) the observed background scattering from region β can be neglected owing to the detector collimation and hence the background corrected scattering from the sample is given by

$$I_S^E(\theta) = I_{S,back}^E(\theta) - I_{back}^E(\theta). \qquad [5.5]$$

At low angles the attenuation of the sample must be taken into consideration and the intensity for a cadmium sample of similar dimensions to the sample is measured (Bertagnolli *et al* 1976). Since cadmium is highly absorbing for typical thermal neutron energies, its transmission is negligible ($T_S(\theta) \approx 0$) such that the measured intensity from a cadmium rod can be written as

$$I_{Cd,back}^E(\theta) = I_\alpha(\theta) + I_\gamma(\theta). \qquad [5.6]$$

The cadmium therefore determines the contribution to the background that is not affected by the presence of the sample and the contribution from β is given by

$$I_\beta(\theta) = I_{back}^E(\theta) - I_{Cd,back}^E(\theta). \qquad [5.7]$$

Equation 5.4 can therefore be rearrange by substituting in equations 5.6 and 5.7 to give

$$\begin{aligned} I_S^E(\theta) &= I_{S,back}^E(\theta) - I_\alpha(\theta) - I_\gamma(\theta) - T_S(\theta)\, I_\beta(\theta). \\ &= I_{S,back}^E(\theta) - I_{Cd,back}^E(\theta) - T_S(\theta)\,[I_{back}^E(\theta) - I_{Cd,back}^E(\theta)]. \end{aligned} \qquad [5.8]$$

Note that the cadmium correction is only valid at low angles; for $2\theta > 12$ ° the detector sees neutrons scattered from the cadmium oxide layer such that $I_{Cd,back}^E(\theta) >$

I^E_{back} (θ). The background corrections given in equations 5.5 and 5.8 are used at high and low angles respectively. The transmission coefficient $T_S(\theta)$ for a bare cylindrical sample is given by the Paalman and Pings (1962) attenuation factor $A_{S,S}(\theta)$ where $A_{S,S}(\theta)$ represents the attenuation of a neutron scattered in the sample due to the presence of the sample. These attenuation factor can be written more generally as $A_{i,j}(\theta)$ for a neutron scattered in the medium i and attenuated in medium j.

5.6 THE ATTENUATION AND MULTIPLE SCATTERING

The scattering from a sample corrected only for background can be expressed in terms of the multiple scattering cross-section $M_S(\theta)$ and the attenuation factor $A_{S,S}(\theta)$ by

$$I^E_S(\theta) = a(\theta)\, N_S\, A_{S,S}(\theta) \left[F_S(Q) + \frac{\sigma_S \Delta_S}{4\pi} \right] \qquad [5.9]$$

$$= a(\theta)\, N_S\, A_{S,S}(\theta)\, [F_S(Q)] + M_S(\theta) \qquad [5.10]$$

where

$$M_S(\theta) = N_S\, A_{S,S}(\theta)\, \frac{\sigma_S \Delta_S}{4\pi}, \qquad [5.11]$$

$a(\theta)$ is the normalisation factor, N_S is the total number of scattering centres, σ_S is the sample scattering cross section, $F_S(Q)$ is defined by equation 4.34 and represents the total structure factor corrected for background, container, heater and multiple scattering effects and Δ_S is the ratio of the multiple scattering to single scattering (Soper and Egelstaff 1980).

5.7 VANADIUM NORMALISATION

The normalisation term $a(\theta)$ is determined using a vanadium rod of similar dimensions to the sample. Vanadium is an isotropic elastic scattering material (Mayers 1984) with a small coherent cross-section (Sears 1992) such that the measured background corrected intensity can be written as

$$I_V^E(\theta) = a(\theta)\, N_V\, A_{V,V}(\theta)\left[F_V(Q) + \frac{\sigma_V \Delta_V}{4\pi}\right] \qquad [5.12]$$

where

$$F_V(Q) = b_{V,inc}^2\,(1+P_V(\theta)) \qquad [5.13]$$

and $P_V(\theta)$ is the inelasticity correction (Yarnell *et al* 1973). Equation 5.12 can be rearranged to give the normalisation factor

$$a(\theta) = \frac{I_V^E(\theta)}{A_{V,V}(\theta) N_V\, b_{V,inc}^2\,[1+P_V(\theta)] + M_V(\theta)}\,. \qquad [5.14]$$

Consider the more generalised situation of a sample in a container inside a heater (or furnace). Let $I_{SCH}^E(\theta)$, $I_{CH}^E(\theta)$ and $I_H^E(\theta)$ represent the observed diffraction patterns, corrected for background scattering, for the sample in the container in the heater, empty container in the heater and the empty heater respectively. Then it follows that

$$I_{SCH}^E(\theta) = A_{S,SCH}(\theta)\, I_S(\theta) + A_{C,SCH}(\theta)\, I_C(\theta) + A_{H,SCH}(\theta)\, I_H(\theta) + a(\theta) M_{SCH}(\theta).$$

$$I_{CH}^E(\theta) = A_{C,CH}(\theta)\, I_C(\theta) + A_{H,CH}(\theta)\, I_H + a(\theta) M_{CH}(\theta)$$

$$I_H^E(\theta) = A_{H,H}(\theta)\, I_H(\theta) + a(\theta) M_H(\theta)$$

where $I_S(\theta)$, $I_C(\theta)$ and $I_H(\theta)$ are the intensities for singly scattered neutrons from the sample, container and heater respectively. $A_{i,j}(\theta)$ is the attenuation factor for material i in the presence of material(s) j where i,j = S, C or H and $M_i(\theta)$ denotes the multiple scattering cross-section. Solving these equations yields $I_S(\theta)$ and hence $F_S(\theta)$ since $I_S(\theta) \equiv N_S F_S(\theta)$.

$$I_S(\theta) \equiv F_S(Q) = Q_1\left\{\left[\frac{I_{SCH}^E}{a(\theta)} - M_{SCH}(\theta)\right] - Q_2\left[\frac{I_{CH}^E(\theta)}{a(\theta)} - M_{CH}(\theta)\right] - Q_3\left[\frac{I_H^E(\theta)}{a(\theta)} - M_H(\theta)\right]\right\} \qquad [5.15]$$

where

$$Q_1 = \frac{N_S}{A_{S,SCH}(\theta)},$$

$$Q_2 = \frac{A_{C,SCH}(\theta)}{A_{C,CH}(\theta)}$$

and

$$Q_3 = \frac{1}{A_{H,H}(\theta)}\left[A_{H,SCH}(\theta) - \left(\frac{A_{C,SCH}(\theta)A_{H,CH}(\theta)}{A_{C,CH}(\theta)}\right)\right].$$

5.8 DATA ANALYSIS

A series of programs was used to extract F(Q) from the experimental data. The analysis routine is given in Figure 5.3.

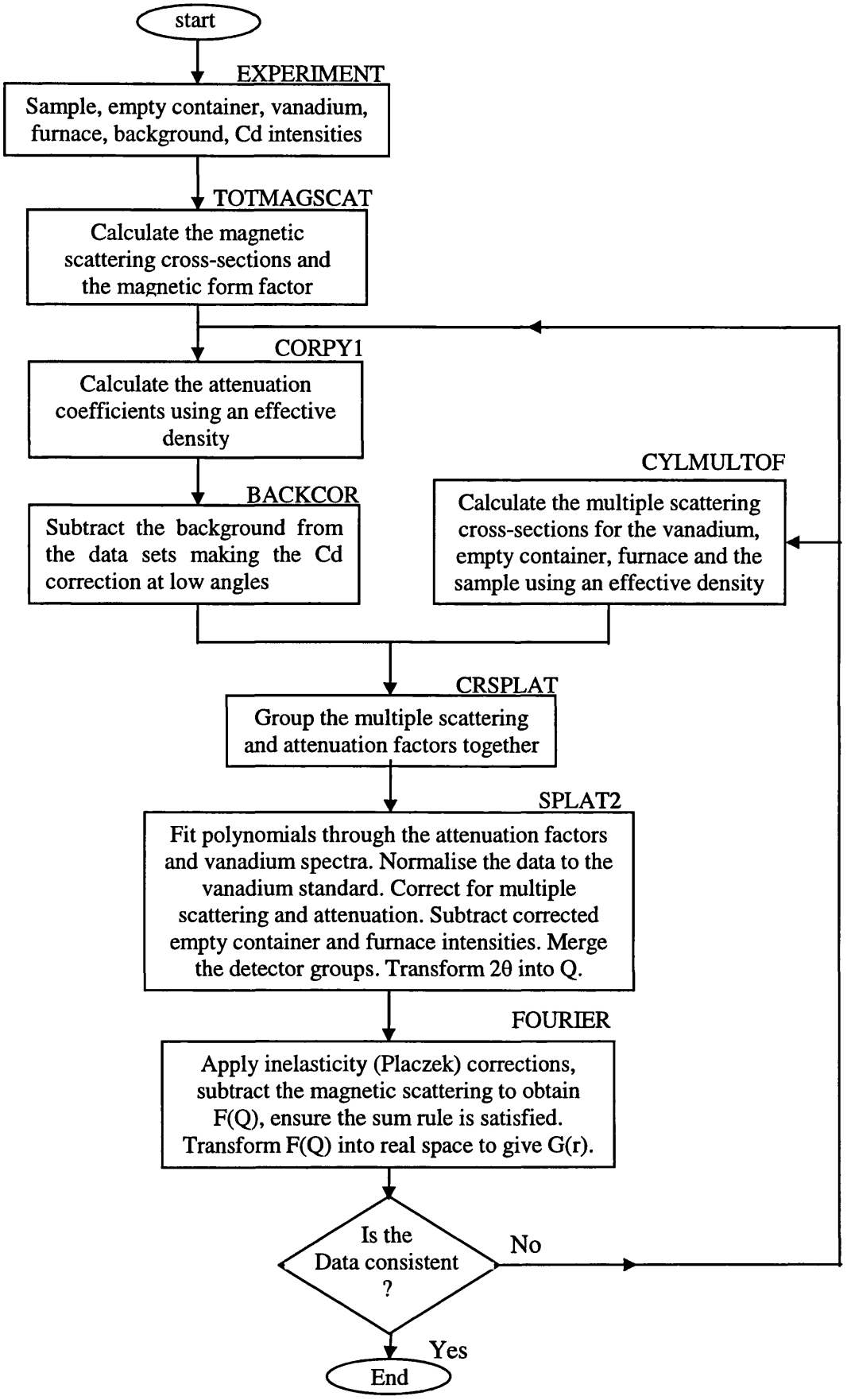

Figure 5.3. The correction procedure for results obtained using the D4C instrument.

5.9 SELF-CONSISTENCY CHECKS

During the data analysis procedure a series of checks must be performed to ensure that the reciprocal and real space data obtained are free from substantial systematic errors:

[1] The total structure factors F(Q) must oscillate around zero at high Q since the $S_{\alpha\beta}(Q)$ must tend to unity in this limit.

[2] The sum rule relation must be satisfied (Enderby *et al* 1966)

$$\int_0^\infty Q^2 F(Q) dQ = 2\pi^2 n_0 G(0) \qquad [5.16]$$

where

$$G(0) = - \sum_\alpha \sum_\beta c_\alpha c_\beta b_\alpha b_\beta \,, \qquad [5.17]$$

c_α is the atomic fraction of chemical species α and b_α is the coherent scattering length of α.

[3] The method of Fourier back-transformation

When F(Q) is Fourier-transformed into real space to give G(r) unphysical low r oscillations arise due to truncation effects and statistical noise. The low-r oscillation can be set equal to G(0) such that G(r) = G(0) in the region $0 \leq r \leq r_0$ where r_0 is the minimum distance between neighbouring atoms. If all the features greater than r_0 are real and those in the region $0 \leq r \leq r_0$ are unphysical and contain no structural information then the back Fourier transform in Q space should be identical to the original F(Q) (Salmon and Benmore 1992).

Note that the consistency checks [1], [2] and [3] also apply to all of the difference functions.

5.10 MODELLING THE DATA

As described in section 4.9 the real space data sets are fitted using a sum of Gaussians to represent peaks in the individual pair distribution functions. Owing to the overlap between different correlations, e.g. the O-O and R-O correlations given in Chapters 6 and 7, the difference functions were first modelled since these have fewer correlations than the total pair distribution function. The Gaussian parameters, namely the position, coordination number and width, were thus obtained and these parameters were then used to start the fitting of the total pair distribution functions. Consistency checks are therefore performed to ensure the modelled data is sensible.

The Gaussian fitting procedure is intended to remove the effect of the finite measurement window function M(Q) on the real space data sets. The sum of the fitted Gaussians, when joined onto the data set at larger r obtained by direct Fourier transform of the original reciprocal space data set, should therefore give a back Fourier transform in good agreement with the original Q-space data set. This provides another consistency check on the modelling procedure.

The real space data sets were fitted using a χ^2 minimisation procedure (Bevington and Robinson 1992) and the quality of the fit is expressed in terms of the R_χ factor

$$R_\chi = \left(\frac{\sum_i \left[D'_{exp}(r_i) - D'_{fit}(r_i) \right]^2}{\sum_i \left[D'_{exp}(r_i) \right]^2} \right)^{1/2} \qquad [5.18]$$

as defined by Grimley *et al* (1990), where $D'_{exp}(r)$ is the experimental data and $D'_{fit}(r)$ is the fit.

5.11 HYDROGEN CORRECTION

In a neutron experiment, minute amounts of hydrogen give rise to an intense incoherent signal. The ratio between the hydrogen coherent and incoherent bound scattering cross sections is 1:45, such that the presence of a small quantity of hydrogen will have a significant effect on the incoherent part of the effective differential scattering cross section (equation 4.22) whilst leaving the F(Q) term essentially unchanged (Salmon and Lond 1992). When necessary, small hydrogen corrections were made using the experimentally determined differential scattering cross section given by Chieux *et al* (1984).

REFERENCES

Bertagnolli H, Chieux P and Zeidler M.D. 1976. *Molecular Physics.* **32.** No. 3. p. 759.

Bevington P.R and Robinson D.K. 1992. *Data reduction and error analysis for the physical sciences.* 2nd ed. McGraw-Hill. London. UK.

Chieux P, de Kouchkovsky R and Boucher B. 1984. *Journal of Physics F; Met. Phys.* **14.** p. 2239.

Enderby J.E, North D.M and Egelstaff P.A. 1966. *Philosophical Magazine.* **14.** p. 961.

Grimley D.I, Wright A.C and Sinclair R.N. 1990. *Journal of Non-Crystalline Solids.* **119.** p. 49.

Mayers J. 1984. *Nuclear Instruments and Methods in Physics Research.* **221.** p. 609.

Paalman H.H and Pings C.J. 1962. *Journals of Applied Physics.* **8.** p. 2635.

Salmon P.S and Benmore C.J. 1992. *Recent advances in the Physics of Fluids.* Ed. Howells W.S and Soper A.K. Adam Hilger: Bristol. p. F225.

Salmon P.S and Lond P.B. 1992. *Journal of Physics; Condensed Matter.* **4.** p. 5249.

Soper A.K and Egelstaff A. 1980. *Nuclear Instruments and Methods.* **178.** p. 415.

Sears V.F. 1992 *Neutron News.* **3.** No. 3. p. 26.

Yarnell J.L, Katz M.J, Wenzel R.G and Koeing S.H. 1973. *Physical Review A.* **7.** no.6. p. 2130.

CHAPTER 6
THE STRUCTURE OF LANTHANUM AND CERIUM PHOSPHATE GLASSES USING ISOMORPHIC SUBSTITUTION IN NEUTRON DIFFRACTION.

6.1 INTRODUCTION

Rare-earth phosphate glasses with stoichiometries close to those of the meta-phosphate RP_3O_9 and ultra-phosphate RP_5O_{14} compositions have shown considerable promise in the lasers and optoelectronics industry owing to their desirable optical properties (Cole *et al* 1999).

Fundamental to an understanding of the physico-chemical and opto-electronic properties in these materials is a knowledge of their structure at the partial pair distribution function, $g_{\alpha\beta}(r)$, level. For samples prepared by fusing e.g. RP_3O_9 in a platinum crucible, this presents a challenging experimental task as the glasses comprise three chemical species and are described by six overlapping $g_{\alpha\beta}(r)$ (Hoppe *et al* 1998a). Glasses with superior mechanical properties that enable fibres to be drawn are, however, routinely prepared by fusing a suitable rare-earth oxide with P_2O_5 in an alumina crucible (Cole *et al* 1999, 2001a). There is an attendant incorporation of Al into the structure that was not realised until recently (Cole *et al* 1999) and which further complicates the problem through the introduction of an additional four $g_{\alpha\beta}(r)$ (section 4.8). Thus, although a battery of techniques have been applied to investigate the structure of rare-earth phosphate glasses and trends associated with the lanthanide contraction (section 1.5) have been observed, such as a shortening of the R-O nearest neighbour distance, significant differences in the structural parameters have been reported (see Table 6.1). Of particular importance are those regarding the nearest-neighbour O-(P)-O and R-O coordination numbers as these parameters give information on the connectivity of the PO_4 network, as described by the ratio of bridging to terminal oxygen sites O_B:O_T (Hoppe 1996), and on the interlinking of R-centred polyhedra (Hoppe *et al* 2001) respectively. Existing data is, however, unreliable e.g. for $(Ce_2O_3)_{0.235}(P_2O_5)_{0.775}$ an R-O coordination number of 4.8(5),

Reference	Sample		ratios			calculated	P-O_T			P-O_B			O-(P)-O			R-O			P-(OP)-O			P-P			R-P		
			R :	P :	O	O-O C_N	r (Å)	C_N	σ (Å)	r (Å)	C_N	σ (Å)	r (Å)	C_N	σ (Å)	r (Å)	C_N	σ (Å)	r (Å)	C_N	σ (Å)	r (Å)	C_N	σ (Å)	r (Å)	C_N	σ (Å)
Anderson *et al* 1998	$(La_2O_3)_{0.1999}(Gd_2O_3)_{0.0001}$	EXAFS	1.00	4.00	11.50	4.17	-	-	-	-	-	-	-	-	-	2.42(3)	7.3(1.2)	0.12(8)	-	-	-	-	-	-	3.54(4)	5.9(4.4)	0.14(15)
Anderson *et al* 1999	$(P_2O_5)_{0.8000}$	EXAFS	1.00	4.00	11.50	4.17	-	-	-	-	-	-	-	-	-	2.42(3)	7.3(1.2)	0.12(8)	-	-	-	-	-	-	3.54(4)	-	-
Cole *et al* 2001a	$(La_2O_3)_{0.225}(P_2O_5)_{0.775}$	EXAFS	1.00	3.44	10.11	4.09	-	-	-	-	-	-	-	-	-	2.427(11)	8.4(9)	0.09(3)	-	-	-	-	-	-	-	-	-
Hoppe *et al* 1998	$(La_2O_3)_{0.25}(P_2O_5)_{0.75}$	X-ray & Neutron	1.00	3.00	9.00	4.00	1.484(5)	1.90(10)	0.04(1)	1.604(5)	2.05(10)	0.05(1)	2.553(15)	3.9(3)	0.09(1)	2.458(15)	7.1(5)	0.08(1)	-	-	-	-	-	-	-	-	-
			1.00	3.00	9.00	4.00	1.484(5)	1.90(10)	0.04(1)	1.604(5)	2.05(10)	0.05(1)	2.53	3.9	0.09	$r_{R\text{-}O}^1$ = 2.45, C_N = 5.5, $r_{R\text{-}O}^2$ = 2.55, C_N =1.7			-	-	-	-	-	-	-	-	-
Hoppe *et al* 2002	$(La_2O_3)_{0.28}(P_2O_5)_{0.72}$	X-ray	1.00	2.57	7.93	3.89	mean P-O; r(Å) = 1.531(10) and total C_N = 4.05(15)						2.52	3.89	0.08(1)	2.44(2)	6.1(3)	-	-	-	-	-	-	-	-	-
																$r_{R\text{-}O}^1$ = 2.420(10), C_N = 5.3			-	-	-	-	-	-	-	-	-
	$(La_2O_3)_{0.233}(P_2O_5)_{0.72}(SiO_2)_{0.048}$		1.00	3.09	9.43	3.93	mean P-O; r(Å) = 1.531(10) and total C_N = 3.90(15)						2.52	3.94	0.08(1)	2.43(2)	6.4(3)	-	-	-	-	-	-	-	-	-
																$r_{R\text{-}O}^1$ = 2.430(10), C_N = 5.2(2)			-	-	-	-	-	-	-	-	-
													mean O-(P)-O and total C_N			mean R-O and total C_N									mean R-P and total C_N		
present work	$La_{0.0670}P_{0.2224}O_{0.6865}Al_{0.0241}$	Neutron	1.00	3.32	10.25	3.89	1.505(9)	1.85(15)	0.045(5)	1.60(1)	2.0(1)	0.090(5)	2.495(9)	3.75(20)	-	2.64(9)	7.25(20)	-	2.94(2)	2.6(1)	0.09(1)	2.98(2)	2.0(1)	0.10(1)	3.67(9)	7.0(4)	-
	$La_{0.0709}P_{0.2197}O_{0.6877}Al_{0.0217}$ - D4C		1.00	3.10	9.70	3.83	1.49(1)	1.95(1)	0.045(5)	1.595(9)	2.1(1)	0.090(5)	2.48(1)	3.95(20)	-	2.63(9)	7.45(20)	-	2.94(2)	2.67(9)	0.10(1)	2.98(2)	2.0(1)	0.10(1)	3.67(9)	7.0(4)	-
	$La_{0.0309}Ce_{0.0354}P_{0.2195}O_{0.6888}Al_{0.0254}$ - D4C		1.00	3.31	10.39	3.82	1.49(1)	1.90(1)	0.045(5)	1.59(1)	2.1(1)	0.090(5)	2.48(1)	3.95(20)	-	2.63(9)	7.45(20)	-	2.94(2)	2.67(9)	0.10(1)	2.98(2)	2.0(1)	0.10(1)	3.67(9)	7.0(4)	-
	$La_{0.0309}Ce_{0.0354}P_{0.2195}O_{0.6888}Al_{0.0254}$ - GLAD		1.00	3.31	10.39	3.82	1.505(9)	1.85(15)	0.045(5)	1.60(1)	2.0(1)	0.090(5)	2.49(1)	3.75(20)	-	2.64(9)	7.25(20)	-	2.94(2)	2.67(9)	0.09(1)	2.98(2)	2.0(1)	0.10(1)	3.67(9)	7.0(4)	-
Anderson *et al* 1999	$(Ce_2O_3)_{0.235}(P_2O_5)_{0.765}$	EXAFS	1.00	3.26	9.64	4.05	-	-	-	-	-	-	-	-	-	2.35(1)	4.8(5)	0.08(4)	-	-	-	-	-	-	-	-	-
Cole *et al* 1999	$(Ce_2O_3)_{0.197}(P_2O_5)_{0.803}$	Neutron	1.00	4.08	11.69	4.18	1.49(1)	1.8(4)	0.05(1)	1.60(1)	1.8(4)	0.07(3)	2.50(1)	3.4(3)	0.08(4)	2.42(2)	6.0(6)	0.09(3)	2.82(3)	4.0(5)	0.13(7)	3.02(4)	2.8(9)	0.08(1)	-	-	-
	$(Ce_2O_3)_{0.235}(P_2O_5)_{0.765}$		1.00	3.26	9.64	4.05	1.49(1)	1.9(4)	0.03(3)	1.60(1)	1.9(4)	0.05(3)	2.50(1)	3.4(3)	0.08(4)	2.43(2)	5.8(6)	0.08(3)	2.81(3)	3.8(5)	0.14(7)	3.01(4)	2.9(9)	0.07(1)	-	-	-
Cole *et al* 2001b	$(Ce_2O_3)_{0.235}(P_2O_5)_{0.765}$	X-ray	1.00	3.26	9.64	4.05	mean P-O; r (Å) = 1.54(1), C_N = 3.9(3), σ (Å) = 0.07(3)						2.63(4)	4.7(9)	0.07(6)	2.42(2)	6.5(6)	0.09(5)	-	-	-	2.94(4)	2.4(1.3)	0.07(6)	3.70(2)	7.6(3.0)	0.15(8)
Mountjoy *et al* 2001	$(Ce_2O_3)_{0.197}(P_2O_5)_{0.803}$	EXAFS &	1.00	4.08	11.69	4.18	-	-	-	-	-	-	-	-	-	2.39(1)	5.0(5)	0.11(5)	-	-	-	-	-	-	3.76(9)	6*	0.3(2)
	$(Ce_2O_3)_{0.235}(P_2O_5)_{0.765}$	XANES	1.00	3.26	9.64	4.05	-	-	-	-	-	-	-	-	-	2.39(1)	5.2(4)	0.11(5)	-	-	-	-	-	-	3.77(8)	6*	0.3(2)
Anderson *et al* 1999	$(Pr_2O_3)_{0.254}(P_2O_5)_{0.746}$	EXAFS	1.00	2.94	8.84	3.99	-	-	-	-	-	-	-	-	-	2.367(7)	6.7(3)	0.10(4)	-	-	-	-	-	-	3.40(4)	-	-
Bowron *et al* 1996a	$(Pr_6O_{11})_{0.216}(P_2O_5)_{0.784}$	EXAFS	1.00	1.23	4.90	3.00	-	-	-	-	-	-	-	-	-	2.380(2)	7.1(2)	0.11(2)	-	-	-	-	-	-	2.920(4)	1.4(2)	0.09(4)
Bowron *et al* 1996b	$(Pr_2O_3)_{0.216}(P_2O_5)_{0.784}$	X-ray	1.00	1.23	4.90	3.00	mean P-O distance 1.57(5), C_N = 4.4						mean O-(P)-O and R-O distance 2.43(5). R-O C_N = 5.3						-	-	-	-	-	-	-	-	-
Cole *et al* 2001b	$(Pr_2O_3)_{0.216}(P_2O_5)_{0.784}$	X-ray	1.00	1.23	4.90	3.00	mean P-O; r = 1.55(1), C_N = 5.0(4), σ (Å) = 0.03(3)						2.53(3)	5.3(8)	0.05(5)	2.38(2)	6.6(7)	0.08(5)	-	-	-	2.93(2)	2.7(9)	0.03(4)	3.71(3)	8.9(3.1)	0.14(7)
Anderson *et al* 1999	$(Nd_2O_3)_{0.187}(P_2O_5)_{0.813}$	EXAFS	1.00	4.35	12.37	4.22	-	-	-	-	-	-	-	-	-	2.34(1)	8.6(3)	0.14(2)	-	-	-	-	-	-	3.44 (3)	-	-
Bowron *et al* 1996a	$(Nd_2O_3)_{0.235}(P_2O_5)_{0.765}$	EXAFS	1.00	3.26	9.64	4.05	-	-	-	-	-	-	-	-	-	2.35(1)	10.4(2.7)	0.14(5)	-	-	-	-	-	-	2.92(10)	6.8(16.6)	0.2(2)
Cole *et al* 1999	$(Nd_2O_3)_{0.187}(P_2O_5)_{0.813}$	Neutron	1.00	4.35	12.37	4.22	1.49(1)	1.9(4)	0.04(3)	1.60(1)	1.8(4)	0.06(3)	2.49(1)	3.3(3)	0.08(4)	2.39(2)	5.3(6)	0.09(3)	2.78(3)	4.6(5)	0.17(7)	3.01(4)	2.5(9)	0.05(3)	-	-	-
Cole *et al* 2001a	$(Nd_2O_3)_{0.187}(P_2O_5)_{0.813}$	EXAFS	1.00	4.35	12.37	4.22	-	-	-	-	-	-	-	-	-	2.369(7)	7(1)	0.08(3)	-	-	-	-	-	-	-	-	-
Cole *et al* 2001b	$(Nd_2O_3)_{0.187}(P_2O_5)_{0.813}$	X-ray	1.00	4.35	12.37	4.22	mean P-O; r(Å) = 1.55(1), C_N 3.8(3), σ (Å) = 0.03(3)						2.56(2)	4.7(7)	0.05(5)	2.36(2)	6.4(6)	0.10(6)	-	-	-	2.95(2)	2.5(8)	0.05(4)	3.67(2)	8.6(3.0)	0.14(6)
Mountjoy *et al* 2001	$(Nd_2O_3)_{0.187}(P_2O_5)_{0.813}$	EXAFS & XANES	1.00	4.35	12.37	4.22	-	-	-	-	-	-	-	-	-	2.37(1)	5.4(4)	0.12(4)	-	-	-	-	-	-	3.90(3)	6*	0.19(9)
Hoppe *et al* 2001	$(Nd_2O_3)_{0.25}(P_2O_5)_{0.75}$	X-ray & Neutron	1.00	3.00	9.00	4.00	1.490(5)	2.10(10)	0.04(1)	1.600(5)	2.10(10)	0.07(2)	2.515(15)	4.07(20)	0.08(1)	2.395(15)	6.6(3)	-									
							mean P-O; r(Å) = 1.545(10), C_N = 4.2(2)									$r_{R\text{-}O}^1$ = 2.36, C_N = 4.7, $r_{R\text{-}O}^2$ = 2.48*, C_N =1.9			-	-	-	-	-	-	-	-	-
	$(Nd_2O_3)_{0.20}(P_2O_5)_{0.80}$		1.00	4.00	11.50	4.17	1.470(5)	1.73(10)	0.02(1)	1.580(5)	2.22(10)	0.06(2)	2.515*	4.17*	0.08(1)	2.405(15)	6.9(3)	-									
							mean P-O; r(Å) = 1.532(10), C_N = 3.95(20)									$r_{R\text{-}O}^1$ = 2.385, C_N = 5.5, $r_{R\text{-}O}^2$ = 2.48*, C_N =1.4			-	-	-	-	-	-	-	-	-
Karabulut *et al* 2002	$(Nd_2O_3)_{0.254}(P_2O_5)_{0.72.4}(SiO_2)_{0.022}$	EXAFS	1.00	2.85	8.71	3.93	-	-	-	-	-	-	-	-	-	2.37(1)	6.4(9)	0.07	-	-	-	-	-	-	3.87(3)	2.2(9)	0.08(2)
Anderson *et al* 1998	$(Sm_2O_3)_{0.224}(P_2O_5)_{0.776}$	EXAFS	1.00	4.13	11.82	4.19	-	-	-	-	-	-	-	-	-	2.31(1)	6.9(3)	0.10(3)	-	-	-	-	-	-	3.40(2)	16.3(7.1)	0.25(14)
Anderson *et al* 1999	$(Sm_2O_3)_{0.196}(P_2O_5)_{0.085}$	EXAFS	1.00	3.46	10.16	4.09	-	-	-	-	-	-	-	-	-	2.31(1)	6.9(3)	0.10(3)	-	-	-	-	-	-	3.40(2)	-	-
Cole *et al* 2001a	$(Sm_2O_3)_{0.226}(P_2O_5)_{0.774}$	EXAFS	1.00	3.42	10.06	4.08	-	-	-	-	-	-	-	-	-	2.316(9)	6.9(7)	0.08(3)	-	-	-	-	-	-	-	-	-
Cole *et al* 2001b	$(Sm_2O_3)_{0.212}(P_2O_5)_{0.788}$	X-ray	1.00	3.72	10.79	4.13	mean P-O; r(Å) = 1.56(1), C_N = 3.7(3), σ (Å) = 0.05(3)						2.57(3)	5.3(8)	0.06(5)	2.33(2)	6.5(6)	0.1(5)	-	-	-	2.96(5)	2.8(9)	0.08(6)	3.67(1)	9.5(2.4)	0.16(6)
Anderson *et al* 1998	$(Eu_2O_3)_{0.218}(P_2O_5)_{0.782}$	EXAFS	1.00	3.59	10.47	4.11	-	-	-	-	-	-	-	-	-	2.31(1)	6.2(3)	0.09(3)	-	-	-	-	-	-	3.34(5)	5.0(4.1)	0.20(17)
Anderson *et al* 1999	$(Eu_2O_3)_{0.218}(P_2O_5)_{0.782}$	EXAFS	1.00	3.59	10.47	4.11	-	-	-	-	-	-	-	-	-	2.31(1)	6.2(3)	0.09(3)	-	-	-	-	-	-	3.34(5)	-	-
Bowron *et al* 1996a	$(Eu_2O_3)_{0.252}(P_2O_5)_{0.748}$	EXAFS	1.00	2.97	8.92	3.99	-	-	-	-	-	-	-	-	-	2.280(2)	7.6(2)	0.11(3)	-	-	-	-	-	-	3.64(2)	1.6(8)	0.07(8)
Bowron *et al* 1996b	$(Eu_2O_3)_{0.252}(P_2O_5)_{0.748}$	X-ray	1.00	2.97	8.92	3.99	mean P-O; r(Å) = 1.58(5), C_N = 4.4						mean O-(P)-O and R-O distance 2.36(5). R-O C_N = 8.5						-	-	-	-	-	-	-	-	-
Cole *et al* 2001a	$(Eu_2O_3)_{0.208}(P_2O_5)_{0.792}$	EXAFS	1.00	3.81	11.02	4.15	-	-	-	-	-	-	-	-	-	2.329(4)	6.5(8)	0.07(3)	-	-	-	-	-	-	-	-	-
Cole *et al* 2001b	$(Eu_2O_3)_{0.252}(P_2O_5)_{0.748}$	X-ray	1.00	2.97	8.92	3.99	mean P-O; r (Å) = 1.57(1), C_N = 4.4(4), σ = 0.03(3)						2.55(3)	7.3(8)	0.06(5)	2.33(2)	5.6(6)	0.06(5)				2.96(3)	3.0(1.3)	0.03(4)	3.67(1)	8.4(2.1)	0.15(5)
Mountjoy *et al* 2001	$(Eu_2O_3)_{0.218}(P_2O_5)_{0.782}$	EXAFS & XANES	1.00	3.59	10.47	4.11										2.31(1)	6.9(5)	0.11(4)	-	-	-	-	-	-	3.81(3)	6*	0.2(1)
Anderson *et al* 1998	$(Gd_2O_3)_{0.229}(P_2O_5)_{0.771}$	EXAFS	1.00	3.37	9.92	4.07	-	-	-	-	-	-	-	-	-	2.28(1)	5.0(4)	0.08(4)	-	-	-	-	-	-	-	-	-
Anderson *et al* 1999	$(Gd_2O_3)_{0.229}(P_2O_5)_{0.771}$	EXAFS	1.00	3.37	9.92	4.07	-	-	-	-	-	-	-	-	-	2.285(1)	6.5(4)	-	-	-	-	-	-	-	3.18(6)	-	-
Bowron *et al* 1996a	$(Gd_2O_3)_{0.25}(P_2O_5)_{0.75}$	EXAFS	1.00	3.00	9.00	4.00	-	-	-	-	-	-	-	-	-	2.270(2)	5.7(3)	0.08(3)	-	-	-	-	-	-	3.230(6)	1.4(2)	0.08(4)
Cole *et al* 2001a	$(Gd_2O_3)_{0.229}(P_2O_5)_{0.771}$	EXAFS	1.00	3.37	9.92	4.07	-	-	-	-	-	-	-	-	-	2.302(7)	6.7(7)	0.08(4)	-	-	-	-	-	-	-	-	-
Cole *et al* 2001b	$(Gd_2O_3)_{0.229}(P_2O_5)_{0.771}$	X-ray	1.00	3.37	9.92	4.07	mean P-O; r (Å) = 1.55(1), C_N = 4.0(3), σ = 0.03(3)						2.55(3)	4.7(8)	0.08(5)	2.30(2)	7.1(6)	0.09(4)	-	-	-	2.95(3)	2.7(10)	0.08(5)	3.64(1)	9.7(2.4)	0.14(5)

Table 6.1. A summary of the structural studies on rare earth phosphate glasses. Individually fitted R-O correlations are identified by the superscripts.

Where results are presented for a range of temperatures the room temperature values are quoted.
* indicates these values were fixed during the fitting.

5.2(4), 5.8(6) and 6.5(6) has been reported and the O-(P)-O coordination number varies between 3.4(3) and 4.7(9) (Table 6.1).

The object of this chapter is to employ the method of isomorphic substitution in neutron diffraction to create difference functions that, essentially, separate those $g_{\alpha\beta}(r)$ involving the rare-earth ions R^{3+} from the remainder. The method has recently been successfully employed to study the structure of several molten trivalent rare-earth halides (Wasse and Salmon 1999, Wasse *et al* 2000). The experiments will focus on R-P-O-Al glasses of very similar compositions which comprise La^{3+} or Ce^{3+} that are at the large cation radius end of the rare earth series. Isomorphism is anticipated from the comparable radii of La^{3+} (1.16 Å) and Ce^{3+} (1.14 Å) (reported for eight fold coordinated ions – see Shannon 1976) and their similar Pettifor (1986) chemical parameters $\chi(La) = 0.705$ and $\chi(Ce) = 0.7025$. Unlike previous studies the role of the Al impurities in the glass structure will be taken into explicit account.

6.2. THE STRUCTURE OF RARE EARTH PHOSPHATE CRYSTALS AND P_2O_5.

In order to understand the structure of rare earth phosphate glasses it is important to understand the structures of the crystalline phases. The structure of rare earth phosphates are known to vary along the lanthanide series due to the lanthanide contraction (section 1.5). For example, large rare earths ions such as La^{3+} and Nd^{3+} form orthorhombic meta-phosphate crystals with a space group $C222_1$ and $Z = 4$ where the rare earth ion is surrounded by eight oxygen nearest neighbours (Matuszewski *et al* 1988, Hong 1974a). Smaller rare earth ions such as Yb^{3+} form monoclinic meta-phosphate crystals with a space group $P2_1/C$ and $Z = 12$ where the rare earth ion is surrounded by six oxygen nearest neighbours (Hong 1974b).

The skeletal structure of NdP_3O_9 is illustrated in Figures 6.1-6.3 (Hong 1974a). Figure 6.1 illustrates an ac projection of the PO_4 tretrahedra, Figure 6.2 illustrates an ab projection showing how the PO_4 tretrahedra are connected to the Nd^{3+} ions and Figure 6.3 shows a bc projection showing the arrangement of NdO_8

dodecahedra. The cell contains two independent PO_4 tetrahedra as shown in Figure 6.1. The tetrahedron around P(1) is quite regular while the one around P(2) is irregular. The network is connected by neighbouring phosphate groups corner sharing a single oxygen atom. There is no sign of tetrahedra edge sharing two oxygen atoms. Nd^{3+} ions hold together the chains of PO_4 together as shown in Figure 6.2.

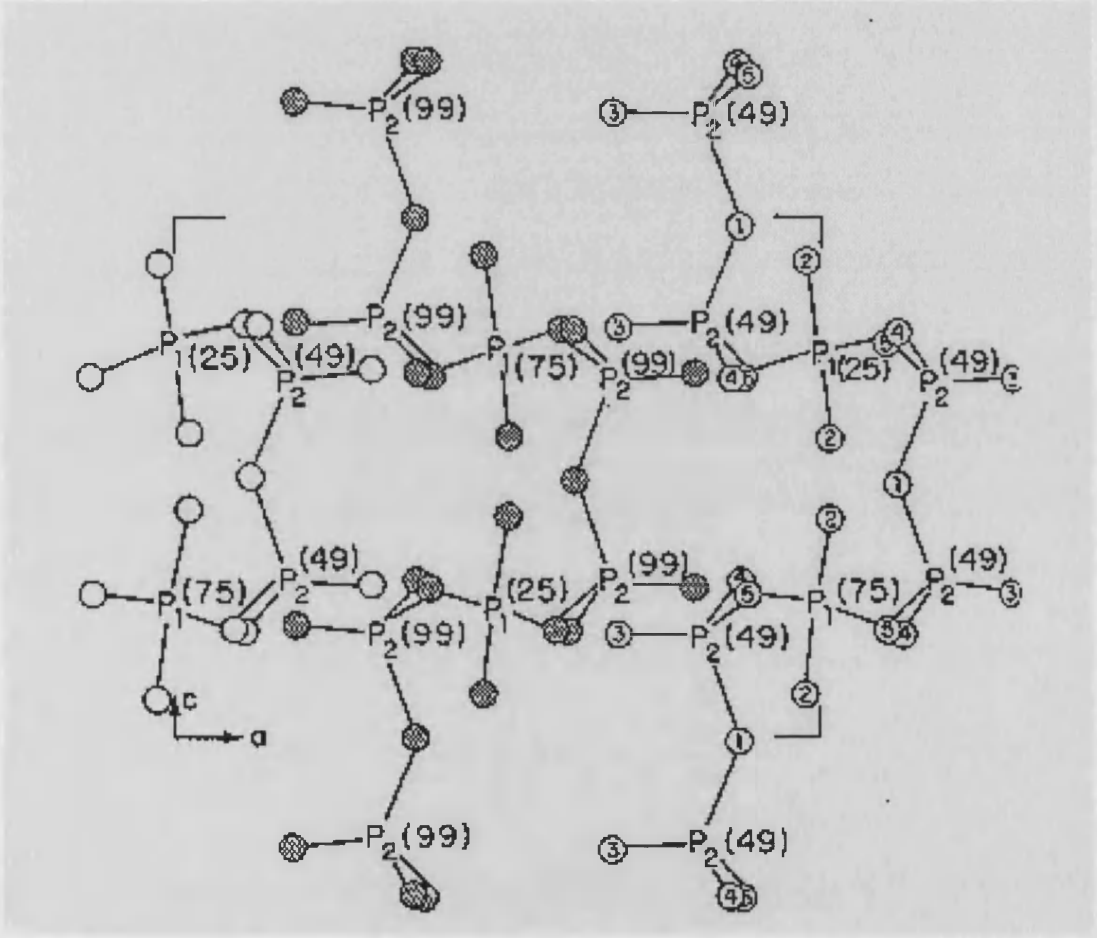

Figure 6.1. An ac projection of the arrangement of PO_4 tetrahedra in NdP_3O_9, showing the corrugated ribbons (formed by corner sharing) that run parallel to the c axis (Hong 1974a).

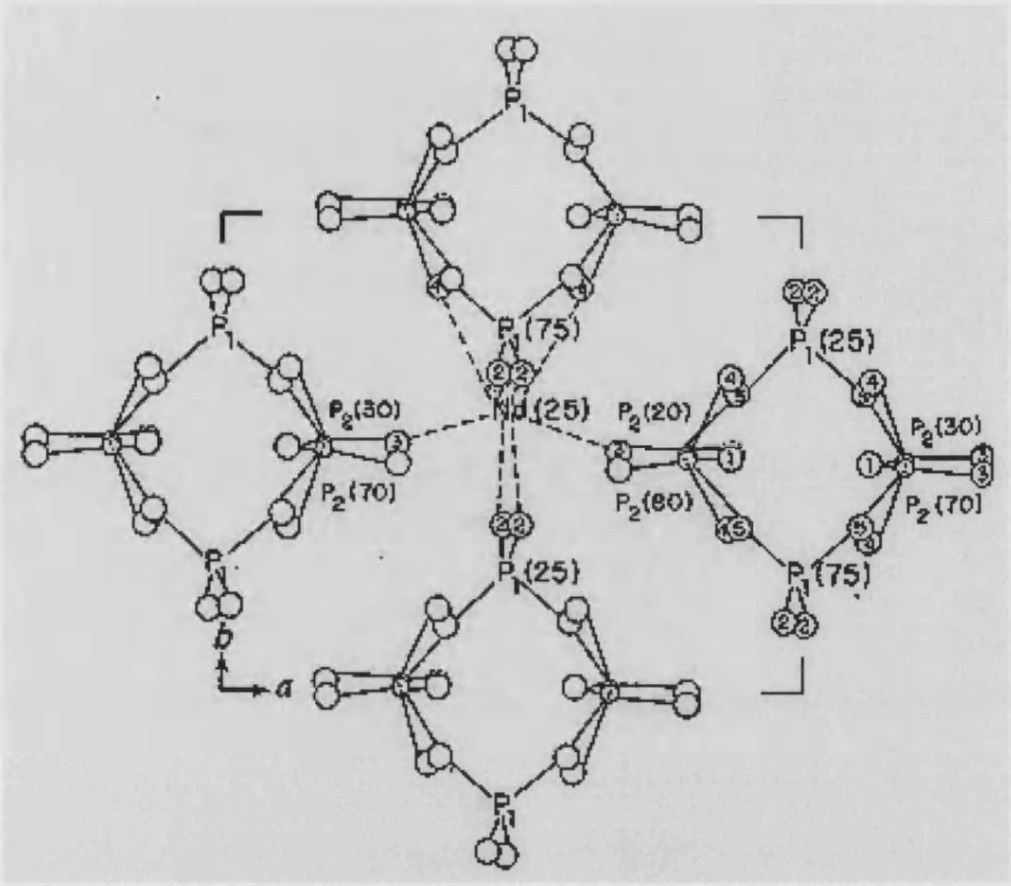

Figure 6.2. An ab projection of the NdP_3O_9 structure, showing how the PO_4 tetrahedra are connected by Nd^{3+} ions (Hong 1974a).

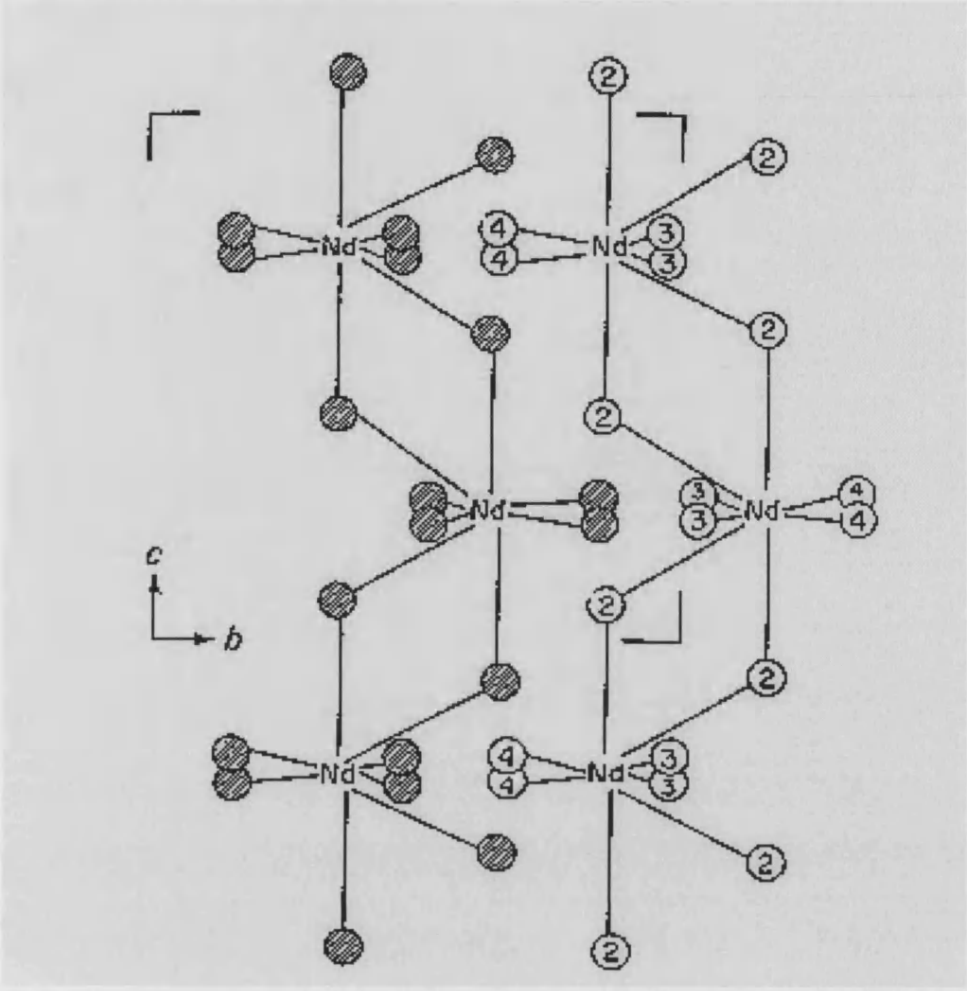

Figure 6.3. A bc projection of the arrangement of NdO_8 dodecahedra in NdP_3O_9, showing the zigzag chains (formed by edge sharing) that runs parallel to the c axis (Hong 1974a).

Detailed structural data on trivalent meta-phosphate crystals is available for the La^{3+}, Nd^{3+}, Er^{3+} and Yb^{3+} ions. Many of the previous structural studies of phosphate glasses have therefore been analysed with reference to ultra-phosphate as well as meta-phosphate crystals and the glasses are often referred to as a hybrid between meta and ultra-phosphates (Cole *et al* 1999, 2001a). The skeletons of meta-phosphates RP_3O_9 and ultra-phosphates RP_5O_{14} crystals are formed by PO_4 tetrahedra. Corner sharing of PO_4 tetrahedra, resulting in 'infinite' chains, forms the basis of meta-phosphate crystals which have an O:P ratio of three and an O_T:O_B ratio of 2:1. In ultra-phosphate crystals the phosphate chains are cross-linked and have an O:P ratio of 2.8 and an O_T:O_B ratio of 4:3. In addition there are orthophosphate crystals RPO_4

where all the PO_4^{3-} tetrahedra are isolated, the O:P ratio is 4:1 and there are no O_B atoms.

In the crystalline (Stachel 1995, Arbib *et al* 1996) and glassy (Hoppe *et al* 1998b) phases of P_2O_5 the network is built from PO_4 tetrahedra comprising three bridging oxygen O_B and one terminal oxygen O_T as shown in Figure 6.4.

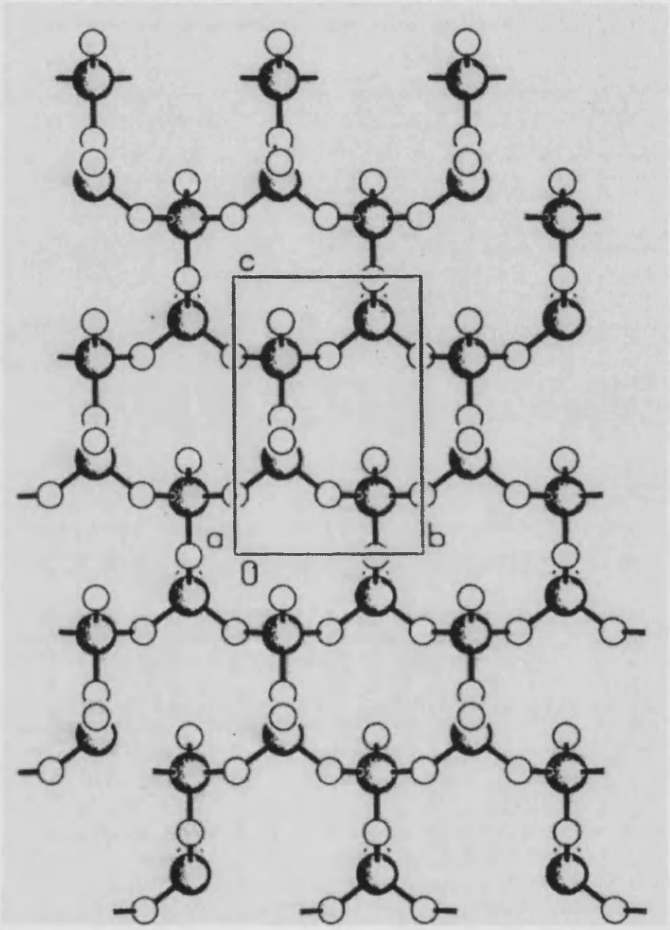

Figure 6.4. The structure of a sheet of o'-$(P_2O_5)_\infty$ (Stachel 1995).

In the model of Hoppe (1996) the addition of network modifiers depolymerises the network through the breakage of P-O-P bonds. If y is the number of oxygen added per P_2O_5 unit the P:O_B:O_T ratio changes from 2:3:2 in pure P_2O_5 to 2 : (3-y) : 2(1+y) in the modified material. A coordination number $\bar{n}_O^O = 24/(5+y)$, where $\bar{n}_\beta^\alpha$ represents the

average number of atoms of type α surrounding an atom of type β, then follows by taking oxygen-oxygen coordination numbers of 6 and 3 for the O_B and O_T sites respectively (Hoppe 1996). This gives observed coordination numbers $\bar{n}_O^O$ of 4.8 for crystalline P_2O_5 (Stachel 1995, Arbib *et al* 1996), 4.29 for the crystalline ultraphosphates RP_5O_{14} (Hong 1974b), 4.0 for the crystalline meta-phosphates RP_3O_9 (Hong 1974a,b) and 3.0 for crystalline orthophosphates (Mullica *et al* 1984). The compositions of the latter maybe expressed as $(R_2O_3)_x(P_2O_5)_{1-x}$ where x = 1/6, 1/4 and 1/2 for the ultra-phosphate, meta-phosphate and ortho-phosphate phases respectively such that the $R:O_T$ ratio is given by 1 : (1+2x)/x. In both the meta and ultra-phosphate phases of the large rare earth ions, R^{3+} is bound to eight O_T while the number of O_T available per cation is eight for the ultra-phosphate but only six for the meta-phosphate phase. Hence several of the O_T atoms are shared between R-centred polyhedra at the meta-phosphate stoichiometry.

6.3 THE ROLE OF ALUMINIUM IN PHOSPHATE GLASSES.

As discussed in Chapter 2, compositional analysis of phosphate glasses prepared in alumina crucibles confirms the presence of aluminium at the level of approximately two atomic percent. The number of nearest neighbour oxygen around aluminium $\bar{n}_{Al}^O$ can be 4, 5 or 6 (Cole *et al* 1999, Karabulut *et al* 2001). Aluminium meta-phosphate crystals have been prepared in which Al^{3+} is octahedrally coordinated with an Al-O distance of 1.884 Å (Van der Meer, 1976)[†]. By comparison the Al-O distance is 1.73 Å for tetrahedrally coordinated aluminium (Sowa *et al* 1990). From the Al-O distance and the O-Al-O bond angle the second nearest neighbour distance O-(Al)-O can be estimated for the four and six fold configurations where O-(Al)-O denotes O-O correlations for atoms bridged by aluminium. Six fold coordinated Al has an O-Al-O angle of 90° and an Al-O distance of 1.884 Å (Van der Meer 1976) giving an O-(Al)-O distance of $\sqrt{2}\ r_{O-Al}$ = 2.66 Å. Four fold coordinated Al would result in an O-(Al)-O distance of $\sqrt{8/3}\ r_{O-Al}$ = 2.833 Å. In an Al centred octahedron,

[†] The sum of the Shannon (1976) radii for the four fold coordinated Al^{3+} and O^{2-} is 1.79 Å while for 6-fold coordinated Al^{3+} and O^{2-} it is 1.94 Å.

each Al in surrounded by six oxygen and each oxygen will have four nearest neighbour oxygen at a distance of $\sqrt{2}\ r_{O-Al}$ and one other oxygen at a distance of $2\,r_{O-Al}$.

On the basis of the phosphate network model (Hoppe 1996), the $P:O_B:O_T$ ratio is 2:(3-y):(2+2y) (see section 6.2). Let the P:Al ratio in the R-P-O-Al glasses be denoted by 2:z. Then for octahedral coordination of Al, 6z of the $(2+2y)O_T$ will be bound to Al to give a coordination number of O around O at a distance $\sqrt{2}\ r_{O-Al}$ equal to

$$\bar{n}_O^{-o} = \frac{(6z)4}{(5+y)}. \qquad [6.1]$$

The P:O:Al ratio can be written as 1: c_O/c_P : c_{Al}/c_P. Hence equation 6.1 can be written as

$$\bar{n}_O^{-o} = \frac{12c_{Al}}{c_P}\frac{4}{(5+y)} \quad . \qquad [6.2]$$

In an Al centred tetrahedron, each oxygen will have three nearest neighbour oxygen at a distance of $\sqrt{8/3}\ r_{O-Al}$. Assuming that the Al again bonds to terminal oxygen O_T, the O-(Al)-O coordination number corresponding to four fold coordinated Al in the glassy phase is given by

$$\bar{n}_O^{-o} = \frac{4(2c_{Al})}{c_P}\frac{3}{(5+y)} \ . \qquad [6.3]$$

6.4 PREPARING THE GLASSY SAMPLES

The glasses were prepared using the method outlined in Chapter 2. As stated in this chapter it is not possible to prepare samples of an exact composition due to the phosphorus pentoxide losses that occur during the heating process and the leaching of Al into the glass from the crucibles. Therefore to ensure that glasses used for the isomorphic substitution experiments were as near identical in composition as possible a series of glasses were prepared and characterised as shown in Table 6.2.

Glass	c_R (± 0.0002)	c_P (± 0.0002)	c_O (± 0.0002)	c_{Al} (± 0.0002)	density (g cm^{-3}) (± 0.01)
LaA	0.0670	0.2224	0.6865	0.0241	3.25
LaB	0.0709	0.2197	0.6877	0.0217	3.29
LaC	0.0663	0.2105	0.7040	0.0192	3.28
LaCeD	0.0778 c_{La} 0.0401 : c_{Ce} 0.0377	0.2089	0.6970	0.0164	
LaCeE	0.0772 c_{La} 0.0363 : c_{Ce} 0.0409	0.2169	0.6848	0.0211	3.37
LaCeF	0.0663 c_{La} 0.0309 : c_{Ce} 0.0354	0.2195	0.6888	0.0254	3.32
CeG	0.0766	0.2064	0.6833	0.0337	3.24
CeH	0.0751	0.2178	0.6779	0.0292	3.37
CeI	0.0773	0.2143	0.6805	0.0280	3.35

Table 6.2. Compositions and densities of La/ Ce phosphate glasses.

The coefficients of $S_{\alpha\beta}(Q)$ in the total structure factors and difference functions were calculated using the concentrations given in Table 6.2 and the scattering lengths b_{La} = 0.824(4), b_{Ce} = 0.484(2), b_P = 0.513(1), b_O = 0.5803(4) and b_{Al} = 0.3449(5) fm (Sears 1992). The coefficients for the first order difference functions were calculated by subtracting one total structure factor from another as described in section 4.8. The only contributions present in an ideal first order difference are terms containing the rare earth ion, therefore all α-β correlations where $\alpha \neq R$ and $\beta \neq R$ are denoted 'contaminants'. The level of isomorphism between pairs of samples was

estimated by defining a coefficient ξ_R as the ratio of the sum of the modulus of the coefficients involving R to the sum of modulus of the contamination coefficients. The coefficients for two pairs of samples are listed in Table 6.3. This shows that the pair denoted by LaB and LaCeF have a minimal amount of contamination with a coefficient ξ_R of 9.3 compared with a coefficient ξ_R of 0.12 for the LaA and LaCeD pair. The nine glasses manufactured allowed 27 unique first order difference combinations to be studied and a summary of the corresponding ξ_R values are given in Table 6.4.

	LaA	LaB	LaC	LaCeD	LaCeE	LaCeF	CeG	CeH	CeI
LaA	-	-	-	0.3615	1.353	5.279	1.569	2.366	2.279
LaB	-	-	-	0.781	2.973	9.312	1.804	2.686	2.606
LaC	-	-	-	0.73	0.6114	1.155	1.086	1.281	1.287
LaCeD	-	-	-	-	-	-	1.093	1.107	1.296
LaCeE	-	-	-	-	-	-	1.363	2.252	2.195
LaCeF	-	-	-	-	-	-	0.5413	0.8657	0.7488
CeG	-	-	-	-	-	-	-	-	-
CeH	-	-	-	-	-	-	-	-	-
CeI	-	-	-	-	-	-	-	-	-

Table 6.4. A summary of the contamination coefficients ξ_R for all the first order difference combinations obtained for the samples listed in Table 6.2.

A summary of the coefficients of $S_{\alpha\beta}(Q)$ for the total minus weighted difference function $\Delta_F(Q)$ obtained for the LaB and LaCeF pair is given in Table 6.5. A corresponding coefficient ξ_F was defined in an analogous fashion to ξ_R and takes a value of $\xi_F = 20.3$ for this pair.

While the effect of contaminants on the difference functions $\Delta_R(Q)$ and $\Delta_F(Q)$ is relatively small for the optimum choice of sample pairs, their effect on the second order difference function $S_{RR}(Q)$ can be considerable. Owing to the level of contamination for the La and Ce glasses an accurate second order difference function could not be obtained for the available samples.

Correlation	$F(Q)_{LaB}$ (mbarn)	$F(Q)_{LaCeF}$ (mbarn)	$\Delta_R(Q)$ $\{F(Q)_{LaB} - F(Q)_{LaCeF}\}$ (mbarn)	$F(Q)_{LaA}$ (mbarn)	$F(Q)_{LaCeD}$ (mbarn)	$\Delta_R(Q)$ $\{F(Q)_{LaA} - F(Q)_{LaCeD}\}$ (mbarn)
R-R	3.41 (4)	1.81 (2)	1.60 (2)	3.05 (4)	2.92 (3)	0.12 (4)
R-P	13.17 (8)	9.59 (5)	3.58 (5)	12.59 (8)	11.59 (6)	1.0 (1)
R-O	46.6 (3)	34.0 (2)	12.6 (2)	44.0 (3)	43.7 (2)	0.3 (3)
R-Al	0.87 (1)	0.747 (7)	0.126 (7)	0.917 (9)	0.610 (8)	0.31 (1)
P-P	12.71 (6)	12.68 (6)	0.02 (6)	13.01 (6)	11.48 (5)	1.53 (8)
P-O	90.0 (2)	90.0 (2)	-0.1 (2)	90.9 (2)	86.7 (2)	4.2 (3)
P-Al	1.69 (2)	1.98 (2)	-0.29 (2)	1.90 (2)	1.21 (2)	0.69 (2)
O-O	159.3 (2)	159.8 (2)	-0.5 (2)	158.7 (2)	163.6 (2)	-4.9 (3)
O-Al	5.97 (6)	7.01 (6)	-1.05 (6)	6.62 (6)	4.56 (6)	2.06 (8)
Al-Al	0.056 (1)	0.077 (1)	-0.021 (1)	0.069 (1)	0.032 (1)	0.037 (1)

Table 6.3. Coefficients of the $S_{\alpha\beta}(Q)$ for the total structure factors, F(Q), and the first order difference functions, $\Delta_R(Q)$, obtained by subtracting the F(Q) for the sample pairings of LaB-LaCeF and LaA-LaCeD.

Correlation	F(Q) LaB (mbarn)	F(Q) LaCeF (mbarn)	$\Delta_F(Q) = -3.543*F(Q)_{LaB} + 4.543*F(Q)_{LaCeF}$ (mbarn)
R-R	3.41 (4)	1.81 (2)	-3.8 (2)
R-P	13.17 (8)	9.59 (5)	-3.1 (4)
R-O	46.6 (3)	34.0 (2)	-11 (1)
R-Al	0.87 (1)	0.747 (7)	0.30 (5)
P-P	12.71 (6)	12.68 (6)	12.6 (3)
P-O	90.0 (2)	90.0 (2)	90 (1)
P-Al	1.69 (2)	1.98 (2)	3.01 (9)
O-O	159.3 (2)	159.8 (2)	161 (1)
O-Al	5.97 (6)	7.01 (6)	10.7 (3)
Al-Al	0.056 (1)	0.077 (1)	0.152 (7)

Table 6.5. Coefficients of the $S_{\alpha\beta}(Q)$ for the total structure factors and the total minus weighted difference function, $\Delta_F(Q)$, obtained for the pair of samples LaB and LaCeF.

As shown in Table 6.4 there are two combinations, LaA – LaCeF and LaB – LaCeF, for which the level of contamination is a minimum. These three glasses were therefore chosen for investigation by using neutron diffraction. Samples LaA and LaCeF were studied using the instrument GLAD at the Intense Pulsed Neutron Source, Argonne National Laboratory and samples LaB and LaCeF were studied using the instrument D4C at the Institut Laue-Langevin, Grenoble (see section 5.2).

6.5. EXPERIMENTAL PROCEDURE

The D4C instrument was operated at an incident wavelength of 0.70995 Å to give a measurement range of $0.33 \leq Q(Å^{-1}) \leq 16.5$, whilst use of GLAD gave an extended Q range of $0.35 \leq Q(Å^{-1}) \leq 24.95$. For the GLAD experiments the rare-earth phosphate glasses were sealed in a cylindrical vanadium container of internal diameter 9.27 mm and 0.254 mm wall thickness. For the D4C experiments the rare-earth phosphate glasses were sealed in a cylindrical vanadium container of internal diameter 7 mm and 0.1 mm wall thickness. Diffraction patterns were taken for the samples in their container, the empty container and a vanadium rod of dimensions comparable to the sample for normalisation purposes. The intensity for a cadmium neutron-absorbing rod of similar diameter to the sample was also measured, on D4C, to account for the effect of the sample self-shielding on the background count rate at small scattering angles. Due to the large range of incident neutron energies associated with the GLAD instrument a cadmium measurement was not recorded; as the absorption resonance of Cd has a finite width in energy. The total paramagnetic scattering cross-section of Ce^{3+} at the D4C incident wavelength was 0.311 barn (Wasse and Salmon 1999). The data analysis procedure outlined in section 5.8 was followed.

6.6 RESULTS.

The differential scattering cross section, $F_S(Q)$, corrected for background, container, heater and multiple scattering effects (equation 4.34) for LaB and LaCeF is given in Figure 6.5. For LaCeF, the paramagnetic differential scattering cross section $[(d\sigma/d\Omega)_{mag}/N\eta_0]$ of Ce^{3+} (equation 4.40) is also shown. Note that lanthanum ions do not have any unpaired f-electrons and therefore do not have a paramagnetic scattering cross section.

In order to extract the total structure factor, F(Q), for the LaB sample from $F_S(Q)$ and $(d\sigma/d\Omega)_{mag}$ (equation 4.42) it was necessary to make a small hydrogen correction. This resulted from the unfortunate presence of solvent used to clean the

sample containers. However, the hydrogen content was small, at the level of ≈ 0.1 mol %, and as discussed in section 5.11 it will only have a major effect on the inelasticity corrections. The hydrogen correction is illustrated in Figure 6.5.

The total structure factors, F(Q), for LaB and LaCeF are shown in Figure 6.6 and the corresponding total pair distribution functions, G′(r), are shown in Figure 6.7. There is close agreement between the F(Q) functions and the back Fourier transforms of their corresponding G′(r) after the unphysical low r oscillation are set equal to the G(0) limit (Figure 6.7) which indicates that the data corrections have been properly applied. The F(Q) function obtained from the GLAD experiments for LaA and LaCeF samples are also shown in Figure 6.6. The extended Q range of this diffractometer results in G′(r) functions, shown in Figure 6.7, having sharper peaks i.e. the effect of the modification function M(r) is smaller (section 4.9).

The first order difference function $\Delta_R(Q)$ obtained for the LaB and LaCeF samples and the back Fourier transform of $\Delta G'_R(r)$ with the unphysical low r oscillations set equal to $\Delta G_R(0)$ (Figure 6.9) are in close agreement as illustrated in Figure 6.8. This again indicates that the data corrections have been applied properly. The GLAD data was not used to obtain a first order difference function owing to the greater level of contaminants for the LaA and LaCeF pairing (Table 6.4) and the greater statistical noise on the measured total structure factors.

The total minus weighted difference function $\Delta_F(Q)$ is shown in Figure 6.10 and the corresponding $\Delta G'_F(r)$ is shown in Figure 6.11. Again there is agreement between $\Delta_F(Q)$ and the back Fourier transform of $\Delta G'_F(r)$ with the unphysical low r oscillations set equal to $\Delta G_F(0)$.

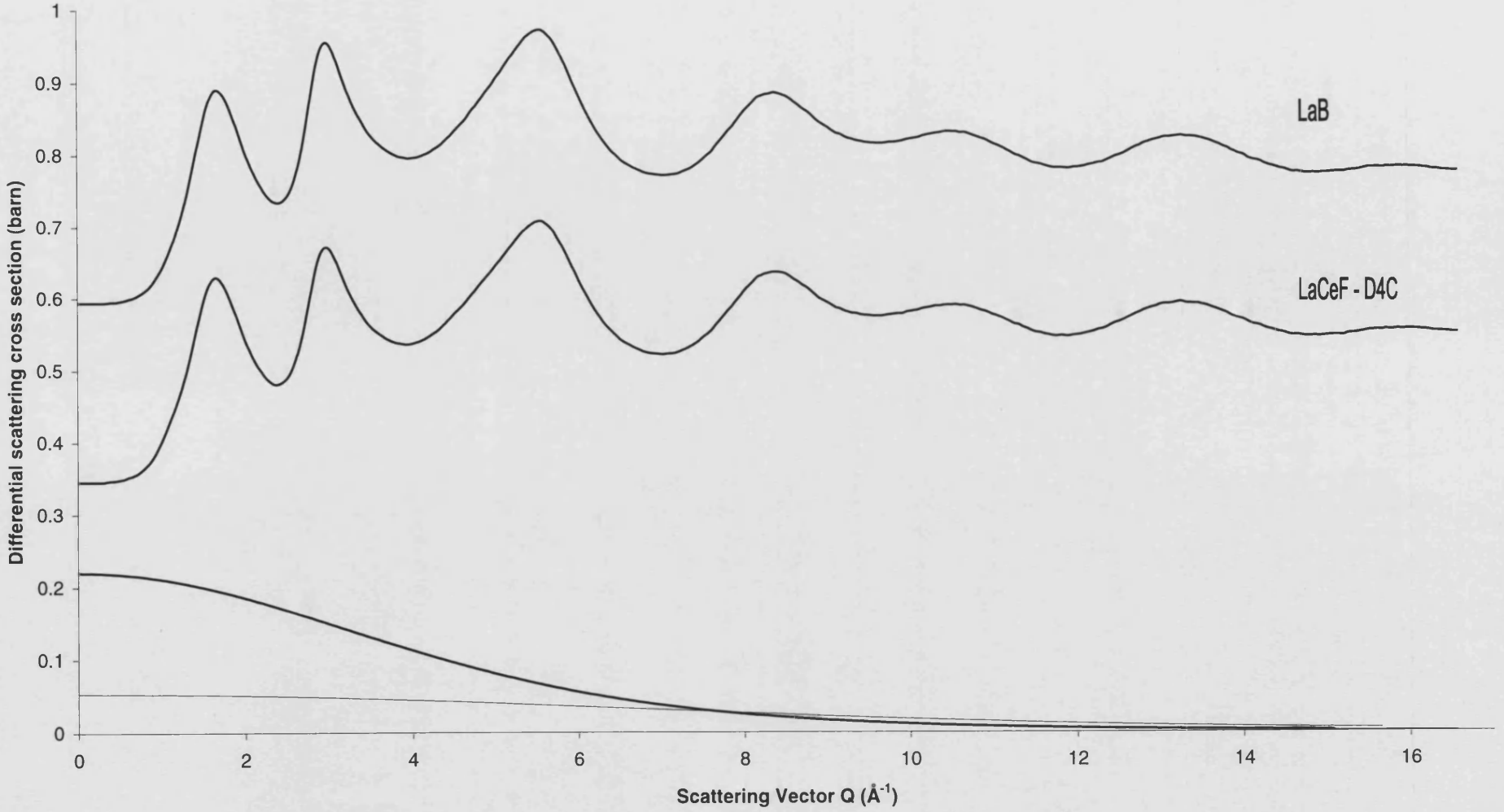

Figure 6.5. $F_S(Q)$ for LaB and LaCeF,
the cerium magnetic form factor scaled by 20 for LaCeF (solid curve) and the hydrogen correction (fient curve).

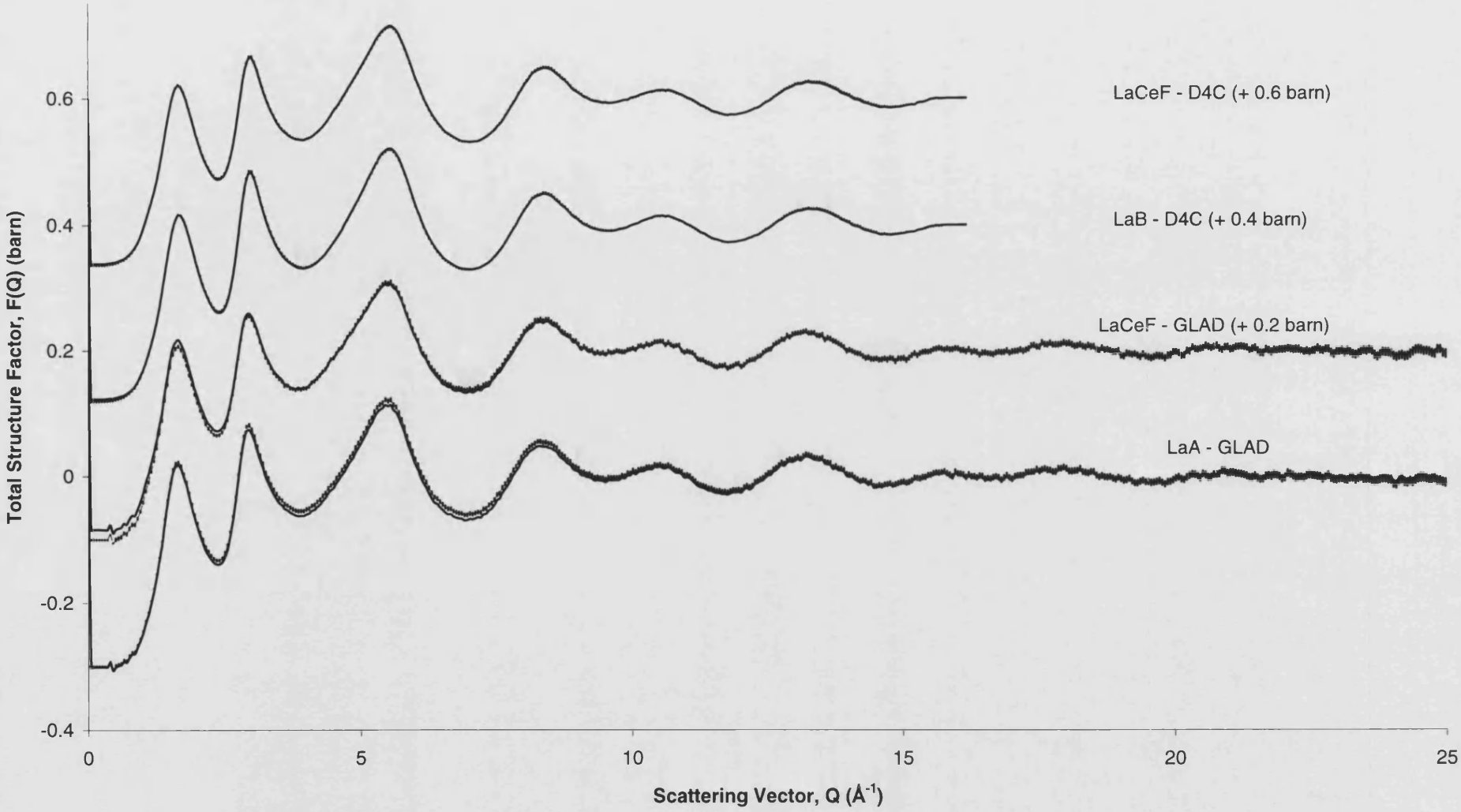

Figure 6.6. The total structure factors, F(Q) (points with error bars) and the Fourier backtransforms of the G'(r) given by the solid curves in Figure 6.7 (solid curve) for the LaA, LaB and LaCeF samples.

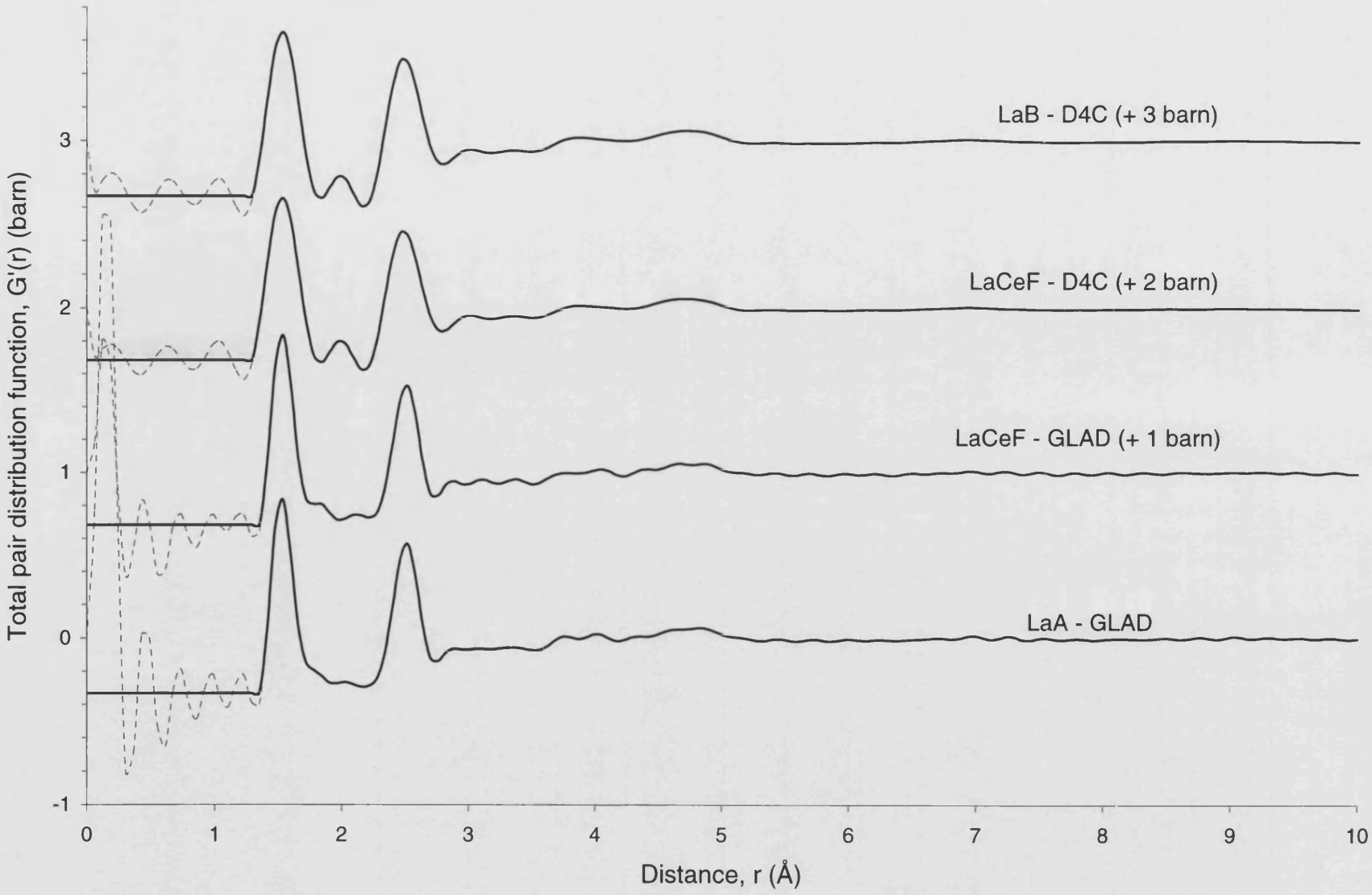

Figure 6.7. The real space functions G'(r) (solid curve). The unphysical low r oscillations are shown by the dashed curves.

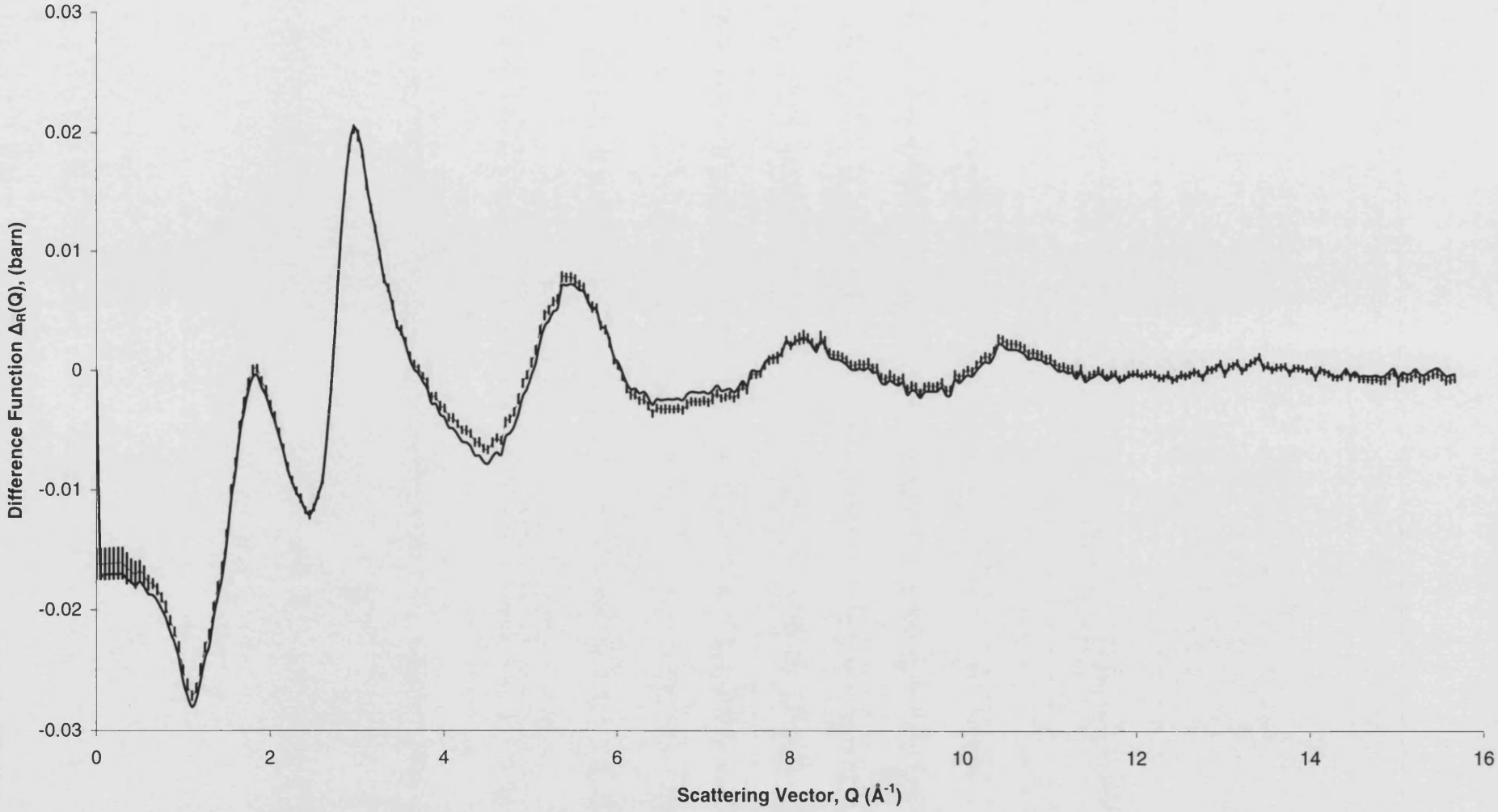

Figure 6.8. The difference function, $\Delta_R(Q)$, obtained for the LaB and LaCeF samples (points with error bars) and the Fourier backtransform of $\Delta G'_R(r)$ (solid curve) given by the solid curve in Figure 6.9.

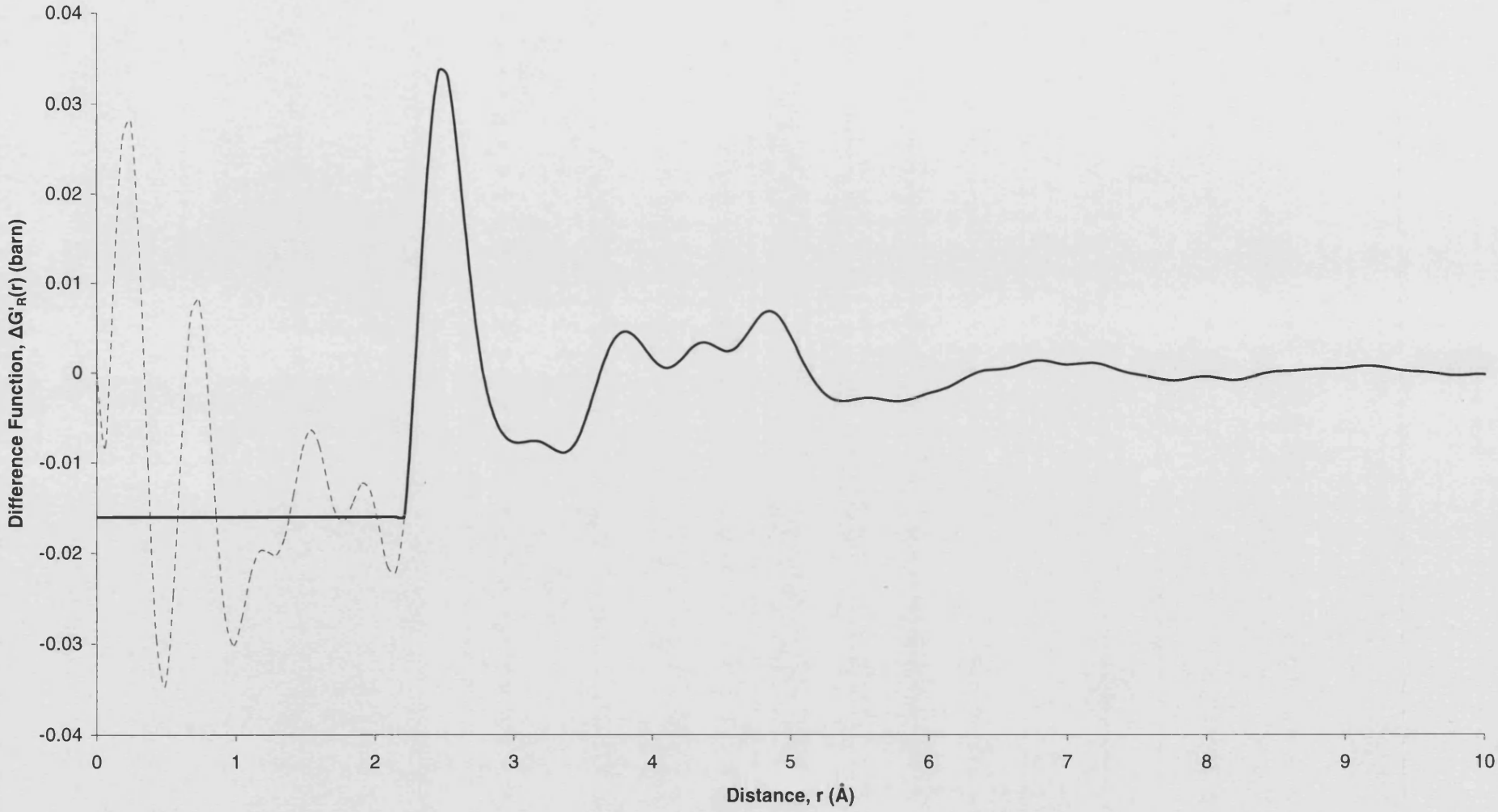

Figure 6.9. The real space function $\Delta G'_R(r)$ (solid curve) obtained by Fourier transforming $\Delta_R(Q)$ given by the points with error bars in Figure 6.8. The low r unphysical oscillations are shown by the dashed curve.

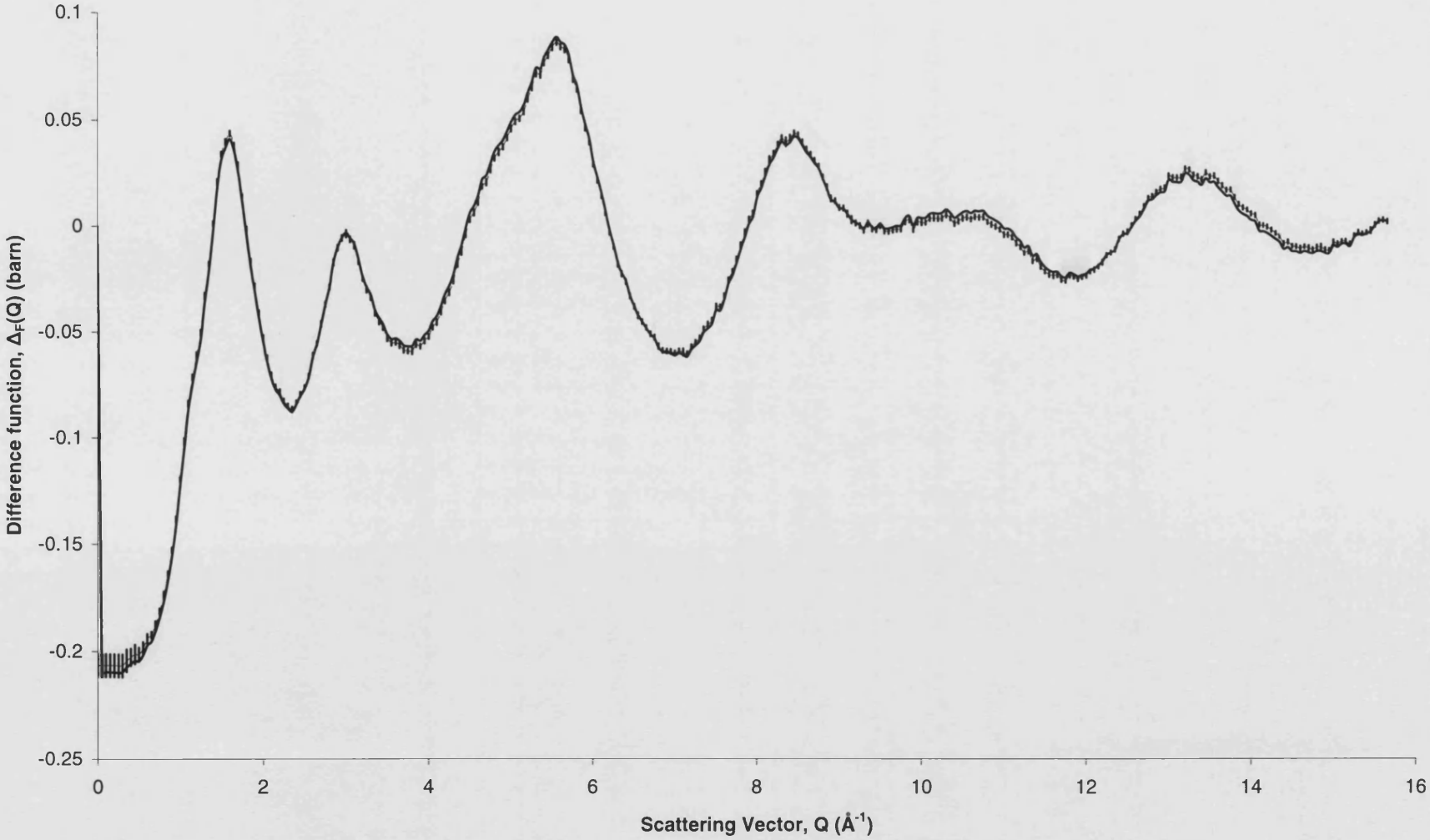

Figure 6.10. The difference function, $\Delta_F(Q)$, obtained for the LaB and LaCeF samples (points with error bars) and the Fourier backtransform of $\Delta G'_F(r)$ (solid curve) given by the solid curve in Figure 6.11.

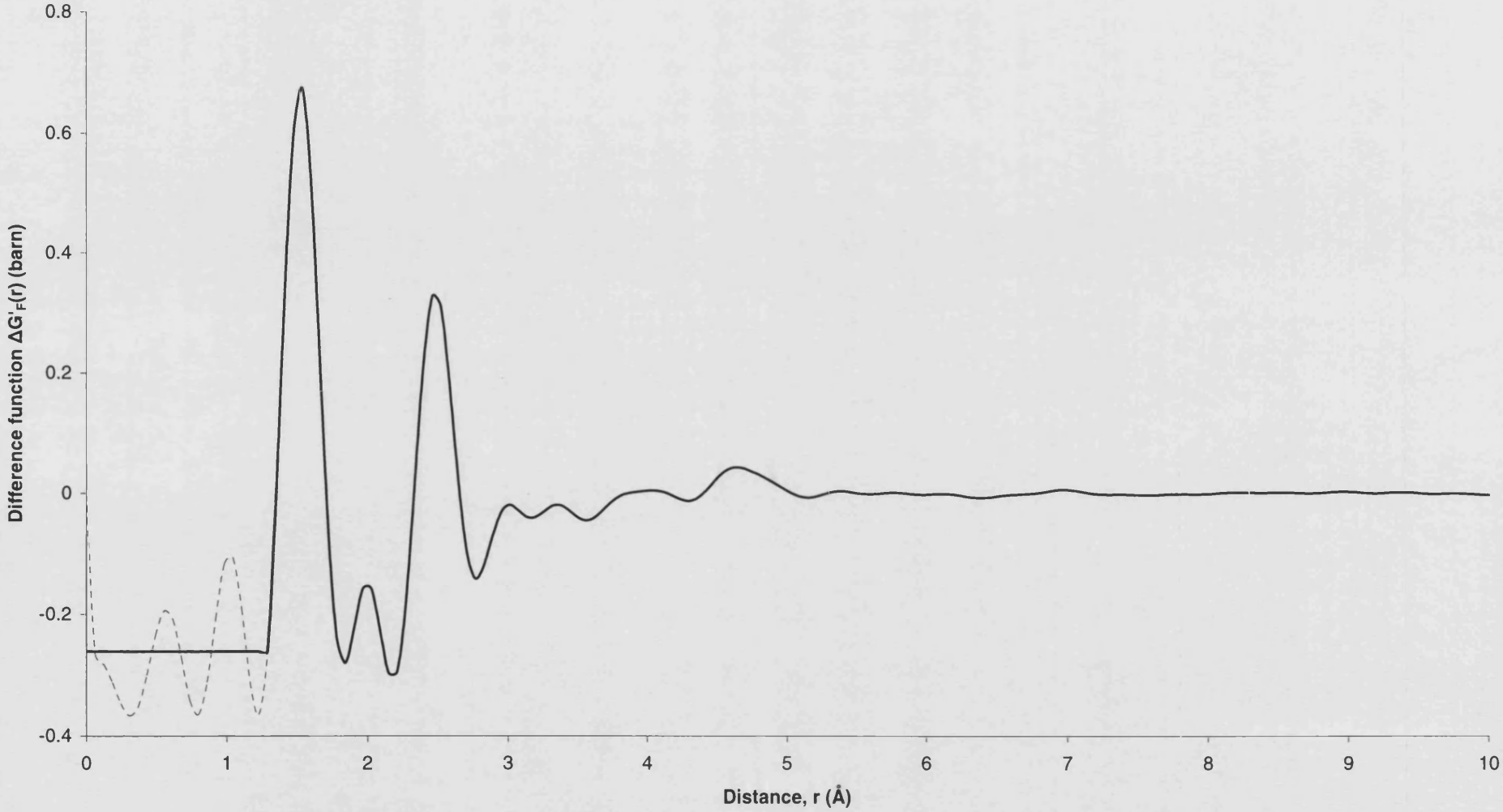

Figure 6.11. The real space function $\Delta G'_F(r)$ (solid curve) obtained by Fourier transforming $\Delta_F(Q)$ given by the points with error bars in Figure 6.10. The unphysical low r oscillations are shown by the dashed curve.

The first order difference function $\Delta D'_R(r)$ was modelled first, using the fitting procedure outlined in section 4.9, since this function has the fewest contributing $g_{\alpha\beta}(r)$ (section 4.8). The measured function $\Delta D'_R(r)$, the individual convoluted Gaussians, their sum and the residual are shown in Figure 6.12. The R_χ value for the fitting region of $2.0 \leq r$ (Å) ≤ 3.5 is 0.023 (section 5.10). The parameters describing the fitted Gaussians are summarised in Table 6.6.

By comparison with the crystal structures of the rare-earth meta-phosphates (Matuszewski *et al* 1988), ultra-phosphates (Cole *et al* 2000) and ortho-phosphates (Hughes and Mariano 1995) the R-α correlations were assigned. In crystalline LaP_3O_9 the shortest La-O, La-P and La-La distances are at 2.415 Å, 3.29 Å and 4.3 Å respectively and the second nearest-neighbour La-O distance is at 3.97 Å (Matuszewski *et al* 1988). In crystalline LaP_5O_{14} the shortest La-O, La-P and La-La distances are at 2.46 Å, 3.67 Å and 5.25 Å respectively and the second nearest-neighbour La-O distance is at 4.26 Å (Cole *et al* 2000). In crystalline $LaPO_4$ the shortest La-O, La-P and La- La distances are at 2.47 Å, 3.22 Å and 4.10 Å respectively and the second nearest-neighbour La-O distance is at 3.86 Å (Hughes and Mariano 1995). Hence only R-O correlations are expected for $r \leq 3.2$ Å and $\Delta D'_R(r)$ was modelled accordingly.

The nearest-neighbour R-O correlations could not be modelled by a single Gaussian. Instead, they were best represented by four separate peaks as shown in Figure 6.12 i.e. the R-O coordination environment is asymmetric The mean R-O distances of 2.46, 2.485, 2.73 and 3.09 Å compare with La-O distances of 2.415, 2.435, 2.49 and 2.75 Å in crystalline LaP_3O_9 (Matuszewski *et al* 1988). The total R-O coordination number of 7.45 compares with a coordination number of eight in crystalline LaP_3O_9 (Matuszewski *et al* 1988). Beyond about 3 Å the broadening of peaks means that it is difficult to clearly resolve neighbouring correlations. However, only R-P correlations are expected as the next nearest neighbours and the data was therefore modelled with Gaussians having R-P coordination numbers of 1, 2, 2 and 2 at distances of 3.30, 3.58, 3.75 and 3.85 Å respectively. These values compare with R-P coordination numbers of 1, 2, 2 and 2 at distances of 3.29, 3.75, 3.85 and 3.87 Å respectively for crystalline LaP_3O_9 (Matuszewski *et al* 1988). Although the longer R-P

correlations may not be accurately represented, as shown by the discrepancy between the data and fitted model at $r \geq 3.7$ Å in Figure 6.12, the shorter R-P correlations should be reasonably well modelled in the region of overlap with the R-O peaks, $3.0 \leq r$ (Å) ≤ 3.4. The R-P peaks are broad and overlap considerably as shown in Figure 6.12; therefore the uncertainties in the individual peak positions and peak widths are large as reflected by the errors quoted in Table 6.6. As described in section 6.4 the measured $\Delta D'_R(r)$ will have a small contribution from O-O correlations. The Gaussian parameters used to represent these correlations were obtained from modelling the total minus weighted difference function $\Delta D'_F(r)$ (see below).

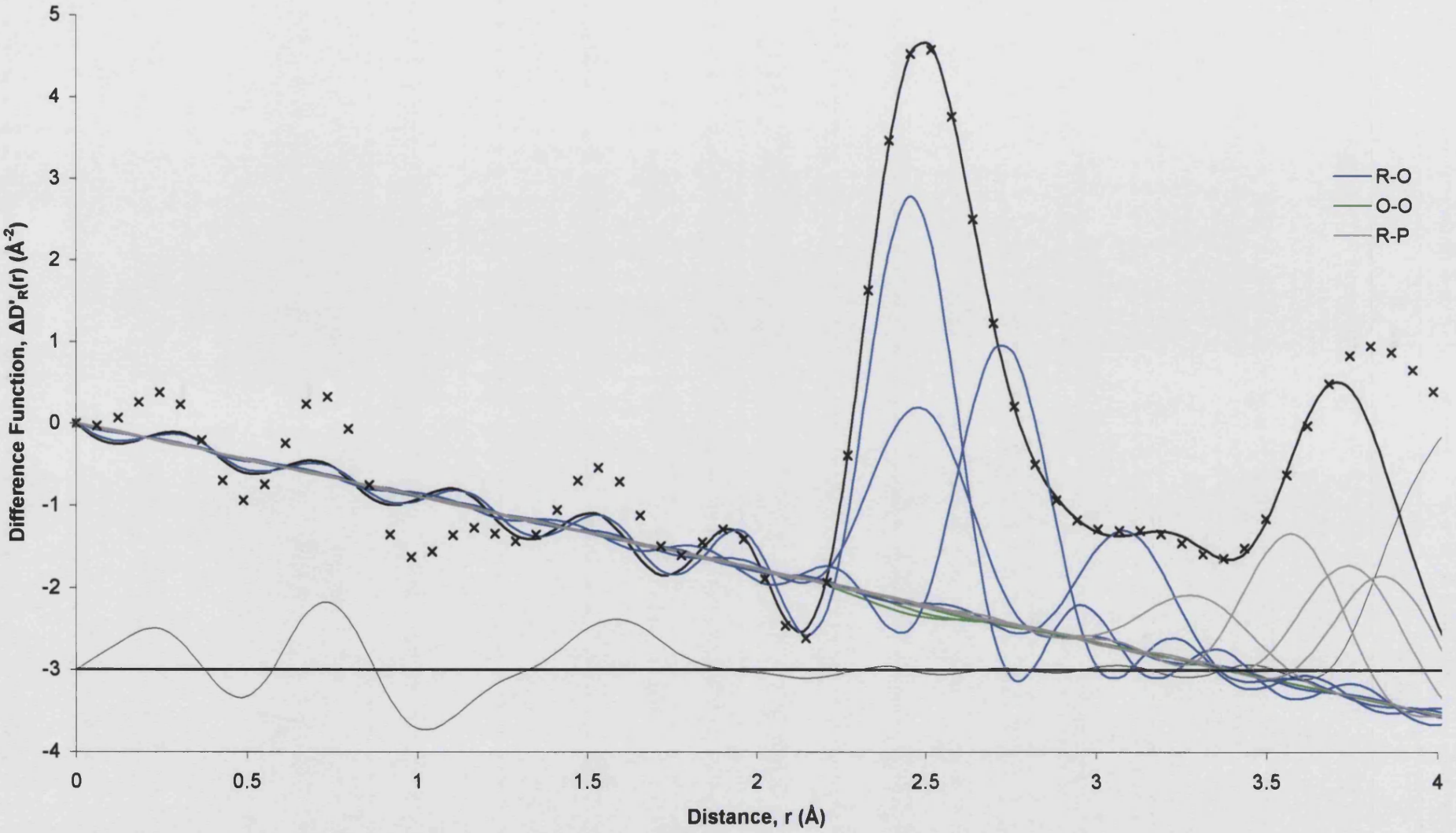

Figure 6.12. The difference function $\Delta D'_R(r)$ (crosses), the fitted data given by the sum of the Gaussians convoluted with the modification function M(r) (solid curve) and the residual offset by -3 barn (feint curve).

	r (Å)	C_N	σ (Å)
P-O_T	-	-	-
P-O_B	-	-	-
Al-O	-	-	-
R-O	2.460 (10)	2.60 (10)	0.070 (10)
R-O	2.485 (9)	1.70 (10)	0.122 (9)
O-(P)-O	2.455 (9)	2.50 (10)	0.110 (10)
O-(P)-O	2.525 (9)	1.45 (9)	0.085 (9)
O-(Al)-O	2.65 (1)	0.80 (10)	0.115 (9)
R-O	2.73 (1)	2.05 (9)	0.078 (9)
P-O	-	-	-
P-P	-	-	-
R-O	3.09 (2)	1.1 (2)	0.100(10)
R-P	3.30 (5)	1.0 (2)	0.145 (9)
R-P	3.58 (5)	2.0 (2)	0.115 (9)
R-P	3.75 (5)	2.0 (2)	0.13 (1)
R-P	3.85 (5)	2.0 (2)	0.13 (1)

Table 6.6. A summary of the Gaussian parameters used to model the first order difference function $\Delta D'_R(r)$. Small contributions from the O-(P)-O and O-(Al)-O correlations are included to account for the small levels of contamination. The parameters for these correlations were taken from the fit to $\Delta D'_F(r)$ (see Table 6.7).

Next, the total minus weighted difference function, $\Delta D'_F(r)$, was modelled since this also has fewer contributing $g_{\alpha\beta}(r)$ than the total pair distribution function $D'(r)$. The measured $\Delta D'_F(r)$, the individual convoluted Gaussians, their sum and the residual are shown in Figure 6.13. The R_χ value for the fitting region of $1.2 \leq r(Å) \leq 2.8$ Å is 0.025. The parameters describing the fitted Gaussians are summarised in Table 6.7.

By comparison with the crystal structures of the rare-earth meta-phosphates (Matuszewski *et al* 1988), ultra-phosphates (Cole *et al* 2000) and ortho-phosphates (Hughes and Mariano 1995) the α-β correlations, where $\alpha \neq R$ and $\beta \neq R$, were assigned. In crystalline LaP_3O_9 the shortest P-O, O-O and P-P distances are at 1.502 Å, 2.45 Å and 2.78 Å respectively (Matuszewski *et al* 1988). In crystalline LaP_5O_{14} the shortest P-O, O-O and P-P distances are at 1.46 Å, 2.39 Å and 2.90 Å respectively (Cole *et al* 2000). In crystalline $LaPO_4$ the shortest P-O, O-O and P-P distances are at 1.52 Å, 2.44 Å and 4.05 Å respectively (Hughes and Mariano 1995). The present phosphate glasses contain aluminium impurities (Table 6.2) and NMR results indicate that this aluminium can be 4, 5 or 6 fold coordinated (Cole *et al* 1999). In crystalline $Al(PO_3)_3$ Al is surrounded by six nearest neighbours at a distance of 1.88 Å (Van der Meer 1976) whereas Al centred tetrahedra have a nearest neighbour Al-O distance of ≈ 1.73 Å (Sowa *et al* 1990). Hence only P-O correlations are expected under the first peak, $1.3 \leq r(Å) \leq 1.7$, and $\Delta D'_F(r)$ was modelled accordingly.

The P-O peak was best modelled using two Gaussians, one corresponding to a C_N of 1.9(1) O_T around P at a distance of 1.49 Å and the other to a C_N of 1.9(1) O_B around P at a distance of 1.59 Å. These values compare with $\bar{n}_P^{O_T} = 2$ at a distance of 1.502 Å and $\bar{n}_P^{O_B} = 2$ at a distance of 1.57 Å for crystalline LaP_3O_9 (Matuszewski *et al* 1988). The total P-O coordination number is 4.0 within the experimental error as expected for a phosphate network.

Al-O correlations are expected to be next in the region $1.7 \leq r(Å) \leq 1.9$ followed by O-O correlations in the region $2.3 \leq r(Å) \leq 2.6$. However, the Al-O correlations have a small weighting factor compared to the P-O and O-O correlations (see Table 6.5) and the effect of the modification function M(r) on the P-O and O-(P)-

O correlations is significant in the region where the Al-O correlations occur. Therefore it was decided to model the O-(P)-O correlations next.

The O-(P)-O correlations were initially modelled with a single peak centred at 2.485 Å (Table 6.1). However a better fit was obtained by splitting the O-(P)-O correlations into two peaks centred at 2.455 and 2.525 Å (Table 6.6), a strategy that finds support on the basis of the distribution of O-(P)-O distances between 2.45 and 2.61 Å in the crystalline phase of LaP_3O_9 (Matuszewski *et al* 1988). The total O-(P)-O C_N of 3.95 compares with a value of 3.8 calculated on the basis of the phosphate network model of Hoppe (1996) which is described in section 6.2.

The Al-O correlations in $\Delta D'_F(r)$ were best modelled using a Gaussian centred at 1.88 Å, consistent with there being a large number of Al centred octahedra, as opposed to a Gaussian centred at the distance of 1.73 Å expected for Al centred tetrahedra. However, the modelled Al-O coordination number was 4.5(5) suggesting a range of Al environments.

The O-(Al)-O correlations were modelled using a distance of $\sqrt{2}\ r_{O-Al} = 2.66$ Å consistent with there being a large proportion of six fold coordinated Al as opposed to the longer distance of $\sqrt{8/3}\ r_{O-Al} = 2.833$ Å consistent with four fold coordinated Al. The starting value of the O-(Al)-O coordination number was set at 0.8 as obtained from equation 6.1, which is consistent with the majority of Al atoms being in an octahedral environment (see section 6.3).

Beyond about 2.75 Å the broad and overlapping peaks means that it is difficult to clearly resolve neighbouring correlations and there is a corresponding greater uncertainty in the Gaussian parameters as shown in Table 6.7. A modelling of the P-(OP)-O and P-(O)-P correlations was nevertheless undertaken, in part to provide a smooth overlap region beyond 2.5 Å to assist with modelling the shorter ranged O-(P)-O and O-(Al)-O correlations. The P-(O)-P distances and coordination numbers were fixed using values taken from the crystalline phase of LaP_3O_9 (Matuszewski *et al* 1988). The P-(OP)-O correlations were also modelled to account for the minimum at $\approx$ 2.75 Å. The latter is not expected to be an accurate representation as the

crystalline phase of LaP_3O_9 shows a range of overlapping P-(OP)-O and O-O correlations for r > 2.9 Å (Matuszewski *et al* 1988). The modelled P-(OP)-O distance is 2.94 Å which is considerably shorter than the distance of 3.17 Å for crystalline lanthanum meta-phosphate (Matuszewski *et al* 1988). However, shorter distances of 3.07 Å are given for crystalline AlP_3O_9 (Van der Meer 1976) and even shorter distances of 2.78 and 2.86 Å have been reported for glassy rare earth phosphates (Cole *et al* 1999).

As described in section 6.4 the measured $\Delta D'_F(r)$ will have a small contribution from R-O correlations. The Gaussian parameters used to represent these correlations were obtained from modelling the first order difference function, $\Delta D'_R(r)$, and are given in Table 6.6.

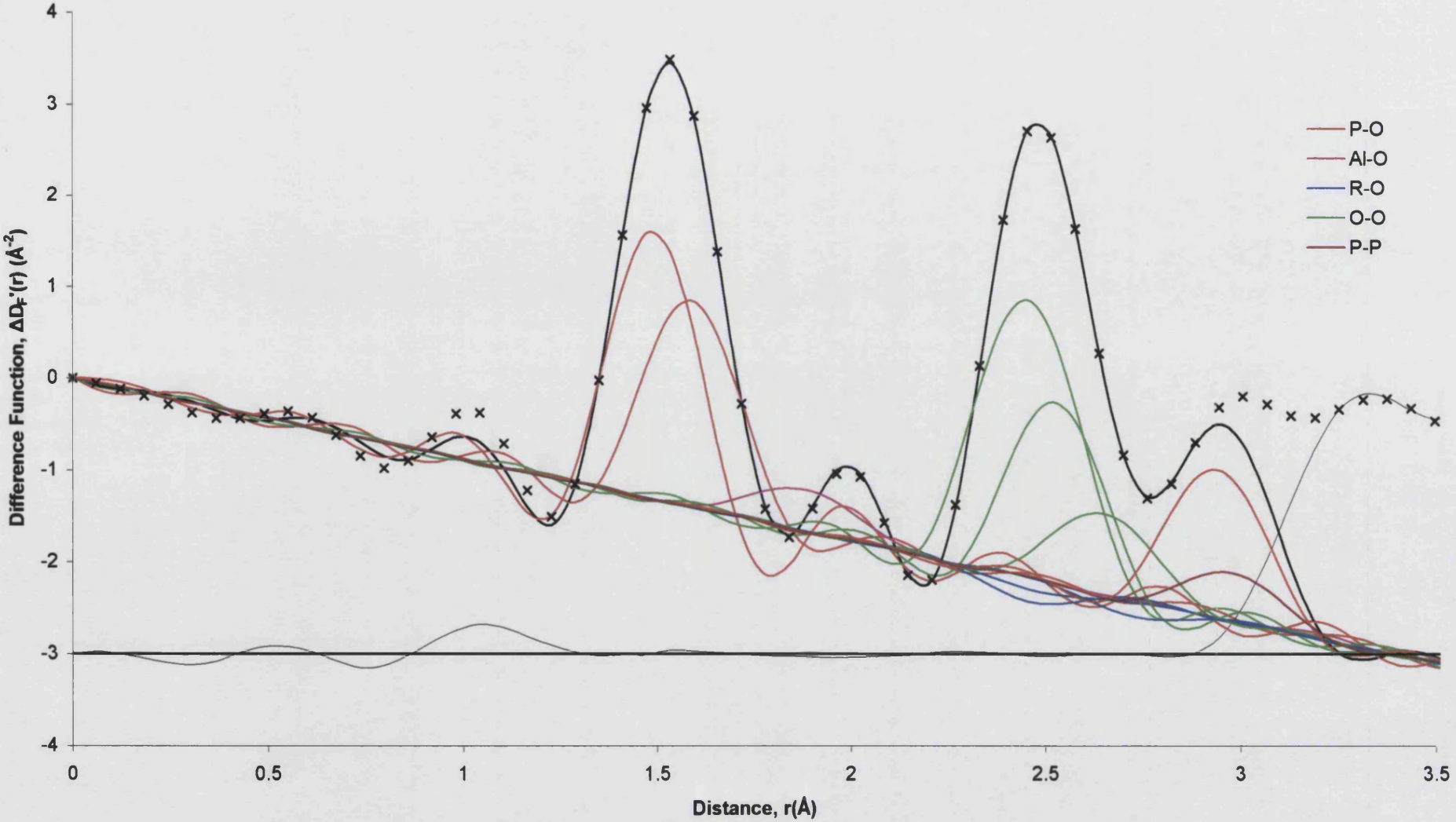

Figure 6.13. The difference function $\Delta D'_F(r)$ (crosses), the fitted data given by the sum of the Gaussians convoluted with the modification function M(r) (solid curve) and the residual offset by -3 barn (feint curve).

	r (Å)	C_N	σ (Å)
P-O_T	1.490 (10)	1.9 (1)	0.045 (5)
P-O_B	1.590 (10)	1.9 (1)	0.090 (5)
Al-O	1.88 (3)	4.5 (5)	0.120 (10)
R-O	2.46 (1)	2.6 (1)	0.070 (10)
R-O	2.485 (9)	1.7 (1)	0.122 (9)
O-(P)-O	2.455 (9)	2.5 (1)	0.110 (10)
O-(P)-O	2.525 (9)	1.45 (9)	0.085 (9)
O-(Al)-O	2.65 (1)	0.8 (1)	0.115 (9)
R-O	2.73 (1)	2.05 (9)	0.078 (9)
P-O	2.94 (2)	2.67 (9)	0.10 (1)
P-P	2.98 (2)	2.0 (1)	0.10 (1)
R-O	-	-	-
R-P	-	-	-
R-P	-	-	-
R-P	-	-	-
R-P	-	-	-

Table 6.7. A summary of the Gaussian parameters used to model the total minus weighted function $\Delta D'_F(r)$. Small contributions from the R-O correlations are included to account for the small levels of contamination. The parameters for these correlations were taken from the fit to $\Delta D'_R(r)$ (see Table 6.6).

Once self-consistent Gaussian parameters were obtained for the difference functions $\Delta D'_R(r)$ and $\Delta D'_F(r)$ these values were used to start the fitting process for the corresponding total pair distribution functions D'(r). The measured D'(r), the individual convoluted Gaussians, their sum and the residual for LaB (D4C), LaCeF (D4C), LaA (GLAD) and LaCeF (GLAD) are given in Figures 6.14 – 6.17. The R_χ values for LaB (D4C), LaCeF (D4C), LaA (GLAD) and LaCeF (GLAD) for $1.2 \leq r$ (Å) ≤ 2.8 are 0.016, 0.017, 0.061 and 0.057 respectively and the parameters used to model the Gaussians are given in Tables 6.8 and 6.9. The extended Q range of the GLAD instrument meant that the modification function M(r) has a smaller effect on D(r). Consequently the peaks in D'(r) for LaA (GLAD) and LaCeF-(GLAD) were sharper than those for the D4C data.

In general small refinements to the Gaussian parameters were required to obtain the best fits to D'(r). The Al-O Gaussian parameters were found to be the exception. The Al-O peak position in D'(r) and $\Delta D'_F(r)$ is the same at 1.88 Å, consistent with the majority of Al being six fold coordinated (Van der Meer 1976). However, the D'(r) functions were best represented using Al-O coordination numbers of 5.5(5) or 6.0(5) whilst $\Delta D'_F(r)$ was best represented by a smaller Al-O coordination number of 4.5(5). It was also found that the real space region $2.0 \leq r$ (Å) ≤ 2.2 could not be modelled for the samples LaA (GLAD) and LaCeF (GLAD) on the basis of the structure of crystalline phosphates, for example the nearest neighbour P-O_T and P-O_B distances ($\approx$ 1.5 and 1.6 Å) are too short to occur in this region and the shortest La-O, O-(P)-O, P-P, P-(OP)-O, La-P and La-La distances of 2.42, 2.45, 2.98, 3.17, 3.29 and 4.32 Å respectively in LaP_3O_9 are too long to occur in this region. The Al-O bond length is also too short to occur in the region $2.0 \leq r$ (Å) ≤ 2.2, as the longest Al-O distance is $\approx$ 1.88 Å corresponding to six fold coordinated Al in crystalline AlP_3O_9 (Van der Meer 1976). It was also found that the fitted peak positions of the P-O_T and P-O_B correlations were shifted by about + 0.01 Å for the GLAD results compared to the D4C results. This suggests that there is a small systematic error associated with the calibration of the diffractometer Q scale.

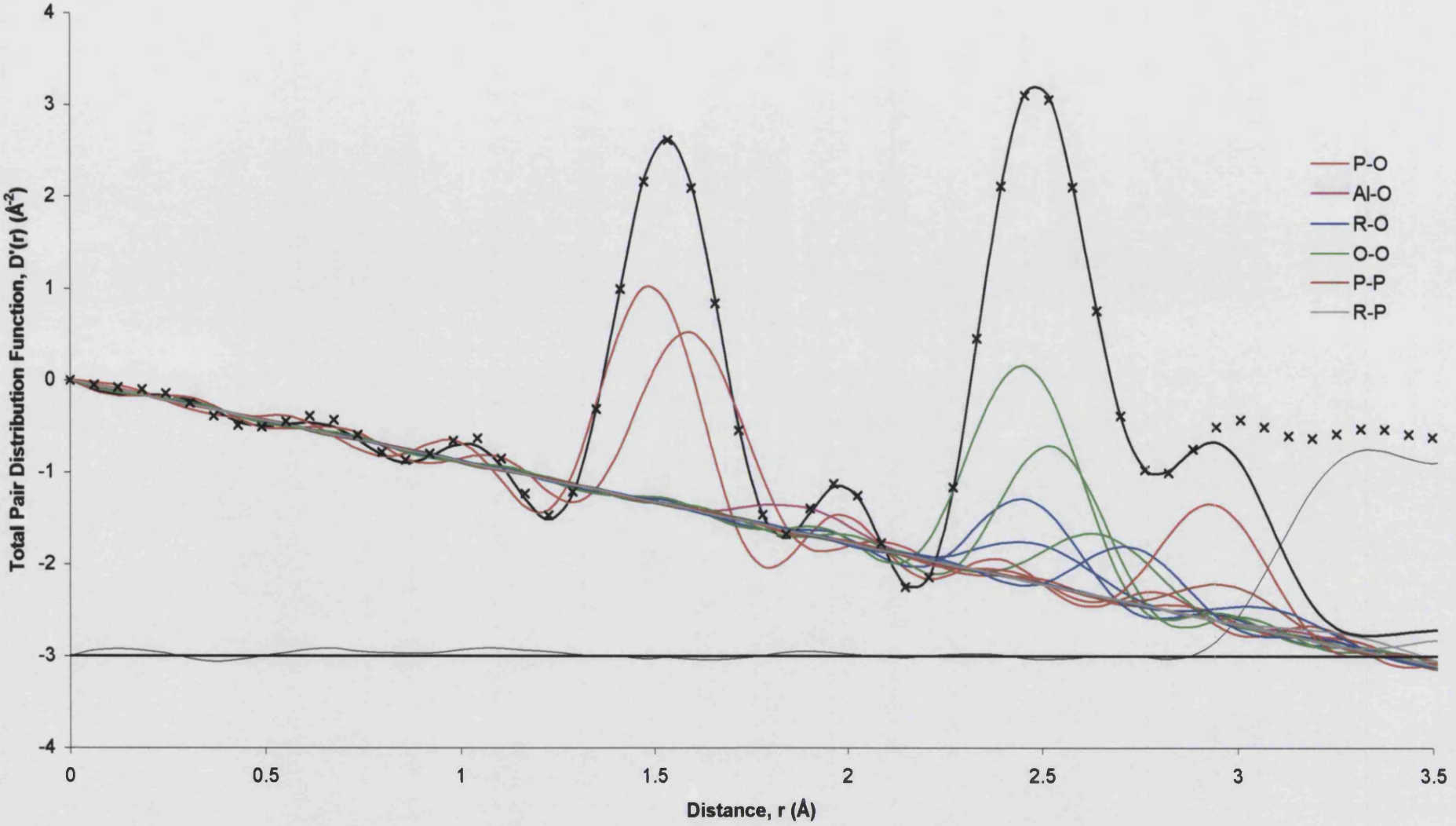

Figure 6.14. The total pair distribution function D'(r) (crosses), the modelled data given by the sum of the Gaussians convoluted with the modification function M(r) (solid curve) and the residual offset by -3 barn (feint curve) for LaB.

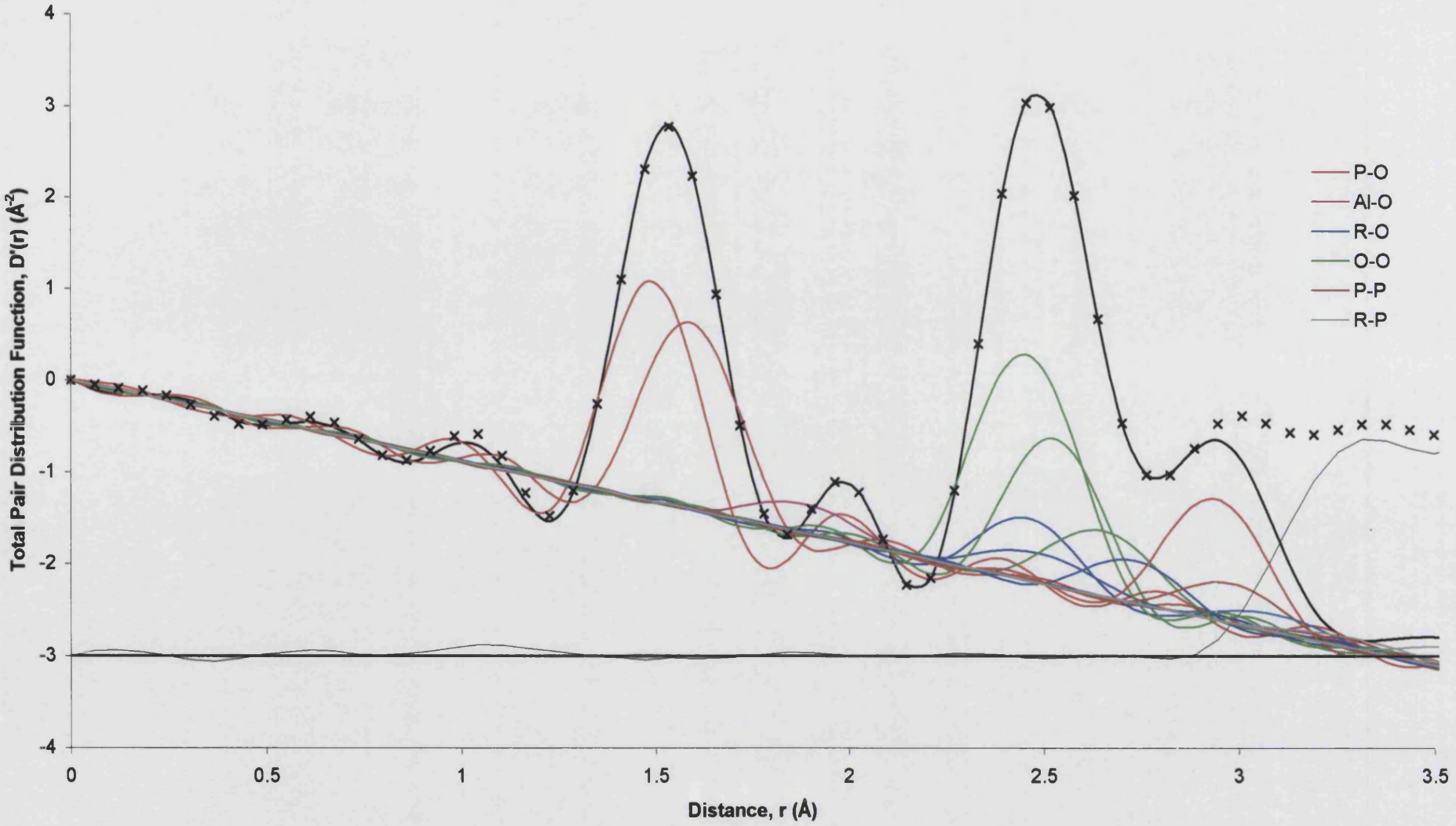

Figure 6.15. The total pair distribution function D'(r) (crosses), the fitted data given by the sum of the Gaussians convoluted with the modification function M(r) (solid curve) and the residual offset by -3 barn (feint curve) for LaCeF -D4C.

	LaB (D4C)			LaCeF (D4C)		
	r (Å)	C_N	σ (Å)	r (Å)	C_N	σ (Å)
P-O_T	1.490 (10)	1.95 (10)	0.045 (5)	1.490 (10)	1.90 (10)	0.045 (5)
P-O_B	1.595 (10)	2.10 (10)	0.090 (5)	1.590 (10)	2.10 (10)	0.090 (5)
Al-O	1.88 (3)	6.0 (5)	0.105 (9)	1.88 (3)	5.5 (5)	0.105 (9)
R-O	2.460 (10)	2.60 (10)	0.070 (10)	2.460 (10)	2.60 (10)	0.070 (10)
R-O	2.485 (9)	1.70 (10)	0.122 (9)	2.485 (9)	1.70 (10)	0.122 (9)
O-(P)-O	2.455 (9)	2.50 (10)	0.110 (10)	2.455 (9)	2.50 (10)	0.110 (10)
O-(P)-O	2.525 (9)	1.45 (9)	0.085 (9)	2.525 (9)	1.45 (9)	0.085 (9)
O-(Al)-O	2.65 (1)	0.80 (10)	0.115 (9)	2.65 (1)	0.80 (10)	0.115 (9)
R-O	2.73 (1)	2.05 (9)	0.078 (9)	2.73 (1)	2.05 (9)	0.078 (9)
P-O	2.94 (2)	2.67 (9)	0.10 (1)	2.94 (2)	2.67 (9)	0.10 (1)
P-P	2.98 (2)	2.0 (1)	0.10 (1)	2.98 (2)	2.0 (1)	0.10 (1)
R-O	3.09 (2)	1.1 (1)	0.10 (1)	3.09 (2)	1.1 (1)	0.10 (1)
R-P	3.30 (5)	1.0 (2)	0.145 (9)	3.30 (5)	1.0 (2)	0.145 (9)
R-P	3.58 (5)	2.0 (2)	0.115 (9)	3.58 (5)	2.0 (2)	0.115 (9)
R-P	3.75 (5)	2.0 (2)	0.13 (1)	3.75 (5)	2.0 (2)	0.13 (1)
R-P	3.85 (5)	2.0 (2)	0.13 (1)	3.85 (5)	2.0 (2)	0.13 (1)

Table 6.8. A summary of the Gaussian parameters used to model the total pair distribution function D′(r) for the LaB and LaCeF glasses.

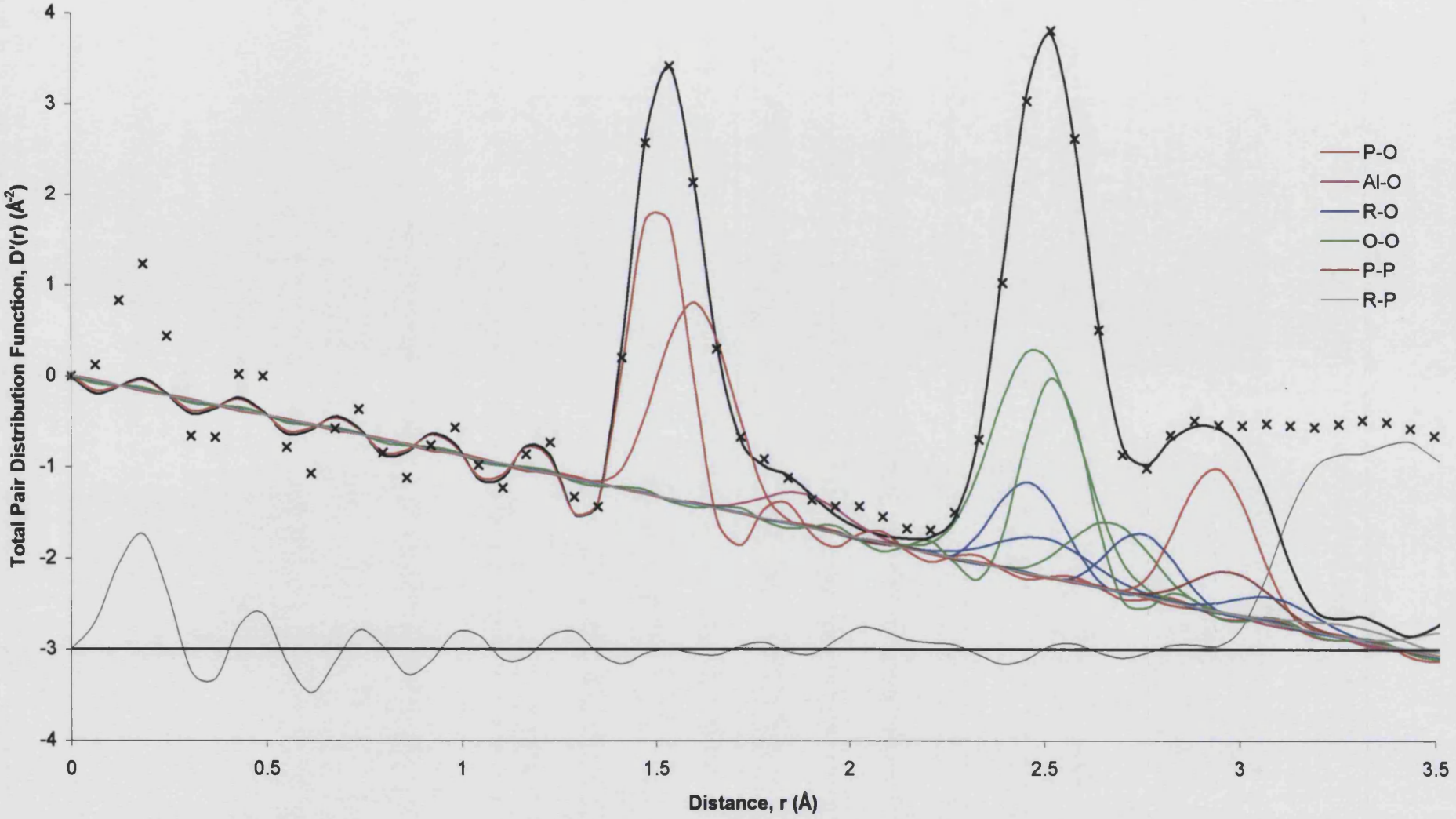

Figure 6.16. The total pair distribution function D'(r) (crosses), the fitted data given by the sum of the Gaussians convoluted with the modification function M(r) (solid curve) and the residual offset by -3 barn (feint curve) for LaA - GLAD.

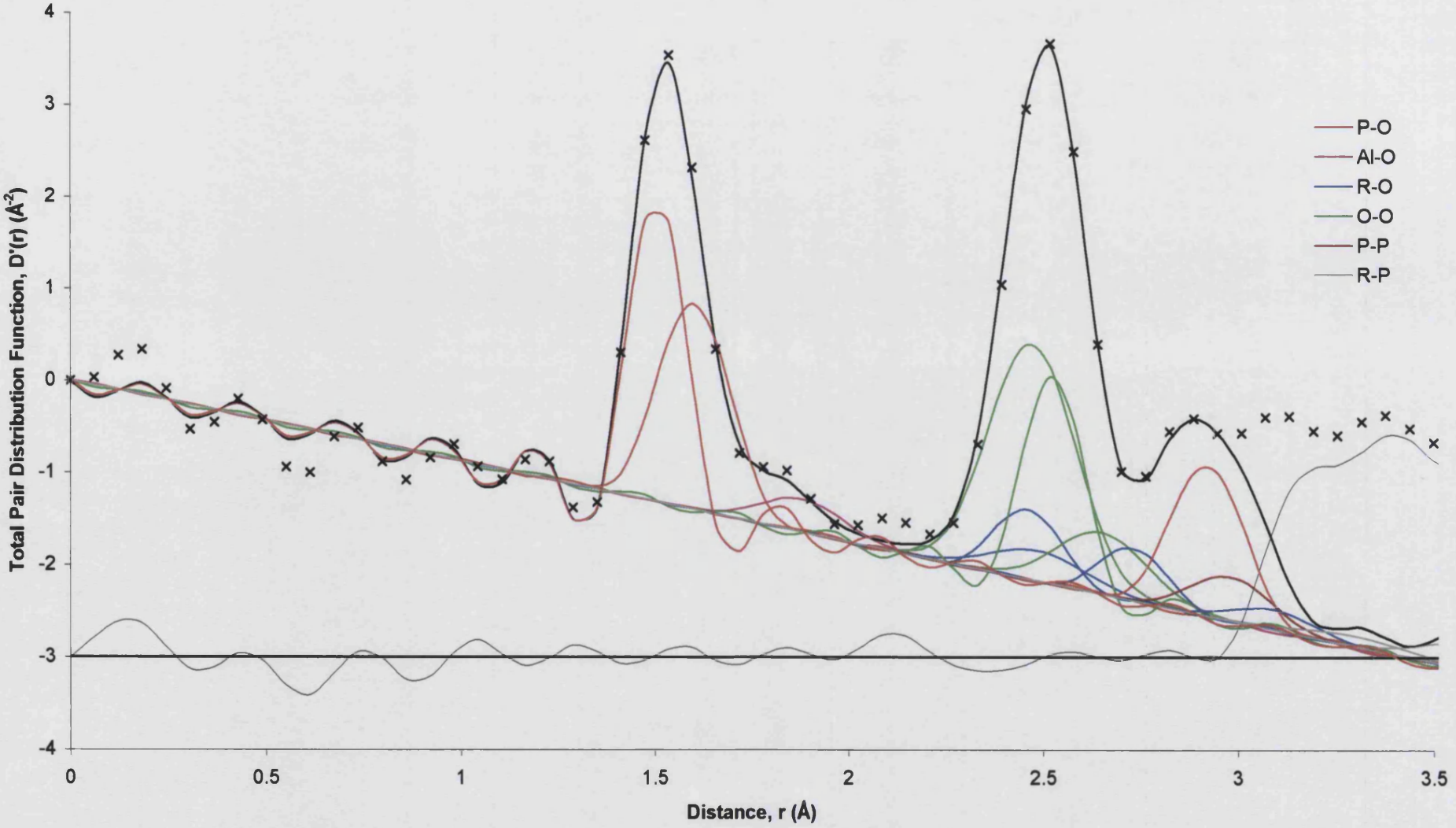

Figure 6.17. The total pair distribution function D'(r) (crosses), the fitted data given by the sum of the Gaussians convoluted with the modification function M(r) (solid curve) and the residual offset by -3 barn (feint curve) for LaCeF GLAD.

	LaA (GLAD)			LaCeF (GLAD)		
	r (Å)	C_N	σ (Å)	r (Å)	C_N	σ (Å)
P-O_T	1.505 (9)	1.85 (15)	0.045 (5)	1.505 (9)	1.85 (0.15)	0.045 (5)
P-O_B	1.600 (10)	2.00 (10)	0.090 (5)	1.600 (10)	2.00 (10)	0.090 (5)
Al-O	1.88 (3)	6.0 (5)	0.105 (9)	1.88 (3)	5.5 (5)	0.105 (9)
R-O	2.46 (1)	2.6 (1)	0.080 (10)	2.46 (1)	2.6 (1)	0.08 (1)
R-O	2.495 (9)	1.6 (1)	0.122 (9)	2.485 (9)	1.6 (1)	0.122 (9)
O-(P)-O	2.48 (1)	2.4 (1)	0.11 (1)	2.47 (1)	2.4 (1)	0.11 (1)
O-(P)-O	2.525 (9)	1.35 (9)	0.06 (1)	2.525 (9)	1.35 (9)	0.06 (1)
O-(Al)-O	2.67 (1)	0.7 (1)	0.10 (1)	2.65 (1)	0.7 (1)	0.115 (9)
R-O	2.75 (1)	1.95 (9)	0.078 (9)	2.73 (1)	2.05 (9)	0.078 (9)
P-O	2.94 (2)	2.6 (1)	0.09 (1)	2.92 (2)	2.67 (9)	0.09 (1)
P-P	2.98 (2)	2.0 (1)	0.10 (1)	2.98 (2)	2.0 (1)	0.10 (1)
R-O	3.09 (2)	1.1 (1)	0.10 (1)	3.09 (2)	1.1 (1)	0.10 (1)
R-P	3.30 (5)	1.0 (2)	0.145 (9)	3.30 (5)	1.0 (1)	0.145 (9)
R-P	3.58 (5)	2.0 (2)	0.115 (9)	3.58 (5)	2.0 (2)	0.115 (9)
R-P	3.75 (5)	2.0 (2)	0.13 (1)	3.75 (5)	2.0 (2)	0.13 (1)
R-P	3.85 (5)	2.0 (2)	0.13 (1)	3.85 (5)	2.0 (2)	0.13 (1)

Table 6.9. A summary of the Gaussian parameters used to model the total pair distribution function D′(r) for the LaA and LaCeF glasses.

6.7. DISCUSSION.

The present results represent the first difference functions obtained for rare earth phosphate glasses allowing unprecedented information to be obtained on the O-(Al)-O correlations and the splitting of the O-(P)-O and R-O correlation. Furthermore the data were for the first time analysed taking into explicit consideration the impurity correlations that result from the Al which is incorporated when phosphate glasses are prepared using the method outlined in Chapter 2. This is important because the majority of glasses listed in Table 6.1 were made using alumina crucibles but no account was taken of either the Al content or its effect on the structure. A fully quantitative comparison of the present results with those for other rare earth phosphate glasses is hampered in this respect and is also made difficult because the quoted R:P:O ratios are often different (see Table 6.1).

The nearest neighbour R-O correlations are asymmetric and are best represented using four separate peaks (Figure 6.12). Previous studies on amorphous samples have by and large been unable to resolve the R-O peak due to its overlap with the O-(P)-O correlations. Most of the analyses have assumed that the R-O correlations can be represented by a single Gaussian. The total R-O coordination number of 7.25 - 7.45 obtained in the present work is consistent with the EXAFS results of Anderson *et al* (1998, 1999) for lanthanum phosphate glasses. However, this is probably fortuitous as the nearest neighbour R-O correlations were represented by a single Gaussian and in other studies the R-O coordination number is usually underestimated (Table 6.1). For example, coordination numbers of 4.8, 5.2, 5.8 and 6.5 have been reported for glassy $(Ce_2O_3)_{0.235}(P_2O_5)_{0.765}$ (see Table 6.1). Since the R-O and O-(P)-O peaks occupy the same real space region, it is possible to over estimate the O-(P)-O coordination number at the expense of the R-O coordination number or vice versa. However, this does not appear to be the case for glassy $(Ce_2O_3)_{0.235}(P_2O_5)_{0.765}$. For example, Cole *et al* (2001b) reported an O-(P)-O coordination number of 4.7 and an R-O coordination number of 6.5, whereas in a previous publication Cole *et al* (1999) reported an O-(P)-O coordination number of 3.4 and an R-O coordination number of 5.8. The effectiveness of the data normalisation in these studies is therefore questionable.

It is notable that for the present glasses, the total coordination number of the first three R-O peaks in the region $2.3 \leq r$ (Å) ≤ 2.9 Å is $\approx 6.3(3)$ which is consistent with the total C_N values given by Hoppe *et al* (2001, 2002), Karabulut *et al* (2002) and Cole *et al* (2001b) (the latter obtain an average of 6.5 ± 0.6). This implies that previous studies have correctly reported the R-O C_N in the region $2.3 \leq r$ (Å) ≤ 2.9 but were unable to account for the full extent of the nearest neighbour R-O correlations due to the limitations of modelling with a single symmetric peak. Hoppe *et al* (1998a) have reported that a better fit to their diffraction data for La^{3+} and Nd^{3+} based glasses is however obtained upon splitting the R-O peak to give an asymmetric distribution of nearest neighbour correlations as found in this study.

The nearest neighbour R-P correlations in the present work were modelled using four Gaussians having coordination numbers of 1, 2, 2, 2, as found in crystalline LaP_3O_9 (Matuszewski *et al* 1988). The position of the first Gaussian is at 3.30(2) Å and the second is at 3.58(2) Å and $\Delta D'_R(r)$ is satisfactorily modelled by these peaks in the region $3.3 \leq r$ (Å) ≤ 3.7 Å. The present results contrast with those found previously (see Table 6.1). For example, in the EXAFS study of Bowron *et al* (1996a) an R-P nearest neighbour distance of 2.92, 2.92, 3.64 and 3.23 Å was reported for the large R^{3+} ions Pr^{3+}, Nd^{3+}, Eu^{3+} and Gd^{3+} respectively with corresponding coordination numbers of 1.4(2), 6.8(16.6), 1.6(8) and 1.3(3). The nearest neighbour R-P distance for Pr^{3+} and Nd^{3+} is therefore much too short. The R-P correlations are characterised by a broad distribution of nearest neighbour distances as shown in Figure 6.12; hence previous modelling of the R-P correlations was severely limited by the use of a single Gaussian peak.

The peak positions and coordination numbers used to model the nearest neighbour P-O_B and P-O_T correlations in the present work are in agreement with the values for rare earth phosphate glasses previously reported (Table 6.1). The peak width for the P-O_T Gaussian is in good agreement with the values given in Table 6.1. However, the P-O_B peak width is slightly broader than that previously reported for the glassy phase but still lies within the quoted errors; see Cole *et al* (1999), Hoppe *et al* (2001). To date only neutron diffraction experiments have been able to resolve the P-O_B and P-O_T correlations by use of an extended Q-space measurement range. The available x-ray data was unable to resolve the P-O_B and P-O_T correlations, hence only

mean P-O values were given. The mean P-O positions and total coordination numbers previously reported (Table 6.1) are, however, in agreement with the present work. The EXAFS and XANES data are taken for the K, L_I and L_{III} absorption edges of the rare earth ions and are not therefore sensitive to P-O correlations.

The O-(P)-O correlations for the present data sets were modelled using two O-(P)-O Gaussian peaks. Previous studies on amorphous samples have been unable to resolve the splitting of the O-(P)-O peaks due to the overlapping R-O correlations. The total experimental O-(P)-O C_N values of 3.75(20) - 3.95(20) are consistent with the calculated value of 3.85, obtained using the phosphate network model of Hoppe (1996) as described in section 6.2. The experimental O-(P)-O C_N values of Hoppe (1998a, 2001, 2002) are in agreement with the values calculated using this model and are in good agreement with the present work. By contrast, Cole *et al* (2001b) have reported O-(P)-O C_N values between 4.7 and 7.3 whereas the model predicts values of $\approx$ 4.0. These experimental results are outside the margins of error for the $\bar{n}_O^O$ values expected on the basis of the phosphate network model (Hoppe 1996) which gives coordination numbers of 4.0, 4.29 and 4.8 for meta-phosphates, ultra-phosphates and P_2O_5 respectively.

An O-(P)-O C_N greater than 4.0 can be explained in part since Cole *et al* (2001b) neglected the O-(Al)-O correlations which occur in the same real space region as shown in Figures 6.12-6.17, Nevertheless C_N values above 5.0 cannot be justified even allowing for this influence as insufficient Al is likely to be present. For example, the estimated O-(P)-O C_N for $(Eu_2O_3)_{0.252}(P_2O_5)_{0.748}$ is 3.99. Therefore to achieve a total O-O C_N of 7.3, the O-(Al)-O C_N would have to be 3.3. Equation 6.2 was derived on the basis that Al is octahedrally rather than tetrahedrally coordinated by oxygen and therefore gives a maximum O-(Al)-O first nearest neighbour coordination number. By using this equation the Al atomic fraction was estimated to be c_{Al} = 0.10 a value that is significantly higher than the maximum value of c_{Al} = 0.035 found in any of the present work on rare earth phosphate glasses (Chapters 3, 6 and 7) in which the Al content was quantified. This suggests that the O-(P)-O C_N value reported by Cole *et al* (2001b) is significantly too large. Hence it is concluded that these values are non-physical and represent a serious limitation of the modelling

procedure previously applied to the total pair distribution functions which contain many overlapping correlations. By contrast, in the neutron diffraction work of Cole *et al* (1999) experimental O-(P)-O C_N values of 3.4 and 3.3 were reported for Ce^{3+} and Nd^{3+} based phosphate glasses. These appear to be underestimates (see Table 6.1) since values of 4.0 – 4.2 are expected using the phosphate network model (Hoppe 1996).

The data for the present work are best modelled using an Al-O distance of 1.88 Å, consistent with there being a large number of Al centred octahedra, as opposed to the distance of 1.73 Å expected for Al centred tetrahedra. However, the Al-O coordination numbers varied between 4.5 and 6.0 depending on the function being modelled suggesting a range of Al environments in agreement with the recent NMR studies. The O-(Al)-O coordination number in the fitting procedure was constrained at a value 0.7-0.8 consistent with the majority of Al atoms being in an octahedral environment (see section 6.3). The modelled O-(P)-O coordination numbers of 3.75 - 3.95 are therefore likely to be under-estimates. For example, if the Al was 50% octahedrally coordinated and 50% tetrahedrally coordinated then the estimated O-(Al)-O C_N would be 0.4 at a distance $\sqrt{2}\ r_{O-Al}$ = 2.66 Å and 0.2 at a distance $\sqrt{8/3}\ r_{O-Al}$ = 2.833 Å as opposed to 0.8 at a distance $\sqrt{2}\ r_{O-Al}$ = 2.66 Å. A reasonable amount of overlap exists for these two O-(Al)-O correlations such that the overall first nearest neighbour O-(Al)-O C_N of 0.8 will be reduced by $\approx$ 0.3. Therefore to compensate, the fitted O-(P)-O C_N would have to be increased by the same amount i.e. from values of 3.75-3.95 to 4.05-4.15. On the basis of the phosphate network model of Hoppe (1996) an O-(P)-O C_N of 3.85(4) is expected for these glasses. This suggests that the phosphate network model underestimates the number of O_B atoms in the present glasses: the O_T and O_B atoms have O-O coordination numbers of 3 and 6 respectively (see section 6.2). This is consistent with the presence of Al impurities strengthening the glassy network. Compared to R-P-O glasses, those containing Al are less brittle and can be drawn into fibres (see Chapter 2 and Chapter 9).

6.8. CONCLUSIONS.

The total structure factors of lanthanum and cerium phosphate glasses were measured using neutron diffraction. The first order difference and total minus weighted difference functions were obtained by combining the total structure factors. The difference functions and the total structure factors can be modelled self-consistently, using the same Gaussian input parameters (distance, coordination number and peak width), confirming that the method of isomorphic substitution is valid at the difference function level of the present results. The overall validity of the results was checked by modelling the total structure factor measured for a different sample using a different diffractometer, GLAD. Unprecedented information on the structure of rare earth phosphate glasses thus obtained, allowed the O-O and R-O correlations to be resolved unambiguously.

The P-O bond distances and coordination numbers are in agreement with previous work confirming that the glass network is made from PO_4 tetradedra.

The Al-O correlations were explicitly modelled and the distance and coordination numbers were found to be consistent with a large proportion of Al being octahedrally coordinated. This is important as it enabled the O-(Al)-O peak position and coordination number to be extracted. Since the O-(Al)-O correlations appear in the same real space region as O-(P)-O correlations, information on the O-(Al)-O correlations allowed the O-(P)-O correlations to be modelled with greater accuracy.

Information on the connectivity of the network is provided by the O-(P)-O coordination number. The measured values of 3.95(14) and 3.75(14), for the glasses measured using D4C and GLAD respectively, are in agreement with a value of 3.85(4) calculated using the phosphate network model (Hoppe 1996). This is consistent with the experimental results presented by Hoppe *et al* (1998a, 2001, 2002) but not the results presented by Cole *et al* (1999, 2001b). The O-(P)-O coordination number indicates that the O_T : O_B ratio is 0.68 - 0.75 which compares with a value of 0.72(2) calculated using the phosphate network model (Hoppe 1996) and a value of 0.67 for pure meta-phosphates.

The R-O coordination number is consistent with that found in crystalline La meta-phosphate but the correlations are more asymmetrically distributed. A range of R-O distances has been suggested in the work of Hoppe (2001, 2002). However this study was made at the total structure factor level where the overlap of correlations made this assignment ambiguous. Use of the first order difference function enabled the additional R-O correlations, for $r > 3.0$ Å to be modelled, resulting in a total coordination number greater than previously reported and more inline with the crystalline values.

REFERENCES

Anderson R, Brennan T, Mountjoy G, Newport R.J and Saunders G.A. 1998. *Journal of Non-Crystalline Solids.* **232-234**. p. 286.

Anderson R, Brennan T, Cole J.M, Mountjoy G, Pickup D.M, Newport R.J and Saunders G.A. 1999. *Journal of Materials Research.* **14**. (12) p. 4706.

Arbib E.H, Elouadi B, Chaminade J.P and Darriet D. 1996. *Journal of Solid State Chemistry.* **127**. p. 350.

Bowron D.T, Newport R.J. Rainford R.D, Saunders G.A and Senin H.B. 1996a. *Physical Review B.* **53**. (9) p. 5268.

Bowron D.T, Bushnell-Wye G, Newport R.J. Rainford R.D and Saunders G.A. 1996b. *Journal of Physical: Condensed Matter.* **8**. p. 3337.

Cole J.M, van Eck E.R.H, Mountjoy G, Newport R.J, Brennan T and Saunders G.A. 1999. *Journal of Physics: Condensed Matter.* **11**. p. 9165.

Cole J.M, Lees M.R, Howard J.A.K, Newport R.J, Saunders G.A and Schonherr E. 2000. *Journal of Solid State Chemistry.* **150**. p. 377.

Cole J.M, Newport R.J, Bowron D.T, Pettifer R.F, Mountjoy G, Brennan T and Saunders G.A. 2001a. *Journal of Physics Condensed Matter.* **13**. p. 6659.

Cole J.M, van Eck E.R.H, Mountjoy G, Anderon R, Brennan T, Bushenell-Wye G, Newport R.J, and Saunders G.A. 2001b. *Journal of Physics: Condensed Matter.* **13**. p. 4105.

Hong H.Y.P. Acta *Crystallographic.* 1974a. **B30**. p. 468.

Hong H.Y.P. Acta *Crystallographic.* 1974b. **B30**. p. 1857.

Hoppe U. *Journal of Non-Crystalline Solids.* 1996. **195**. p.138.

Hoppe U, Kranold R, Stachel D, Barz A and Hannon A.C. 1998a. *Journal of Non-Crystalline Solids.* **232-234**. p. 44.

Hoppe U, Walter G, Kranold R and Stachel D. 1998b. *Zeitschrift fur Naturforschung.* **53a**. p. 93.

Hoppe U, Ebendorff-Heidepriem H, Neuefeind J and Bowron D. Zeitschrift fur Naturforschung. 2001. **56a**. p. 237.

Hoppe U, Metwalli E, Brow R.K and Neuefeind J. 2002. *Journal of Non-Crystalline Solids.* **297**. p. 263.

Hughes J.M and Mariano A.N 1995. *American Mineralogist.* **80**. p. 21.

Karabulut M, Metwalli E and Brow R.K. 2001. *Journal of Non-Crystalline Solids.* **283**. p. 211.

Karabulut M, Marasinghe G.K, Metwalli E, Wittenauer A.K and Brow R.K. 2002. *Physical Review B.* **65**. p. 104206.

Mountjoy G, Cole J.M, Brennan T, Newport R.J, Saunders G.A and Wallidge G.W. 2001. Journal of *Non-Crystalline Solids.* **279**. p. 20.

Matuszewski J, Kropiwnicka J and Znamierowska 1988. T. *Journal of Solid State Chemistry.* **75**. p. 285.

Mullica D.F, Milligan W.O, Grossie D.A, Beall G.W and Boatner L.A. 1984. *Inorganica Chimica Acta.* **95**. p. 231.

Pettifor D.G. 1986. *Journal of Physics C: Solid State Physics.* **19**. p. 285

Sears V.F. 1992. *Neutron News.* **3**. p. 26.

Shannon R.D. 1976. *Acta Crystallographic.* **A32**. p. 751.

Sowa H, Macavei J and Schulz H. 1990. *Zeitschrift fur Kristallographie.* **192**. p. 119.

Stachel D. 1995. *Acta Crystallographic.* **C51**. p. 1049.

Van der Meer H. 1976. Acta *Crystallographic.* **B32**. p. 2423.

Wasse J.C and Salmon P.S. 1999. *Journal of Physics; Condensed Matter.* **11**. p. 1381.

Wasse J.C, Salmon P.S and Delaplane R.G. 2000. *Journal of Physics; Condensed Matter.* **12**. p. 9539.

CHAPTER 7
THE STRUCTURE OF DYSPROSIUM AND HOLMIUM PHOSPHATE GLASSES USING ISOMORPHIC SUBSTITUTION IN NEUTRON DIFFRACTION.

7.1 INTRODUCTION

The object of this chapter is to employ the method of isomorphic substitution in neutron diffraction to measure the second order difference function $g_{RR}(r)$ and hence separate the remaining correlations into difference functions that involve either R-μ or μ-μ. The method has recently been successfully employed to study the structure of several molten trivalent rare-earth halides (Wasse and Salmon 1999, Wasse *et al* 2000) and other rare earth phosphate glasses containing large rare earth ions (Chapter 6). The experiments will focus on R-P-O-Al glasses of very similar compositions which comprise Dy^{3+} or Ho^{3+} that are at the small cation radius end of the rare earth series. Isomorphism is anticipated from the comparable radii of Dy^{3+} (0.912 Å) and Ho^{3+} (0.901 Å) (reported for six fold coordinated ions – see Shannon 1976) and their similar Pettifor (1986) chemical parameters χ(Dy) = 0.685 and χ(Ho) = 0.6825. Unlike previous studies of phosphate glasses comparing small rare earth ions (Table 7.1) the role of the Al impurities in the glass structure will be taken into explicit account.

As described in section 6.1, the structure of rare earth phosphate glasses prepared using alumina crucibles presents a challenging experimental task as the glasses comprise four chemical species and are described by ten overlapping $g_{\alpha\beta}(r)$. Thus, although a battery of techniques have been applied to investigate the structure of rare-earth phosphate glasses, significant differences in the structural parameters have been reported (see Table 7.1). Existing data is, however, unreliable e.g. in studies of $(Tb_2O_3)_{0.263}(P_2O_5)_{0.737}$ the O-(P)-O coordination number is reported to be 3.4(3) or 4.8(8) and the R-O coordination number varies between 5.8(2) and 8.0(2) (Table 7.1).

Reference	Sample		ratios			calculated	P-O_T			P-O_B			O-(P)-O			R-O			P-(OH)-O			P-P			R-P		
			R :	P :	O	O-O C_N	r (Å)	C_N	σ (Å)	r (Å)	C_N	σ (Å)	r (Å)	C_N	σ (Å)	r (Å)	C_N	σ (Å)	r (Å)	C_N	σ (Å)	r (Å)	C_N	σ (Å)	r (Å)	C_N	σ (Å)
Anderson *et al* 1999	$(Tb_2O_3)_{0.263}(P_2O_5)_{0.737}$	EXAFS	1.00	2.80	8.51	3.95	-	-	-	-	-	-	-	-	-	2.267(1)	5.8(2)	0.09(2)	-	-	-	-	-	-	-	-	-
Bowron *et al* 1995	$(Tb_2O_3)_{0.26}(P_2O_5)_{0.74}$	X-ray	1.00	2.85	8.62	3.96	mean P-O distance 1.58(5)									mean R-O and O-(P)-O distance 2.34(5)			-	-	-	-	-	-	-	-	-
Bowron *et al* 1995	$(Tb_2O_3)_{0.26}(P_2O_5)_{0.74}$	EXAFS	1.00	2.85	8.62	3.96	-	-	-	-	-	-	-	-	-	2.250(2)	7.0(2)	0.08(1)	-	-	-	-	-	-	-	-	-
Bowron *et al* 1996(a)	$(Tb_2O_3)_{0.26}(P_2O_5)_{0.74}$	EXAFS	1.00	2.85	8.62	3.96	-	-	-	-	-	-	-	-	-	2.250(2)	8.0(2)	0.08(1)	-	-	-	-	-	-	-	-	-
Bowron *et al* 1996(b)	$(Tb_2O_3)_{0.26}(P_2O_5)_{0.74}$	x-ray	1.00	2.85	8.62	3.96	mean P-O distance 1.58(5)									mean R-O and O-(P)-O distance 2.34(5)			-	-	-	-	-	-	-	-	-
Cole *et al* 1999	$(Tb_2O_3)_{0.263}(P_2O_5)_{0.737}$	Neutron	1.00	2.80	8.51	3.95	1.49(1)	1.7(4)	0.04(3)	1.60(1)	1.9(4)	0.08(3)	2.50(1)	3.4(3)	0.09(4)	2.27(2)	5.8(6)	0.12(4)	2.86(3)	5.1(5)	0.16(7)	3.00(4)	2.0(9)	0.09(4)	-	-	-
Cole *et al* 2001(b)	$(Tb_2O_3)_{0.263}(P_2O_5)_{0.737}$	X-ray	1.00	2.80	8.51	3.95	mean P-O; r (Å) = 1.56(1), C_N = 3.8(3), σ (Å) = 0.04(3)						2.58(3)	4.8(8)	0.04(5)	2.32(2)	6.6(6)	0.10(4)	-	-	-	2.96(4)	4.1(1.3)	0.09(6)	3.65(1)	9.7(2.6)	0.17(5)
Anderson *et al* 1999	$(Dy_2O_3)_{0.225}(P_2O_5)_{0.775}$	EXAFS	1.00	3.44	10.11	4.09	-	-	-	-	-	-	-	-	-	2.22(1)	5.5(3)	0.08(3)	-	-	-	-	-	-	-	-	-
Cole *et al* 2001(a)	$(Dy_2O_3)_{0.225}(P_2O_5)_{0.775}$	EXAFS	1.00	3.44	10.11	4.09	-	-	-	-	-	-	-	-	-	2.270(7)	5.7(7)	0.08(3)	-	-	-	-	-	-	-	-	-
Cole *et al* 2001(b)	$(Dy_2O_3)_{0.225}(P_2O_5)_{0.775}$	X-ray	1.00	3.44	10.11	4.09	mean P-O; r (Å) = 1.57(1), C_N = 3.5(4), σ (Å) = 0.05(4)						2.61(2)	4.9(7)	0.08(5)	2.26(1)	6.5(5)	0.09(4)				3.00(3)	3.6(12)	0.08(5)	3.60(1)	9.6(2.4)	0.16(5)
													mean O-(P)-O and total C_N			mean R-O and total C_N									mean R-P and total C_N		
present work	$Dy_{0.072}P_{0.2083}O_{0.7013}Al_{0.0181}$	neutron	1.00	2.88	9.70	3.56	1.495(10)	2.05(10)	0.050(5)	1.585(10)	2.10(10)	0.085(5)	2.48	3.60	-	2.32	6.7(2)	-	2.94(1)	4.0(1)	0.130(10)	2.98(2)	2.0(1)	0.100(10)	3.55	7.00(14)	-
	$Dy_{0.0378}Ho_{0.0356}P_{0.2080}O_{0.6986}Al_{0.0184}$		1.00	2.84	9.48	3.59	1.495(10)	2.05(10)	0.055(5)	1.585(10)	2.10(10)	0.085(5)	2.49	3.60	-	2.32	6.7(2)	-	2.94(1)	4.0(1)	0.130(10)	2.98(2)	2.0(1)	0.100(10)	3.55	7.00(14)	-
	$Ho_{0.0748}P_{0.2065}O_{0.7012}Al_{0.0186}$		1.00	2.77	9.40	3.53	1.495(10)	2.05(10)	0.050(5)	1.590(10)	2.10(10)	0.090(5)	2.48	3.65	-	2.32	6.7(2)	-	2.94(1)	4.0(1)	0.130(10)	2.98(2)	2.0(1)	0.100(10)	3.55	7.00(14)	-
Anderson *et al* 1999	$(Ho_2O_3)_{0.231}(P_2O_5)_{0.769}$	EXAFS	1.00	3.33	9.82	4.07	-	-	-	-	-	-	-	-	-	2.228(2)	5.8(4)	0.08(3)	-	-	-	-	-	-	3.12(6)	-	-
Bowron *et al* 1996(a)	$(Ho_2O_3)_{0.231}(P_2O_5)_{0.769}$	EXAFS	1.00	3.33	9.82	4.07	-	-	-	-	-	-	-	-	-	2.200(1)	7.0(1)	0.10(1)	-	-	-	-	-	-	-	-	-
Cole *et al* 2001(b)	$(Ho_2O_3)_{0.231}(P_2O_5)_{0.769}$	X-ray	1.00	3.33	9.82	4.07	mean P-O; r (Å) = 1.55(1), C_N = 3.9(3), σ (Å) = 0.03(3)						2.55(2)	5.9(7)	0.07(5)	2.24(1)	5.8(5)	0.08(4)				2.98(3)	3.4(12)	0.08(5)	3.59(1)	8.7(2.2)	0.15(5)
Anderson *et al* 1999	$(Er_2O_3)_{0.239}(P_2O_5)_{0.761}$	EXAFS	1.00	3.18	9.46	4.04	-	-	-	-	-	-	-	-	-	2.225(5)	5.7(4)	0.07(3)	-	-	-	-	-	-	-	-	-
Cole *et al* 2001(a)	$(Er_2O_3)_{0.239}(P_2O_5)_{0.761}$	EXAFS	1.00	3.18	9.46	4.04	-	-	-	-	-	-	-	-	-	2.234(7)	6.3(7)	0.09(3)	-	-	-	-	-	-	-	-	-
Cole *et al* 2001(b)	$(Er_2O_3)_{0.239}(P_2O_5)_{0.761}$	X-ray	1.00	3.18	9.46	4.04	mean P-O; r (Å) = 1.55(1), C_N = 3.9(4), σ (Å) = 0.05(4)						2.58(2)	4.9(8)	0.09(5)	2.23(1)	6.6(5)	0.09(4)	-	-	-	2.97(3)	3.4(12)	0.10(5)	3.58(1)	8.9(2.2)	0.14(5)
Karabulut *et al* 2002	$(Er_2O_3)_{0.227}(P_2O_5)_{0.723}$	EXAFS	1.00	3.19	9.46	4.04										2.37(1)	6.4(9)	0.07(2)							3.87(3)	2.2(9)	0.08(3)

Table 7.1. A summary of the structural studies on rare earth phosphate glasses comprising small cations.

7.2 CRYSTAL STRUCTURE OF RARE EARTH PHOSPHATES

In order to understand the structure of rare earth phosphate glasses it is important to understand the structures of the crystalline phases. Smaller rare earth ions such as Yb^{3+} form monoclinic meta-phosphate crystals with a space group $P2_1/C$ and Z = 12 where the rare earth ion is surrounded by six oxygen nearest neighbours (Hong 1974) and monoclinic ultra-phosphates with a space group C2/c (No. 15) and Z = 8 where the rare earth ion is surrounded by eight oxygen nearest neighbours (Hong and Pierce 1974).

The skeletal structure of YbP_3O_9 is illustrated in Figures 7.1 and 7.2 (Hong 1974). Figure 7.1 illustrates an ab projection of the PO_4 tretrahedra and Figure 7.2 illustrates a bc projection showing how the PO_4 tretrahedra are connected to the Yb^{3+} ions and the arrangement of YbO_6 octahedra. The basic structural units are helical ribbons, $(PO_3)_n$, formed by neighbouring phosphate groups corner sharing a single oxygen atom. There is no sign of tetrahedra edge sharing two oxygen atoms. The ribbons run along the c axis and are joined to each other by Yb-O bonds. Each Yb^{3+} ion is coordinated with six O atoms to form slightly distorted octahedra that are isolated from each other with no O atom common to any two Yb atoms (Figure 7.2).

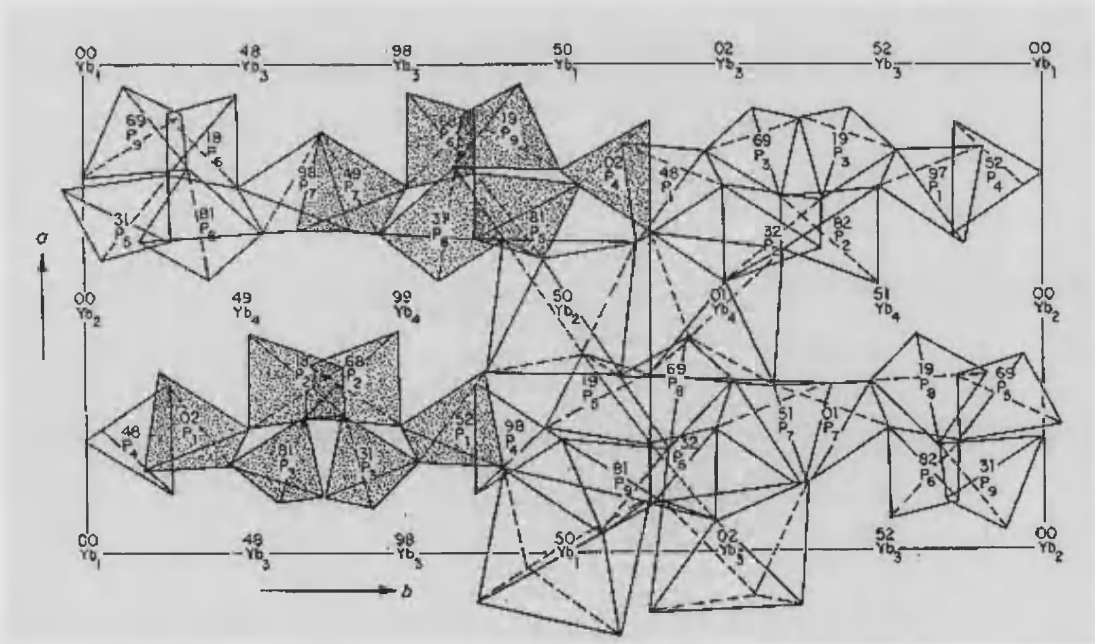

Figure 7.1. An ab projection of the arrangement of PO_4 tetrahedra and YbO_6 octahedra in YbP_3O_9. The octahedra are slightly distorted (Hong 1974).

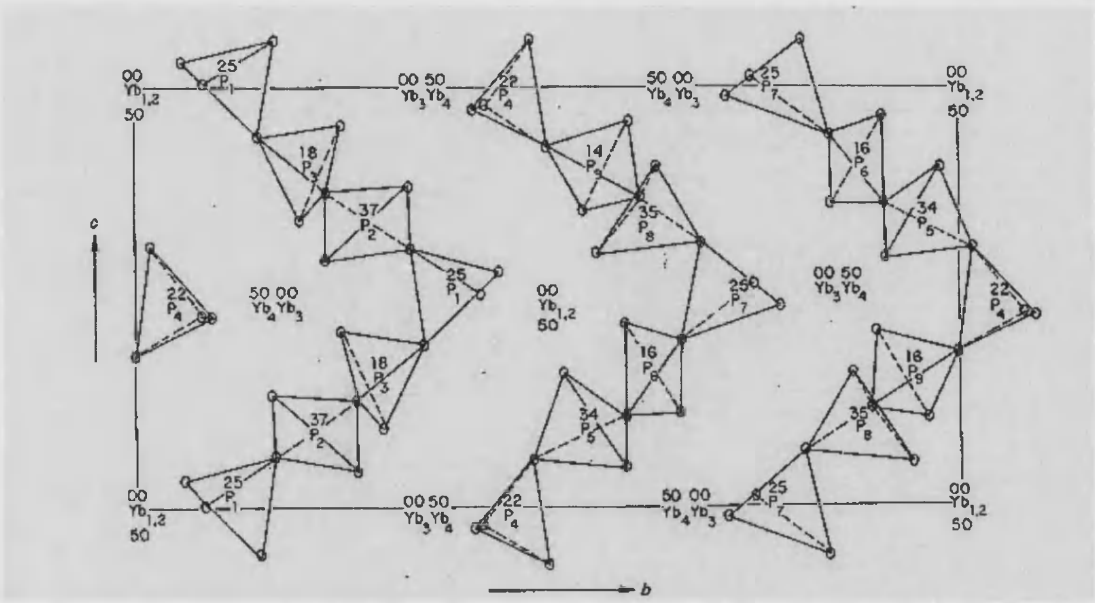

Figure 7.2. A bc projection of the arrangement of PO_4 tetrahedra in YbP_3O_9, showing the ribbons that run helically along the c axis (Hong 1974).

The skeletal structure of HoP_5O_{14} is illustrated in Figure 7.3 (Hong and Pierce 1974). Figure 7.3 illustrates an ab projection of the PO_4 tretrahedra showing how the PO_4 tretrahedra are connected to the Ho^{3+} ions and the arrangement of HoO_8 dodecahedra. The basic structural units are phosphate groups corner sharing a single oxygen atom. There is no sign of tetrahedra edge sharing two oxygen atoms. Each Ho^{3+} ion is coordinated with eight O atoms and no two rare earth ions share a common nearest neighbour oxygen (Figure 7.3).

In the meta-phosphate the $R:O_T$ ratio is 1:6 and the R-O coordination number is six and in the ultra-phosphate the $R:O_T$ ratio is 1:8 and the R-O coordination number is eight. Hence the rare earth ions form isolated octahedral or dodecahedra with no oxygen atom common to any two rare earth atoms.

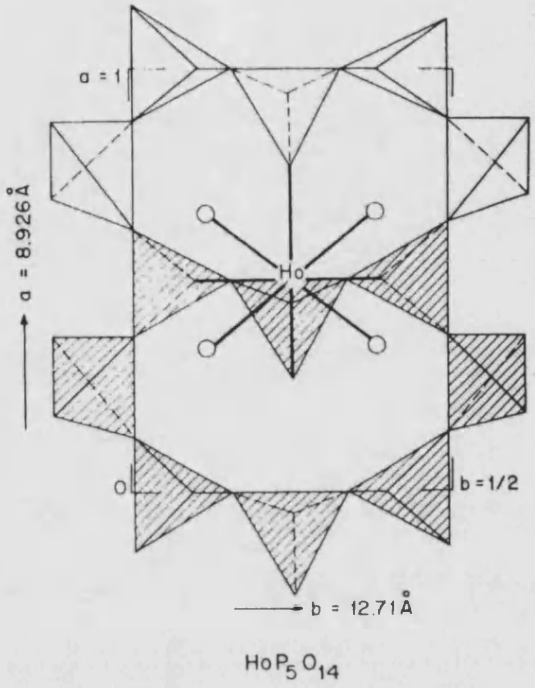

Figure 7.3. An ab projection showing the linkage of PO_4 tetrahedra in orthorhombic - III HoP_5O_{14} (Hong and Pierce 1974).

7.3 PREPARING THE GLASSY SAMPLES

The glasses were prepared using the method outlined in Chapter 2. As stated in this chapter it is not possible to prepare samples of an exact composition due to the phosphorus pentoxide losses that occur during the heating process and the leaching of Al into the glass from the crucibles. Therefore to ensure that the glasses used for the isomorphic substitution experiments were as near identical in composition as possible a series of glasses were prepared and characterised as shown in Table 7.2.

Glass	c_R (± 0.0002)	c_P (± 0.0002)	c_O (± 0.0002)	c_{Al} (± 0.0002)	ρ (g cm^{-3}) (± 0.01)
DyA	0.0723	0.2127	0.6961	0.0189	3.49
DyB	0.0745	0.2111	0.6939	0.0205	3.55
DyC	0.0723	0.2083	0.7013	0.0181	3.53
DyHoD	0.0747 c_{Dy} 0.0364 : c_{Ho} 0.0383	0.2033	0.7005	0.0215	3.64
DyHoE	0.0737 c_{Dy} 0.0378 : c_{Ho} 0.0359	0.2090	0.6989	0.0184	3.62
HoF	0.0794	0.1982	0.6984	0.0240	3.77
HoG	0.0746	0.2065	0.7012	0.0186	3.64
HoH	0.0789	0.19.98	0.6980	0.0234	3.72

Table 7.2. Compositions and densities of Dy/ Ho phosphate glasses.

The coefficients of $S_{\alpha\beta}(Q)$ in the total structure factors and difference functions were calculated using the concentrations given in Table 7.2 and the scattering lengths b_{Ho} = 0.801(8), b_P = 0.513(1), b_O = 0.5803(4) and b_{Al} = 0.3449(5) fm (Sears 1992). Due to a resonance for ^{164}Dy at -1.88 eV the scattering length of Dy^{3+} is dependent on the incident neutron energy. The scattering length of Dy^{3+} was therefore calculated using the method of Cossy *et al* (1989) which is described in detail in section 7.4. A value of b_{Dy} = 1.602(20) fm at an incident energy of 162.3 meV was calculated which compares with the value of 1.69(2) fm at an incident energy of 25.3 meV given by Sears (1992).

The level of isomorphism between pairs of samples was estimated using the coefficient ξ_R defined in section 6.4. The 8 glasses manufactured allow 21 unique first order difference combinations to be studied and a summary of the corresponding ξ_R values is given in Table 7.3. Three samples, one containing only Dy^{3+} ions, one containing only Ho^{3+} ions and the other containing a mixture of Dy^{3+} and Ho^{3+} ions, are required to form the second order difference function $g_{RR}(r)$ (section 4.8). The comparison of Table 7.3 shows that the amount of contamination is minimised by taking the combination of DyC, DyHoE and HoG. These three glasses were therefore chosen for investigation by using neutron diffraction and were studied using the instrument D4C at the Institut Laue-Langevin, Grenoble (see section 5.2). The coefficients for the difference functions were calculated as described in section 4.8 and are given in Table 7.4 for the samples denoted by DyC, DyHoE and HoG.

	DyA	DyB	DyC	DyHoD	DyHoE	HoF	HoG	HoH
DyA	-	-	-	4.57	10.68	6.35	13.24	7.22
DyB	-	-	-	5.64	10.52	7.23	12.94	8.30
DyC	-	-	-	7.89	25.15	7.14	55.90	7.87
DyHoD	-	-	-	-	-	6.46	11.28	7.86
DyHoE	-	-	-	-	-	3.94	15.99	4.44
HoF	-	-	-	-	-	-	-	-
HoG	-	-	-	-	-	-	-	-
HoH	-	-	-	-	-	-	-	-

Table 7.3. A summary of the contamination coefficients ξ_R for all the first order difference combinations obtained for the samples listed in Table 7.2.

In Tables 7.4 and 7.5, and following the definitions given in Chapter 4, the first order difference functions are given by

$$\Delta_R^{(1)}(Q) = F(Q)_{DyC} - F(Q)_{HoG},$$
$$\Delta_R^{(2)}(Q) = F(Q)_{DyC} - F(Q)_{DyHoE},$$
$$\Delta_R^{(3)}(Q) = F(Q)_{DyHoE} - F(Q)_{HoG} \qquad [7.1]$$

and the total minus weighted difference functions, where the R-μ correlations are eliminated, are given by

$$\Delta_F^{(1)}(Q) = [b_{Dy} F(Q)_{HoG} - b_{Ho} F(Q)_{DyC}] / (b_{Dy} - b_{Ho})$$
$$\Delta_F^{(2)}(Q) = [b_{Dy} F(Q)_{DyHoE} - b_{Dy/Ho} F(Q)_{DyC}] / (b_{Dy} - b_{Dy/Ho})$$

and

$$\Delta_F^{(3)}(Q) = [b_{Ho} F(Q)_{DyHoE} - b_{Dy/Ho} F(Q)_{HoG}] / (b_{Ho} - b_{Dy/Ho}). \quad [7.2]$$

where $b_{Dy/Ho}$ is the scattering length of R in the DyHoE glass.

The second order difference function is given by

$$[S_{RR}(Q) - 1] = \frac{\Delta_R^{(2)}(Q) - \gamma \Delta_R^{(1)}(Q)}{c_R^2 \gamma (1-\gamma) (b_{Dy} - b_{Ho})^2} \quad [7.3]$$

where

$$\gamma = \frac{b_{Dy} - b_{Dy/Ho}}{b_{Dy} - b_{Ho}}. \quad [7.4]$$

The rare earth- matrix difference functions are given by

$$\Delta_{R\mu}^{(1)}(Q) = \Delta_R^{(1)}(Q) - c_R^2 [b_{Dy}^2 - b_{Ho}^2] [S_{RR}(Q) - 1],$$
$$\Delta_{R\mu}^{(2)}(Q) = \Delta_R^{(2)}(Q) - c_R^2 [b_{Dy}^2 - b_{Dy/Ho}^2] [S_{RR}(Q) - 1],$$
$$\Delta_{R\mu}^{(3)}(Q) = \Delta_R^{(3)}(Q) - c_R^2 [b_{Dy/Ho}^2 - b_{Ho}^2] [S_{RR}(Q) - 1] \quad [7.5]$$

and the matrix-matrix difference functions are given by

$$\Delta_{\mu\mu}^{(1)}(Q) = \Delta_F^{(1)}(Q) + c_R^2 b_{Dy} b_{Ho} [S_{RR}(Q) - 1],$$
$$\Delta_{\mu\mu}^{(2)}(Q) = \Delta_F^{(2)}(Q) + c_R^2 b_{Dy} b_{Dy/Ho} [S_{RR}(Q) - 1],$$
$$\Delta_{\mu\mu}^{(3)}(Q) = \Delta_F^{(3)}(Q) + c_R^2 b_{Dy/Ho} b_{Ho} [S_{RR}(Q) - 1]. \quad [7.6]$$

	$S_{RR}(Q)$	$S_{RP}Q)$	$S_{RO}Q)$	$S_{RAl}(Q)$	$S_{PP}(Q)$	$S_{PO}(Q)$	$S_{PAl}(Q)$	$S_{OO}(Q)$	$S_{OAl}(Q)$	$S_{AlAl}(Q)$
$F(Q)_{DyC}$	13.42	24.76	94.30	1.45	11.41	86.96	1.33	165.63	5.08	0.04
$F(Q)_{DyHoE}$	7.97	19.14	72.40	1.13	11.50	86.98	1.36	164.50	5.15	0.04
$F(Q)_{HoG}$	3.57	12.66	48.65	0.77	11.22	86.19	1.36	165.55	5.22	0.04
$\Delta_R^{(1)}(Q)$	9.85	12.09	45.66	0.68	0.20	0.77	-0.03	0.09	-0.14	0.00
$\Delta_R^{(2)}(Q)$	5.46	5.62	21.90	0.31	-0.08	-0.01	-0.03	1.13	-0.07	0.00
$\Delta_R^{(3)}(Q)$	4.39	6.48	23.76	0.37	0.28	0.79	0.00	-1.05	-0.07	0.00
$\Delta_F^{(1)}(Q)$	-6.28	0.57	2.99	0.09	11.02	85.41	1.38	165.46	5.36	0.04
$\Delta_F^{(2)}(Q)$	-8.93	1.75	4.57	0.16	11.75	87.02	1.44	161.00	5.35	0.04
$\Delta_F^{(3)}(Q)$	-5.01	0.01	2.22	0.05	10.67	84.65	1.35	167.59	5.36	0.04
$S_{RR}(Q)$	0.65	-0.28	-0.36	-0.02	-0.18	-0.39	-0.01	1.09	0.00	0.00
$\Delta_{R\mu}^{(1)}(Q)$	2.05	15.53	50.22	0.89	2.37	5.48	0.15	-13.00	-0.15	0.00
$\Delta_{R\mu}^{(2)}(Q)$	1.00	7.58	24.51	0.44	1.14	2.67	0.07	-6.35	-0.08	0.00
$\Delta_{R\mu}^{(3)}(Q)$	1.05	7.95	25.71	0.46	1.20	2.81	0.08	-6.66	-0.08	0.00
$\Delta_{\mu\mu}^{(1)}(Q)$	-1.07	-1.72	-0.05	-0.06	9.60	82.28	1.26	174.21	5.37	0.04
$\Delta_{\mu\mu}^{(2)}(Q)$	-1.07	-1.72	-0.05	-0.06	9.60	82.28	1.26	174.21	5.37	0.04
$\Delta_{\mu\mu}^{(3)}(Q)$	-1.07	-1.72	-0.05	-0.06	9.60	82.28	1.26	174.21	5.37	0.04

Table 7.4. Coefficients of the partial structure factors (in mbarns) calculated using the concentrations given in Table 7.2

	$S_{RR}(Q)$	$S_{RP}Q)$	$S_{RO}Q)$	$S_{RAl}(Q)$	$S_{PP}(Q)$	$S_{PO}(Q)$	$S_{PAl}(Q)$	$S_{OO}(Q)$	$S_{OAl}(Q)$	$S_{AlAl}(Q)$
$F(Q)_{DyC}$	13.88	25.13	95.78	1.49	11.38	86.71	1.35	165.23	5.15	0.04
$F(Q)_{DyHoE}$	7.97	19.04	72.56	1.13	11.38	86.71	1.35	165.23	5.15	0.04
$F(Q)_{HoG}$	3.47	12.57	47.89	0.75	11.38	86.71	1.35	165.23	5.15	0.04
$\Delta_R^{(1)}(Q)$	10.41	12.57	47.89	0.75	-	-	-	-	-	-
$\Delta_R^{(2)}(Q)$	5.91	6.09	23.21	0.36	-	-	-	-	-	-
$\Delta_R^{(3)}(Q)$	4.50	6.47	24.67	0.38	-	-	-	-	-	-
$\Delta_F^{(1)}(Q)$	-6.94	-	-	-	11.38	86.71	1.35	165.23	5.15	0.04
$\Delta_F^{(2)}(Q)$	-10.35	-	-	-	11.38	86.71	1.35	165.23	5.15	0.04
$\Delta_F^{(3)}(Q)$	-5.32	-	-	-	11.38	86.71	1.35	165.23	5.15	0.04
$\Delta_{R\mu}^{(1)}(Q)$	-	13.05	49.75	0.77	-	-	-	-	-	-
$\Delta_{R\mu}^{(2)}(Q)$	-	6.37	24.28	0.38	-	-	-	-	-	-
$\Delta_{R\mu}^{(3)}(Q)$	-	6.68	25.47	0.40	-	-	-	-	-	-
$\Delta_{\mu\mu}^{(1)}(Q)$	-	-	-	-	11.38	86.71	1.35	165.23	5.15	0.04
$\Delta_{\mu\mu}^{(2)}(Q)$	-	-	-	-	11.38	86.71	1.35	165.23	5.15	0.04
$\Delta_{\mu\mu}^{(3)}(Q)$	-	-	-	-	11.38	86.71	1.35	165.23	5.15	0.04

Table 7.5. Coefficients of the partial structure factors (in mbarns) calculated using the average concentrations.

The data sets were analysed using the concentrations shown in Table 7.2 which give the $S_{\alpha\beta}(Q)$ coefficients shown in Table 7.4. The results were also analysed using the average concentrations: $\overline{c_R} = 0.0735 \pm 0.0012$ (1.6%), $\overline{c_P} = 0.2079 \pm 0.0013$ (0.6 %), $\overline{c_O} = 0.7005 \pm 0.014$ (0.2%), $\overline{c_{Al}} = 0.0184 \pm 0.0003$ (1.4%). The coefficients corresponding to the average concentrations are given in Table 7.5.

7.4 Dysprosium Scattering Length

Due to a resonance for ^{164}Dy at −1.88 eV the absorption cross section and scattering lengths of this isotope are dependent on the incident neutron energy. Their values were calculated using the method described by Cossy *et al* (1989). The coherent scattering length at the incident neutron energy E is given by

$$b(E) = b_r(E) + ib_i(E) \qquad [7.7]$$

where the real part

$$b_r(E) = b_r(E_0) + 9.103 \times 10^3 \left(\frac{A+1}{A}\right)^2 \left[\sum_j g\Gamma^0_{nj}\left(\frac{E-E_j}{4(E-E_j)^2+\Gamma_j^2} - \frac{E_0-E_j}{4(E_0-E_j)^2+\Gamma_j^2}\right)\right] \qquad [7.8]$$

and the imaginary part

$$b_i(E) = b_i(E_0) + 4.551 \times 10^3 \left(\frac{A+1}{A}\right)^2 \left[\sum_j g\Gamma^0_{nj}\Gamma_j\left(\frac{1}{4(E-E_j)^2+\Gamma_j^2} - \frac{1}{4(E_0-E_j)^2+\Gamma_j^2}\right)\right] \qquad [7.9].$$

$b_r(E_0)$ and $b_i(E_0)$ are the measured real and imaginary parts of the bound scattering length (in fm) at a reference energy E_0, A is the nuclear mass, Γ_j is the total width of the resonance (normally $\Gamma_j \approx \Gamma_\lambda$ the radiative width) in meV, g is the spin weight factor and Γ^0_{nj} is the reduced neutron width at 1 eV defined by

$$\Gamma^0_{nj} = \Gamma_n \sqrt{1\,eV/E} \qquad [7.10]$$

where Γ_n is the neutron width at the resonance energy. The absorption cross-section at the incident neutron wavelength, λ, is given by

$$\sigma_{abs} = 2\lambda b_i \, . \qquad [7.11]$$

7.5. EXPERIMENTAL PROCEDURE

The D4C instrument was operated at an incident wavelength of 0.70995 Å to give a measurement range of $0.33 \leq Q(Å^{-1}) \leq 16.5$. The rare-earth phosphate glasses were sealed in a cylindrical vanadium container of internal diameter 7 mm and 0.1 mm wall thickness. Diffraction patterns were taken for the samples in their container, the empty container and a vanadium rod of dimensions comparable to the sample for normalisation purposes. The intensity for a cadmium neutron-absorbing rod of similar diameter to the sample was also measured to account for the effect of the sample self-shielding on the background count rate at small scattering angles. The total paramagnetic scattering cross-sections of Dy^{3+} and Ho^{3+} at the D4C incident wavelength were 5.488 and 5.449 barn respectively (Wasse *et al* 2000). The data analysis procedure outlined in section 5.8 was followed.

7.6 RESULTS.

The results presented in this section were all obtained using the average concentrations and the corresponding partial structure factor coefficients given in Table 7.5. The effect of using these weighting factors, as opposed to the weighting factors presented in Table 7.4 which were calculated using the concentrations found for the EPMA analysis, was not found to be significant. The choice of coefficients has no effect on the peak positions and only a small effect on the coordination numbers. For example, if an R-O coordination number of 6.0 was obtained for the total structure factors $F(Q)_{DyC}$, $F(Q)_{DyHoE}$ and $F(Q)_{HoG}$ using the parameters in Table 7.4 then the corresponding values obtained using the parameters in Table 7.5 are 5.9, 6.0 and 6.1 respectively.

The differential scattering cross section, $F_S(Q)$, corrected for background, container, heater and multiple scattering effects (equation 4.34) for the DyC, DyHoE and HoG samples is given in Figure 7.4. For DyC and HoG, the paramagnetic differential scattering cross sections $[(d\sigma/d\Omega)_{mag}/N\eta_0]$ of Dy^{3+} and Ho^{3+} (equation 4.40) are also shown.

In order to extract the total structure factor, F(Q), for the DyC sample from $F_S(Q)$ and $(d\sigma/d\Omega)_{mag}$ (equation 4.42) it was necessary to make a small hydrogen correction. This resulted from the unfortunate presence of solvent used to clean the sample containers. However, the hydrogen content was small, at the level of ≈ 0.25 mol %, and as discussed in section 5.11 it will only have a major effect on the inelasticity corrections. The hydrogen correction is illustrated in Figure 7.4.

The total structure factors, F(Q), for DyC, DyHoE and HoG are shown in Figure 7.5 and the corresponding total pair distribution functions, G'(r), are shown in Figure 7.6. There is close agreement between the F(Q) functions and the back Fourier transforms of their corresponding G'(r) after the unphysical low r oscillation are set equal to the G(0) limit (Figure 7.6) which indicates that the data corrections have been properly applied.

The first order difference functions $\Delta_R(Q)$ obtained from the combination of the DyC, DyHoE and / or HoG total structure factors are shown in Figure 7.8 together with the back Fourier transforms of the corresponding $\Delta G_R'(r)$ with the unphysical low r oscillations set equal to $\Delta G_R(0)$ (Figure 7.7). The data and the back Fourier transforms are in close agreement which again indicates that the data corrections have been properly applied.

The total minus weighted difference functions $\Delta_F(Q)$ are shown in Figure 7.9 and the corresponding real space functions $\Delta G'_F(r)$ are shown in Figure 7.10. Again there is good agreement between each $\Delta_F(Q)$ and the corresponding back Fourier transform of $\Delta G'_F(r)$ with the unphysical low r oscillations set equal to $\Delta G_F(0)$.

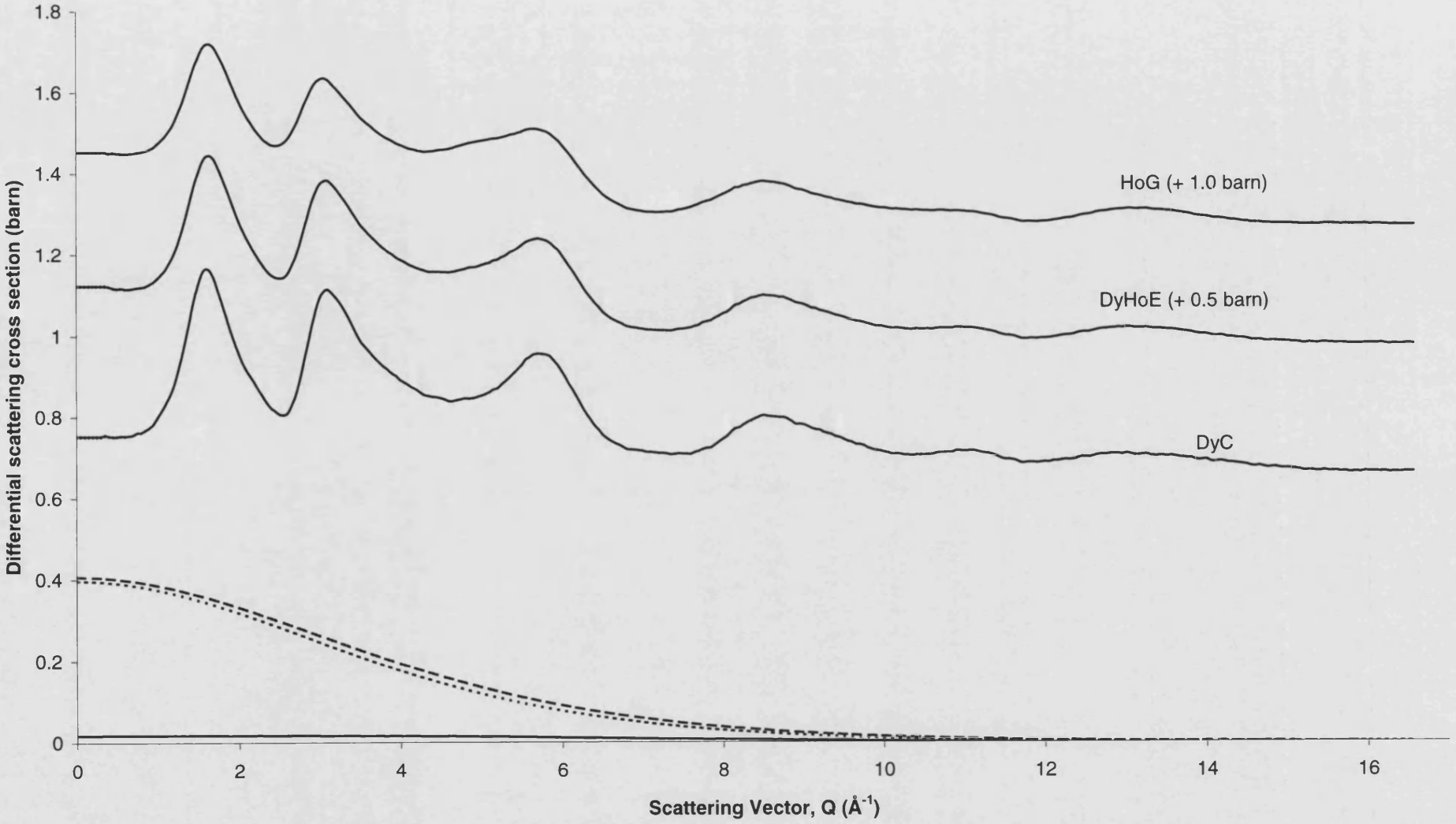

Figure 7.4. $F_S(Q)$ for DyC, DyHoE and HoG, the dysprosium (short dased curve) and the holmium (long dashed curve) magnetic form factors and the hydrogen correction used for DyC (solid curve).

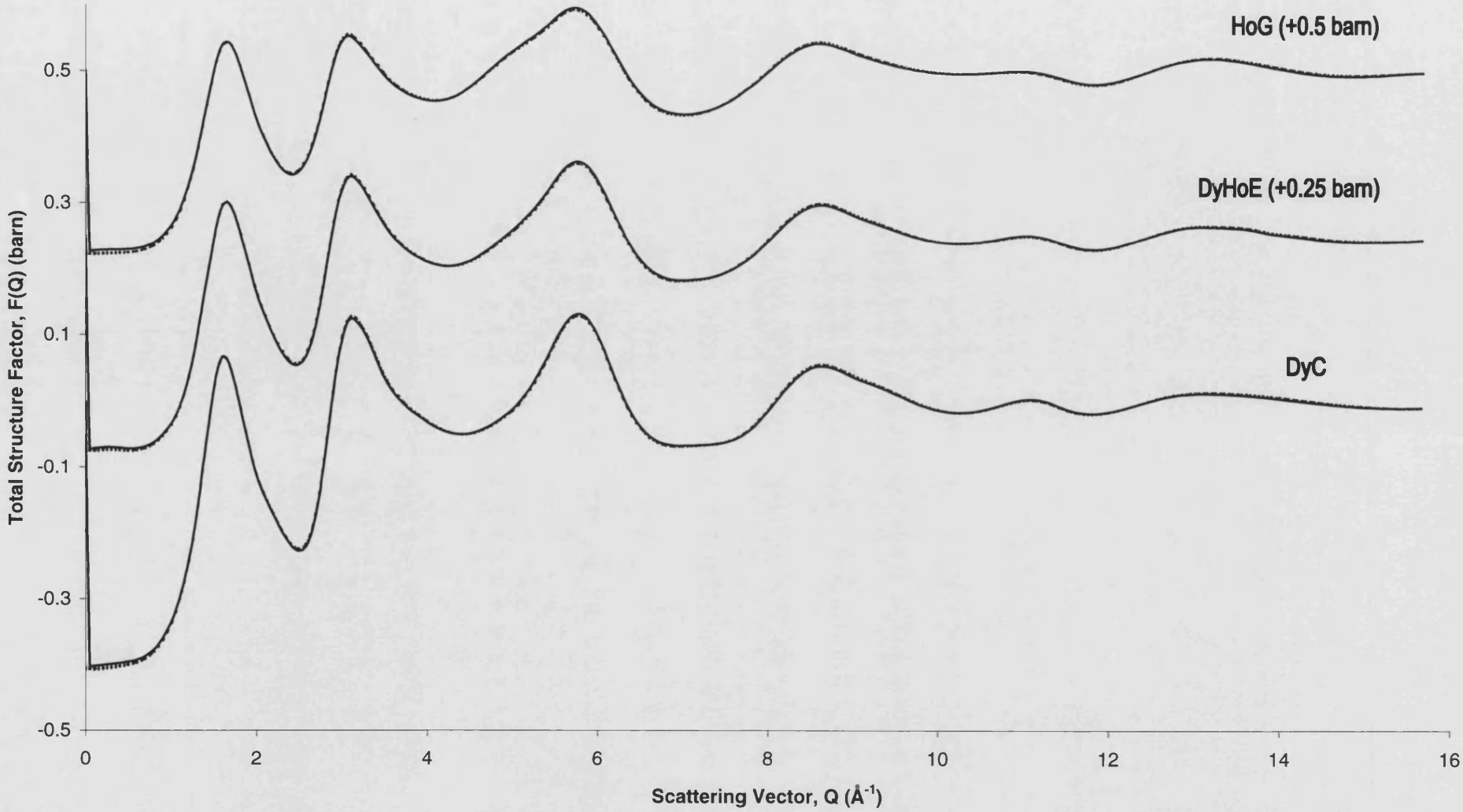

Figure 7.5. The total structure factor, F(Q) (dashed curve with error bars) and the Fourier backtransform of the corresponding G'(r) given by the solid curve in Figure 7.6 (solid curve) for the DyC, DyHoE and HoG samples.

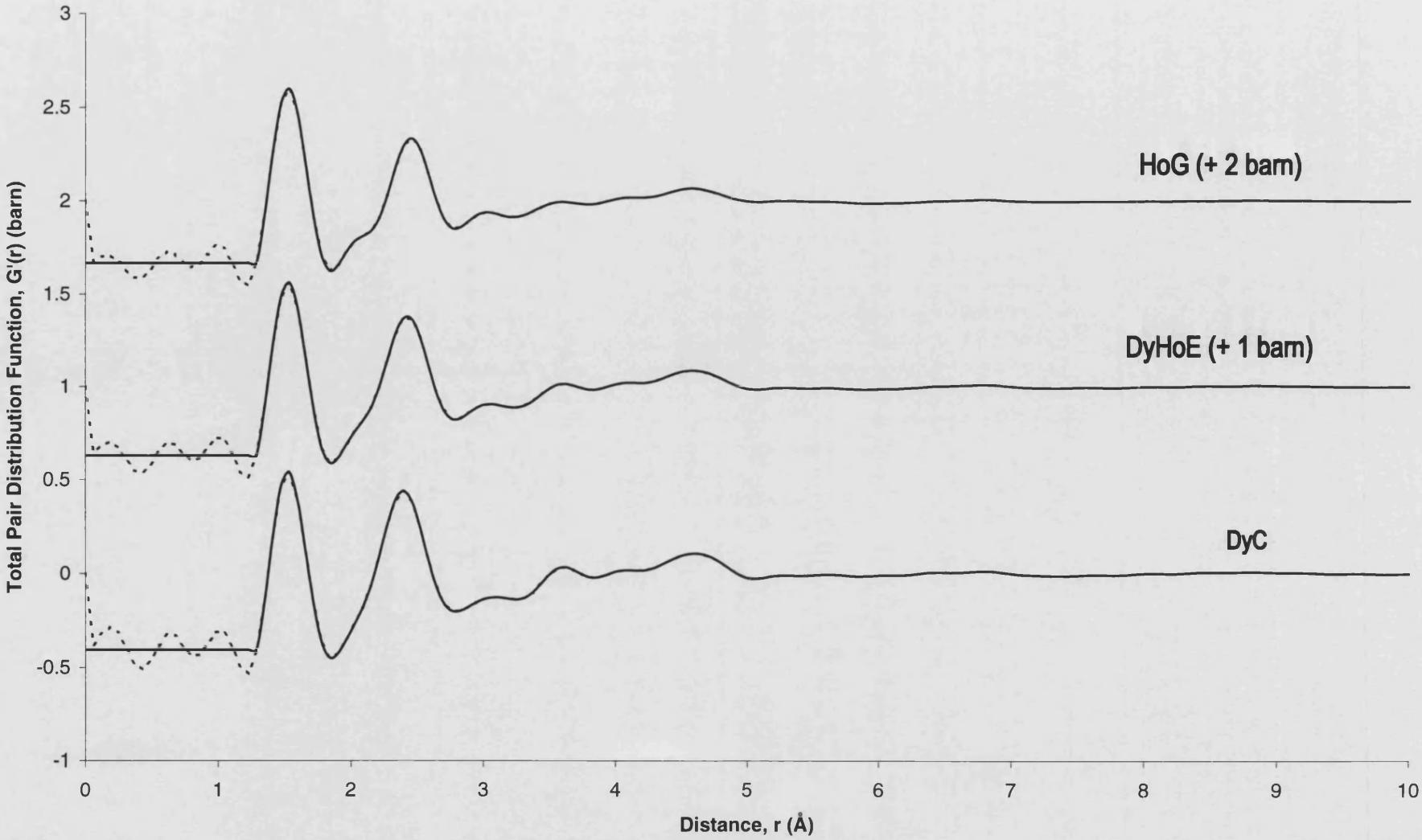

Figure 7.6. The total pair distribution function G'(r) (solid curves) obtained by Fourier transforming the F(Q) given by the points with error bars in Figure 7.5. The unphysical low r oscillations are shown by the dashed curves.

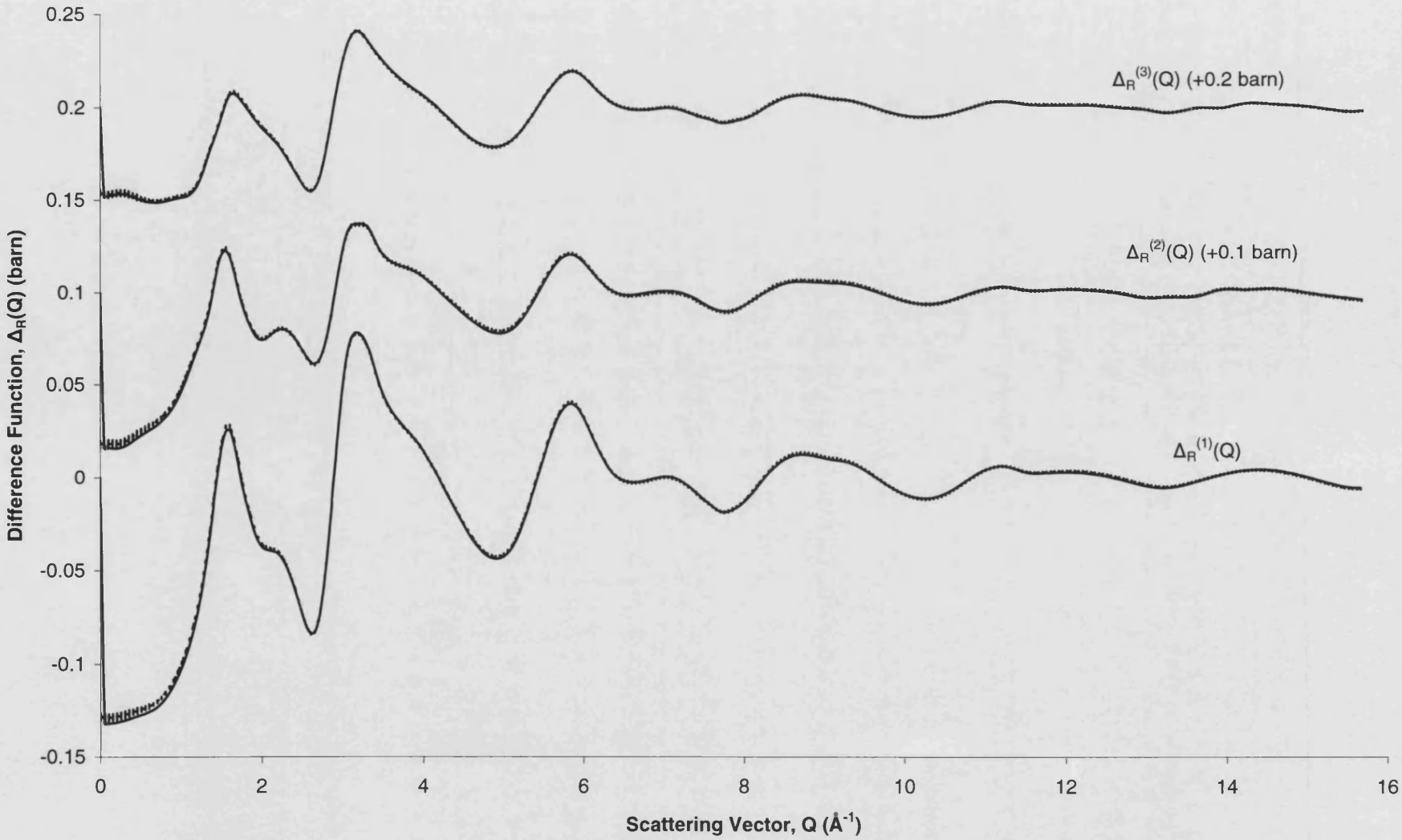

Figure 7.7. The difference functions, $\Delta_R(Q)$, (dashed curves with error bars) and the Fourier backtransforms of the $\Delta G'_R(r)$ (solid curves) given by the solid curves in Figure 7.8.

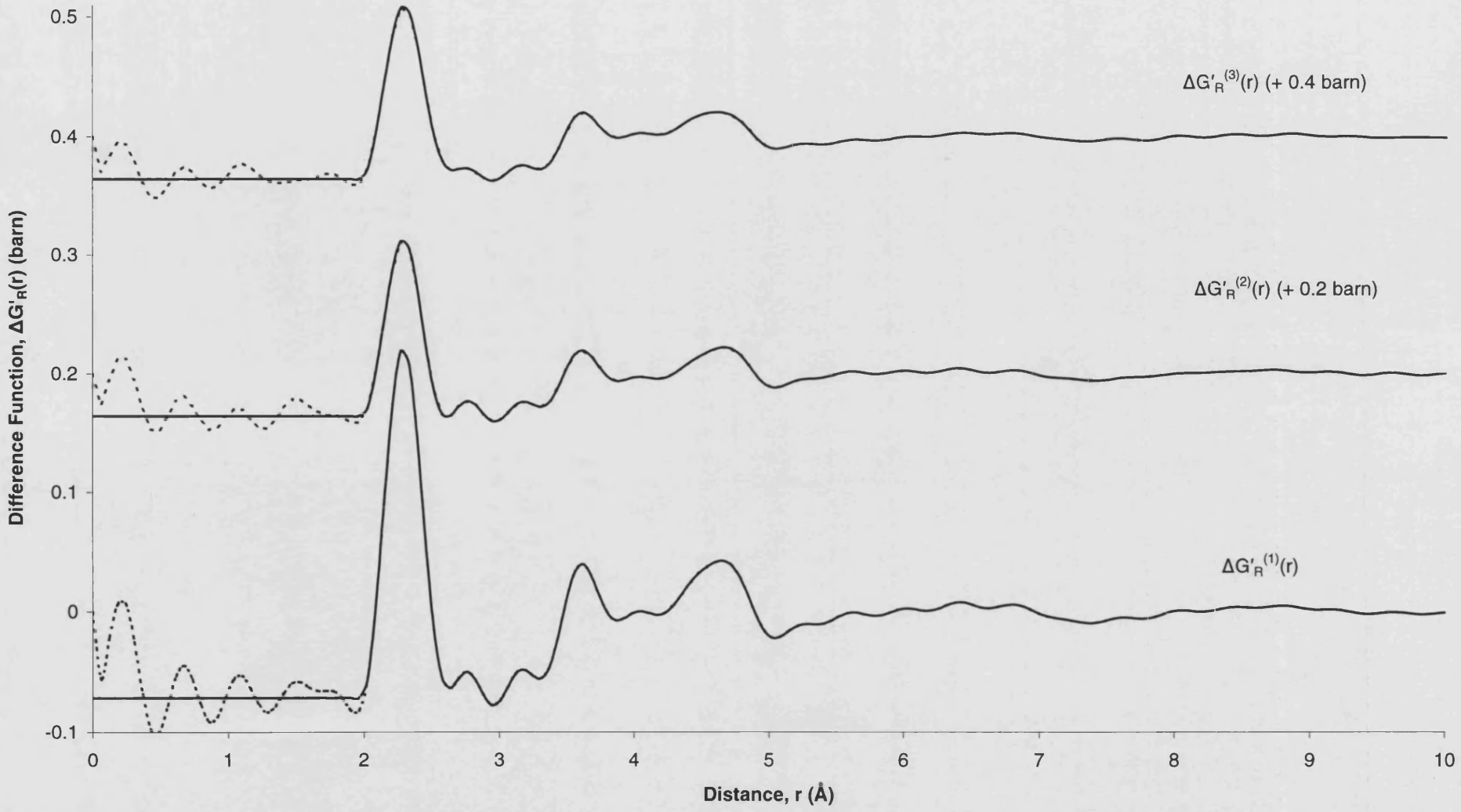

Figure 7.8. The real space functions $\Delta G'_R(r)$ (solid curve) obtained by Fourier transforming the $\Delta_R(Q)$ given by the points with error bars in Figure 7.7. The unphysical low r oscillations are shown by the dashed curves.

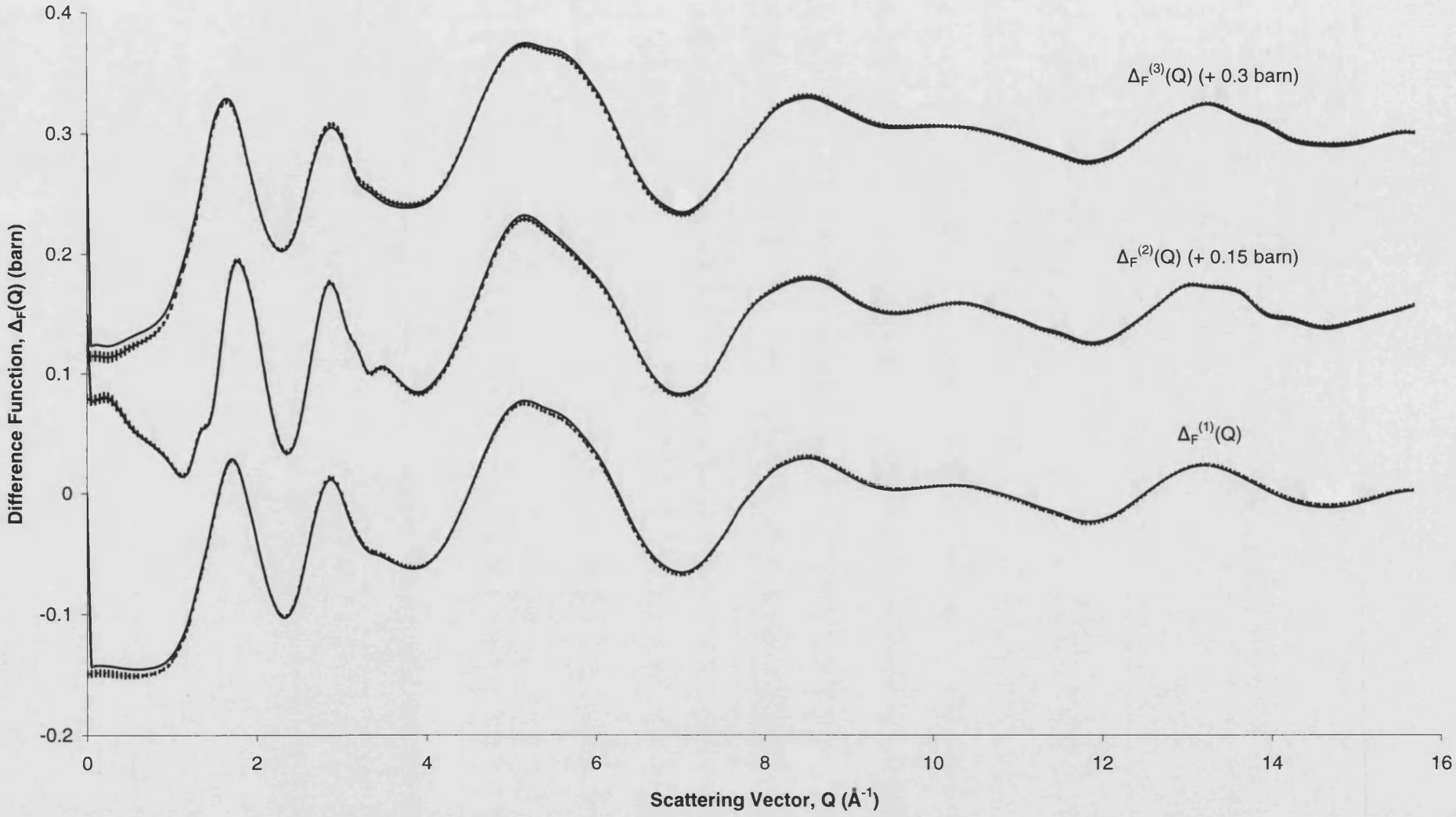

Figure 7.9. The difference functions $\Delta_F(Q)$ (points with error bars) and the Fourier backtransforms of the $\Delta G'_F(r)$ (solid curve) given by the solid curves in Figure 7.10.

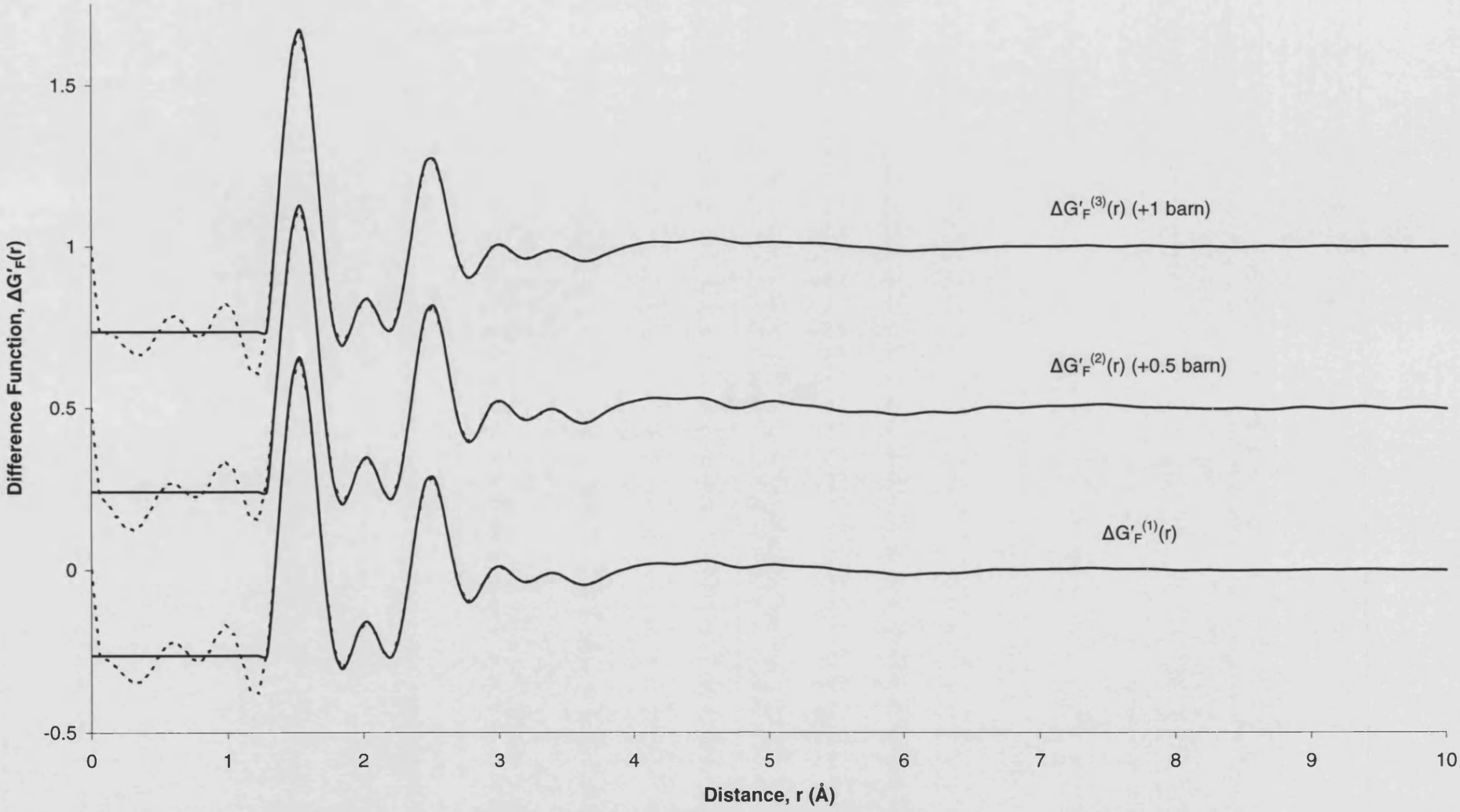

Figure 7.10. The real space functions $\Delta G'_F(r)$ (solid curve) obtained by Fourier transforming the $\Delta_F(Q)$ given by the points with error bars in Figure 7.9. The low r unphysical oscillations are shown by the dashed curves.

The first order difference functions $\Delta D'_R(r)$ were modelled first, using the fitting procedure outlined in section 4.9, since these functions have the fewest contributing $g_{\alpha\beta}(r)$ (section 4.8). The measured functions $\Delta D'_R(r)$, the individual convoluted Gaussians, their sum and the residual are shown in Figures 7.11-7.13. The R_χ values for the fitting region of $2.0 \leq r$ (Å) ≤ 3.0 are 0.0145, 0.0244 and 0.0164 for $\Delta D'_R{}^{(1)}(r)$, $\Delta D'_R{}^{(2)}(r)$ and $\Delta D'_R{}^{(3)}(r)$ respectively (section 5.10). The parameters describing the fitted Gaussians are summarised in Table 7.6.

By comparison with the crystal structures of the rare-earth meta-phosphates (Dorokhova and Karpov 1984), ultra-phosphates (Bagieu *et al* 1973) and ortho-phosphates (Hughes and Mariano 1995) comprising small rare earth ions, the R-α correlations were assigned. In crystalline ErP_3O_9 the shortest Er-O, Er-P and Er-Er distances are at 2.17 Å, 3.49 Å and 5.37 Å respectively and the second nearest-neighbour Er-O distance is at 3.91 Å (Dorokhova and Karpov 1984). In crystalline HoP_5O_{14} the shortest Ho-O, Ho-P and Ho-Ho distances are at 2.29 Å, 3.60 Å and 5.71 Å respectively and the second nearest-neighbour Ho-O distance is at 3.99 Å (Bagieu *et al* 1973). In crystalline $HoPO_4$ the shortest Ho-O, Ho-P and Ho-Ho distances are at 2.31 Å, 3.01 Å and 3.75 Å respectively and the second nearest-neighbour Ho-O distance is at 4.14 Å (Hughes and Mariano 1995). Hence only R-O correlations are expected for $r \leq 3$ Å and $\Delta D'_R(r)$ was modelled accordingly.

The nearest-neighbour R-O correlations could be modelled by a single Gaussian together with another Gaussian at larger r, with a much smaller coordination number (Figures 7.10 - 7.12). The R-O coordination environment is therefore asymmetric. The mean R-O distances of $\approx$ 2.30 and 2.67 Å compare with Er-O distances of 2.17 – 2.29 Å in crystalline ErP_3O_9 (Dorokhova and Karpov 1984). The total R-O coordination number of $\approx$ 6.75 compares with a coordination number of six in crystalline ErP_3O_9 (Dorokhova and Karpov 1984) and a coordination number of eight in crystalline ErP_5O_{14} (Bagieu *et al* 1973). Beyond about 3 Å the broadening of peaks means that it is difficult to clearly resolve neighbouring correlations. However, only R-P correlations are expected as the next nearest neighbours and the data was therefore modelled with Gaussians having R-P coordination numbers of 1.1 and 6 at distances of 3.25 and 3.60 Å respectively. These values compare with an R-P

coordination number of 6 with corresponding R-P distances of 3.50 – 3.76 Å for crystalline ErP_3O_9 (Dorokhova and Karpov 1984). Although the R-P correlations at 3.60 Å may not be accurately represented, due to the overlap from other correlations, the shorter R-P correlations should be reasonably well modelled in the region of overlap between the R-O peaks and the R-P peaks, $3.0 \leq r\ (Å) \leq 3.4$.

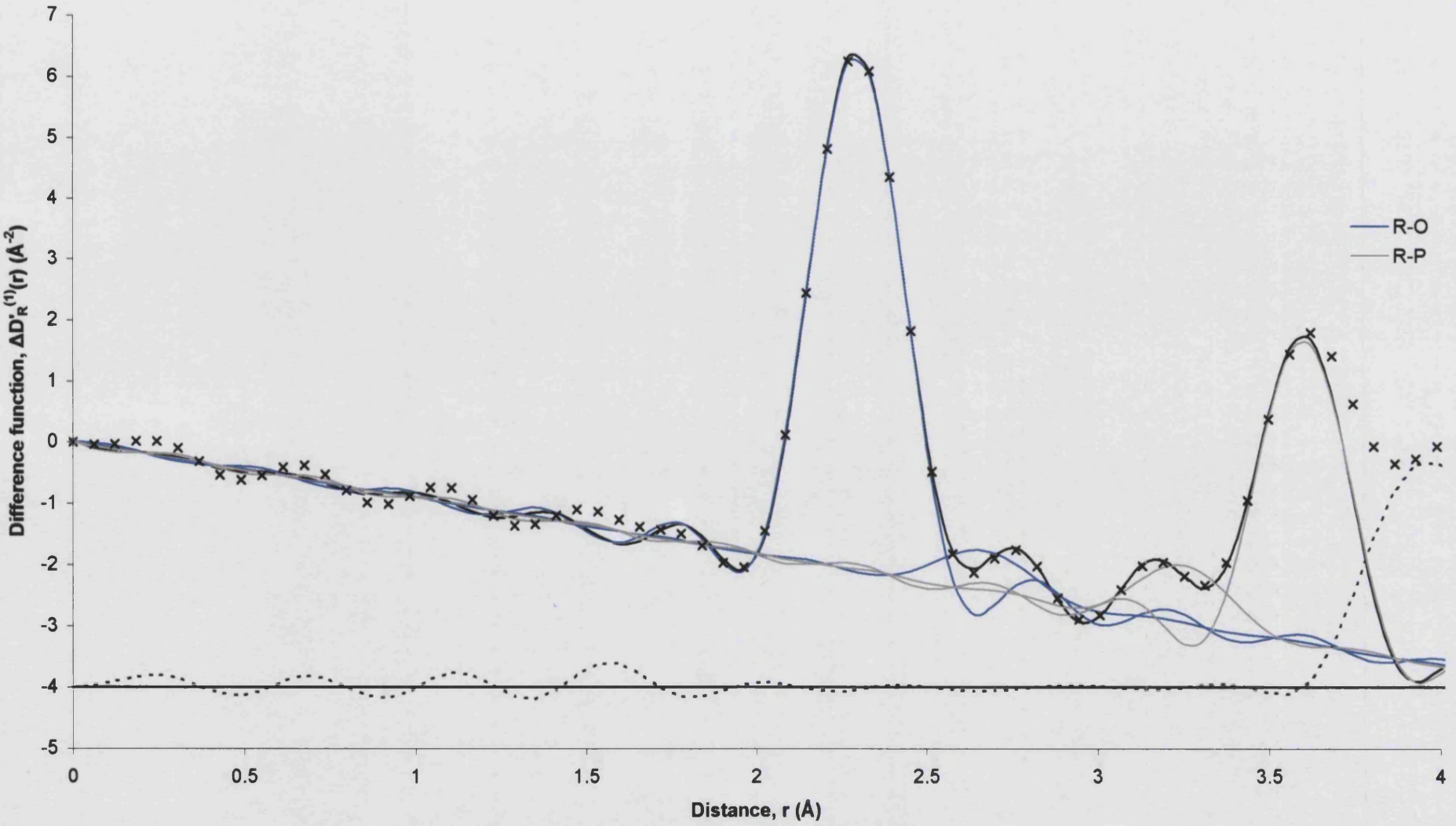

Figure 7.11. The difference function $\Delta D'_R{}^{(1)}(r)$ (crosses), the fitted data (solid curve) and the individual convoluted R-O and R-P Gaussians. The residual (dashed curve) is offset by -4 barn.

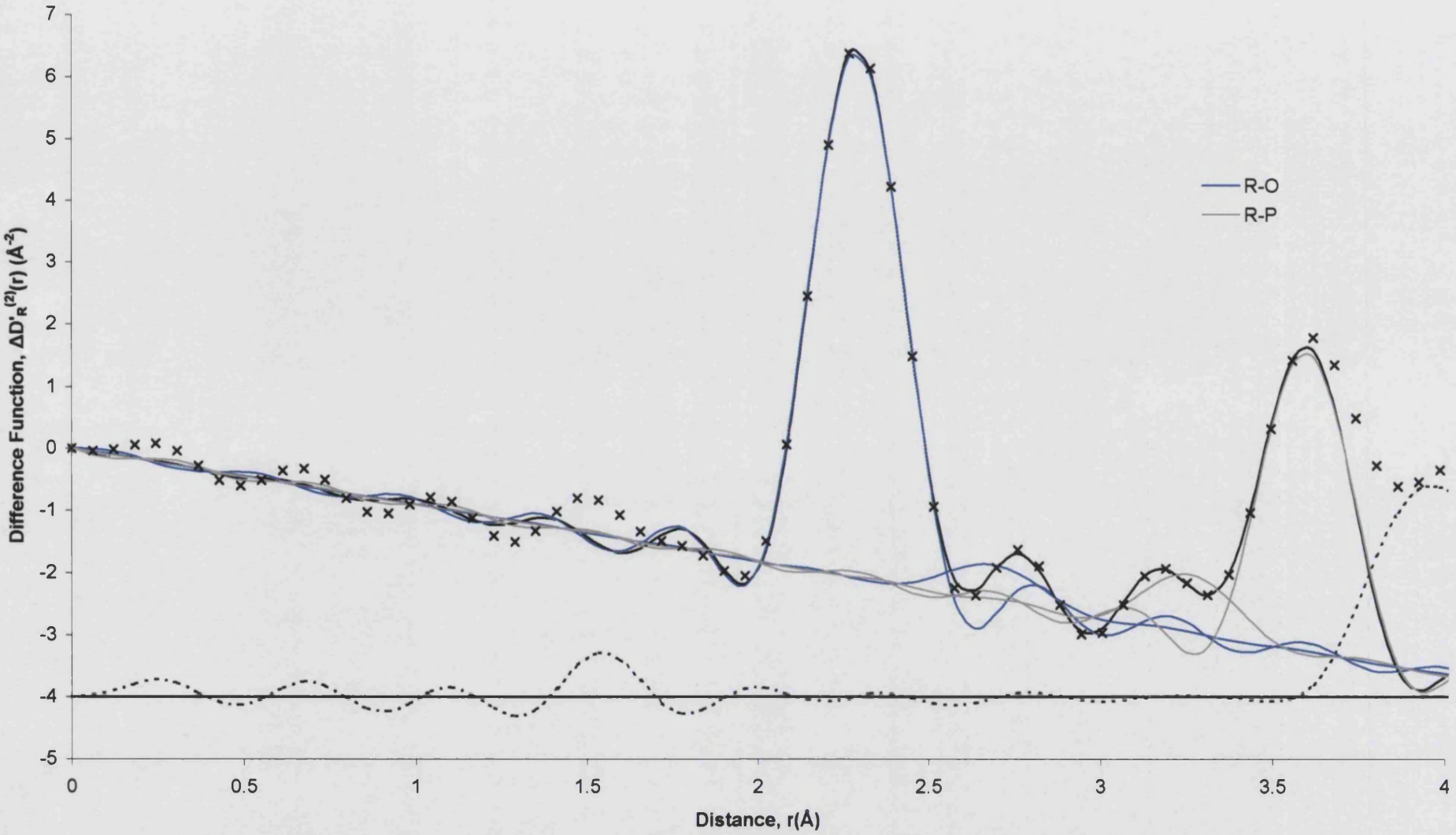

Figure 7.12. The difference function $\Delta D'_R{}^{(2)}(r)$ (crosses), the fitted data (solid curve) and the individual convoluted R-O and R-P Gaussians. The residual (dashed curve) is offset by -4 barn.

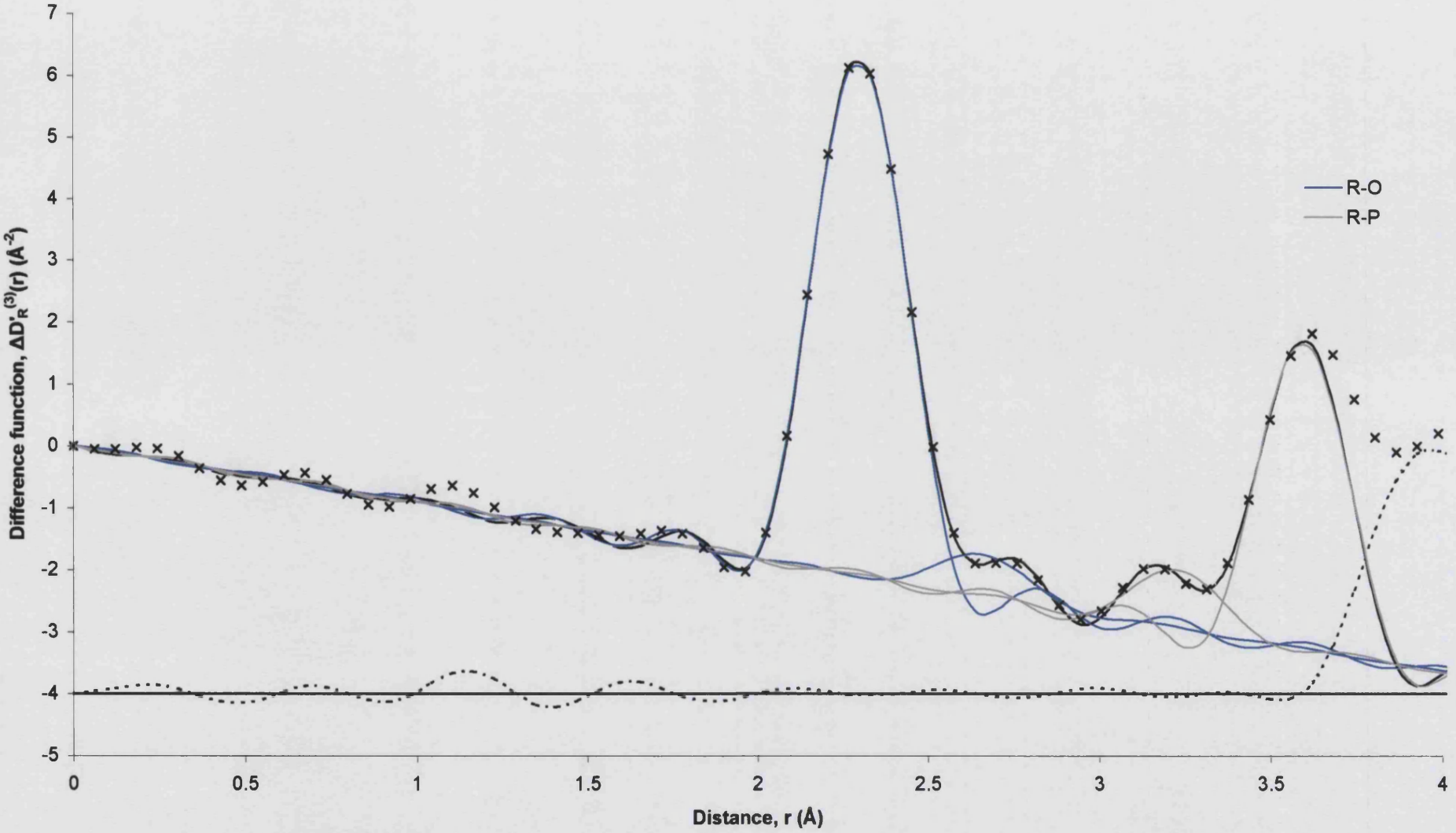

Figure 7.13. The difference function $\Delta D'_R{}^{(3)}(r)$ (crosses), the fitted data (solid curve) and the individual convoluted R-O and R-P Gaussians. The residual (dashed curve) is offset by -4 barn.

	$\Delta D'_R{}^{(1)}(r)$			$\Delta D'_R{}^{(2)}(r)$			$\Delta D'_R{}^{(3)}(r)$		
	r (Å)	C_N	σ (Å)	r (Å)	C_N	σ (Å)	r (Å)	C_N	σ (Å)
R-O	2.295(10)	6.20(10)	0.112(10)	2.292(10)	6.20(10)	0.107(10)	2.30(1)	6.20(10)	0.118(10)
R-O	2.67(1)	0.55(10)	0.108(10)	2.69(1)	0.50(10)	0.110(10)	2.66(1)	0.55(10)	0.110(10)
R-P	3.25(2)	1.1(1)	0.110(10)	3.26(2)	1.1(1)	0.107(10)	3.23(2)	1.00(10)	0.100(10)
R-P	3.60(2)	6.0(1)	0.100(10)	3.60(2)	6.0(1)	0.100(10)	3.595(20)	6.00(10)	0.105(10)

Table 7.6. A summary of the Gaussian parameters used to model the difference functions $\Delta D'_R(r)$.

	$\Delta D'_F{}^{(1)}(r)$			$\Delta D'_F{}^{(2)}(r)$			$\Delta D'_F{}^{(3)}(r)$		
	r (Å)	C_N	σ (Å)	r (Å)	C_N	σ (Å)	r (Å)	C_N	σ (Å)
P-O_T	1.490(10)	2.05(10)	0.055(5)	1.490(10)	2.05(10)	0.065(5)	1.490(10)	2.10(10)	0.055(5)
P-O_B	1.590(10)	2.10(10)	0.090(5)	1.590(10)	2.05(10)	0.090(5)	1.590(10)	2.10(10)	0.085(5)
Al-O	1.880(10)	5.5(5)	0.120(10)	1.880(10)	5.5(5)	0.120(10)	1.880(10)	5.5(5)	0.120(10)
O-(P)-O	2.445(10)	2.2(1)	0.130(10)	2.460(10)	2.2(1)	0.125(10)	2.445(10)	2.2(1)	0.130(10)
O-(P)-O	2.535(10)	1.4(1)	0.055(10)	2.530(10)	1.4(1)	0.050(10)	2.535(10)	1.35(10)	0.060(10)
O-(Al)-O	2.65(1)	0.63(10)	0.115(10)	2.65(1)	0.63(10)	0.115(10)	2.65(1)	0.63(10)	0.115(10)
P-(OP)-O	2.93(1)	4.0(1)	0.130(10)	2.93(1)	4.0(1)	0.130(10)	2.93(1)	4.0(1)	0.130(10)
P-P	2.98(2)	2.0(1)	0.100(10)	2.98(2)	2.0(1)	0.100(10)	2.98(2)	2.0(1)	0.100(10)
O-(R)-O	3.15(2)	1.0(1)	0.105(10)	3.14(2)	1.0(1)	0.105(10)	3.15(2)	1.0(1)	0.105(10)
Al-P	3.15(2)	6.0(5)	0.100(10)	3.15(2)	6.0(5)	0.100(10)	3.15(2)	6.0(5)	0.100(10)

Table 7.7. A summary of the Gaussian parameters used to model the difference functions $\Delta D'_F(r)$.

Next, the total minus weighted difference functions, $\Delta D'_F(r)$, were modelled since these also have fewer contributing $g_{\alpha\beta}(r)$ than the total pair distribution functions $D'(r)$. The measured functions $\Delta D'_F(r)$, the individual convoluted Gaussians, their sum and the residual are shown in Figures 7.14-7.16. The R_χ values for the fitting region of $1.0 \leq r$ (Å) ≤ 3.0 are 0.0237, 0.0277 and 0.0276 for $\Delta D'^{(1)}_F(r)$, $\Delta D'^{(2)}_F(r)$ and $\Delta D'^{(3)}_F(r)$ respectively (section 5.10). The parameters describing the fitted Gaussians are summarised in Table 7.7.

By comparison with the crystal structures of the rare-earth meta-phosphates (Dorokhova and Karpov 1984), ultra-phosphates (Bagieu *et al* 1973) and ortho-phosphates (Hughes and Mariano 1995) the α-β correlations, where $\alpha \neq R$ and $\beta \neq R$, were assigned. In crystalline ErP_3O_9 the shortest P-O, O-O and P-P distances are at 1.41 Å, 2.32 Å and 2.90 Å respectively (Dorokhova and Karpov 1984). In crystalline HoP_5O_{14} the shortest P-O, O-O and P-P distances are at 1.44 Å, 2.38 Å and 2.86 Å respectively (Bagieu *et al* 1973). In crystalline $HoPO_4$ the shortest P-O, O-O and P-P distances are at 1.53 Å, 2.40 Å and 3.75 Å respectively (Hughes and Mariano 1995). The present phosphate glasses contain aluminium impurities (Table 7.2) and NMR results indicate that this aluminium can be 4, 5 or 6 fold coordinated (Cole *et al* 1999). In crystalline $Al(PO_3)_3$, Al is surrounded by six nearest neighbours at a distance of 1.88 Å (Van der Meer 1976) whereas Al centred tetrahedra have a nearest neighbour Al-O distance of ≈ 1.73 Å (Sowa *et al* 1990). Hence only P-O correlations are expected under the first peak, $1.3 \leq r$ (Å) ≤ 1.7, and $\Delta D'_F(r)$ was modelled accordingly.

The P-O peak was best modelled using two Gaussians, one corresponding to a C_N of ≈ 2.05(10) O_T around P at a distance of 1.49 Å and the other to a C_N of ≈ 2.10(10) O_B around P at a distance of 1.59 Å. These values compare with $\bar{n}_P^{O_T} = 2$ and $\bar{n}_P^{O_B} = 2$ for crystalline ErP_3O_9 (Dorokhova and Karpov 1984). The total P-O coordination number is 4.0 within the experimental error as expected for a phosphate network.

Al-O correlations are expected to be next in the region $1.7 \leq r\ (Å) \leq 1.9$ followed by O-O correlations in the region $2.3 \leq r\ (Å) \leq 2.6$. However, the Al-O correlations have a small weighting factor compared to the P-O and O-O correlations (see Table 7.3) and the effect of the modification function M(r) on the P-O and O-(P)-O correlations is significant in the region where the Al-O correlations occur. Therefore it was decided to model the O-(P)-O correlations next.

The O-(P)-O correlations were initially modelled with a single peak centred at 2.48 Å (Table 7.1). However a better fit was obtained by splitting the O-(P)-O correlations into two peaks centred at ≈ 2.455 and 2.53 Å (Table 7.7), a strategy that finds support on the basis of the distribution of O-(P)-O distances between 2.32 and 2.68 Å in the crystalline phase of ErP_3O_9 (Dorokhova and Karpov 1984) and is consistent with the results presented for the larger R^{3+} ions in Chapter 6. The total O-(P)-O C_N of ≈ 3.6 compares with a value of 3.6 calculated on the basis of the phosphate network model of Hoppe (1996) which is described in section 6.2.

The Al-O correlations in $\Delta D'_F(r)$ were best modelled using a Gaussian centred at 1.88 Å, consistent with there being a large number of Al centred octahedra, as opposed to a Gaussian centred at the distance of 1.73 Å expected for Al centred tetrahedra. However, the modelled Al-O coordination number was 5.5(5) suggesting a range of Al environments.

The O-(Al)-O correlations were modelled using a distance of $\sqrt{2}\ r_{O-Al} = 2.66$ Å consistent with there being a large proportion of six fold coordinated Al as opposed to the longer distance of $\sqrt{8/3}\ r_{O-Al} = 2.833$ Å consistent with four fold coordinated Al. The O-(Al)-O coordination number was constrained to be 0.6 ± 0.1 as obtained from equation 6.1, which is consistent with the majority of Al atoms being in an octahedral environment (see section 6.3).

Beyond about 2.75 Å the broad and overlapping peaks means that it is difficult to clearly resolve neighbouring correlations and there is a corresponding greater uncertainty in the Gaussian parameters as shown in Table 7.7. A modelling of the P-(OP)-O, P-(O)-P, O-(R)-O and Al-P correlations was nevertheless undertaken, in part

to provide a smooth overlap region beyond 2.5 Å to assist with modelling the shorter ranged O-(P)-O and O-(Al)-O correlations. The P-(O)-P distances and coordination numbers were constrained using values taken from the crystalline phase of ErP_3O_9 (Dorokhova and Karpov 1984). The P-(OP)-O correlations were also modelled to account for the minimum at ≈ 2.75 Å. The latter is not expected to be an accurate representation as the crystalline phase of ErP_3O_9 shows a range of overlapping P-(OP)-O and O-O correlations for r > 2.9 Å (Dorokhova and Karpov 1984). The modelled P-(OP)-O distance is 2.93 Å which is considerably shorter than the distance of 3.08 Å for crystalline erbium meta-phosphate (Dorokhova and Karpov 1984). However, shorter distances of 2.78 and 2.86 Å have been reported for glassy rare earth phosphates (Cole *et al* 1999). The Al-P distance and coordination numbers were constrained using values taken from the crystalline phase of AlP_3O_9 consistent with six fold coordinated Al (Van der Meer 1976). The weighting factor for these correlations is comparatively small (Table 7.5).

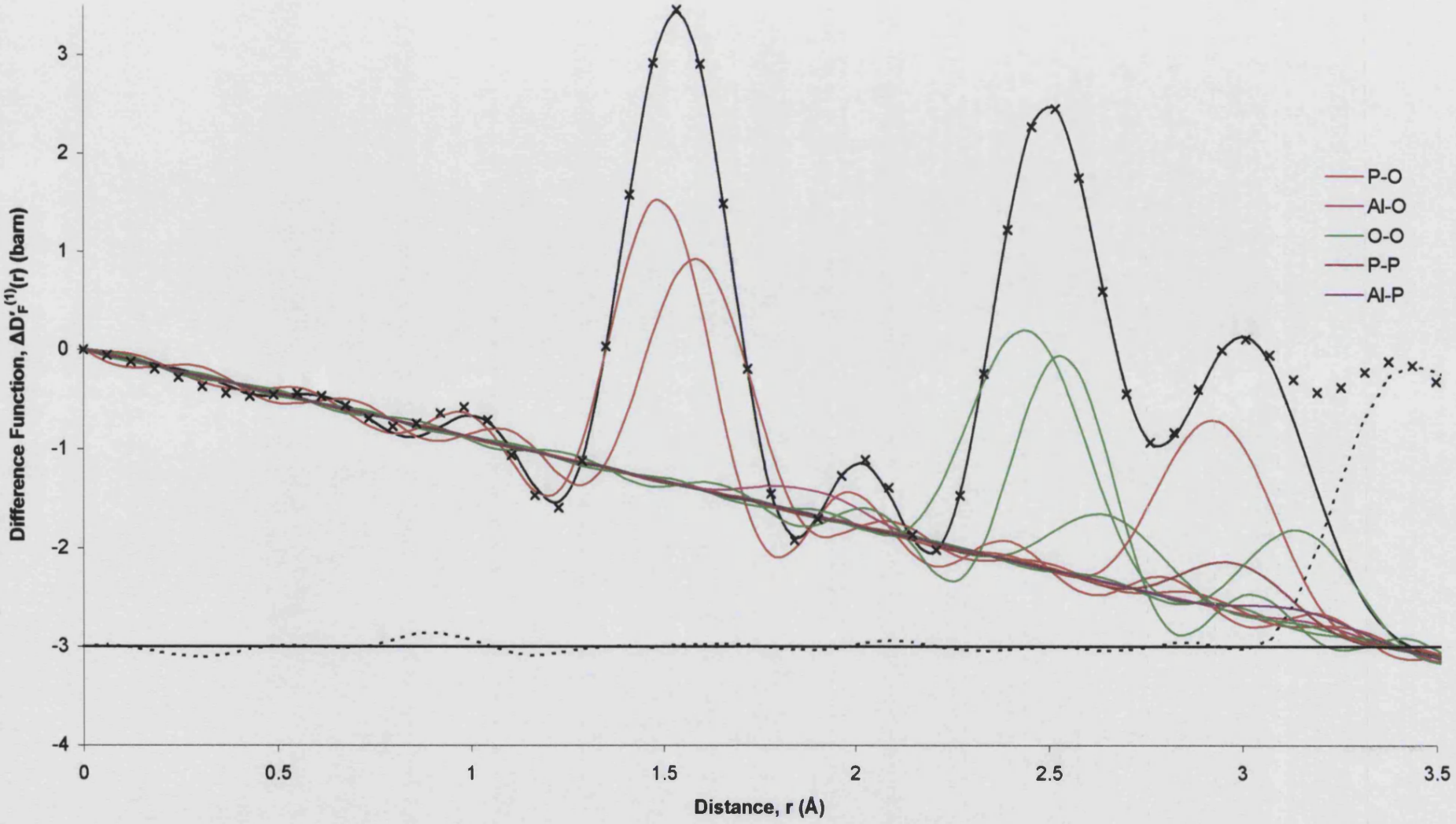

Figure 7.14. The difference function $\Delta D'_F{}^{(1)}(r)$ (crosses), the fitted data (solid curve) and the individual convoluted Gaussians. The residual (dashed curve) is offset by -3 barn.

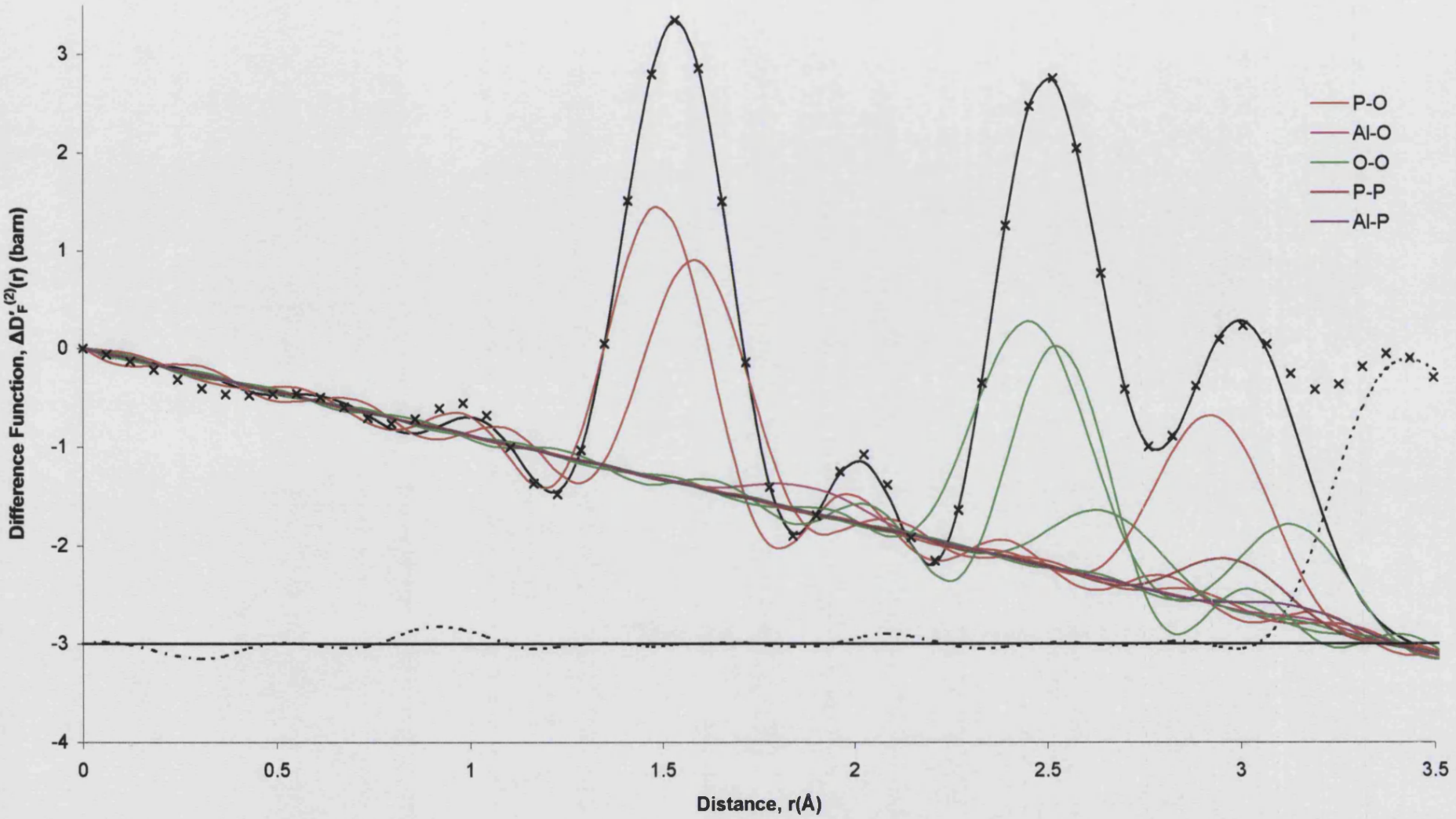

Figure 7.15. The difference function $\Delta D'_F{}^{(2)}(r)$ (crosses), the fitted data (solid curve) and the individual convoluted Gaussians. The residual (dashed curve) is offset by -3 barn.

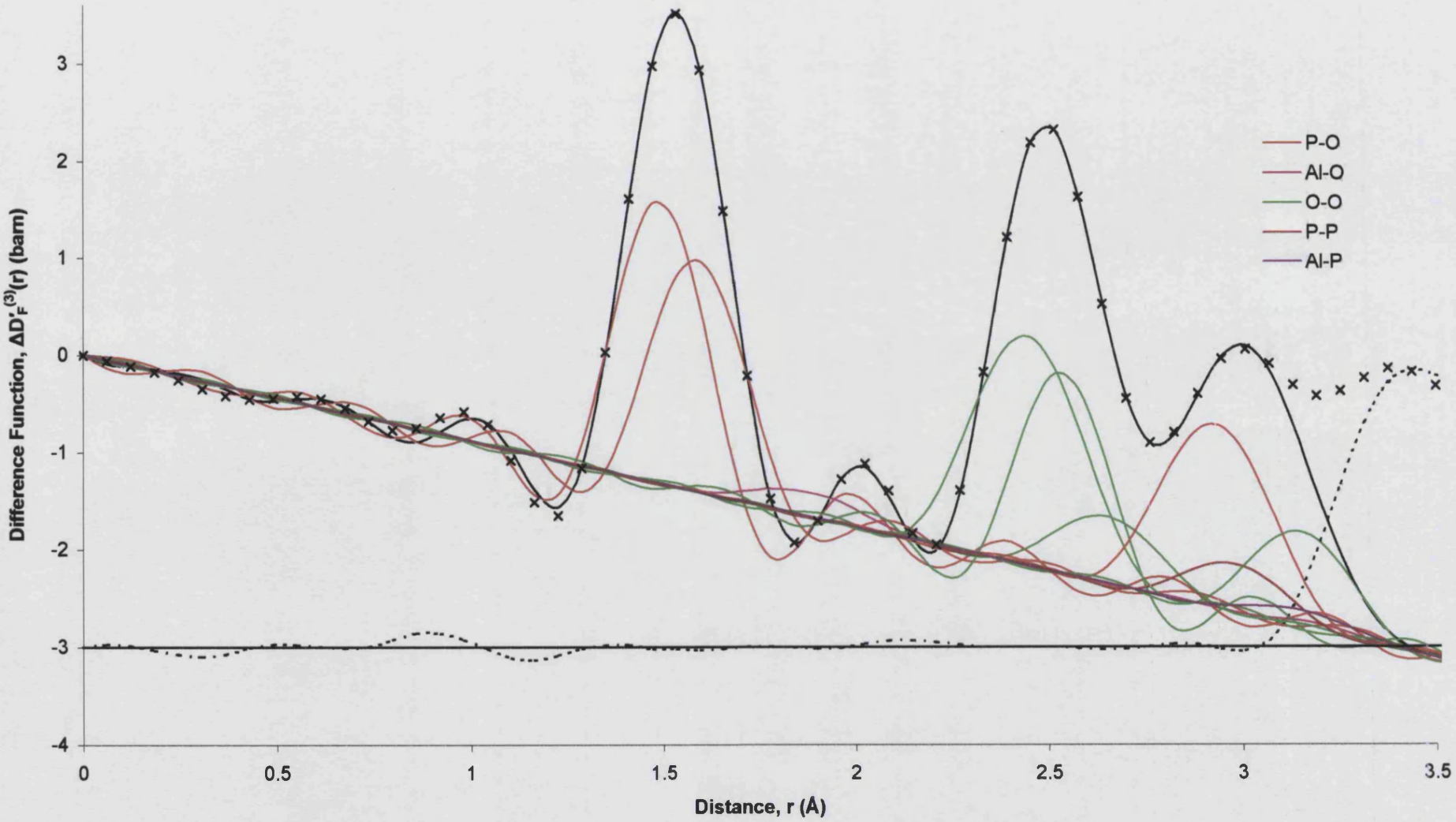

Figure 7.16. The difference function $\Delta D'_F{}^{(3)}(r)$ (crosses), the fitted data (solid curve) and the individual convoluted Gaussians. The residual (dashed curve) is offset by -3 barn.

As described in section 7.3 the level of contamination present was sufficiently small that the difference functions could be modelled assuming perfect isomorphism: unlike the La / Ce glasses presented in Chapter 6, it was not necessary to take the impurities into consideration. Once the difference functions $\Delta D'_R(r)$ and $\Delta G'_F(r)$ had been modelled the Gaussian parameters, r, C_N and σ, were used to start the fitting process for the total pair distribution functions. Small refinements to these parameters were required to obtain the best fits.

D'(r), the individual convoluted Gaussians, the sum of the convoluted Gaussians and the residual for the DyC, DyHoE and HoG samples are given in Figures 7.17 – 7.20 respectively. The R_χ values for DyC, DyHoE and HoG for $1.0 \leq r$ (Å) ≤ 3.0 are 0.0167, 0.0200 and 0.0202 respectively. The Gaussian parameters r, C_N and σ, used to model the real space data for the total pair distribution functions are given in Table 7.8.

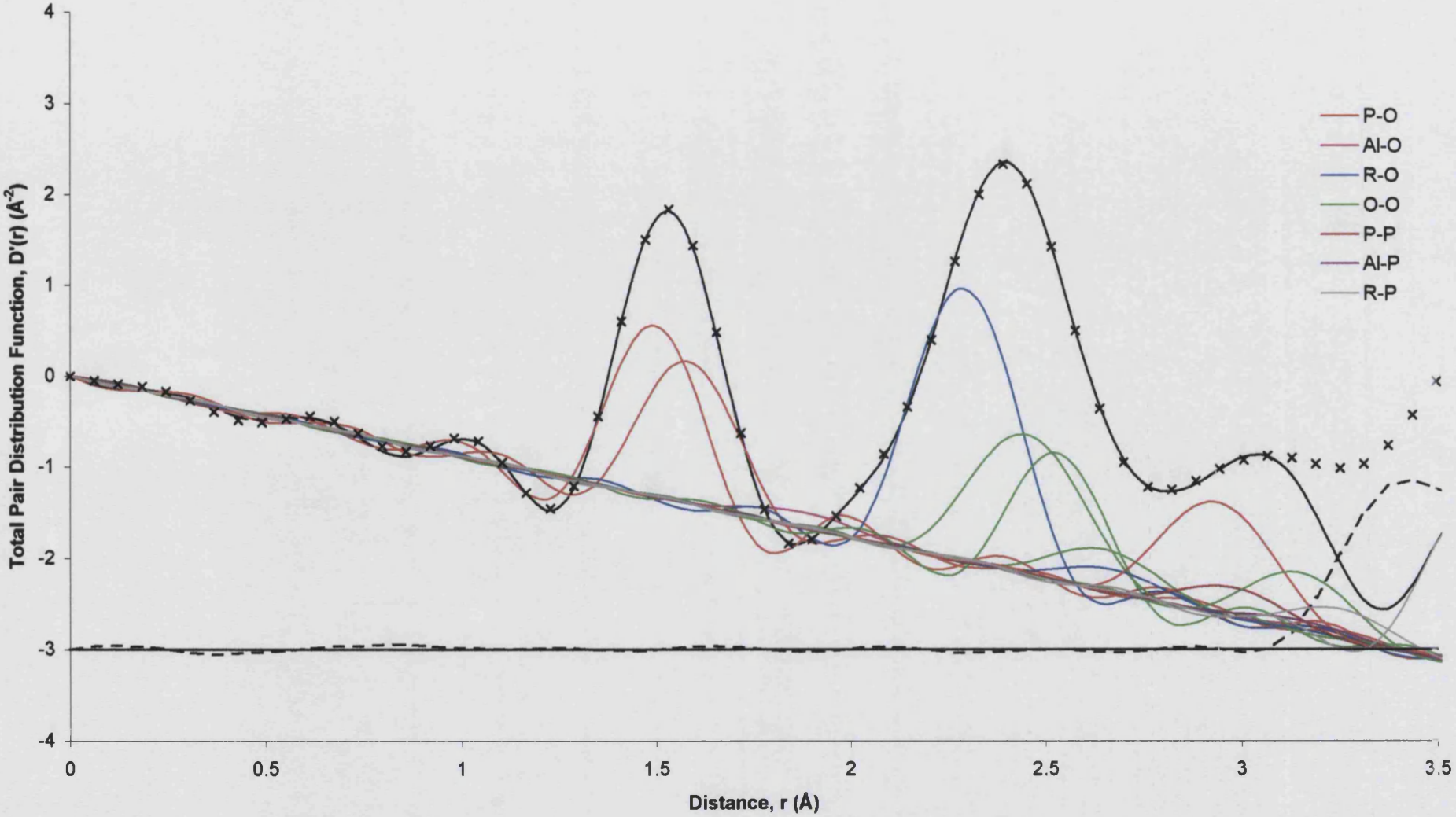

Figure 7.17. The total pair distribution function D'(r) (crosses), the modelled data (solid curve) and the individual convoluted Gaussians for sample DyC. The residual (dashed curve) is offset by -3 barn.

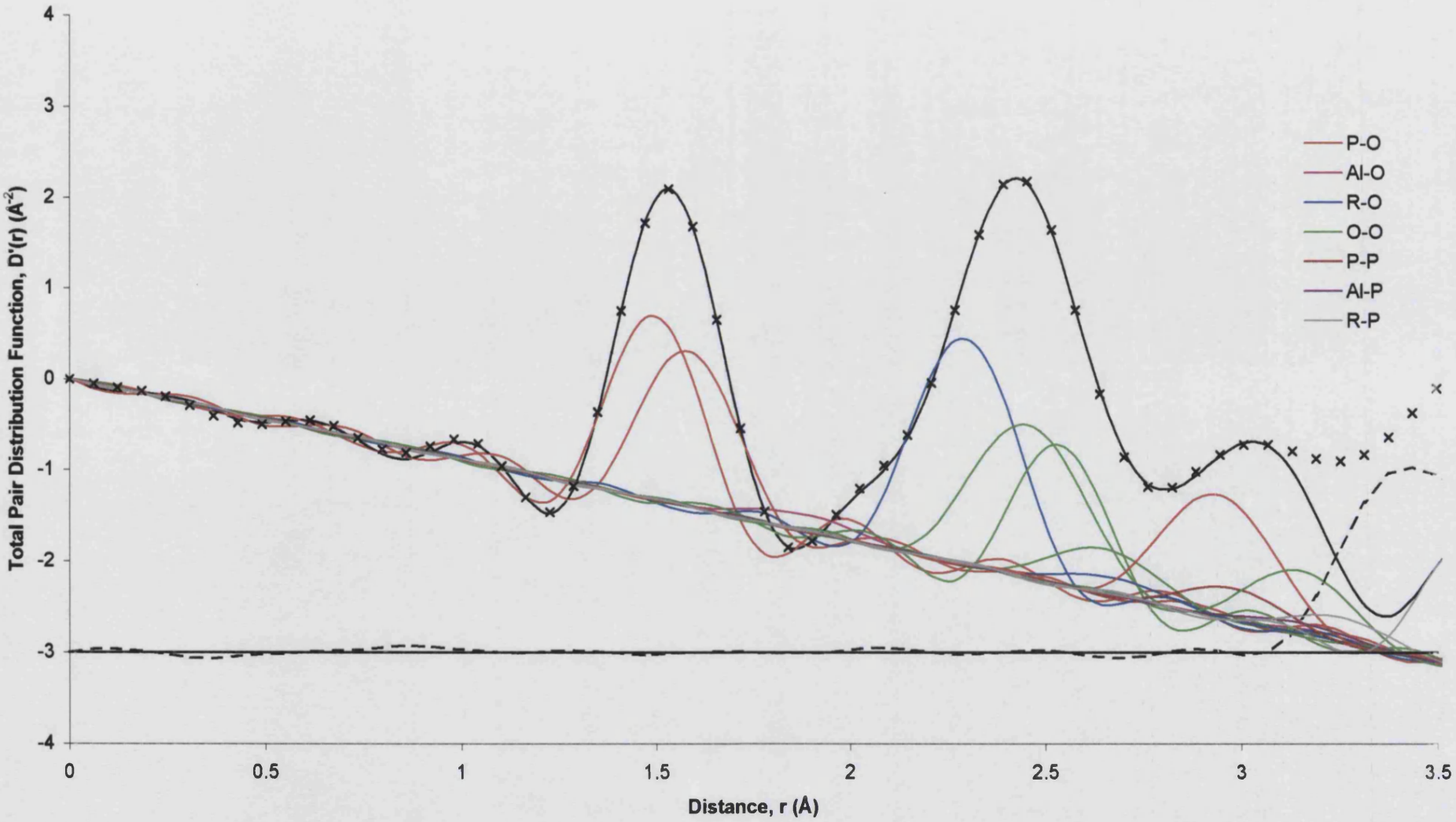

Figure 7.18. The total pair distribution function D'(r) (crosses), the modelled data (solid curve) and the individual convoluted Gaussians for sample DyHoE. The residual (dashed curve) is offset by -3 barn.

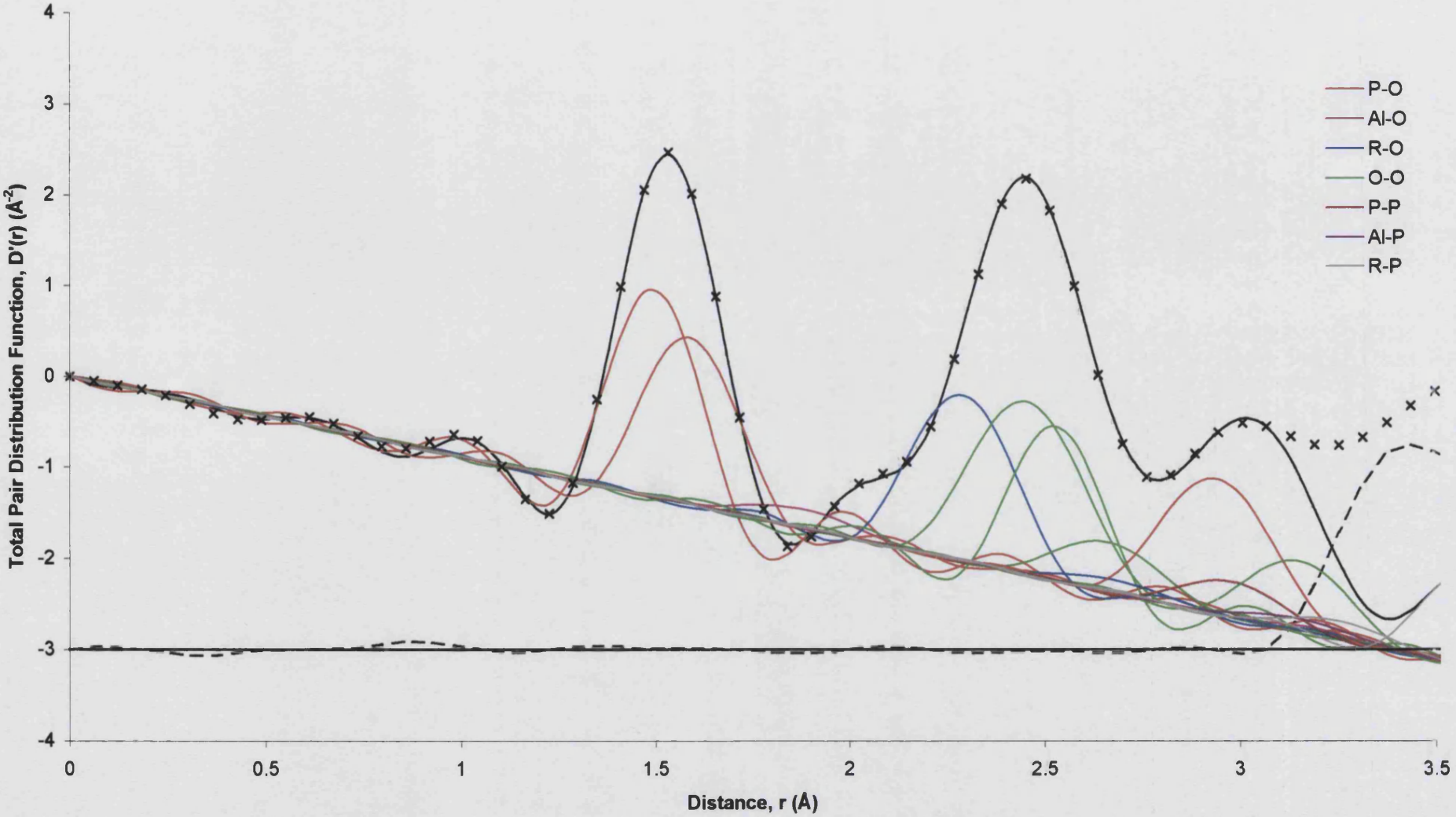

Figure 7.19. The total pair distribution function D'(r) (crosses), the modelled data (solid curve) and the indiviudal convoluted Gaussians for sample HoG. The residual (dashed curve) is offset by -3 barn.

	DyC			DyHoE			HoG		
	r (Å)	C_N	σ (Å)	r (Å)	C_N	σ (Å)	r (Å)	C_N	σ (Å)
P-O_T	1.495(10)	2.05(10)	0.050(5)	1.495(10)	2.05(10)	0.055(5)	1.495(10)	2.05(10)	0.050(5)
P-O_B	1.585(10)	2.10(10)	0.085(5)	1.585(10)	2.10(10)	0.085(5)	1.590(10)	2.10(10)	0.090(5)
Al-O	1.88(1)	5.5(5)	0.120(10)	1.88(1)	5.5(5)	0.120(10)	1.88(1)	5.5(5)	0.120(10)
R-O	2.293(10)	6.15(10)	0.110(10)	2.295(10)	6.15(10)	0.110(10)	2.290(10)	6.15(10)	0.110(10)
O-(P)-O	2.453(10)	2.2(1)	0.130(10)	2.455(10)	2.2(1)	0.130(10)	2.455(10)	2.25(1)	0.130(10)
O-(P)-O	2.53(1)	1.4(1)	0.060(10)	2.535(10)	1.4(1)	0.060(10)	2.53(1)	1.4(1)	0.060(10)
O-(Al)-O	2.65(1)	0.63(10)	0.115(10)	2.65(1)	0.63(10)	0.115(10)	2.66(1)	0.63(10)	0.115(10)
R-O	2.67(1)	0.55(10)	0.100(10)	2.67(1)	0.55(10)	0.100(10)	2.67(1)	0.55(10)	0.110(10)
P-(OP)-O	2.94(1)	4.0(1)	0.130(10)	2.94(1)	4.0(1)	0.130(10)	2.94(1)	4.0(1)	0.130(10)
P-P	2.98(2)	2.0(1)	0.100(10)	2.98(2)	2.0(1)	0.100(10)	2.98(2)	2.0(1)	0.100(10)
O-(R)-O	3.15(2)	1.0(1)	0.105(10)	3.15(2)	1.0(1)	0.105(10)	3.15(2)	1.0(1)	0.105(10)
Al-P	3.15(2)	6.0(5)	0.10(1)	3.15(2)	6.0(5)	0.10(1)	3.15(2)	6.0(5)	0.10(1)
R-P	3.25(2)	1.0(1)	0.10(1)	3.25(2)	1.0(1)	0.10(1)	3.25(2)	1.0(1)	0.10(1)
R-P	3.60(2)	6.0(1)	0.10(1)	3.60(2)	6.0(1)	0.10(1)	3.60(2)	6.0(1)	0.10(1)

Table 7.8. A summary of the Gaussian parameters used to model the total pair distribution function D′(r) for the DyC, DyHoE and HoG glasses.

The partial structure factor, $S_{RR}(Q)$, obtained using equation 4.55 is shown in Figure 7.20 and the corresponding $g'_{RR}(r)$ is shown in Figure 7.21. By comparison with Table 7.4, large negative weighted contaminations are expected for the P-O and R-O correlations at ≈ 1.54 Å and 2.29 Å and a large positive weighted contamination is expected from the O-O correlations at ≈ 2.48 Å. However, the low r oscillations in $g'_{RR}(r)$ show no clear evidence for such contamination. For example, the peak at ≈ 1.54 Å is positive rather than negative, which indicates that it does not arise from unwanted P-O correlations. The peak at 2.21(2) Å is positive rather than negative and is shifted relative to the expected R-O distance, which indicates that it does not arise from unwanted R-O correlations. The peak at 2.55(2) Å is negative rather than positive and is shifted relative to the expected O-O distance, which indicates that it does not arise from unwanted O-O correlations. The low r oscillations extending up to 4.5 Å or 5.1 Å were then set equal to the $g_{RR}(0)$ limit to maintain or eliminate the peak at 4.7 Å. The corresponding Fourier back transforms were then compared with $S_{RR}(Q)$ and it was found that the best agreement over the entire Q-space range was obtained by elimination of the peak at 4.7 Å (Figure 7.20), consistent with a nearest neighbour R-R distance of 5.52(2) Å. The coordination number obtained by integrating this peak over the range $5.1 \leq r\ (Å) \leq 7.2$ is 8.0(2), which compares with an R-R nearest neighbour coordination number of eight found for crystalline ErP_3O_9 (Dorokhova and Karpov 1984) in the region $5.37 \leq r\ (Å) \leq 7.2$.

The dominant features in $S_{RR}(Q)$ are the so-called first sharp diffraction peak at ≈ 1.5 $Å^{-1}$ and a second peak at ≈ 2.45 $Å^{-1}$. To obtain the corresponding real space information the data was smoothly truncated by applying a severe cosine window function extending over the range 4.0 $Å^{-1}$ to 5.0 $Å^{-1}$ and the data Fourier transformed. As shown in Figure 7.23, the resultant $g'_{RR}(r)$ has a first peak at 5.65 Å and no clearly identifiable features at lower r. The corresponding coordination number is 8.8(2).

We therefore conclude that the nearest neighbour R-R correlations in the phosphate glasses extended over the range $5.37 \leq r\ (Å) \leq 7.2$ as shown in Figure 7.21 and give an R-R coordination number of 8.0(2). This compares with a distribution of eight R-R nearest neighbours for crystalline ErP_3O_9 (Dorokhova and Karpov 1984) extending over the range 5.37 – 6.97 Å and a distribution of six nearest neighbours for crystalline HoP_5O_{14} (Bagieu *et al* 1973) extending over the range 5.71 – 7.06 Å.

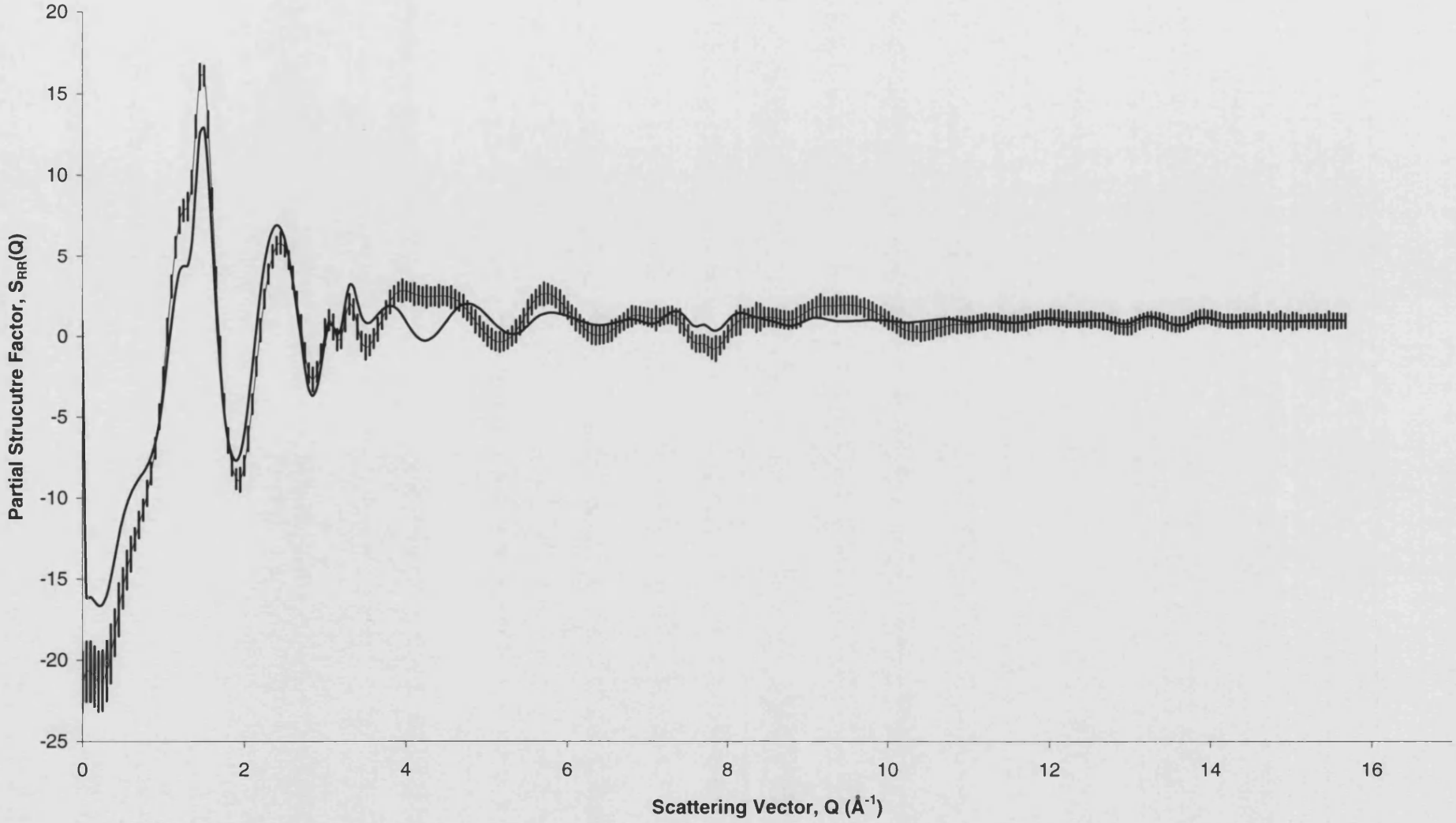

Figure 7.20. The partial structure factor $S_{RR}(Q)$ (dashed curve with errors) and the Fourier backtransform of $g'_{RR}(r)$ given by the solid curve in Figure 7.21.

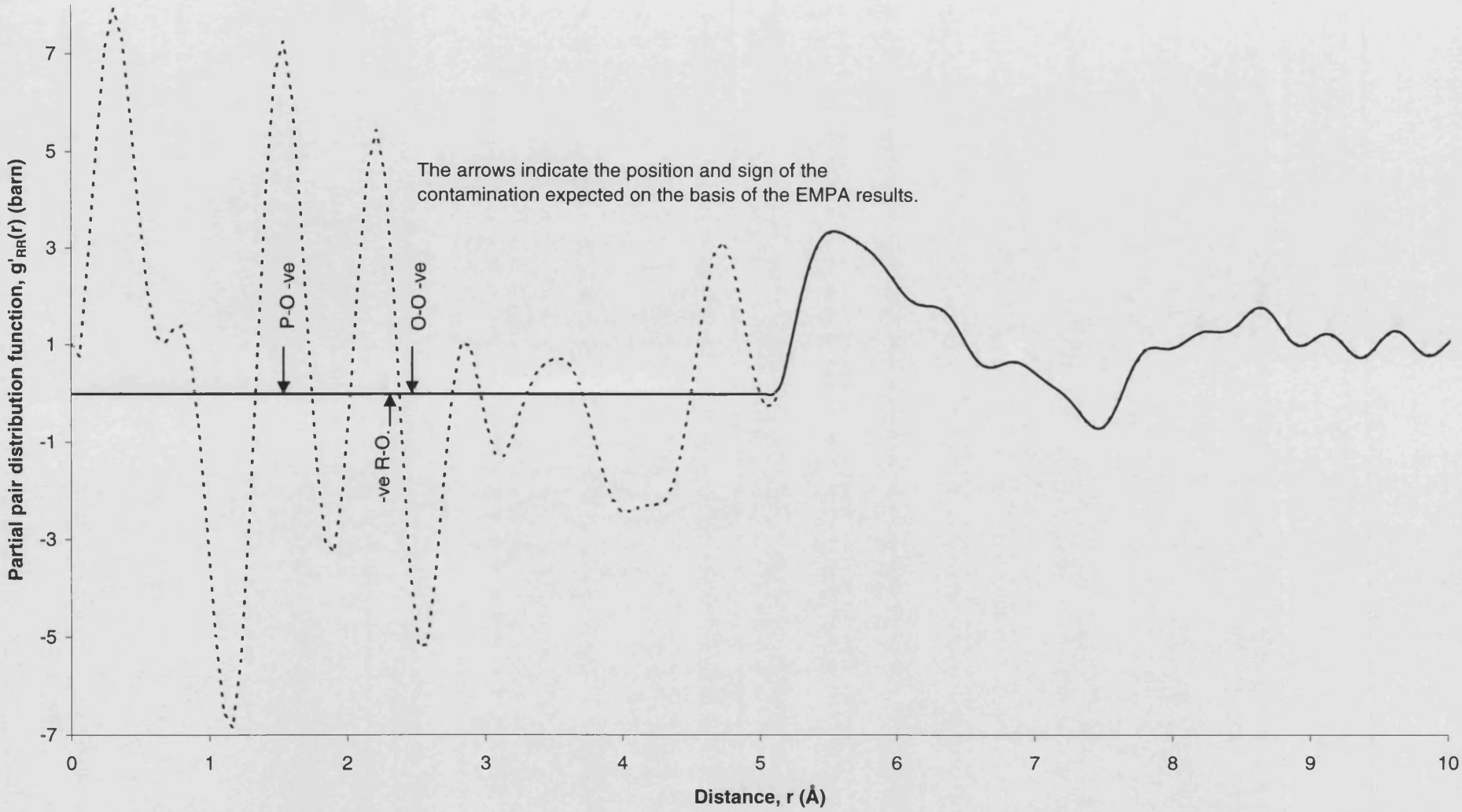

Figure 7.21. The real space function $g'_{RR}(r)$ (solid curve) obtained by Fourier transforming $S_{RR}(Q)$ given by the points with error bars in Figure 7.20. The low r unphysical oscillations are shown by the dashed curve.

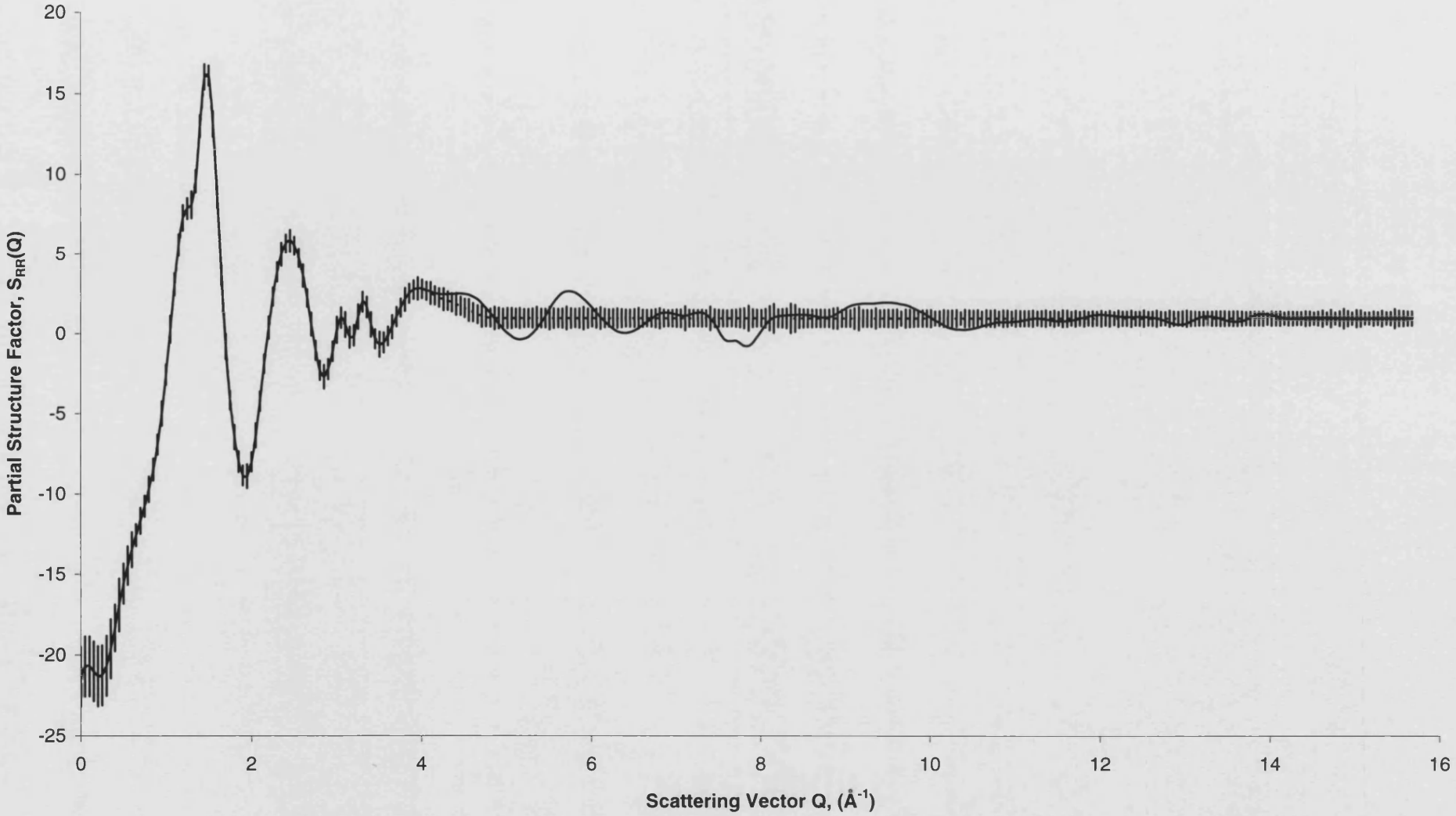

Figure 7.22. The partial structure factor $S_{RR}(Q)$ obtained by applying a cosine window over the region 4.0 - 5.0 $Å^{-1}$ (points with error bars) compared with $S_{RR}(Q)$, given in Figure 7.20 (solid curve).

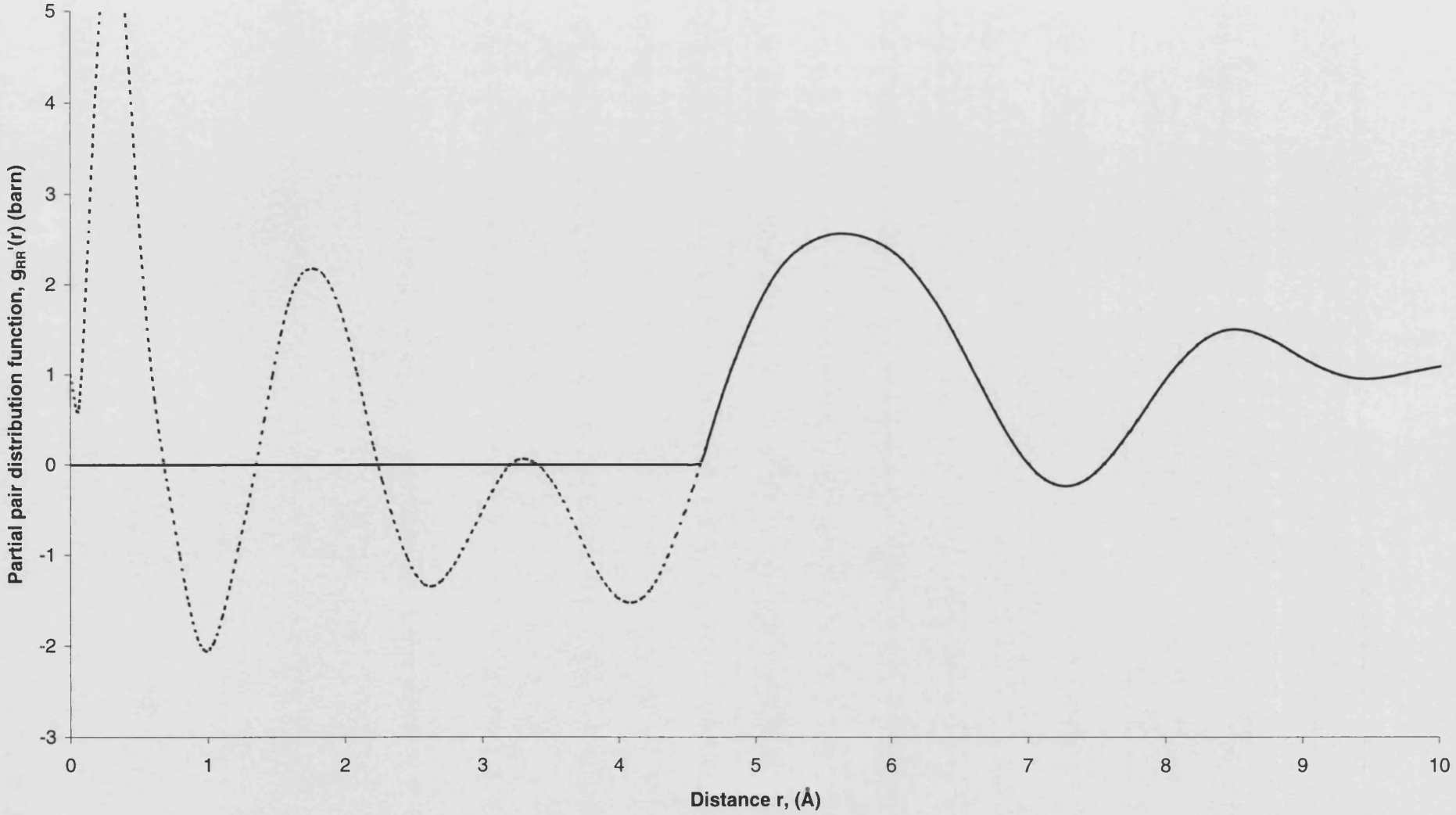

Figure 7.23. The real space function $g'_{RR}(r)$ obtained by Fourier transforming $S_{RR}(Q)$ given by the points with error bars in Figure 7.22.

The metal-matrix difference functions, $\Delta_{R\mu}(Q)$, shown in Figure 7.24 were obtained using equation 7.5 using the partial structure factor, $S_{RR}(Q)$, given by the solid curve in Figure 7.20. This represents the back Fourier transform of $g'_{RR}(r)$, with the low r oscillations set equal to $g_{RR}(0)$, such that the unphysical oscillations in Figure 7.20 do not contribute to the $\Delta G_{R\mu}(r)$ functions. From equation 7.5 it can be seen that $\Delta_{R\mu}^{(1)}(Q) / [b_{Dy} - b_{Ho}] = \Delta_{R\mu}^{(2)}(Q) / [b_{Dy} - b_{Dy/Ho}] = \Delta_{R\mu}^{(3)}(Q) / [b_{Dy/Ho} - b_{Ho}]$ such that the functions $\Delta_{R\mu}^{(1)}(Q) - \frac{b_{Dy} - b_{Ho}}{b_{Dy} - b_{Dy/Ho}} \Delta_{R\mu}^{(2)}(Q)$ and $\Delta_{R\mu}^{(1)}(Q) - \frac{b_{Dy} - b_{Ho}}{b_{Dy/Ho} - b_{Ho}} \Delta_{R\mu}^{(3)}(Q)$ should yield curves with negligible structure if the $\Delta_{R\mu}(Q)$ functions have been accurately measured. This contrasts with the case of the first order difference functions $\Delta_R(Q)$ shown in Figure 7.7 in which $S_{RR}(Q)$ has a marked effect at the lower Q values.

As required, the functions $\Delta_{R\mu}^{(1)}(Q) - \frac{b_{Dy} - b_{Ho}}{b_{Dy} - b_{Dy/Ho}} \Delta_{R\mu}^{(2)}(Q)$ and $\Delta_{R\mu}^{(1)}(Q) - \frac{b_{Dy} - b_{Ho}}{b_{Dy/Ho} - b_{Ho}} \Delta_{R\mu}^{(3)}(Q)$ shown in Figures 7.24 have no obvious structure which is indicative of a negligible contribution to the $\Delta_{R\mu}(Q)$ from the contamination correlations i.e. the neutron diffraction data indicates that the compositions of the different glasses are closer than suggested by the EPMA results. In addition the metal-matrix difference functions, $\Delta_{R\mu}(Q)$, and the back Fourier transforms of the corresponding $\Delta G_{R\mu}'(r)$ with the unphysical low r oscillations set equal to the $\Delta G_{R\mu}(0)$ limit (Figure 7.25) are in close agreement as illustrated in Figure 7.24. The functions $\Delta G'^{(1)}_{R\mu}(r) - \frac{b_{Dy} - b_{Ho}}{b_{Dy} - b_{Dy/Ho}} \Delta G'^{(2)}_{R\mu}(r)$ and $\Delta G_{R\mu}^{(1)}(r) - \frac{b_{Dy} - b_{Ho}}{b_{Dy/Ho} - b_{Ho}} \Delta G'^{(3)}_{R\mu}(r)$ shown in Figure 7.25, also give negligible structure.

The matrix-matrix difference functions, $\Delta_{\mu\mu}(Q)$, were obtained using equation 7.6 using the partial structure factor, $S_{RR}(Q)$, given by the solid curve in Figure 7.20. This represents the back Fourier transform of $g'_{RR}(r)$, with the low r oscillations set equal to $g_{RR}(0)$, such that the unphysical oscillations in Figure 7.20 do not contribute to the $\Delta G_{\mu\mu}(r)$ functions. From equation 7.6 it can be seen that $\Delta_{\mu\mu}^{(1)}(Q) = \Delta_{\mu\mu}^{(2)}(Q) =$

$\Delta_{\mu\mu}^{(3)}(Q)$ such that the functions $\Delta_{\mu\mu}^{(1)}(Q) - \Delta_{\mu\mu}^{(2)}(Q)$ and $\Delta_{\mu\mu}^{(1)}(Q) - \Delta_{\mu\mu}^{(3)}(Q)$ should yield curves with negligible structure if the $\Delta_{\mu\mu}(Q)$ have been accurately measured. This contrasts with the case of the total minus weighted difference functions $\Delta_F(Q)$ shown in Figure 7.9 in which $S_{RR}(Q)$ has a marked effect at the lower Q values.

As required, the difference functions $\Delta_{\mu\mu}^{(1)}(Q) - \Delta_{\mu\mu}^{(2)}(Q)$ and $\Delta_{\mu\mu}^{(1)}(Q) - \Delta_{\mu\mu}^{(3)}(Q)$ shown in Figure 7.26 have no obvious structure which is indicative of a negligible contribution to the $\Delta_{\mu\mu}(Q)$ from the contamination correlations i.e. the neutron diffraction data again indicate that the compositions of the different glasses are closer than suggested by the EPMA results. In addition, the matrix-matrix difference functions, $\Delta_{\mu\mu}(Q)$, and the back Fourier transforms of the corresponding $\Delta G'_{\mu\mu}(r)$, with the unphysical low r oscillations set equal to the $\Delta G_{\mu\mu}(0)$ limit (Figure 7.27), are in close agreement as illustrated in Figure 7.26. The difference functions $\Delta G'^{(1)}_{\mu\mu}(r) - \Delta G'^{(2)}_{\mu\mu}(r)$ and $\Delta G'^{(1)}_{\mu\mu}(r) - \Delta G'^{(3)}_{\mu\mu}(r)$ shown in Figure 7.27 also give negligible structure.

The metal-matrix difference functions $\Delta D'_{R\mu}(r)$ were modelled using the fitting procedure outlined in section 4.9. The measured function $\Delta D'_{R\mu}(r)$, the individual convoluted Gaussians, their sum and the residual are shown in Figures 7.28 - 7.30. The R_χ values for the fitting region of $2.0 \leq r$ (Å) ≤ 3.0 are 0.0161, 0.0246 and 0.0164 for $\Delta D'^{(1)}_{R\mu}(r)$, $\Delta D'^{(2)}_{R\mu}(r)$ and $\Delta D'^{(3)}_{R\mu}(r)$ respectively (section 5.10). The parameters describing the fitted Gaussians are summarised in Table 7.9. The Gaussian parameters used to model the metal-matrix difference functions are identical to those used to model the first order difference functions (Table 7.6), which is expected, since the first physical feature in the partial pair distribution function $g'_{RR}(r)$ occurs at > 5 Å.

Next, the matrix-matrix difference functions, $\Delta D'_{\mu\mu}(r)$, were modelled. The measured function $\Delta D'_{\mu\mu}(r)$, the individual convoluted Gaussians, their sum and the residual are shown in Figures 7.31 - 7.33. The R_χ value for the fitting region of $1.0 \leq r$ (Å) ≤ 3.0 is 0.0237, 0.0274 and 0.0276 for $\Delta D'^{(1)}_{\mu\mu}(r)$, $\Delta D'^{(2)}_{\mu\mu}(r)$ and $\Delta D'^{(3)}_{\mu\mu}(r)$ respectively (section 5.10). The parameters describing the fitted Gaussians are summarised in Table 7.10. The Gaussian parameters used to model the matrix-matrix difference functions are identical to those used to model the total minus weighted difference functions (Table 7.7), which is expected since the first physical feature in the partial structure factor $g'_{RR}(r)$ occurs at > 5 Å.

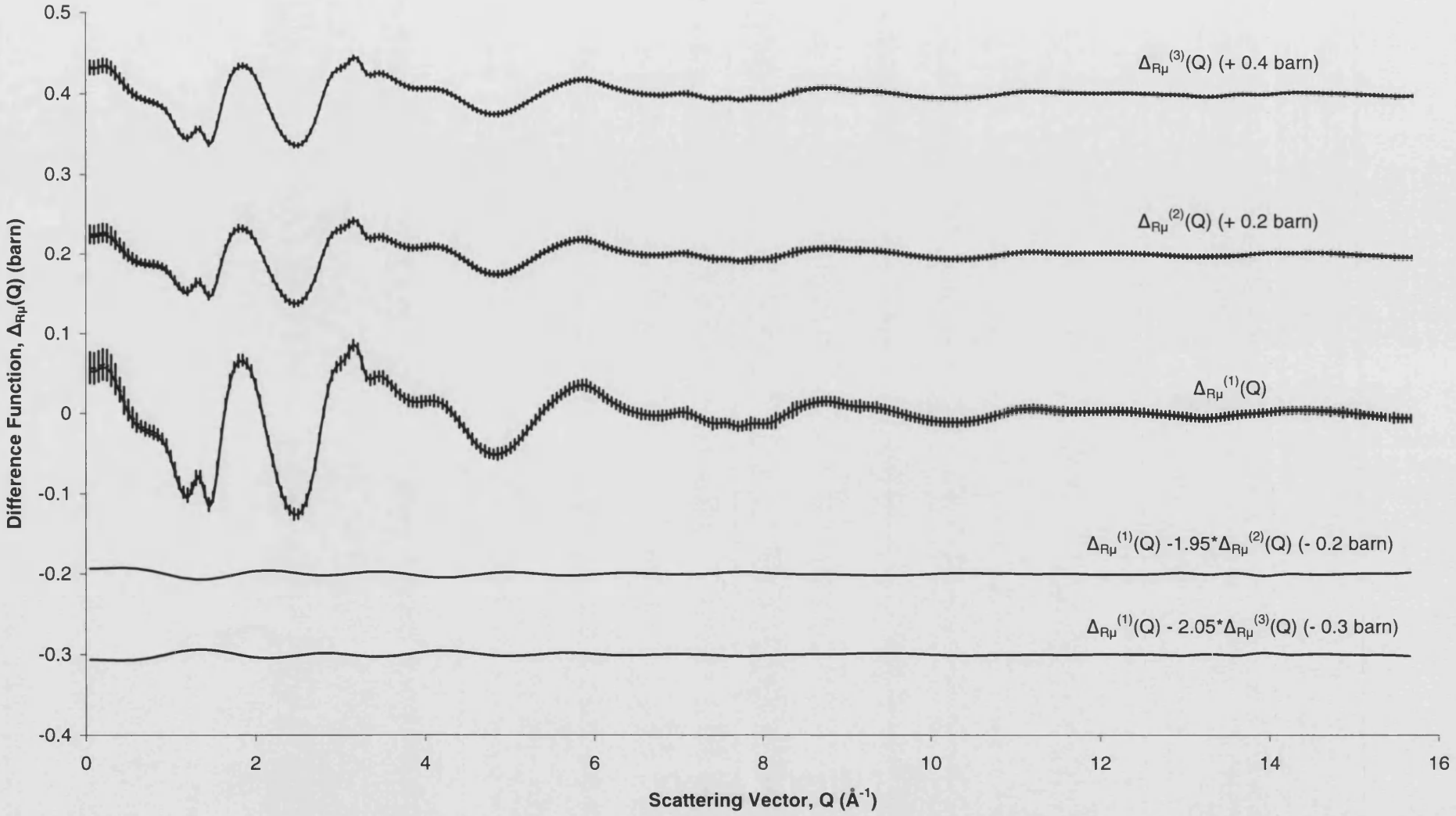

Figure 7.24. The difference functions $\Delta_{R\mu}(Q)$ (dashed curve with error bars) and the Fourier backtransforms of the $\Delta G'_{R\mu}(r)$ (solid curves) given by the solid curves in Figure 7.25.

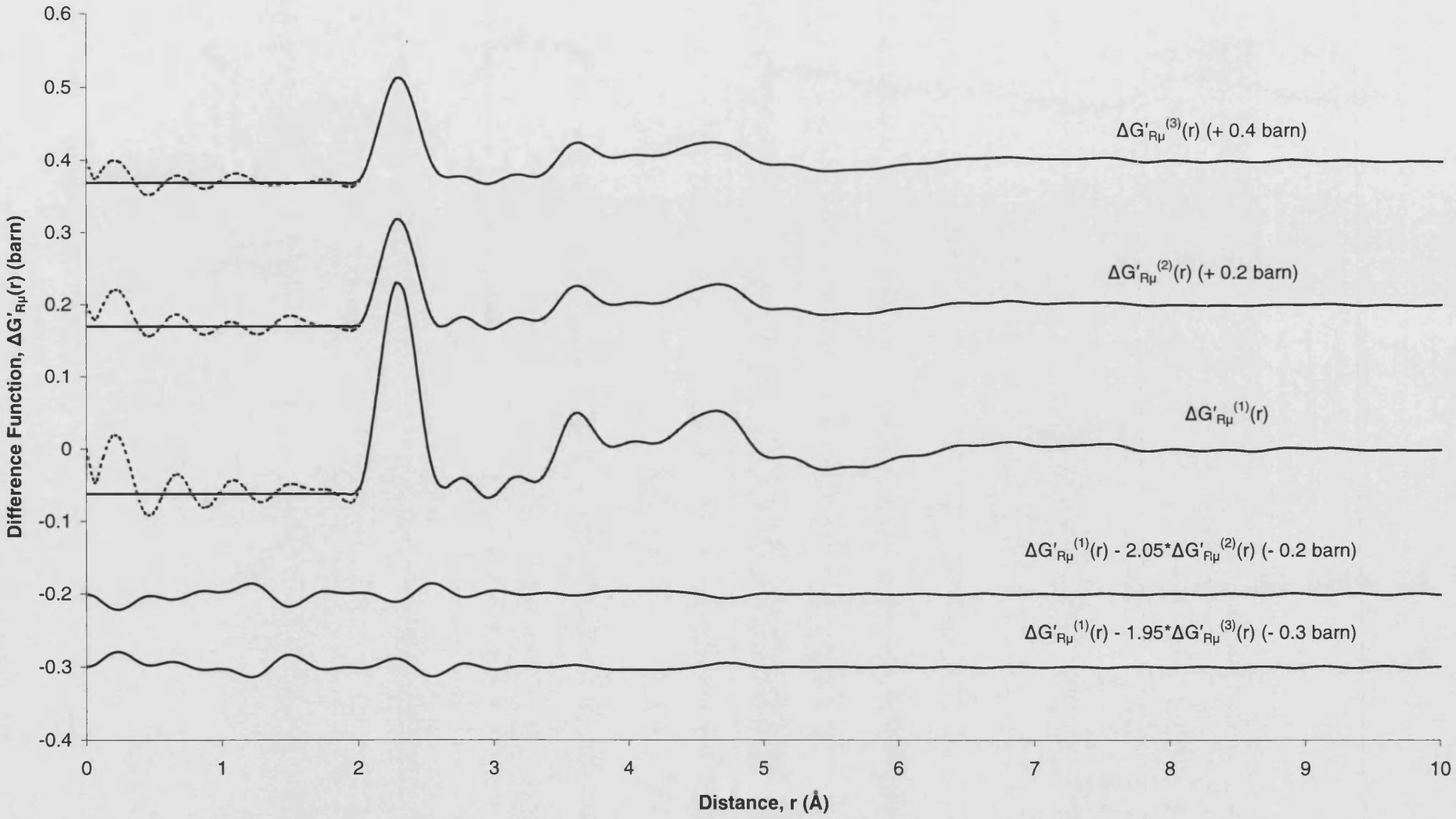

Figure 7.25.The real space functions $\Delta G'_{R\mu}(r)$ (solid curves) obtained by Fourier transforming the $\Delta_{R\mu}(Q)$ given by the dashed curves in Figure 7.24. The unphysical low r oscillations are shown by the dashed curves.

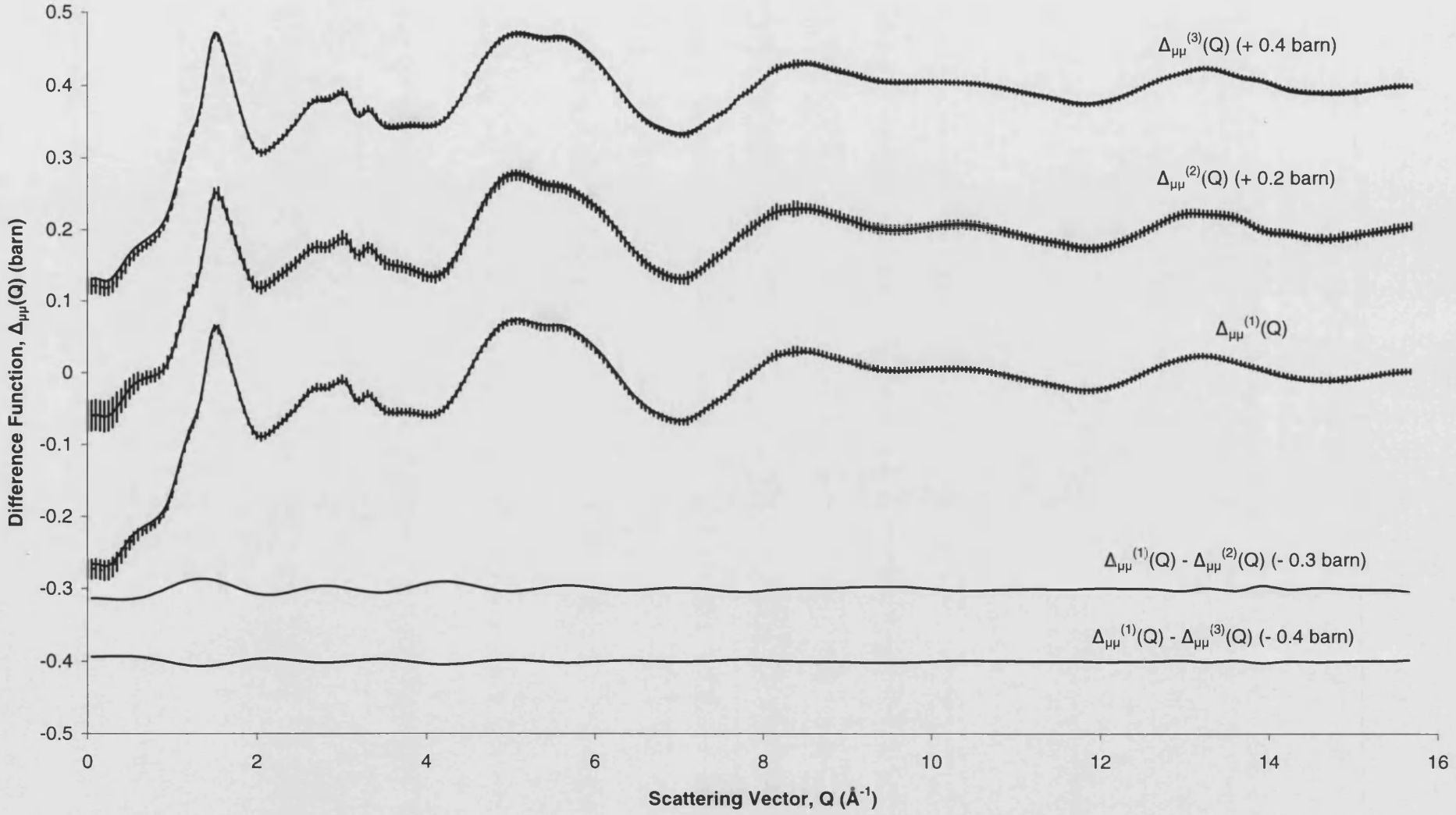

Figure 7.26. The difference functions, $\Delta_{\mu\mu}(Q)$, (dashed curves with error bars) and the Fourier backtransforms of the $\Delta G'_{\mu\mu}(r)$ (solid curve) given by the solid curves in Figure 7.27.

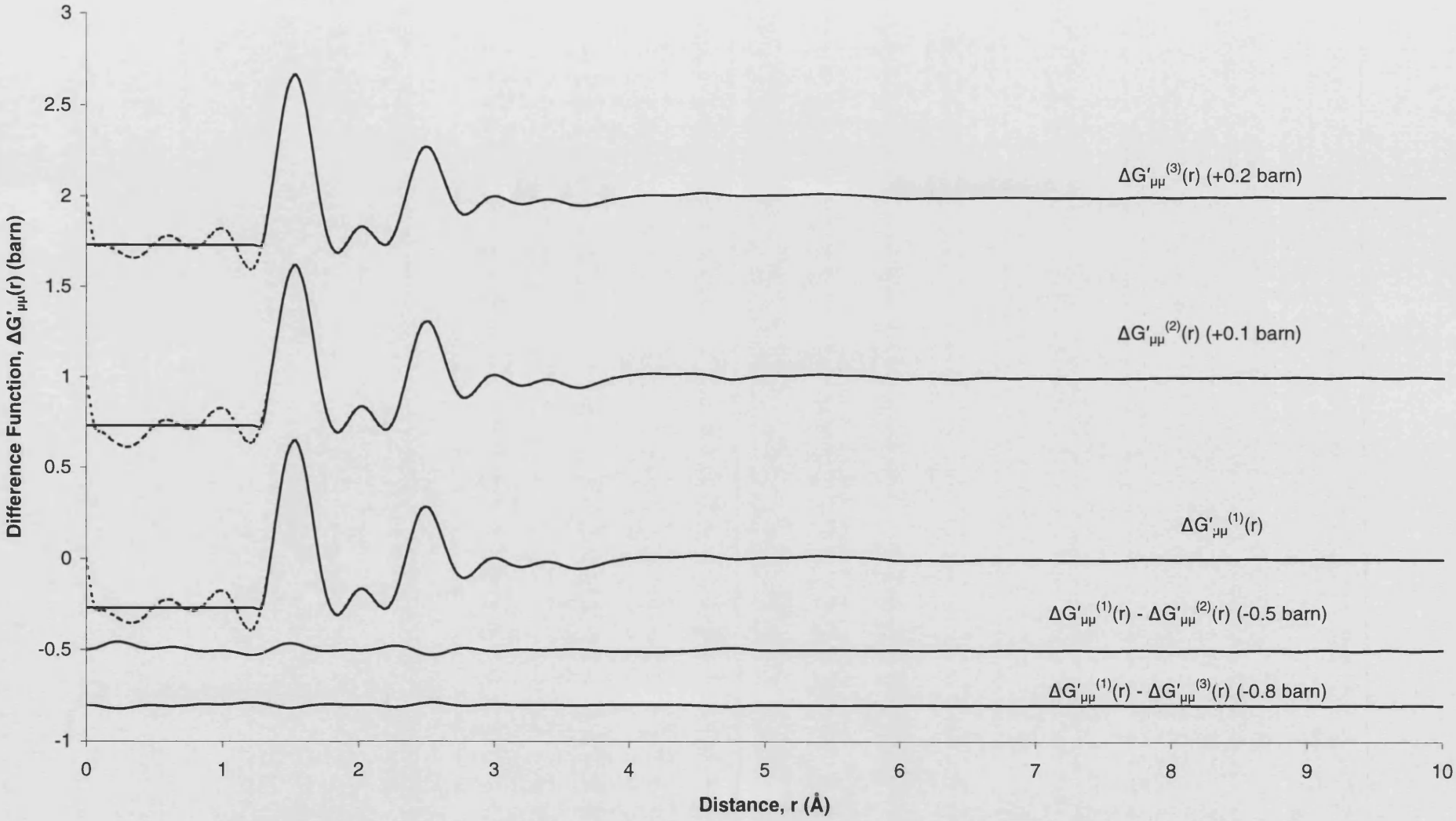

Figure 7.27. The real space functions, $\Delta G'_{\mu\mu}(r)$ (solid curves) obtained by Fourier transforming the $\Delta_{\mu\mu}(Q)$ given by the dashed curves in Figure 7.26. The unphysical low r oscillations are shown by the dashed curves.

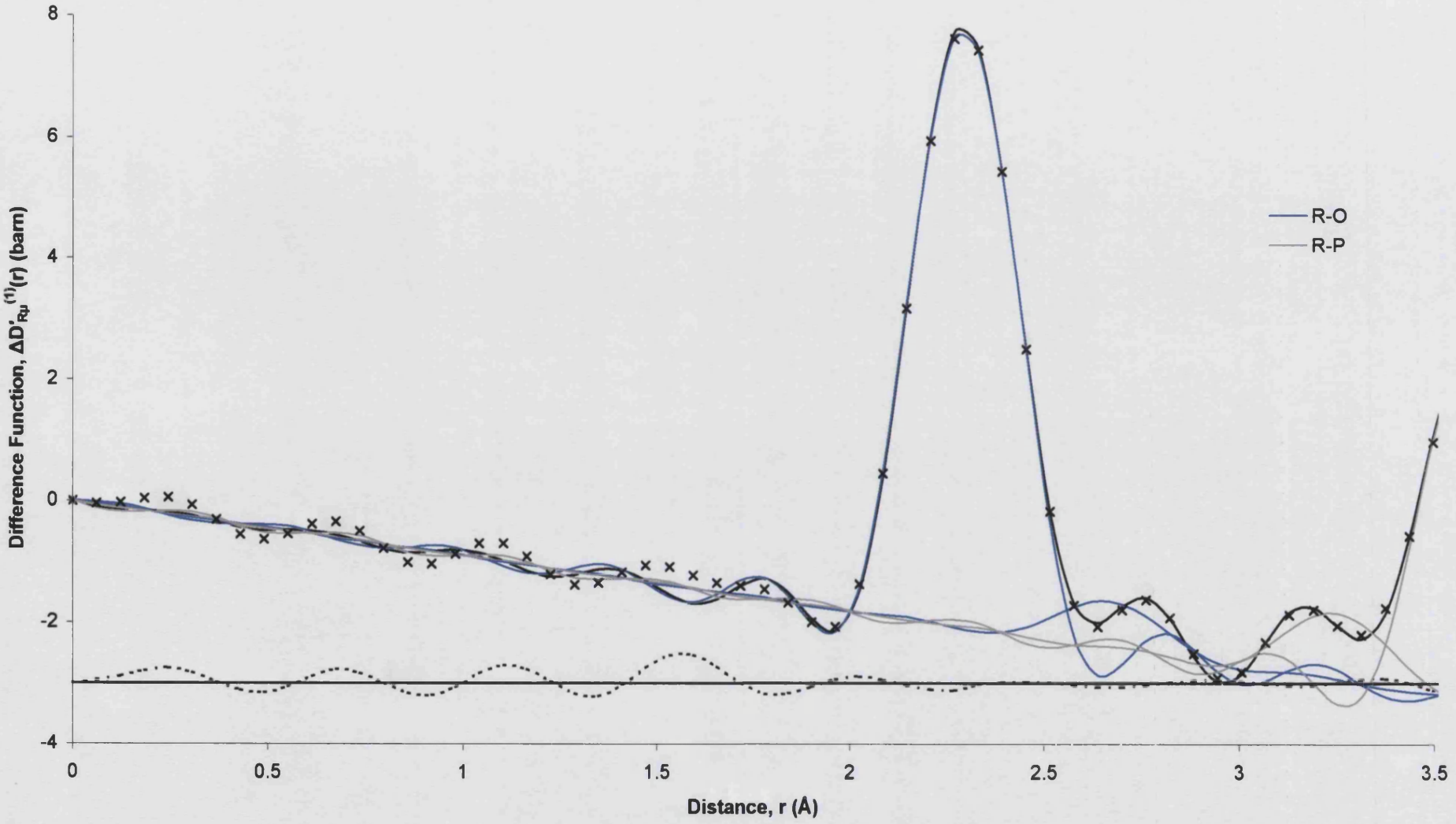

Figure 7.28. The difference function $\Delta D'_{R\mu}{}^{(1)}(r)$ (crosses), the fitted data (solid curve) and the individual convoluted R-O and R-P Gaussians. The residual (dashed curve) is offset by -3 barn.

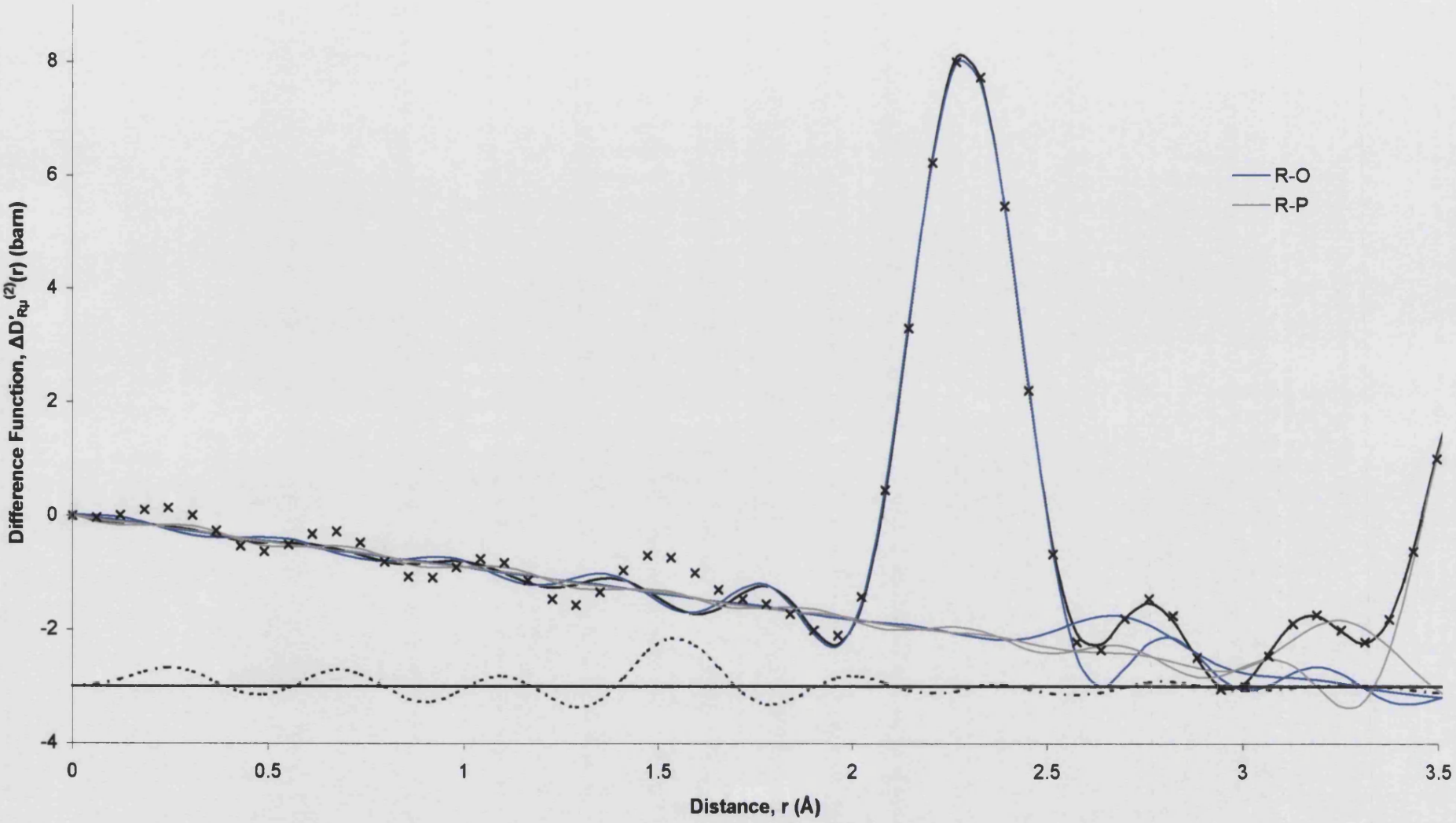

Figure 7.29. The difference function $\Delta D'_{R\mu}{}^{(2)}(r)$ (crosses), the fitted data (solid curve) and the individual convoluted R-O and R-P Gaussians. The residual (dashed curve) is offset by -3 barn.

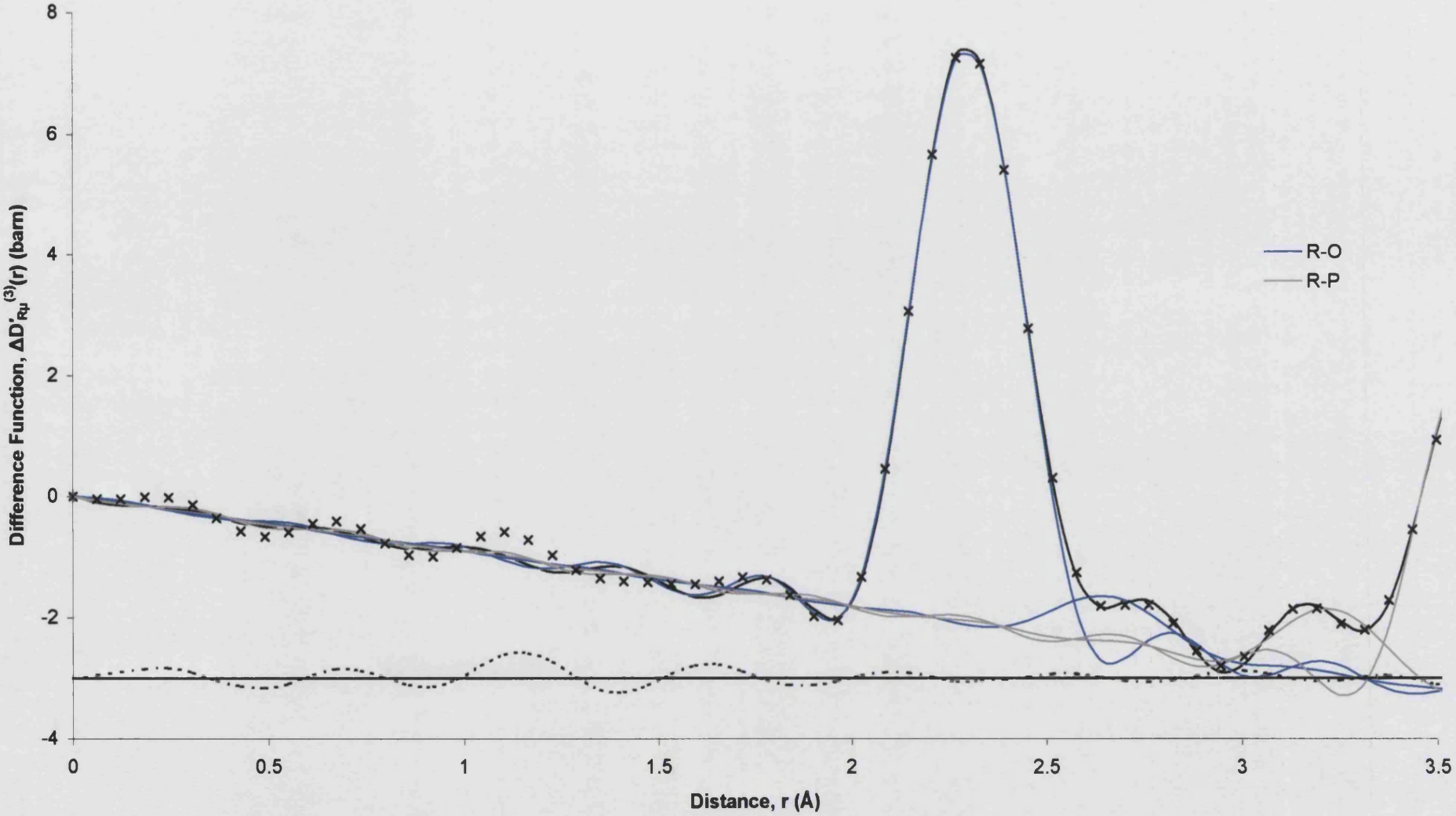

Figure 7.30. The difference function $\Delta D'_{R\mu}{}^{(3)}(r)$ (crosses), the fitted data (solid curve) and the individual convoluted R-O and R-P Gaussians. The residual (dashed curve) is offset by -3 barn.

	$\Delta D'_{R\mu}{}^{(1)}(r)$			$\Delta D'_{R\mu}{}^{(2)}(r)$			$\Delta D'_{R\mu}{}^{(3)}(r)$		
	r (Å)	C_N	σ (Å)	r (Å)	C_N	σ (Å)	r (Å)	C_N	σ (Å)
R-O	2.295(10)	6.20(10)	0.112(10)	2.292(10)	6.20(10)	0.107(10)	2.30(1)	6.20(10)	0.118(10)
R-O	2.67(1)	0.55(10)	0.108(10)	2.69(1)	0.50(10)	0.110(10)	2.66(1)	0.55(10)	0.110(10)
R-P	3.25(2)	1.1(1)	0.110(10)	3.26(2)	1.1(1)	0.107(10)	3.23(2)	1.00(10)	0.100(10)
R-P	3.60(2)	6.0(1)	0.100(10)	3.60(2)	6.0(1)	0.100(10)	3.595(2)	6.00(10)	0.105(10)

Table 7.9. A summary of the Gaussian parameters used to model the difference functions $\Delta D'_{R\mu}(r)$.

	$\Delta D'_{\mu\mu}{}^{(1)}(r)$			$\Delta D'_{\mu\mu}{}^{(2)}(r)$			$\Delta D'_{\mu\mu}{}^{(3)}(r)$		
	r (Å)	C_N	σ (Å)	r (Å)	C_N	σ (Å)	r (Å)	C_N	σ (Å)
P-O_T	1.490(10)	2.05(10)	0.055(5)	1.490(10)	2.05(10)	0.065(5)	1.490(10)	2.10(10)	0.055(5)
P-O_B	1.590(10)	2.10(10)	0.090(5)	1.590(10)	2.05(10)	0.090(5)	1.590(10)	2.10(10)	0.085(5)
Al-O	1.880(10)	5.5(5)	0.120(10)	1.880(10)	5.5(5)	0.120(10)	1.880(10)	5.5(5)	0.120(10)
O-(P)-O	2.445(10)	2.2(1)	0.130(10)	2.460(10)	2.2(1)	0.125(10)	2.445(10)	2.2(1)	0.130(10)
O-(P)-O	2.535(10)	1.4(1)	0.055(10)	2.530(10)	1.4(1)	0.050(10)	2.535(10)	1.35(10)	0.060(10)
O-(Al)-O	2.65(1)	0.63(10)	0.115(10)	2.65(1)	0.63(10)	0.115(10)	2.65(1)	0.63(10)	0.115(10)
P-(OP)-O	2.93(1)	4.0(1)	0.130(10)	2.93(1)	4.0(1)	0.130(10)	2.93(1)	4.0(1)	0.130(10)
P-P	2.98(2)	2.0(1)	0.100(10)	2.98(2)	2.0(1)	0.100(10)	2.98(2)	2.0(1)	0.100(10)
O-(R)-O	3.15(2)	1.0(1)	0.105(10)	3.14(2)	1.0(1)	0.105(10)	3.15(2)	1.0(1)	0.105(10)
Al-P	3.15(2)	6.0(5)	0.100(10)	3.15(2)	6.0(5)	0.100(10)	3.15(2)	6.0(5)	0.100(10)

Table 7.10. A summary of the Gaussian parameters used to model the difference functions $\Delta D'_{\mu\mu}(r)$.

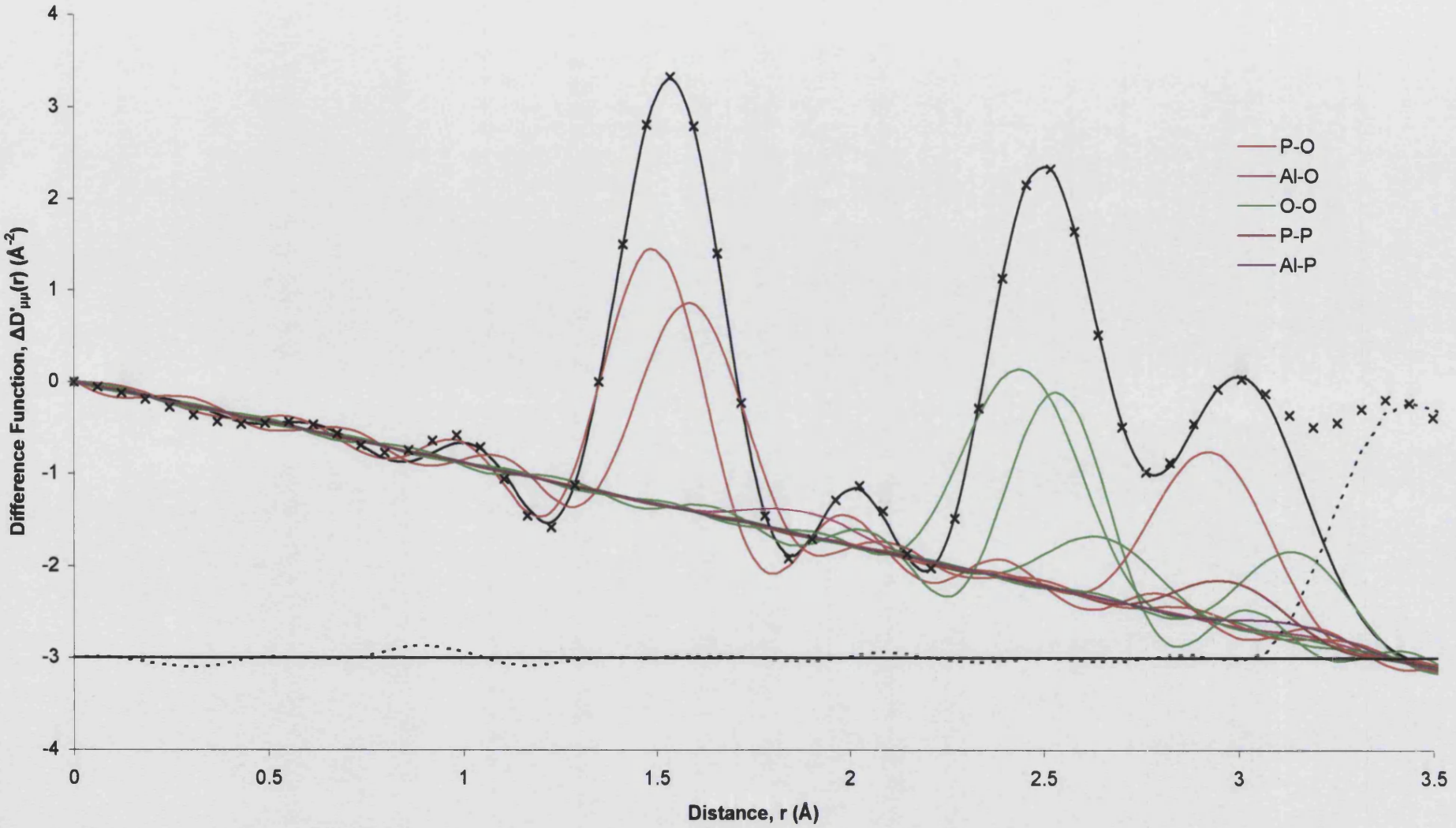

Figure 7.31. The difference function $\Delta D'_{\mu\mu}{}^{(1)}(r)$ (crosses), the fitted data (solid curve) and the individual convoluted Gaussians. The residual (dashed curve) is offset by -3 barn.

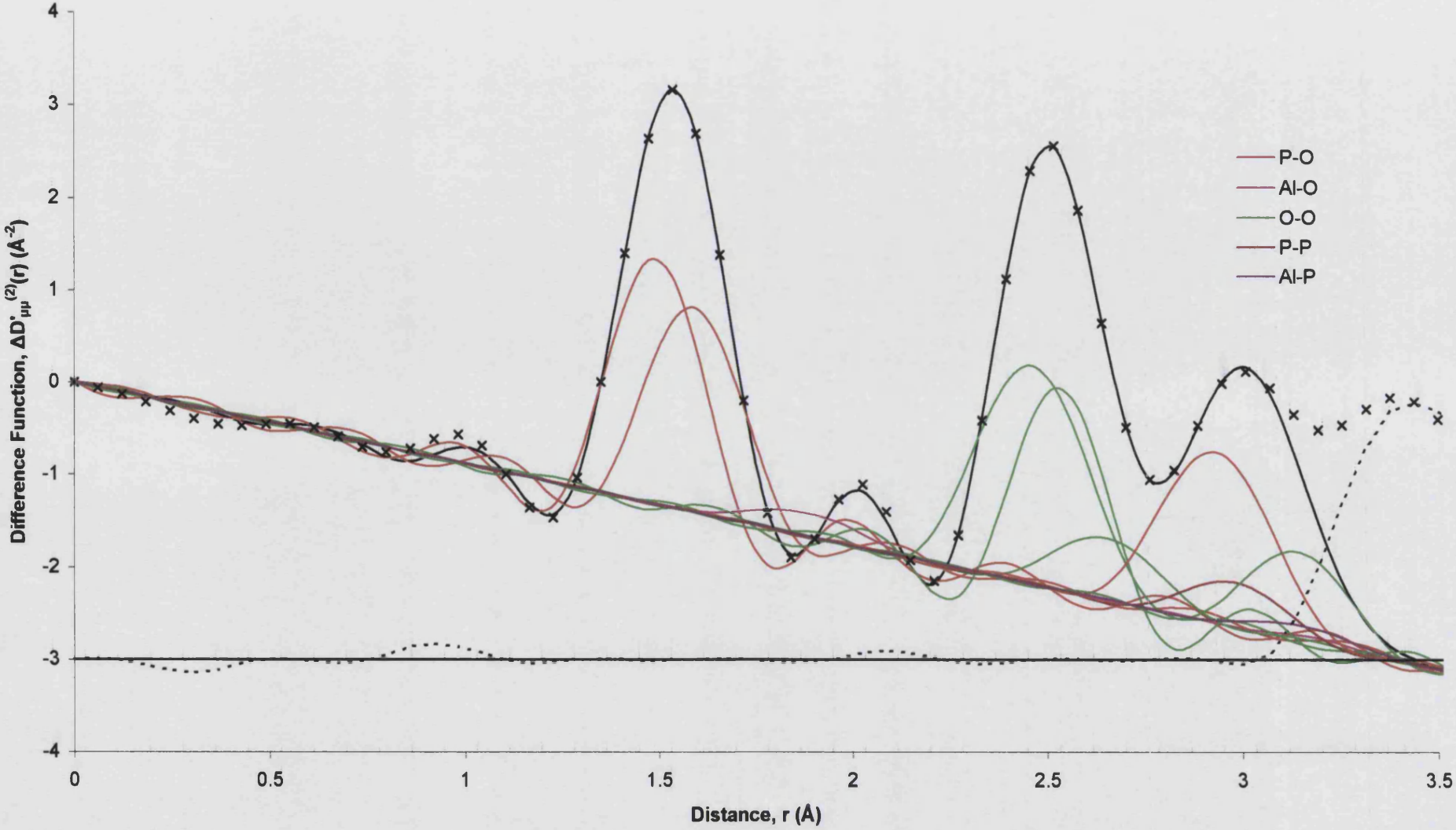

Figure 7.32. The difference function $\Delta D'_{\mu\mu}{}^{(2)}(r)$ (crosses), the fitted data (solid curve) and the individual convoluted Gaussians. The residual (dashed curve) is offset by -3 barn.

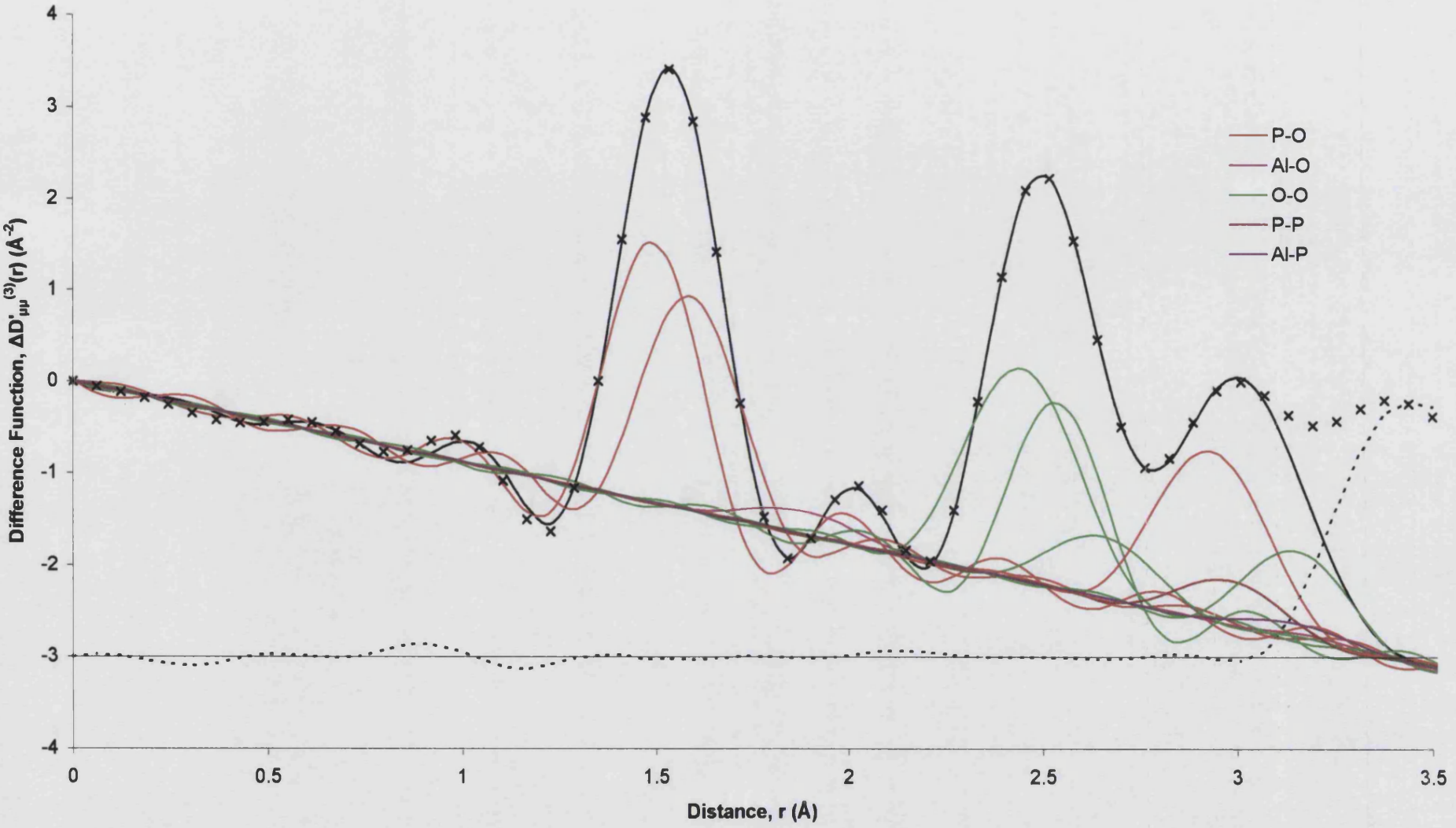

Figure 7.33. The difference function $\Delta D'_{\mu\mu}{}^{(3)}(r)$ (crosses), the fitted data (solid curve) and the individual convoluted Gaussians. The residual (dashed curve) is offset by -3 barn.

7.7. DISCUSSION.

The partial structure factor, $S_{RR}(Q)$, has been measured for the first time for a rare earth phosphate glass. Although serve contamination of this function from unwanted correlations is expected from the small differences in glass compositions measured in the EPMA experiments, no compelling evidence for a substantial contribution from these correlations could be found in the corresponding $g'_{RR}(r)$. The measured difference functions $\Delta_{R\mu}(Q)$ and $\Delta_{\mu\mu}(Q)$ lend support to this observation. Whereas the measured $\Delta_R(Q)$ (Figure 7.7) and $\Delta_F(Q)$ (Figure 7.9) functions show contrasting features especially at lower Q values, there is negligible difference between the (scaled) $\Delta_{R\mu}(Q)$ (Figure 7.24) or $\Delta_{\mu\mu}(Q)$ (Figure 7.26) i.e. the functions $\Delta_{R\mu}^{(1)}(Q) - \frac{b_{Dy}-b_{Ho}}{b_{Dy}-b_{DyHo}}\Delta_{R\mu}^{(2)}(Q)$, $\Delta_{R\mu}^{(1)}(Q) - \frac{b_{Dy}-b_{Ho}}{b_{DyHo}-b_{Ho}}\Delta_{R\mu}^{(3)}(Q)$, $\Delta_{\mu\mu}^{(1)}(Q) - \Delta_{\mu\mu}^{(2)}(Q)$ and $\Delta_{\mu\mu}^{(1)}(Q) - \Delta_{\mu\mu}^{(3)}(Q)$ show no discernable structure. This would not be the case if the $\Delta_{R\mu}(Q)$ or $\Delta_{\mu\mu}(Q)$ functions had a substantial contribution from unwanted correlations. Hence the neutron diffraction experiments indicate that the compositions of the DyC, DyHoE and HoG glasses are closer than expected on the basis of the EPMA results.

The main features in $S_{RR}(Q)$ occur at small Q-values, $0 \leq Q\ (Å^{-1}) \leq 3$. The first peak in $g_{RR}'(r)$ occurs at a correspondingly large r-value of 5.5 Å and integrating over the range $5.1 \leq r\ (Å) \leq 7.2$ gives an R-R coordination number of 8.0(2) consistent with the distribution of eight R-R nearest neighbours in crystalline ErP_3O_9 (Dorokhova and Karpov 1984) extending over the range 5.37 – 6.97 Å. The large r-value of the nearest neighbour R-R correlations means that an analysis of the low r region of $\Delta D'_R(r)$ or $\Delta D'_{R\mu}(r)$ and $\Delta D'_F(r)$ or $\Delta D'_{\mu\mu}(r)$ yield Gaussians described by identical parameters.

Measurement of the $S_{RR}(Q)$, $\Delta_{R\mu}(Q)$ and $\Delta_{\mu\mu}(Q)$ functions has allowed unprecedented information to be obtained on the R-R, O-(Al)-O correlations and the splitting of the nearest neighbour peaks for the O-(P)-O and R-O correlations. Furthermore the data were for the first time analysed taking into explicit consideration the impurity correlations that result from the Al which is incorporated when phosphate glasses are prepared using the method outlined in Chapter 2. This is

important because the majority of glasses listed in Table 7.1 were made using alumina crucibles but no account was taken of either the Al content or its effect on the structure. A fully quantitative comparison of the present results with those for other rare earth phosphate glasses is hampered in this respect and is also made difficult owing to the different quoted R:P:O ratios (see Table 7.1).

The nearest neighbour R-O correlations are asymmetric and are best represented using two separate peaks (Figures 7.10 - 7.12). Previous studies on amorphous samples have by and large been unable to resolve the R-O peak due to its overlap with the O-(P)-O correlations. Most of the analyses have assumed that the R-O correlation can be represented by a single Gaussian. The total R-O coordination number of 6.7, falls approximately in the middle of the range of values previously given (Table 7.1). For example, coordination numbers of 5.8, 7.0 and 8.0 have been reported for glassy $(Tb_2O_3)_{0.26}(P_2O_5)_{0.74}$ (see Table 7.1). Unlike phosphate glasses containing larger R^{3+} ions (Chapter 6) there is less overlap of the R-O and O-(P)-O peaks i.e. they are more clearly separated (see Figures 6.14 and 7.18). However, in the earlier x-ray work of Bowron *et al* (1995) only a mean O-(P)-O / R-O distance was reported.

The nearest neighbour R-P correlations in the present work were modelled using two Gaussians having coordination numbers of ≈ 1 and 6. The position of the first Gaussian is at 3.25(2) Å and the second is at 3.60(2) Å and $\Delta D'_R(r)$ is satisfactorily modelled by these peaks in the region $3.3 \leq r$ (Å) ≤ 3.7 Å. This compares with six R-P nearest neighbours distributed over the range $3.49 \leq r$ (Å) $\leq$ 3.76 Å in crystalline ErP_3O_9 (Dorokhova and Karpov 1984). The present results are in contrast to the EXAFS study of Karabulut *et al* (2002) where an R-P nearest neighbour distance of 3.87 Å was reported for Er^{3+} with a coordination number of 2.2(9) i.e. this nearest neighbour R-P distance is too long and the coordination number is too low.

The peak positions and coordination numbers used to model the nearest neighbour P-O_B and P-O_T correlations in the present work are in agreement with the values for terbium phosphate glasses reported by Cole *et al* (1999). In x-ray studies the P-O_B and P-O_T correlations were not resolvable and the data were not peak fitted,

hence only mean P-O values were given. The mean P-O positions and total coordination numbers previously reported (Table 7.1) are, however, in agreement with the present work. The EXAFS data were taken for the K and L_{III} absorption edges of the rare earth ions and are not therefore sensitive to P-O correlations.

The O-(P)-O correlations for the present data sets were modelled using two O-(P)-O Gaussian peaks, unlike previous studies in which a single O-(P)-O peak was assumed. Unlike glasses doped with the larger R^{3+} ions (Chapter 6) there is less overlap of the first peaks in the R-O and O-(P)-O correlations (Table 7.1). The total experimental O-(P)-O C_N value of 3.60(14) is consistent with value of 3.6, calculated using the phosphate network model of Hoppe (1996) as described in section 6.2. In contrast, Cole *et al* (2001b) have reported O-(P)-O C_N values between 4.8 and 5.9 (± 0.8). These experimental results are outside the margin of error for the $\bar{n}_O^O$ values ≈ 4.0 expected on the basis of the phosphate network model (Hoppe 1996).

An O-(P)-O C_N greater than 4.0 can be explained in part since Cole *et al* (2001b) neglected the O-(Al)-O correlations which occur in the same real space region as shown in Figures 7.13-7.15. Nevertheless C_N values above 5.0 cannot be justified even allowing for this influence as insufficient Al is likely to be present. For example, the estimated O-(P)-O C_N obtained for the phosphate network model for $(Ho_2O_3)_{0.231}(P_2O_5)_{0.769}$ is 4.07. Therefore to achieve the reported total O-O C_N of 5.9, the O-(Al)-O C_N would have to be 1.8. Equation 6.2 was derived on the basis that Al is octahedrally rather than tetrahedrally coordinated by oxygen and therefore gives a maximum O-(Al)-O first nearest neighbour coordination number. By using this equation the Al atomic fraction is estimated to be c_{Al} = 0.05, a value that is significantly higher than the maximum of c_{Al} = 0.035 found in any of the present work on rare earth phosphate glasses (Chapters 3, 6 and 7) in which the Al content was quantified. This suggests that the O-(P)-O C_N value reported by Cole *et al* (2001b) is significantly too large. By contrast, in the neutron diffraction work of Cole *et al* (1999) an O-(P)-O C_N of 3.4 was reported for Tb^{3+} based phosphate glasses. This appears to be an underestimate (see Table 7.1) since a value of 3.95 is expected using the phosphate network model (Hoppe 1996).

The data for the present work are best modelled using an Al-O distance of 1.88 Å, consistent with there being a large number of Al centred octahedral, as opposed to the distance of 1.73 Å expected for Al centred tetrahedra. However, an Al-O coordination number of 5.5 was fitted, suggesting a range of Al environments in agreement with recent NMR studies (Cole *et al* 1999). The O-(Al)-O coordination number used in the fitting procedure was constrained to be 0.6 ± 0.1 consistent with the majority of Al atoms being in an octahedral environment (see section 6.3). The modelled O-(P)-O coordination number of ≈ 3.6 is therefore likely to be an under-estimate. For example, if the Al was 50% octahedrally coordinated and 50% tetrahedrally coordinated then the estimated O-(Al)-O C_N would be 0.3 at a distance $\sqrt{2}\ r_{O-Al}$ = 2.66 Å (equation 6.2) and 0.15 at a distance $\sqrt{8/3}\ r_{O-Al}$ = 2.833 Å (equation 6.3) as opposed to a C_N of 0.6 at $\sqrt{2}\ r_{O-Al}$ = 2.66 Å. A reasonable amount of overlap exists for these two O-(Al)-O correlations, so the overall first nearest neighbour O-(Al)-O C_N of 0.6 will to between 0.3 – 0.375. Therefore to compensate, the fitted O-(P)-O C_N would have to be increased accordingly i.e. from a value of 3.6 to a value between 3.825 and 3.9. On the basis of the phosphate network model of Hoppe (1996) an O-(P)-O C_N of 3.6 is expected for these glasses. This suggests that the phosphate network model underestimates the number of O_B atoms on the basis that the O_T and O_B atoms have O-O coordination numbers of 3 and 6 respectively (see section 6.2). This is consistent with the presence of Al impurities strengthening the glassy network. Compared to R-P-O glasses, those containing Al are less brittle and can be drawn into fibres (see Chapter 2 and Chapter 9).

7.8. CONCLUSIONS.

The total structure factors of dysprosium and holmium phosphate glasses were measured using neutron diffraction. Hence, the partial structure factor, $S_{RR}(Q)$, and the difference functions $\Delta_{R\mu}(Q)$, $\Delta_{\mu\mu}(Q)$, $\Delta_R(Q)$ and $\Delta_F(Q)$ were obtained for the first time for a rare earth phosphate glass. These functions showed negligible contamination from unwanted correlations which was expected on the basis of the EPMA results. The neutron diffraction experiments indicate, therefore, that the compositions of the DyC, DyHoE and HoG glasses are closer than anticipated.

The main features in $S_{RR}(Q)$ occur at small Q-values, $0 \leq Q\ (\text{Å}^{-1}) \leq 3$. The first peak in $g_{RR}'(r)$ occurs at a correspondingly large r-value of 5.5 Å and integrating over the range $5.1 \leq r\ (\text{Å}) \leq 7.2$ gives an R-R coordination number of 8.0(2) consistent with a distribution of eight R-R nearest neighbours in crystalline ErP_3O_9 (Dorokhova and Karpov 1984) extending over the range 5.37 – 6.97 Å. The large r-value of the nearest neighbour R-R correlations means that an analysis of the low r region of $\Delta D'_R(r)$ or $\Delta D'_{R\mu}(r)$ and of $\Delta D'_F(r)$ or $\Delta D'_{\mu\mu}(r)$ yields Gaussians described by identical parameters.

Measurement of $S_{RR}(Q)$ and the related difference functions has allowed unprecedented information to be obtained on the R-R and O-(Al)-O correlations and on the splitting of the nearest neighbour peaks for the O-(P)-O and R-O correlations. Furthermore the data were for the first time analysed taking into explicit consideration the impurity correlations that result from the Al which is incorporated when phosphate glasses are prepared using the method outlined in Chapter 2.

The P-O bond distances and coordination numbers are in agreement with previous work confirming that the glass network is made of PO_4 tetradedra.

The nearest-neighbour R-O correlations could be modelled by a single Gaussian together with another Gaussian at larger r, with a much smaller coordination number (Figures 7.10 - 7.12). The R-O coordination environment is therefore asymmetric although the distribution of bond lengths is much smaller than for the La /

Ce phosphate glasses (Chapter 6). A range of R-O distances has been suggested in the work of Hoppe (2001, 2002) for glasses containing the larger R^{3+} ions but this is the first report of an asymmetric distribution for the smaller rare earth ions. Other neutron and x-ray studies on phosphate glasses containing small rare earth ions have been made at the total structure factor level (Table 7.1) wherein the overlap of correlations made the assignment of the nearest neighbour R-O correlations ambiguous.

The fitted first nearest neighbour Al-O correlations gave a distance and coordination number consistent with a large proportion of Al being octahedrally coordinated. The O-(Al)-O correlations were modelled accordingly which is important given the substantial overlap of the first few peaks in O-(P)-O and O-(Al)-O. The fitted O-(P)-O correlations gave a coordination number of 3.60(14) which is in agreement with the value of 3.6 obtained from the phosphate network model of Hoppe (1996). This implies an O_T : O_B ratio of 0.81 : 0.19 i.e. the network has less O_B and is therefore less rigid than for the larger rare earth phosphate glasses (Chapter 6). The observation from NMR studies of 4, 5 and 6 fold coordinated Al in phosphate glasses suggests, however, that the modelled O-(Al)-O coordination number is an overestimate. By assuming a 1 : 1 ratio of octahedral to tetrahedral Al sites and an associated reduction of the O-(Al)-O coordination number, an increase by $\approx$ 5 % in the fraction of O_B is deduced. This is consistent with the observation that Al impurities strengthen the phosphate glass network. The results are inconsistent with the previous neutron and x-ray results of Cole *et al* (1999, 2001) on rare earth phosphate glasses prepared using alumina crucibles. This can be attributed, in part, to the neglect in these studies of the Al impurity correlations.

REFERENCES

Anderson R, Brennan T, Cole J.M, Mountjoy G, Pickup D.M, Newport R.J and Saunders G.A. 1999. *Journal of Materials Research.* **14.** (12) p. 4706.

Bagieu M, Tordjman I, Durif A and Bassi G. 1973. *Crystal Structure Communications.* **2.** p. 387.

Bowron D.T, Newport R.J. Rainford R.D, Saunders G.A and Senin H.B. 1995. Physical Review B. **51.** (9) p. 5739.

Bowron D.T, Newport R.J. Rainford R.D, Saunders G.A and Senin H.B. 1996a. Physical Review B. **53.** (9) p. 5268.

Bowron D.T, Bushnell-Wye G, Newport R.J. Rainford R.D and Saunders G.A. 1996b. *Journal of Physical: Condensed Matter.* **8.** p. 3337.

Cole J.M, van Eck E.R.H, Mountjoy G, Newport R.J, Brennan T and Saunders G.A. 1999. *Journal of Physics: Condensed Matter.* **11.** p. 9165.

Cole J.M, Newport R.J, Bowron D.T, Pettifer R.F, Mountjoy G, Brennan T and Saunders G.A. 2001a. *Journal of Physics Condensed Matter.* **13.** p. 6659.

Cole J.M, van Eck E.R.H, Mountjoy G, Anderon R, Brennan T, Bushenell-Wye G, Newport R.J, and Saunders G.A. 2001b. *Journal of Physics: Condensed Matter.* **13.** p.4105.

Cossy C, Barnes A.C and Enderby J.E. 1989. *Journal of Chemical Physics.* **90** no 6. p.3254.

Dorokhova G.I and Karpov O.G. 1984. *Kristallografiya.* **29.** p. 677.

Hong H.Y.P. 1974. Acta *Crystallographic.* **B30.** p. 1857.

Hong H.Y.P and Pierce J.W. 1974. *Material Research Bulletin.* **9.** p.179.

Hoppe U. 1996. *Journal of Non-Crystalline Solids.* **195.** p.138.

Hoppe U, Ebendorff-Heidepriem H, Neuefeind J and Bowron D. Zeitschrift fur Naturforschung. 2001. **56a.** p. 237.

Hoppe U, Metwalli E, Brow R.K and Neuefeind J. 2002. *Journal of Non-Crystalline Solids.* **297.** p. 263.

Hughes J.M and Mariano A.N 1995. *American Mineralogist.* **80.** p. 21

Karabulut M, Marasinghe G.K, Metwalli E, Wittenauer A.K and Brow R.K. 2002. *Physical Review B.* **65.** p. 104206.

Pettifor D.G. 1986. *Journal of Physics C: Solid State Physics.* **19.** p. 285.

Sears V.F. 1992. *Neutron News*. **3**. p. 26.

Shannon R.D. 1976. *Acta Crystallographic*. **A32**. p. 751.

Sowa H, Macavei J and Schulz H. 1990. *Zeitschrift fur Kristallographie*. **192**. p. 119.

Van der Meer H. 1976. Acta *Crystallographic*. **B32**. p. 2423.

Wasse J.C and Salmon P.S. 1999. *Journal of Physics; Condensed Matter*. **11**. p. 1381.

Wasse J.C, Salmon P.S and Delaplane G. 2000. *Journal of Physics; Condensed Matter*. **12**. p. 9539.

CHAPTER 8. THE STRUCTURE OF MOLTEN $TbCl_3$

8.1. INTRODUCTION

Neutron diffraction provides information that acts as a useful benchmark for testing interaction models. Trivalent metal chloride systems, MCl_3, present a challenge to the development of a realistic model for their behaviour within a single conceptual framework such as that based on polarisable ions (Hutchinson *et al* 1999, 2000, 2001, Takagi *et al* 1999). This follows from the marked changes observed in their physical behaviour with decreasing cation radius when effects that are sometimes attributed to 'covalency' become increasingly notable. In this context $TbCl_3$ represents an interesting case since Tb^{3+} has a radius that is intermediate between large cations such as La^{3+} and small ones such as Y^{3+}. For example, $LaCl_3$ crystallises in the UCl_3-type structure, wherein La^{3+} is 9-fold coordinated by anions and melts with a volume change $\Delta V / V_m$ of 16%, where $\Delta V = V_m - V_{RT}$; V_m is the molar volume of the liquid at the melting point temperature T_m and V_{RT} is the molar volume of the salt at room temperature. YCl_3 crystallises in the $AlCl_3$ structure, wherein Y^{3+} is octahedrally coordinated by anions, and has a negligible volume change on melting of $\Delta V / V_m$ = 0.6 - 3.0 % (Wasse and Salmon 1999b). By comparison, $TbCl_3$ adopts the $PuBr_3$ structure at room temperature, wherein Tb^{3+} is 8-fold coordinated by anions (Forrester *et al* 1964). It then undergoes a solid-solid phase transition at 510 – 517 °C into a structure consisting of $TbCl_6^{3-}$ double octahedra (Pankratz 1984, Gunsilius *et al* 1988) with a volume change $(V_{HT} - V_{RT}) / V_{HT}$ of 21 %, where V_{HT} is the molar volume of the high temperature phase. It then melts at 582 - 587 °C with a small volume change on melting $(V_m - V_{HT}) / V_m$ of 0.2 % (Pankratz 1984, Wasse and Salmon 1999b).

The partial structure factors of the trivalent metal chlorides have been calculated using Molecular Dynamic simulations (Hutchinson *et al* 1999, 2001). The simulations are based upon an ionic interaction model, which takes into account the polarisation of the ions (the polarisable ion model or P.I.M). In the P.I.M. the ions have an associated dipole moment which is allowed to vary as the electric field on an ion changes when it moves. The interactions of these additional degrees of freedom

with the other dipoles and charges in the system must be taken into account when constructing an appropriate potential. The interactions which determine the magnitude of a dipole are many body effects which depend on the charge-dipole and dipole-dipole interaction and the self-energy needed to create a dipole. Therefore the expression used to calculate the potential energy of a system contains terms corresponding to the short range overlap between electron clouds of the anions, dispersion effects, Coulombic repulsion, charge-dipole and dipole-dipole interactions and a final (self energy) term defined as the energy required for ion polarisation. Only the polarisation for the anion was taken into account when simulating the molten salt structures. For a review of the P.I.M. see Wilson and Madden (1993a, 1993b) and Wilson *et al* (1996).

Molecular dynamics simulations using the P.I.M. have successfully modelled the structures of MX and MCl_2 melts (X=halogen) e.g. Wilson and Madden (1993a, 1993b). Simulations modelling the short-range order of a series of MCl_2 melts were particularly successful. Experimentally the decrease in cation size was seen to be accompanied by a shift in the first peak position of the experimental $g_{MM}(r)$ to a value comparable with the first peak in $g_{ClCl}(r)$. Molecular dynamics simulations using the rigid ion model (R.I.M.) were unable to reproduce these experimental features. However, without invoking covalency it was possible to reproduce this shift in M-M position as a function of decreasing cation size using the P.I.M. It was encouraging to note that in these simulations it was possible to transfer the interaction model to different MCl_2 salts by varying only one parameter – the cation radius. Thus, by extending these simulations to MCl_3 salts the transferability of the P.I.M. for simulating structures can be investigated. The neutron diffraction experiments will provide a useful bench-mark for testing the validity of these simulations for the MCl_3 systems.

In the cases of molten $LaCl_3$ and YCl_3 (Wasse and Salmon 1999a, b) the total structure factor $F(Q)$ was measured by using the LAD diffractometer, at the ISIS pulsed neutron source, which has a large measurement window. For these systems it is found that although molecular dynamics simulations made using the polarisable ion model reproduce the main structural features, a fully quantitative description is not

forthcoming even when the interaction potentials are refined to optimise agreement with diffraction experiments *e.g.* the simulated first peak in the total pair distribution G(r) is too sharp (Hutchinson *et al* 2001).

By comparison, the F(Q) for $TbCl_3$ was measured by using the SLAD diffractometer, at the Studsvik neutron reactor source, which has a measurement window restricted to $Q_{max} \approx 10$ Å^{-1} (Wasse and Salmon 1999b). In this case the experimental G(r) is broadened and can be reproduced by the molecular dynamics results of Hutchinson *et al* (2001) provided a window function with Q_{max} set at the experimental value is applied to the simulated F(Q) on application of equation 4.83. We have therefore been motivated to re-measure F(Q) for molten $TbCl_3$, but over an extended Q-range, in order to determine whether the agreement between experiment and molecular dynamics simulation arises from a regime of ion sizes for which the polarisable ion model works particularly well or from an artefact of a limited measurement window.

8.2. EXPERIMENT

The neutron diffraction experiment was made using the instrument D4C at the Institut Laue-Langevin, Grenoble operating at an incident wavelength of 0.7095 Å to give a measurement range of $0.33 \leq Q(Å^{-1}) \leq 16.5$. The $TbCl_3$ (Aldrich 99.99%) was sealed in a cylindrical silica ampoule of internal diameter 5 mm and 1 mm wall thickness. Diffraction patterns were taken for the sample in its container in a cylindrical vanadium furnace, the empty container in the furnace, the empty furnace and a vanadium rod of dimensions comparable to the sample for normalisation purposes. The intensity for a cadmium neutron-absorbing rod of similar diameter to the sample was also measured to account for the effect of the sample self-shielding on the background count rate at small scattering angles. For further details see section 5.2.

In these experiments the total structure factor

$$F(Q) = c_{Tb}^2 b_{Tb}^2 [S_{TbTb}(Q) - 1] + 2c_{Tb}c_{Cl}b_{Tb}b_{Cl}[S_{TbCl}(Q) - 1] + c_{Cl}^2 b_{Cl}^2 [S_{ClCl}(Q) - 1] \quad [8.1]$$

is measured where Q denotes the magnitude of the scattering vector and $S_{\alpha\beta}(Q)$ a so-called Faber-Ziman partial structure factor. The de-convoluted total pair distribution function is given by

$$G(r) = c_{Tb}^2 b_{Tb}^2 [g_{TbTb}(r) - 1] + 2c_{Tb}c_{Cl}b_{Tb}b_{Cl}[g_{TbCl}(r) - 1] + c_{Cl}^2 b_{Cl}^2 [g_{ClCl}(r) - 1] \quad [8.2]$$

where $g_{\alpha\beta}(r)$ is a partial pair distribution function.

8.3 ANALYSIS

Nisel'son and Lyzkov (1975) give the densities of the molten lanthanide chlorides over the range 900 – 1100 °C. A linear dependence on temperature was noted and the results extrapolated. The density of the melt was also found to be proportional to the molecular weight of the salt, such that

$$\rho = -0.195 + 0.016\,M - 0.735 \times 10^{-3}\,T \quad [8.3]$$

where ρ is the mass density (g cm^{-3}), M is the molecular weight of the salt (g mol^{-1}) and T is the temperature of the melt (°C). The density was calculated to be 3.60 g cm^{-3} and the number density n_0 = 0.0327 $Å^{-3}$ for the experimental temperature of 617 °C.

The concentrations c_{Tb} and c_{Cl} are 0.25 and 0.75 respectively and the scattering lengths b_{Tb} and b_{Cl} are 7.38(3) and 9.5770(8) fm (Sears 1992). Therefore the coefficients of the Tb-Tb, Tb-Cl and Cl-Cl terms in equations (8.1) and (8.2) are 34.0(3), 265(1) and 515.9(1) mbarn respectively. The nuclear cross-sections were taken from Sears (1992).

The data analysis procedure followed the scheme described in section 5.8. $F_S(Q)$ the total structure factor for $TbCl_3$ corrected for background, container, heater and multiple scattering effects is given in Figure 8.1. The total paramagnetic scattering cross-section of Tb^{3+} at the incident wavelength (3.55 barn) was calculated using the method described by Wasse and Salmon (1999b) and its paramagnetic differential scattering cross section was calculated using the method described by Balcar and Lovesey (1989) as outlined in section 4.10. The Tb^{3+} magnetic form factor scaled by c_{Tb} is given in Figure 8.1.

It was necessary to make a small correction for hydrogen, which was estimated to be present at the level of $\approx$ 1 mol % (section 5.11). The hydrogen correction is illustrated in Figure 8.1.

Due to the finite measurement window the data is presented in D′(r) and G′(r) as described in section 4.9. Provided Q_{max} is sufficiently large that the high-Q oscillations in F(Q) are negligible then M(r) will have no discernible effect on G(r). Otherwise the modification function causes a broadening and distortion of the peaks in G(r), effects that become increasingly more significant the smaller the value of Q_{max}.

8.4. RESULTS

The total structure factor F(Q) and the back Fourier transform of G′(r) with the low r oscillations set equal to G(0) for molten $TbCl_3$ (617 °C) are in close agreement as illustrated in Figure 8.3. The total pair distribution function G′(r) is illustrated in Figure 8.2. To investigate the effect of the measurement window, the first two peaks in D′(r) were fitted by representing the individual $rg_{\alpha\beta}(r)$ by Gaussians convoluted with M(r) as given by equation 4.67. The real space data, fitted in D′(r) to $\approx$ 4.0 Å, are illustrated in Figure 8.4. The individual Gaussian parameters are given in Table 8.1 and the R_χ value for $TbCl_3$ for $2.3 \leq r \leq 4.0$ Å is 0.0586. Parameters for the nearest

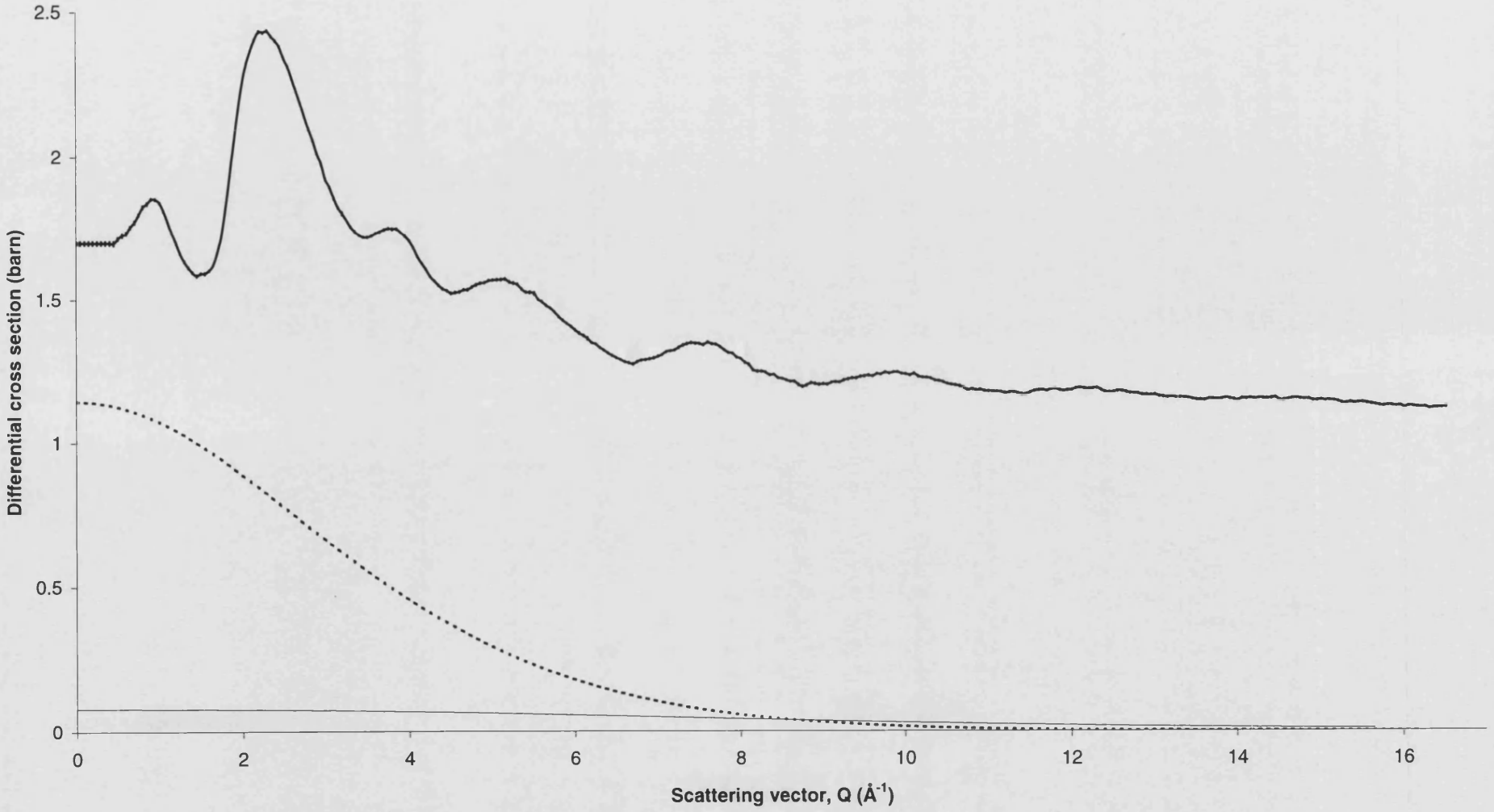

Figure 8.1.$F_S(Q)$ for TbCl3 (solid curve with errors), the Tb^{3+} magnetic scattering cross section scaled by c_{Tb} (dashed curve) and the hydrogen correction (feint curve).

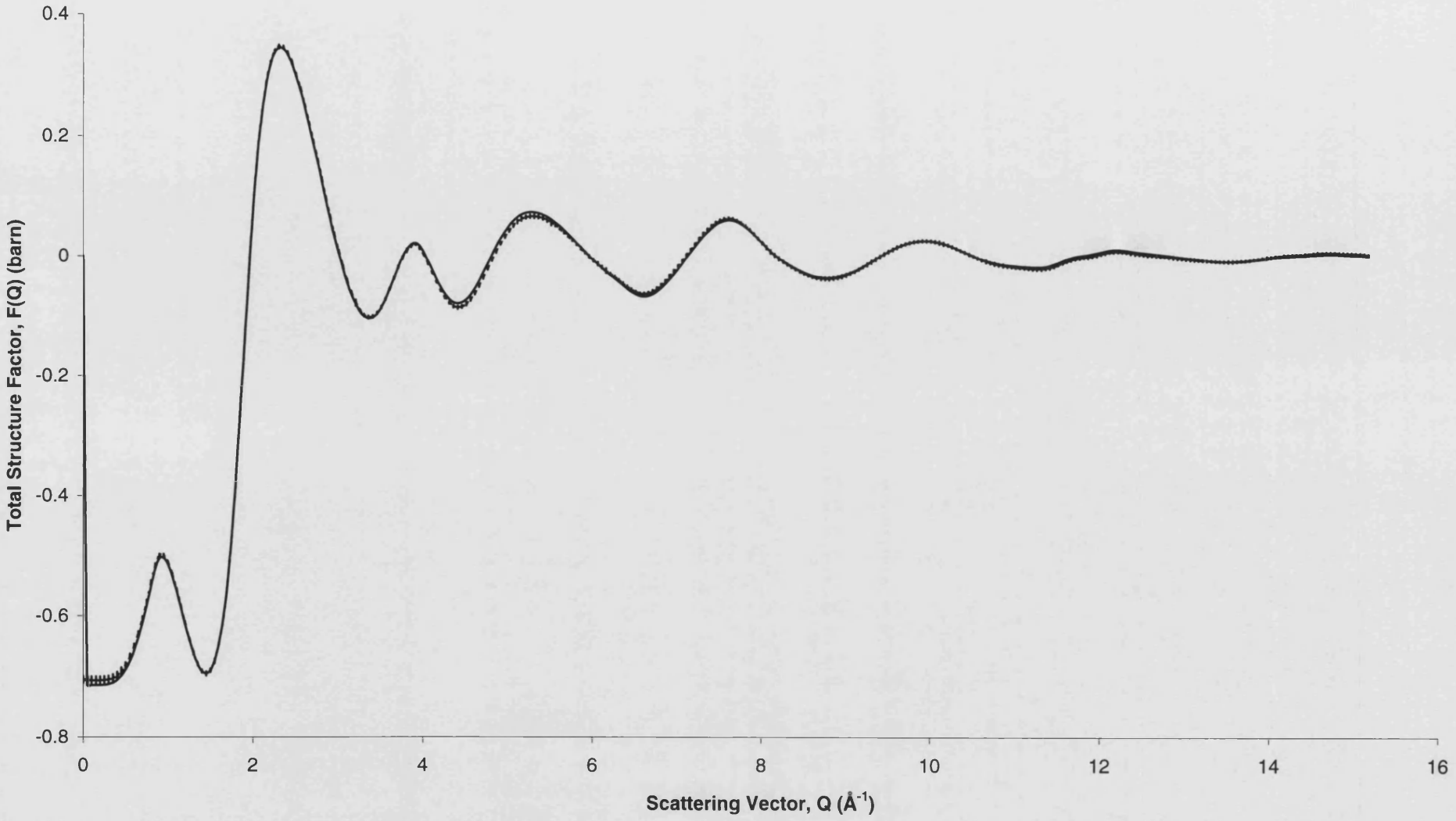

Figure 8.2. The total structure factor, F(Q), (dashed curve with errors) and Fourier backtransform of the G'(r) given by the solid curve in Figure 8.3 (solid curve).

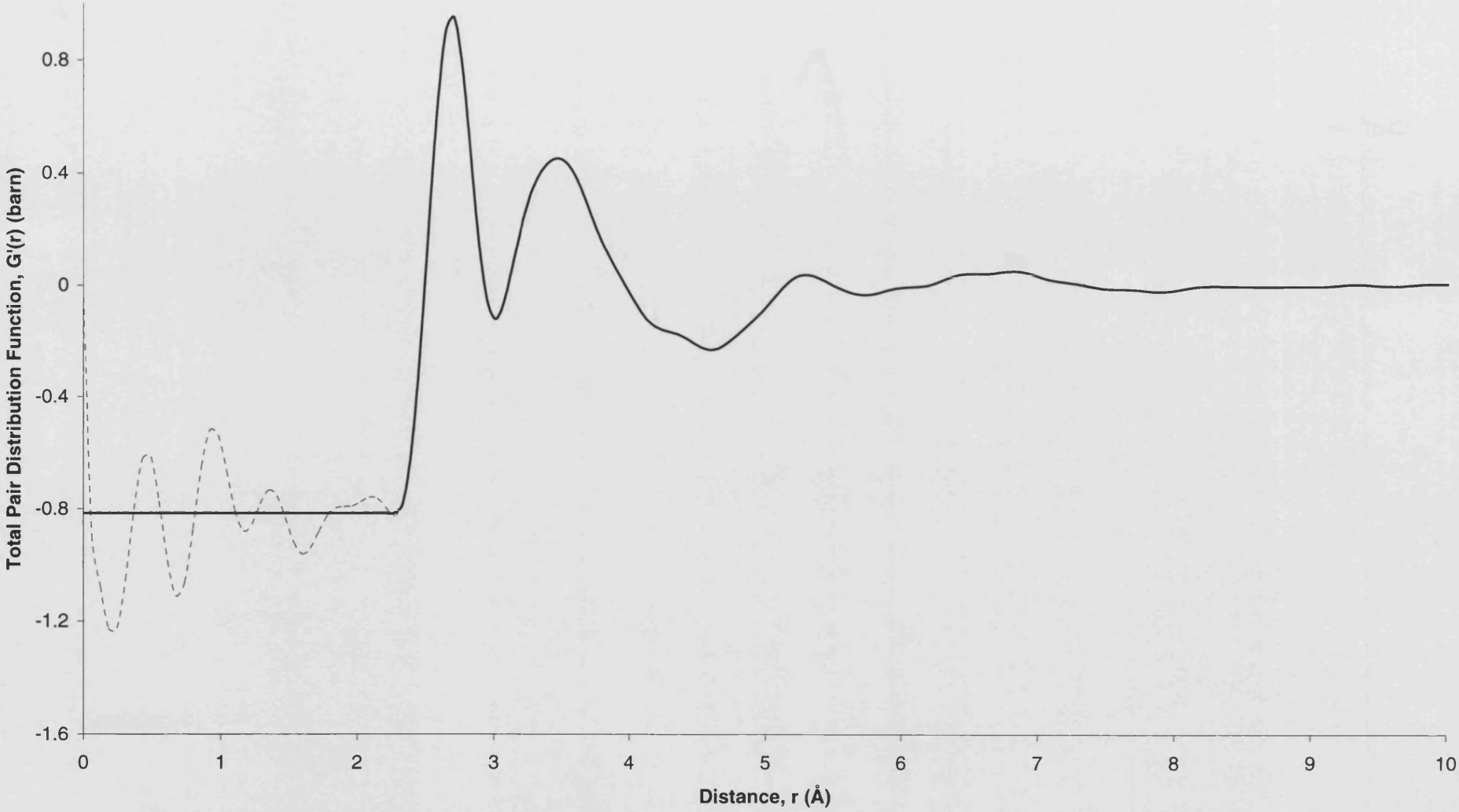

Figure 8.3. The real space function G'(r) (solid curve). The unphysical low r oscillations are shown by the dashed curve.

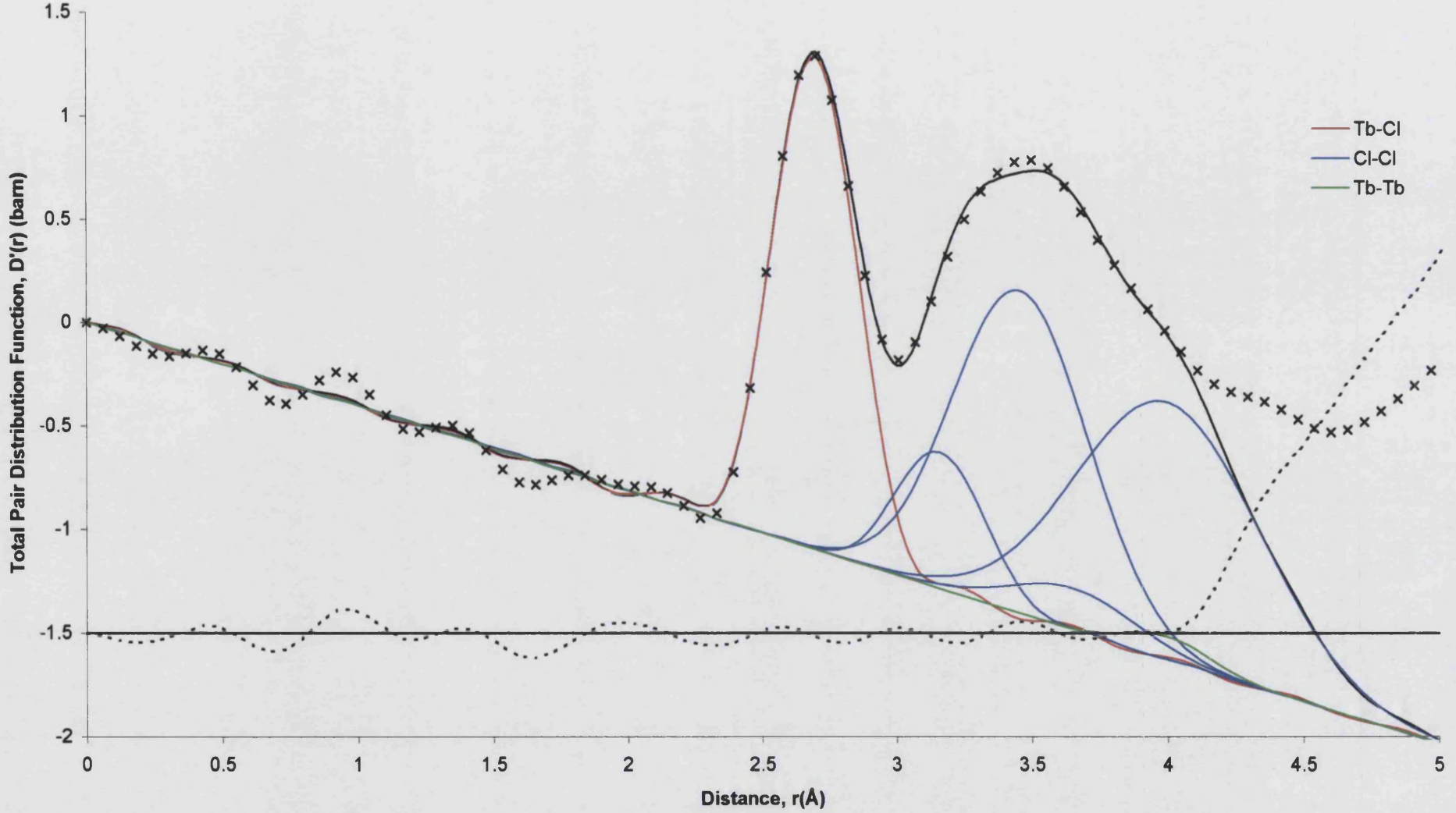

Figure 8.4. The real space function D'(r) (crosses), the fitted data (solid curve) and the individual convoluted Gaussians Tb-Cl, Cl-Cl and Tb-Cl. The residual (dashed curve) is offset by -1.5 barn.

neighbour Tb-Tb correlations were fixed equal to the values consistent with the high temperature crystalline phase (Gunsilius *et al* 1988) during the modelling to allow the Cl-Cl C_N to be determined. By contrast with the SLAD data, no significant distortion of the Gaussians by M(r) could be found for the D4C data and the first peak gave a coordination number $\bar{n}_{Tb}^{Cl}$ = 5.7(2). It was checked that the D4C data, when truncated at the same Q_{max} as the SLAD data, could be fitted by using the same Gaussian parameters e.g. a coordination number $\bar{n}_{Tb}^{Cl}$ = 5.7(2) was also obtained.

	r (Å)	C_N	σ (Å)
Tb-Cl	2.695 (5)	5.7 (2)	0.15 (1)
Cl-Cl	3.16 (1)	1.0 (1)	0.16 (1)
Cl-Cl	3.455 (20)	4.0 (2)	0.25 (2)
Cl-Cl	3.65 (2)	0.5 (1)	0.23 (2)
Cl-Cl	4.0 (2)	5.0 (2)	0.34 (2)
Tb-Tb	4.0*	1.0*	0.15*

Table 8.1. A summary of the Gaussian parameters used to model the total pair distribution function D'(r) for $TbCl_3$. The correlations labelled * were taken from the high temperature crystal structure (Gunsilius *et al* 1988) and were fixed during the modelling procedure.

As illustrated in Figure 8.5, the two F(Q) for molten $TbCl_3$ measured using neutron diffraction are in agreement within the experimental errors and feature a first sharp diffraction peak at 0.93(2) $Å^{-1}$ which is a signature of ionic ordering on an intermediate range length scale (Salmon 1992, 1994). The corresponding G'(r) are shown in Figure 8.6 and reveal that the function obtained from the extended Q-space data set has sharper features and a second peak that is shifted to smaller-r. Nevertheless, the experimental data sets are in good agreement as shown by truncating the present F(Q) at 9.35 $Å^{-1}$ and Fourier transforming. By comparison with the crystalline phase, the first peak at 2.68(2) Å is attributed to Tb-Cl correlations and the second peak at 3.44(2) Å will have a strong contribution from Cl-Cl correlations.

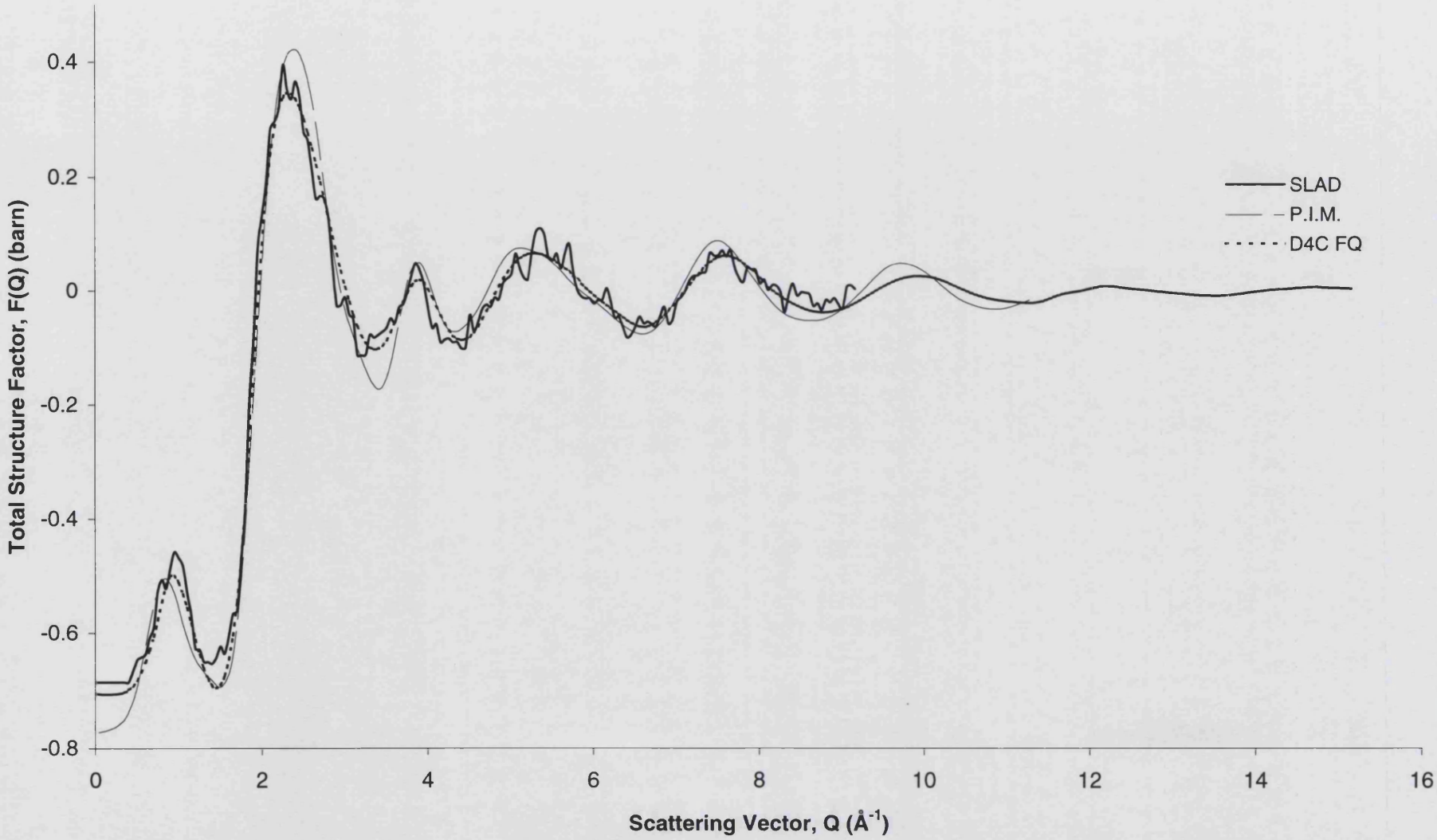

Figure 8.5. The total structure factor measured using D4C and SLAD compared with the total structure factor obtained from the polarisable ion model (P.I.M.) molecular dynamic simulations of Huchinson *et al* (2001).

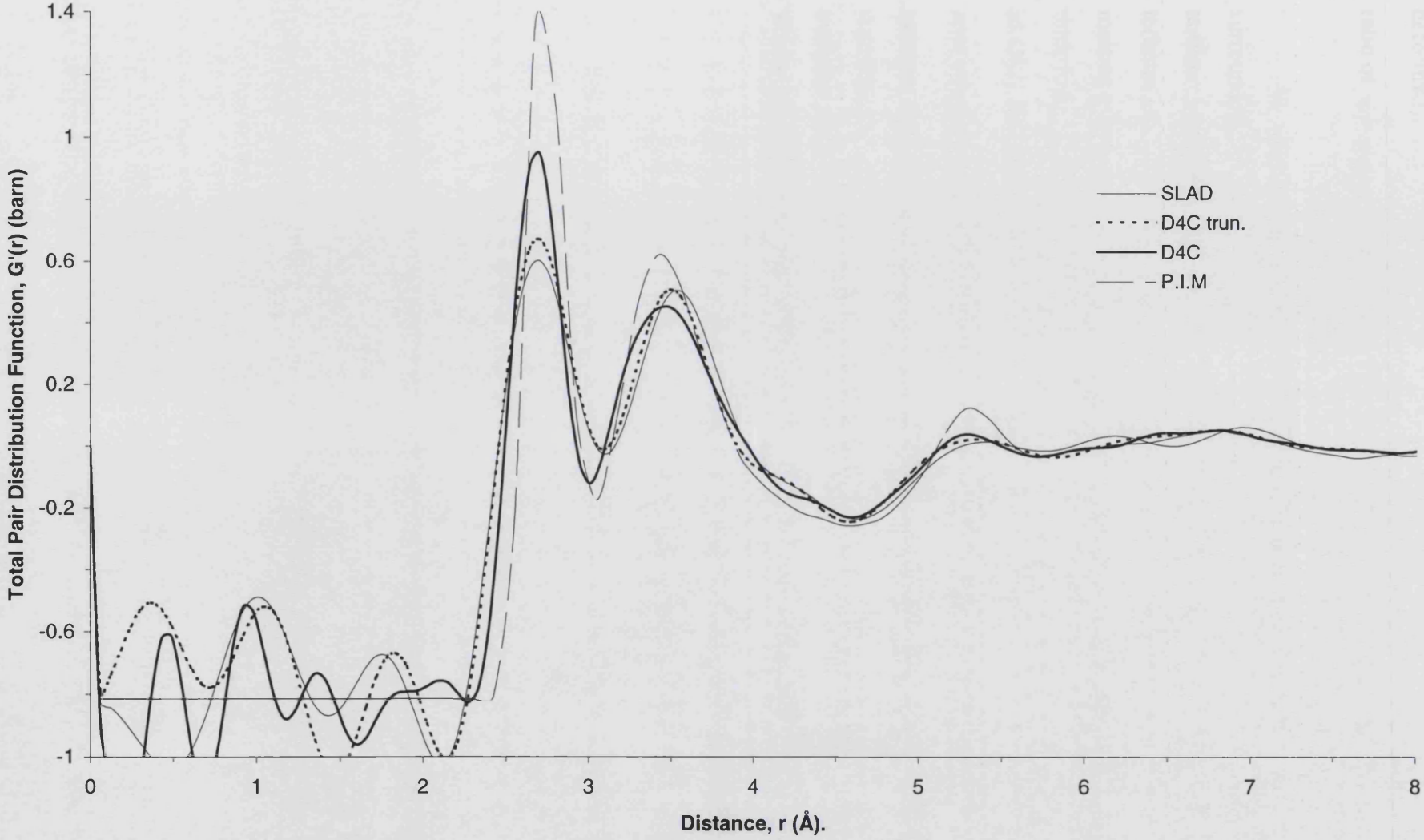

Figure 8.6. The real space function G'(r) obtained from D4C truncated at 15.65 $Å^{-1}$, D4C truncated at 9.35 $Å^{-1}$ (D4C trun.) and SLAD compared with the G(r) obtained from the P.I.M simulation of Hutchinson et al (2001).

The ratio of the first to second peak positions in G′(r) is 1.28(1) which suggests a deformation of MCl_6^{3-} conformations from regular octahedral geometry for which a ratio of $\sqrt{2}$ is expected.

In the high temperature crystalline phase of $TbCl_3$ each chloride ion is surrounded by 13 other chloride ions in the range from 3.53 to 4.58 Å and each terbium ion has one nearest-neighbour terbium ion at 4.02 Å and four next-neighbour terbium ions at 4.85 Å (Gunsilius *et al* 1988). There is a negligible volume change on melting (Wasse and Salmon 1999b) which points to comparable nearest-neighbour inter-ionic separations in the liquid phase. Integrating the area of the first two peaks in G′(r) for the melt to the first minimum at 4.60 Å and assuming $\bar{n}_{Tb}^{Cl} = 6$ gives an area consistent with $\bar{n}_{Cl}^{Cl} = 12.2(3)$ if $\bar{n}_{Tb}^{Tb} = 0$ or $\bar{n}_{Cl}^{Cl} = 12.0(3)$ if $\bar{n}_{Tb}^{Tb} = 1$. Thus, as for systems such as YCl_3 that also melt with a negligible volume change, the cation-anion coordination number does not change substantially on melting but there is some evidence for a reduction in the packing fraction of chloride ions (Saboungi *et al* 1991, Wasse and Salmon 1999b).

8.5. DISCUSSION and CONCLUSIONS

The total structure factor of molten $TbCl_3$ at 617 °C was measured by using neutron diffraction. The data sets are in agreement with previous experimental work but the use of a diffractometer having an extended reciprocal-space measurement window leads to improved resolution in real-space. The new data sets show that significant discrepancies occur between experiment and the polarisable ion model molecular dynamics simulations of Hutchinson *et al* (2001) for $TbCl_3$ in which the interaction potentials were refined to optimise agreement with the previous neutron diffraction results of Wasse and Salmon (1999b). The oscillations in F(Q) at high-Q appear to be out of phase and in real-space the simulated first peak is too sharp. The agreement between the real-space experimental and simulation results reported by Hutchinson *et al* (2001) for liquid $TbCl_3$ is, therefore, largely an artefact of the limited measurement window of the diffractometer used in the previous neutron diffraction work. Thus for $TbCl_3$, as for most other MCl_3 (Hutchinson *et al* 1999, 2001) and MBr_3 (Wasse *et al* 2000, Hutchinson *et al* 2000) systems, notable discrepancies are observed between the simulation and experimental results. The present work therefore demonstrates a need to consider afresh issues such as the cation-anion repulsion and the anion compressibility in different environments if a truly transferable model for the interactions in trivalent metal halides is to be developed within the framework of the polarisable ion model across the entire range of ion size ratios.

REFERENCES

Balcar E and Lovesey S.W. 1989. *Theory of Magnetic Neutron and Phonon Scattering.* Oxford Science Publications. UK.

Forrester J.D, Zalkin A, Templeton D.H. and Wallmann J.C. 1964. *Inorganic Chemistry.* **3.** p. 185.

Gunsilius H, Borrmann H, Simon A and Urland W. 1988. *Z. Naturforsch.* b **43.** p. 1023.

Hutchinson F, Rowley A.J, Walters M.K, Wilson M, Madden P.A, Wasse J.C and Salmon P.S. 1999. *Journal of Chemical Physics.* **111.** p. 2028.

Hutchinson F, Wilson M and Madden P.A. 2000. *Journal of Physics: Condensed Matter.* **12.** p. 10389.

Hutchinson F, Wilson M. and Madden P.A. 2001. *Molecular Physics.* **99.** p. 811.

Nisel'son L.A and Lyzlov Y.N. 1975. Dokl. Akad. Nauk. SSSR. **220**. p. 608.

Pankratz L.B 1984 *Thermodynamic Properties of Halides.* (Washington DC: US Bureau of Mines) bulletin 674.

Saboungi M-L, Price D.L, Scamehorn C and Tosi M.P. 1991. *Europhysics. Letters.* **15**. p. 283.

Salmon P.S. 1992. *Proc. Royal Society London.* A **437** p. 591.

Salmon P.S. 1994. *Proc. Royal Society London.* A **445** p. 351.

Sears V.F. 1992. *Neutron News* **3.** p. 26.

Takagi R, Hutchinson F, Madden P.A, Adya A.K and Gaune-Escard M 1999 *Journal of Physics: Condensed. Matter.* **11.** p. 645.

Wasse J.C and Salmon P.S. 1999a. *Journal of Physics: Condensed. Matter.* **11.** p. 1381.

Wasse J.C and Salmon P.S. 1999b. *Journal of Physics: Condensed. Matter.* **11.** p. 9293.

Wasse J.C, Salmon P.S and Delaplane R.G 2000. *Journal of Physics: Condensed. Matter.* **12.** p. 9539.

Wilson M and Madden P.A. 1993a. *Journal of Physics: Condensed Matter.* **5**. p. 687.

Wilson M and Madden P.A. 1993b. *Journal of Physics: Condensed Matter.* **5**. p.6833.

Wilson N. T, Wilson M, Madden P.A and Pyper N.C. 1996. *Journal of Chemical Physics.* **105**. p. 11209.

CHAPTER 9

FABRICATION OF RARE EARTH PHOSPHATE GLASS FIBRES AND FIBRE LASERS

9.1. RARE EARTH PHOSPHATE GLASS FIBRES.

9.1.1. INTRODUCTION.

Glass fibres possess many practical advantages over their corresponding bulk samples such as increased path length, the guiding of light using total internal reflection (Figure 9.1), low losses, high power density, compact size and they can be used to manufacture fibre lasers. Rare earth phosphate glasses prepared in platinum crucibles were found to shatter when handled, thus seriously limiting their practical application (section 2.8). However, glasses prepared using the refined method, given in Chapter 2, which contained significant aluminium impurities due to the alumina crucibles used were found to have much better mechanical properties (section 2.8). The physical, mechanical and optical properties of these glasses were assessed further by drawing them into optical fibres.

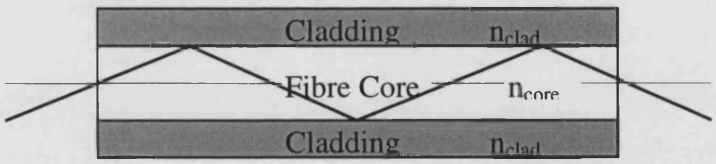

Figure 9.1. The total internal reflection of an optical fibre.

9.1.2 FABRICATION OF RARE EARTH PHOSPHATE GLASS FIBRES.

A silica clad rare earth phosphate glass fibre has been drawn using fibre drawing apparatus see Figure 9.2. A hollow silica tube (outer diameter 20mm, inner diameter 16mm) is placed into a furnace and heated, the soften end is then drawn to produce a taper. A bulk rare earth phosphate glass, manufactured as described in Chapter 2, is then placed inside the tapered silica tube. The tube and sample are placed inside a furnace, operating at 1900 °C. Argon gas is passed through the furnace during the fibre drawing process to prevent the graphite furnace element from oxidising. The tapered end softened in the furnace is then drawn and attached to a fibre collection drum. The dimensions of the fibre (core and cladding) are controlled by the starting dimensions of silica tube and bulk glass sample, the rate at which the bulk glass is fed into the furnace and the diameter and speed of the fibre collection drum. The ratio of the fibre radius, R_{fibre},: bulk radius, R_{bulk}, is described using equation 9.1.

$$\frac{R_{bulk}^2}{R_{fibre}^2} = \frac{v_{draw}}{v_{feed}} \qquad [9.1]$$

where v_{draw} and v_{feed} are the draw and feed rates respectively.

The fibre core size can be reduced further by re-drawing an existing fibre. The original fibre is placed inside another hollow silica tube and is fused to the inside wall tube. The tube is evacuated to prevent air become trapped between successive silica jackets. The tube and fibre are then redrawn. When a fibre is redrawn the core radius of the existing fibre represents R_{bulk}. Each time a fibre is redrawn an extra silica jacket is added to the outside of the fibre. The first silica jacket confines the light to the core by total internal reflection as shown in Figure 9.2, additional silica jackets have no effect on the properties of the fibre other than to make the outer dimensions of the fibre larger and suitable size for handling.

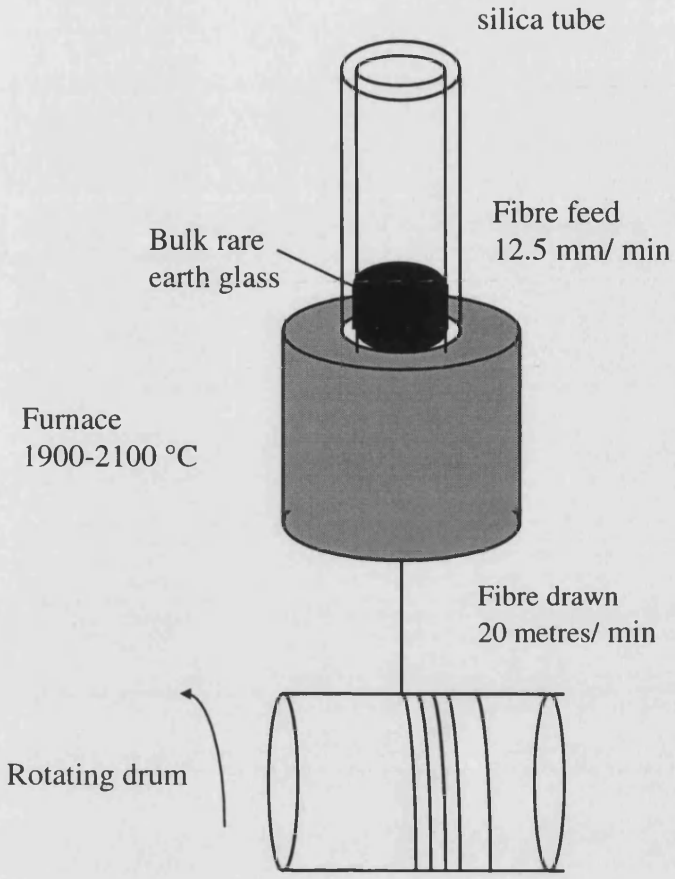

Figure 9.2. The fibre drawing apparatus.

9.1.3 OPTICAL FIBRE PROPERTIES.

An optical fibre consists of a core and a cladding as shown in Figure 9.1. The light propagates down the core of the fibre undergoing total internal reflection when incident on the cladding. The refractive index of the cladding, n_{clad}, must be less than the refractive index of the core, n_{core}, if the ray is to be reflected.

The total number of modes that can propagate in a fibre is given by the V parameter

$$V = \frac{2\pi a}{\lambda}(n_{core}^2 - n_{clad}^2)^{1/2} \qquad [9.2]$$

where λ is the wavelength of light propagating down the core and a is the radius of the core (Wilson and Hawkes 1983). For a fibre to support only a single mode the condition $0 < V < 2.405$ must be satisfied. The refractive indices n_{core} and n_{clad} are reported to be 1.56 and 1.46 respectively (Brennan 1998).

9.2 RARE EARTH PHOSPHATE GLASS LASERS

There has been considerable reference made to the potential these glasses possess for optoelectronic and lasing applications (Ford *et al* 1994, Bowron *et al* 1995a,b, Cole *et al* 1999, Cole *et al* 2001a,b). However, to date no such studies have been performed on these rare earth phosphate glasses prepared at the University of Bath using the methods outlined in Chapter 2. The motivation of this study is therefore to assess whether these glasses posses suitable properties required for manufacturing of lasers, such as, long fluorescence lifetimes, low absorption and high-power density damage threshold.

9.2.1. BASIC LASER THEORY

Three radiative transitions, absorption, stimulated emission and spontaneous emission, can occur between any two given energy levels. These transitions are illustrated in Figure 9.3. The transition levels 2 and 1 have energies E_2 and E_1 respectively (where $E_2 > E_1$). Photons absorbed or emitted have an energy ΔE equal to the difference between the transition levels (E_2-E_1). The frequency, ν, of the radiated or absorbed wave is related to the energy difference by Planck's constant, h, as given in equation 9.3.

$$\nu = \frac{(E_2 - E_1)}{h} \qquad [9.3]$$

Absorption occurs when an electromagnetic wave of frequency ν is incident on the sample. There is a finite probability that the atom will be raised into level 2.

Spontaneous emission is the process where an atom decays to the lower, more stable, energy level, emitting a photon of energy hν. The emitted photons have a broad energy range and a random phase.

Stimulated emission occurs when the sample is irradiated with an electromagnetic wave of frequency ν. Since the wave has the same frequency as the atomic transition there is a finite probability that it will force the atom to undergo the transition from level 2 to level 1. Photons emitted by stimulated emission have the same frequency phase and direction as the stimulating wave.

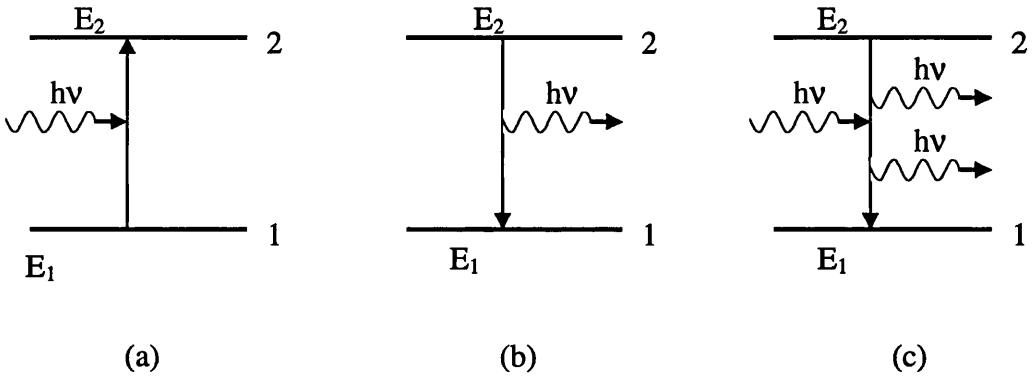

Figure 9.3 Radiative transitions: (a) absorption, (b) spontaneous emission, (c) stimulated emission.

The population of atoms in levels 1 and 2 are represented by N_1 and N_2 respectively. In order to produce the net gain stimulated emission required for lasing a population inversion ($N_2 >> N_{1)}$ must first be created. A population inversion cannot be obtained in a simple two level system. Nd lasers, like most lasers, operate using a four level system as shown in Figure 9.4.

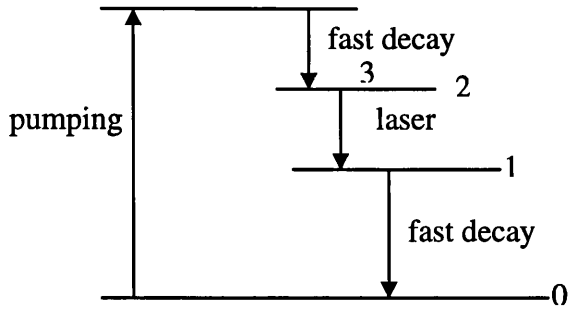

Figure 9.4. Four level laser system

In a four level system atoms are raised from level 0 to level 3, this in known as pumping and can be achieved either optically or by electrical pumping. The atoms quickly decay from level 3 to level 2 creating a population inversion ($N_2 >> N_1$). Levels 1 and 2 are the lower and upper lasing levels. The upper lasing level (2) must be a metastable state i.e. the spontaneous emission lifetime must be sufficiently long that stimulated emission dominates. The transition from level 1 to level 0 is by very fast non-radiative decay. The photon emitted must be confined to the cavity for sufficiently long to stimulate other photon emissions. This causes a cascade effect and ensures the lasing is self-sustaining. The photons are confined within the cavity using a pair of mirrors. Sufficient photons must be reflected back through the active medium to ensure stimulated emission dominates and amplification occurs.

9.3. NEODYMIUM DOPED PHOSPHATE GLASS FIBRE.

9.3.1. MANUFACTURING NEODYMIUM DOPED PHOSPHATE GLASS FIBRE.

A silica clad fibre with a 0.3 % neodymium doped lanthanum phosphate core ($\approx$ diameter 400 μm) has been prepared by drawing a bulk sample in a silica tube (section 9.1). The fibre was then redrawn using a feed at 12.5 mm per minute and a draw at a rate of 20m per minute to reduce the core diameter from 400 μm to $\approx$10 μm (see Figure 9.5).

The active laser medium is the neodymium doped lanthanum phosphate core, composition $Nd_{0.037}La_{0.963}P_{2.704}O_{8.259}Al_{0.02}$. A 0.3 % doping was used to ensure the spontaneous lifetime was sufficiently long that the stimulated emissions dominate the decay process. Fluorescence lifetimes of different concentration Nd doped lanthanum phosphate glasses have been previously reported (Brennan 1998). The 0.3 % doped glass used has a spontaneous lifetime of 269.5 μs compared to the much shorter lifetime of 14.7 μs for a 23 % doped glass (Brennan 1998). For higher rare earth concentrations non-radiative decay can occur due to ion-ion cross relaxation mechanism, this process is called concentration quenching (Brennan 1998).

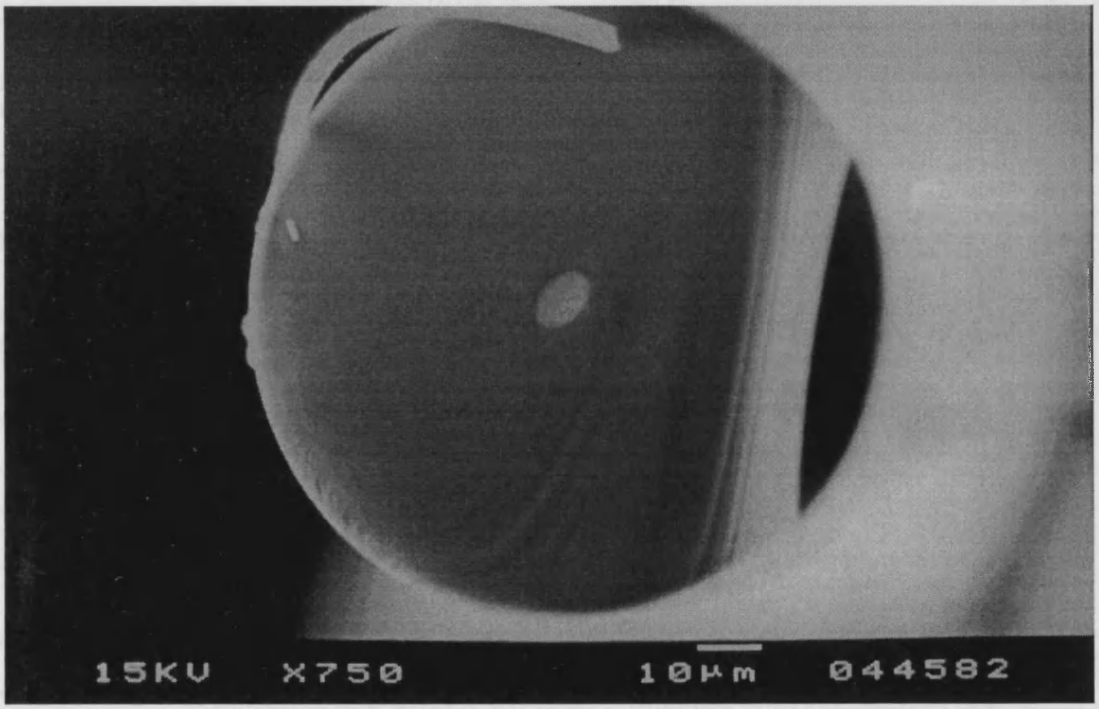

Figure 9.5. A silica clad Nd doped rare earth phosphate glass fibre.

9.3.2. LASER CAVITY

A laser cavity was constructed as shown in Figure 9.6. The first mirror was transparent to the incoming pump radiation whilst reflecting at the longer lasing wavelength of 1060 nm. An input lens with a magnification of 30 times was used to focus the pump light into the core of the fibre. The Nd^{3+} ions fluoresce strongly when

pumped. The fluorescence is confined in the fibre due to total internal reflction (Figure 9.1) and is confined within the cavity by the input and output mirrors. The output mirror (mirror 2) was only partially reflective, transmitting the active laser beam. The reflected light was coupled back into the fibre core using a second input lens. Amplification occurs each time the light is passed through the Nd fibre core. The income light stimulates emission from the Nd^{3+} ions.

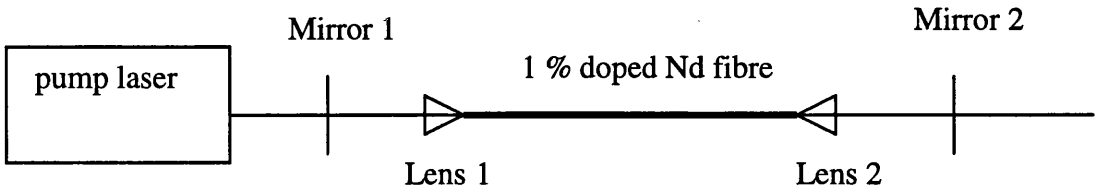

Figure 9.6. Laser cavity set up

9.3.3. RESULTS.

9.3.3.1. TI-SAPPHIRE LASER PUMP SOURCE.

Results are presented for the Nd doped rare earth phosphate fibre laser pumped using a Ti-Sapphire pump laser operating at 860 nm. Figure 9.7 shows the laser output spectrum for a cavity containing a 4-6% reflective output mirror. Figure 9.8 shows the incident input output power curve of the laser for a cavity containing a 4-6% reflective output mirror. The external slope efficiency, given by the gradient, was found to be 25 %.

A second configuration was studied where a 50 % reflective output mirror was used. The laser output emission spectrum is shown in Figure 9.9 and the incident input / output powers are shown in Figure 9.10. The external slope efficiency, given by the gradient, was found to be 19 %. A tuneable laser cavity was constructed by inserting a 1200 lines per mm grating inside the cavity immediately prior to the output mirror. The laser was forced to lase at a single wavelength and was tuneable between 1054 nm and 1062 nm as shown in Figures 9.11 and 9.12.

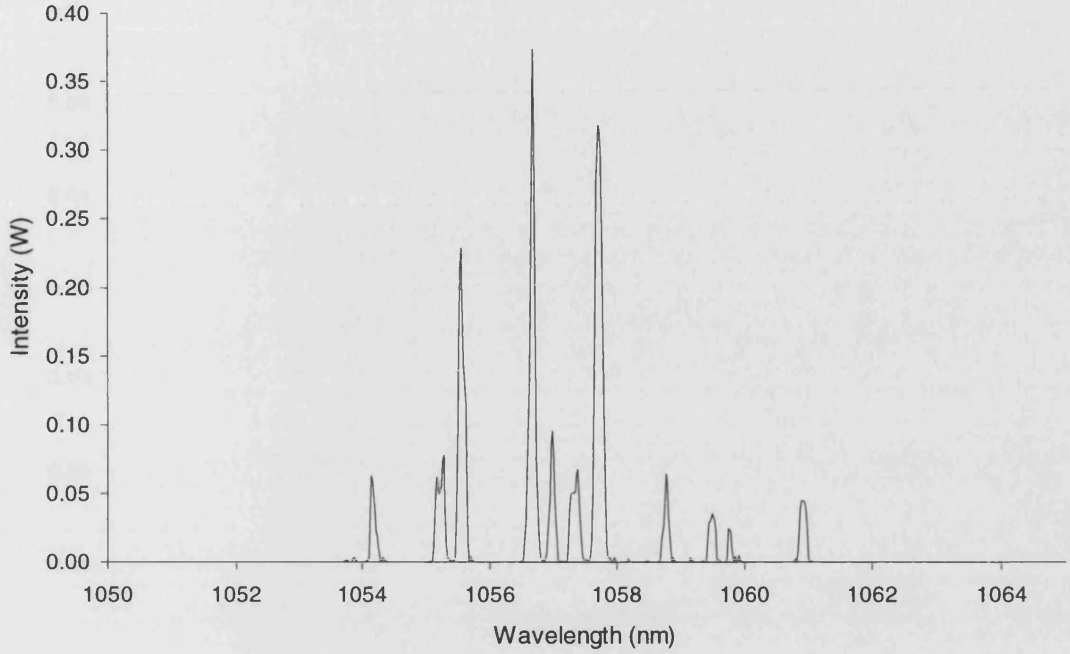

Figure 9.7. The lasing spectrum of the Nd doped fibre laser pumped at 860 nm using a Ti-Sapphire laser with a 4-6 % reflective output mirror.

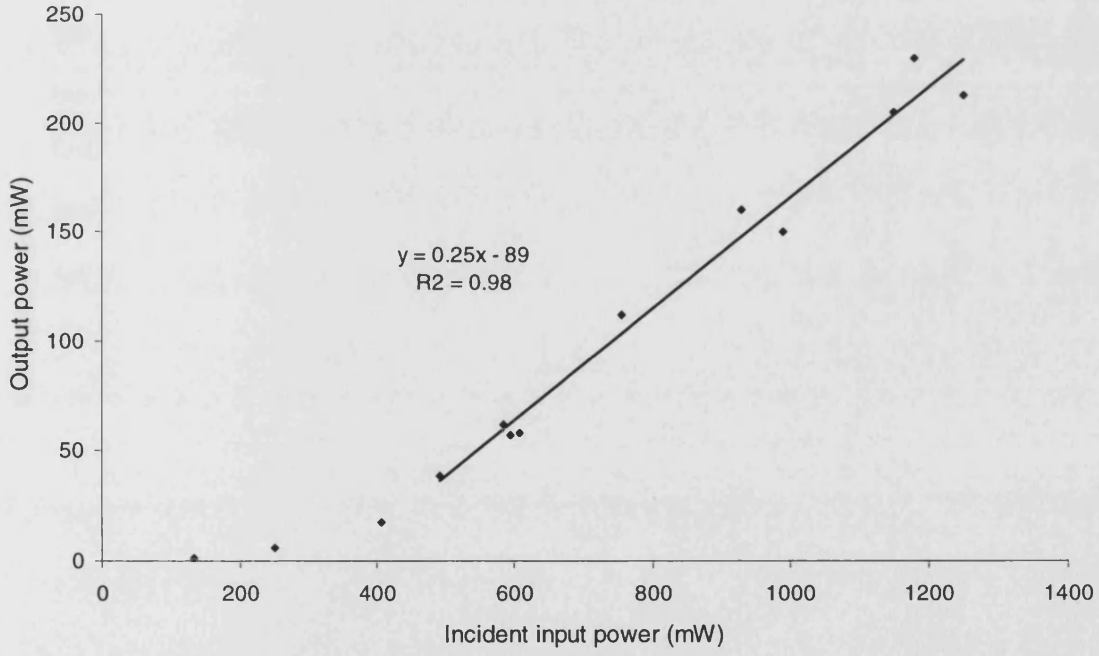

Figure 9.8. The output power from the Nd doped fibre laser as a function of pump power. Using a Ti-Sapphire laser with a 4-6 % reflective output mirror.

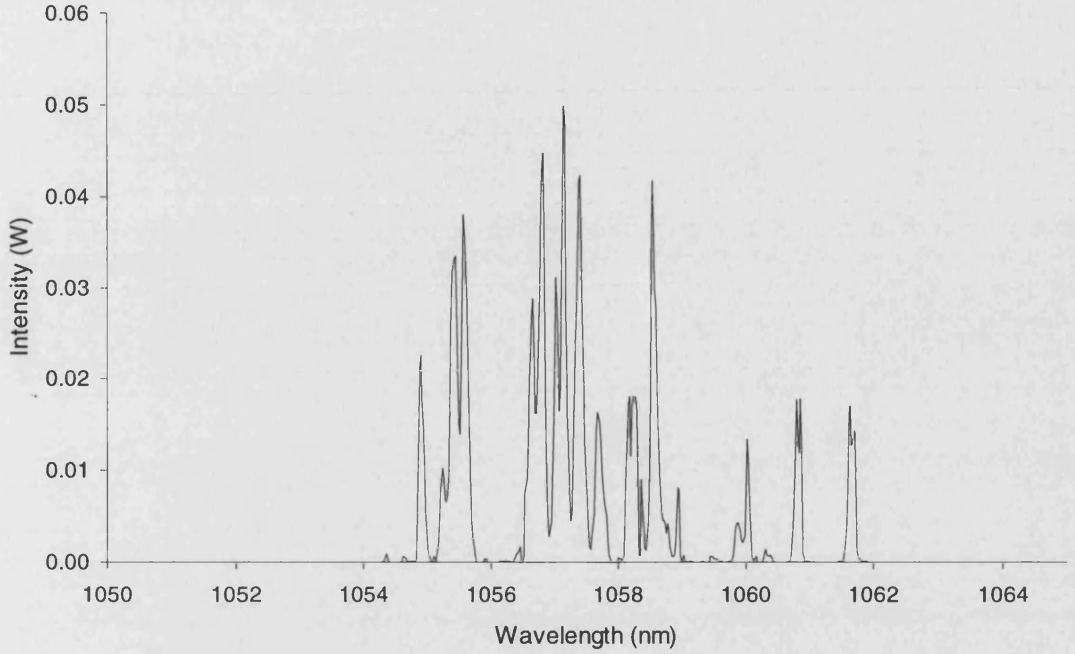

Figure 9.9. The lasing spectrum of the Nd doped fibre laser pumped at 860 nm using a Ti-Sapphire laser with a 50% reflective output mirror.

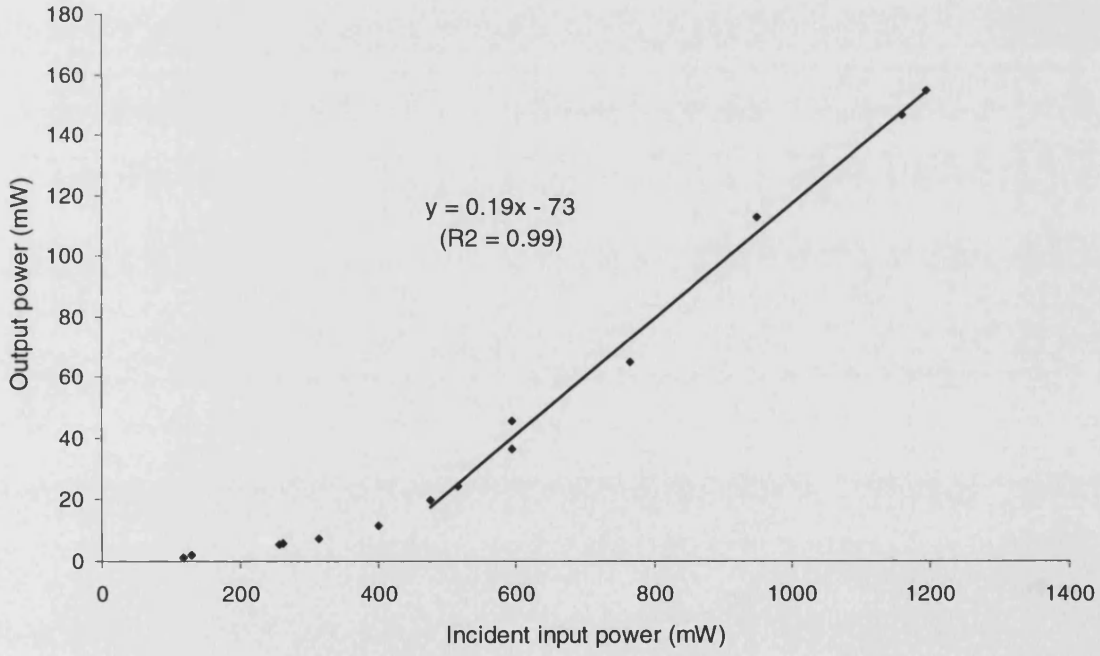

Figure 9.10. The output power from the Nd doped fibre laser as a function of pump power. Using a Ti-Sapphire laser with a 50 % reflective output mirror.

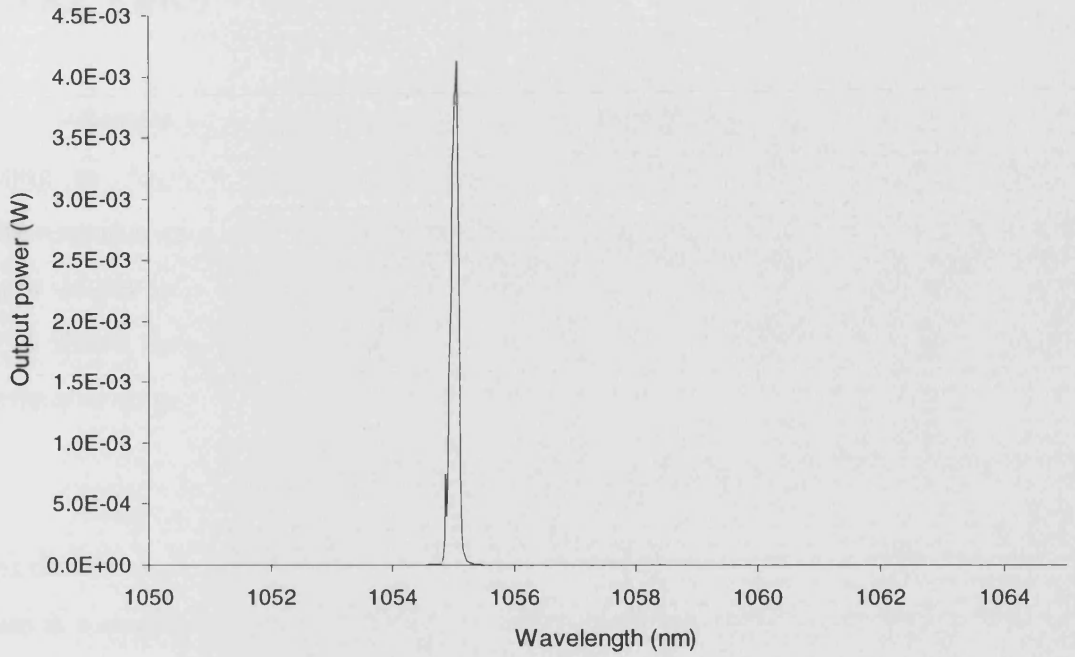

Figure 9.11. The output power from a tuneable Nd doped fibre laser as a function of pump power. Using a Ti-Sapphire laser with a 50 % reflective output mirror.

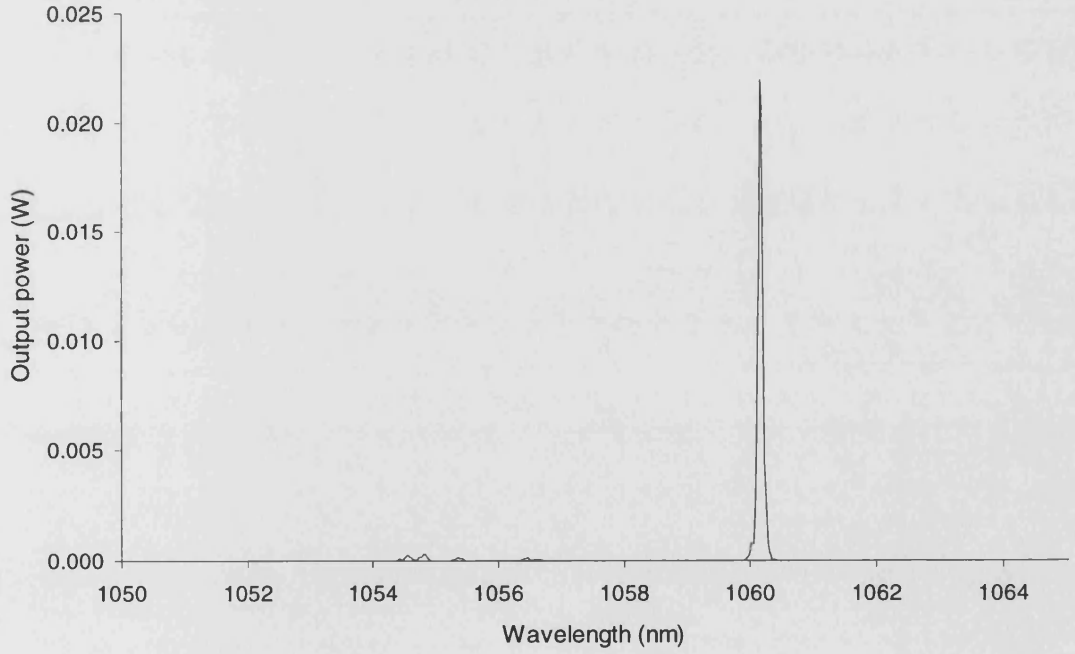

Figure 9.12. The output power from a tuneable Nd doped fibre laser as a function of pump power. Using a Ti-Sapphire laser with a 50 % reflective output mirror.

9.3.3.2. ARGON ION LASER PUMP SOURCE.

Results are presented for the Nd doped rare earth phosphate fibre laser pumped using an Argon ion pump laser operating at 488 nm. Figure 9.13 shows the fluorescence spectra of the Nd doped fibre for a detuned cavity. Figure 9.14 shows the laser output spectrum for a cavity containing a 4-6% reflective output mirror. Figure 9.15 shows the input output power curve of the laser for a cavity containing a 4-6% reflective output mirror.

A tuneable laser cavity was constructed by inserting 1200 lines per mm grating inside the cavity immediately prior to the output mirror. The fibre laser was made to lase at a single wavelength and was tuneable in the range 1054 nm to 1062 nm. Figure 9.16 illustrates the output spectra for the laser operating at several wavelengths.

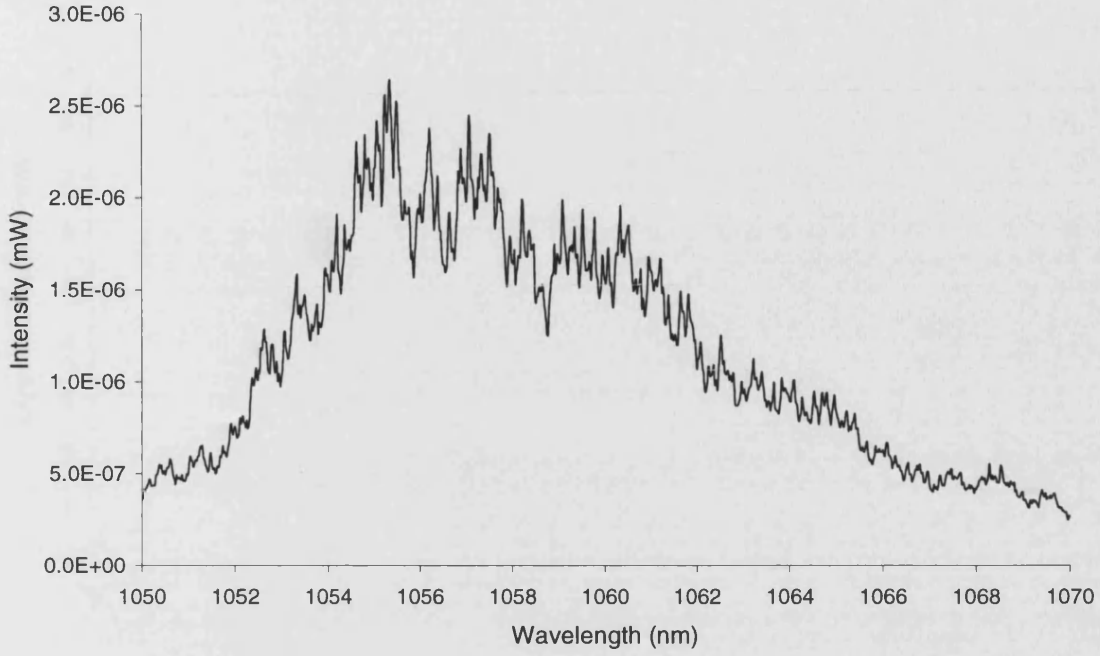

Figure 9.13. The fluorescence spectra for the Nd doped rare earth phosphate glass.

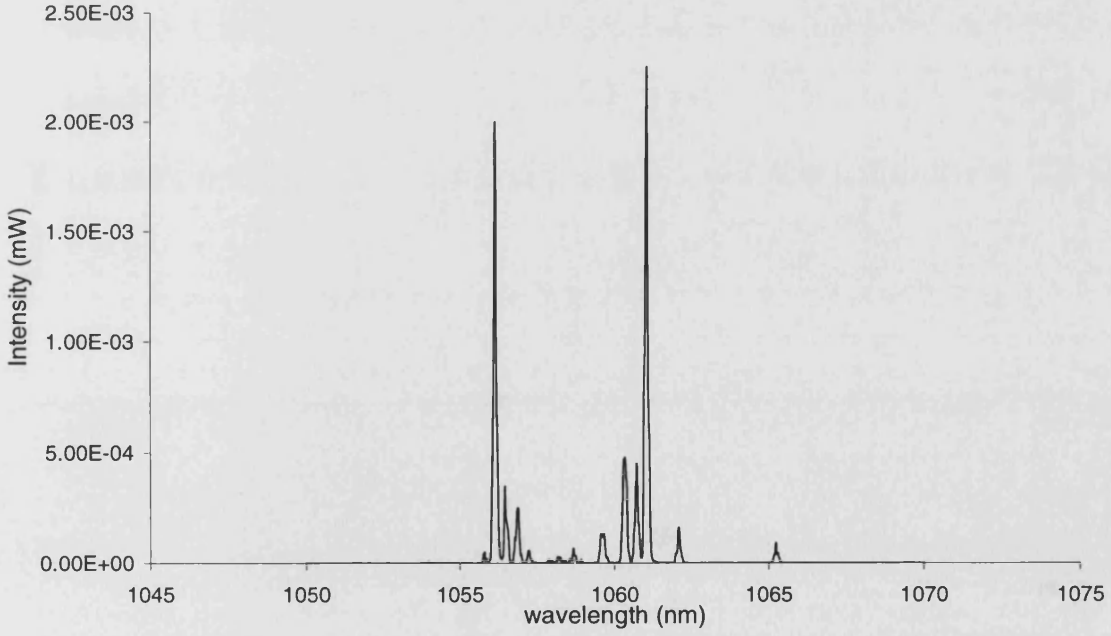

Figure 9.14. The lasing spectra of a 0.3 % doped Nd fibre with a 4-6% reflective output mirror.

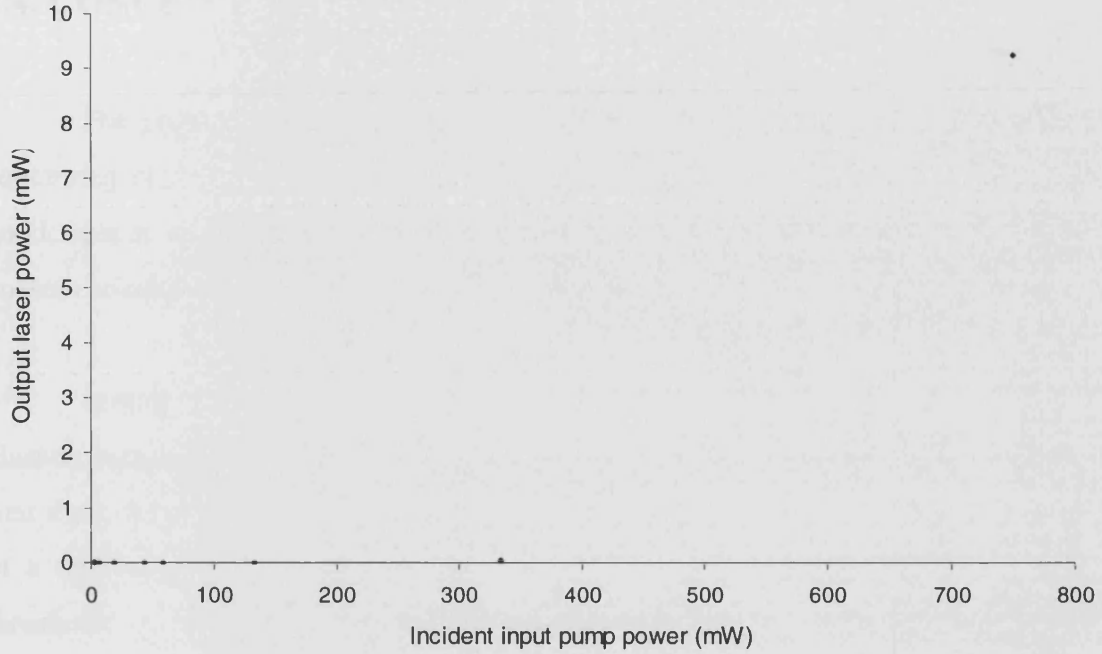

Figure 9.15. The output power from the Nd doped fibre laser as a function of incident input pump power.

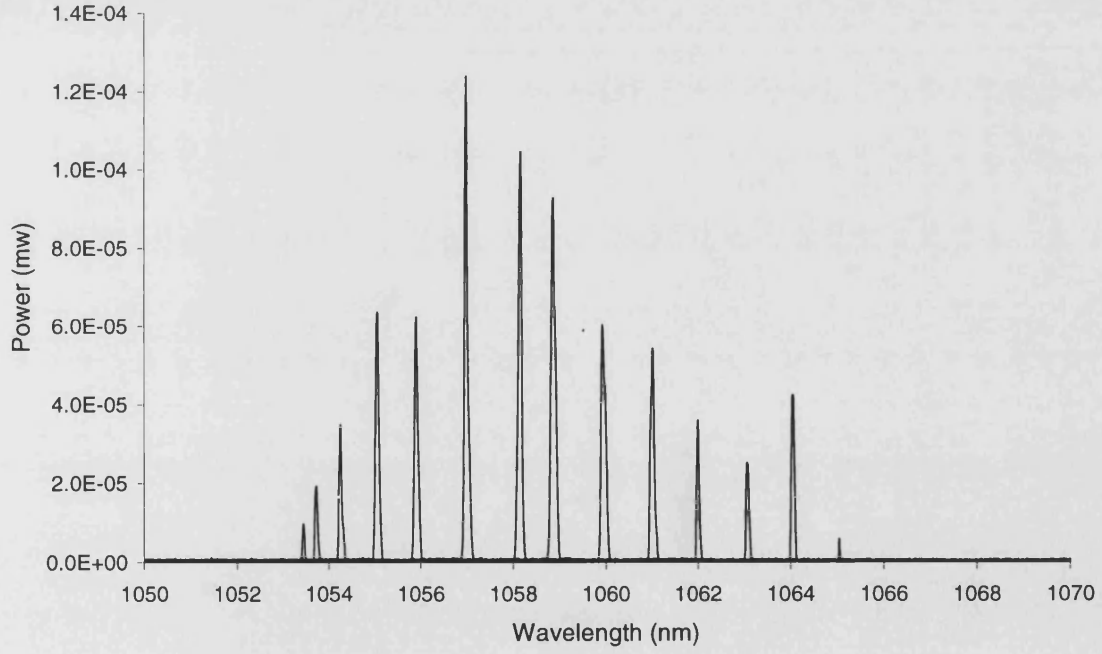

Figure 9.16. A range of spectra taken for the tuneable Nd doped fibre laser.

9.4. CONCLUSIONS AND FUTURE WORK

The preliminary studies on these glasses are very encouraging. Optical fibres containing rare earth phosphate glasses have been manufactured. The fibres are of good optical quality, free from major defects, air bubbles and stress. The fibres possess suitable mechanical properties to allow ease of handling.

Lasing has been successfully demonstrated in these rare earth phosphate glasses, prepared at the University of Bath and described in detail in Chapter 2, of the first time. A laser was made to operate at a single wavelength and was tuneable by use of a diffraction grating. The laser appeared to have a high power density damage threshold.

To fully characterise the fibre laser the losses should be studied, the absorption of the pump and lasing wavelengths. The beam profile, polarisation, coherence length and maximum power density damage threshold should be studied.

REFERENCES

Bowron D.T, Saunders G.A, Newport R.J, Rainford B.D and Senin H.B 1996a. *Physical Review B.* **53**. No. 9. p. 5268.

Bowron D.T, Bushnell-Wye G, Newport R.J, Rainford B.D and Saunders G.A 1996b. *Journal of Physics: Condensed Matter.* **8**. p. 3337.

Ford P.J, Graham C.D, Saunders G.A, Senin H.B and Cooper J.R. 1994. *Journal of Materials Science Letters.* **13**. p. 697.

Cole J.M, van Eck E.R.H, Mountjoy G, Newport R.J, Brennan T and Saunders G.A. 1999. *Journal of Physics: Condensed Matter.* **11**. p. 9165.

Cole J.M, Newport R.J, Bowron D.T, Pettifer R.F, Mountjoy G, Brennan T and Saunders G.A. 2001a. *Journal of Physics Condensed Matter.* **13**. p. 6659.

Cole J.M, van Eck E.R.H, Mountjoy G, Anderon R, Brennan T, Bushenell-Wye G, Newport R.J, and Saunders G.A. 2001b. *Journal of Physics: Condensed Matter.* **13**. p. 4105.

Wilson J and Hawkes J.F.B. 1983.*Optoelectronics: An Introduction.* Prentice-Hall. London UK.

CHAPTER 10
CONCLUSIONS AND FUTURE WORK

In this final chapter the results from the work in all the previous chapters will be summarised and future studies will be discussed.

10.1. MANUFACTURING RARE EARTH PHOSPHATE GLASSES.

In Chapter 2 the method for preparing rare earth phosphate glasses was discussed in detail. These glasses were successfully prepared using a refined version of the methods previously employed at the University of Bath. An attempt was made to understand the chemical steps involved when forming these glasses and great care was taken to minimise variations in sample composition. The glasses formed were of good optical quality, free from visible stresses or bubbles, shatter resistant and resistant to moisture contamination. A thulium phosphate glass was prepared for the first time at the University of Bath, and glasses containing ytterbium were also successfully made. Compositional analysis revealed that use of a self-consistent procedure resulted in glasses of much closer composition than previously found possible. A quantitative analysis highlighted the presence of aluminium impurities within these glasses, which originate from the alumina crucibles.

10.2 FARADAY ROTATION AND MAGNETO-OPTICAL FIGURE OF MERIT FOR RARE EARTH PHOSPHATE GLASSES.

In Chapter 3 the Faraday rotation, optical absorption and the magneto-optical Figure-of-Merit of rare earth phosphate glasses were studied. The wavelength dependence of the Verdet constant for a series of rare earth phosphate glasses was successfully measured. The rotation was found to be a linear function of the applied magnetic field as described by equation 3.1. The larger rotating glasses, containing Ce, Pr, Tb or Dy, were found to obey equation 3.4 allowing values of the transition

wavelength, λ_t, and constant, K, to be determined. Although more complex glasses have a larger rotation per unit concentration, the limited solubility of the rare earth in these glasses means that the total Verdet constant, V, of the Ce and Pr samples is largest for phosphate glasses - see Tables 3.4 – 3.5 (Berger *et al* 1964 and present work). By comparison with the results of Berger *et al* (1964) for phosphate glasses, the addition of aluminium into the glass host appears to have a negligible effect on the Verdet parameters; this is in contrast with silicate glasses whose properties depend heavily on the addition of aluminium (see e.g. Table 3.6).

Of the rare earth phosphate glasses studied, $TbP_{2.94}O_{9.18}Al_{0.26}$ was found to have the largest rare earth ion concentration and the highest Verdet constant, v, resulting in the largest total Verdet constant V. At 1060 nm, V is similar to that recently reported for other Tb glasses and is $\approx$ 50% that of terbium gallium garnet crystals (TGG) used in current isolator systems (see Table 3.6). Current Faraday isolators operating between 1.0 – 1.1 μm have an optical path length of rotating medium of about 40 mm for TGG and 60 mm for Tb glass (see the EOT website). A magnetic field of 0.75 T would be required to produce a 45-degree rotation though a path length of 60 mm in the $TbP_{2.94}O_{9.18}Al_{0.26}$ glass studied.

The absorption coefficient of bulk glasses was measured as a function of wavelength for each of the rare earth phosphate glasses. Absorption peaks were measured and the transitions assigned. The absorption measurements were then used to calculate the magneto optical figure of merit, F, for each of the glasses. For the Ce, Pr, Tb and Dy based glasses it was possible to interpolate values of the Verdet constant, V, allowing F to be calculated over the wavelength range 450-520 Å (excluding regions close to the absorption bands).

10.3 THE STRUCTURE OF RARE EARTH PHOSPHATE GLASSES.

In Chapters 6 and 7 the structure of rare earth phosphate glasses containing large (La / Ce) and small (Dy / Ho) rare earth ions was determined by applying the method of isomorphic substitution in neutron diffraction.

The first order difference and total minus weighted difference functions were obtained for the La / Ce and Dy / Ho glasses by combining the total structure factors. The difference functions and the total structure factors were modelled self-consistently, using the same Gaussian input parameters (distance, coordination number and peak width), confirming that the method of isomorphic substitution is valid at the difference function level of the present results.

The difference functions allowed unprecedented information on the structure of rare earth phosphate glasses to be obtained, thus allowing the O-O and R-O correlations to be resolved unambiguously. The P-O bond distances and coordination numbers are in agreement with previous work confirming that the glass network is made from PO_4 tetradedra.

The Al-O correlations were explicitly modelled and the distance and coordination numbers were found to be consistent with a large proportion of Al being octahedrally coordinated. This is important as it enabled the O-(Al)-O peak position and coordination number to be extracted. Since the O-(Al)-O correlations appear in the same real space region as O-(P)-O correlations, information on the O-(Al)-O correlations allowed the O-(P)-O correlations to be modelled with greater accuracy.

The R-O coordination numbers were consistent with those anticipated on the basis of the crystal structures. The mean nearest neighbour R-O distance for the larger R^{3+} ion was at a longer r-distance ($\approx$ 2.48 Å) than that for the smaller ions ($\approx$ 2.29 Å). The R-O distribution for glasses containing the larger rare earth ions was found to be highly asymmetric whilst glasses containing the smaller R^{3+} could be represented by a single Gaussian with a much smaller Gaussian at a larger r-distance. A range of R-O

distances has been suggested in the work of Hoppe (2001, 2002) for glasses containing the larger R^{3+} ions but this is the first report of an asymmetric distribution for the smaller rare earth ions. The present work shows that the asymmetry of glasses containing the larger R^{3+} ions is much greater than previously reported.

Information on the connectivity of the network is provided by the O-(P)-O coordination number. The measured values for these glasses containing both the larger and smaller R^{3+} are in agreement with values calculated using the phosphate network model (Hoppe 1996). The results are consistent with the experimental results presented by Hoppe *et al* (1998, 2001, 2002) but not the results presented by Cole *et al* (1999, 2001). The O-(P)-O coordination number indicates that the O_T : O_B ratio is ≈ 0.72 : 0.28 for glasses containing the larger R^{3+} ions and 0.81 : 0.19 for glasses containing the smaller R^{3+} ions. This indicates that the phosphate glasses containing the larger rare earth ions have a larger proportion of bridging oxygen and therefore a greater network connectivity.

The partial structure factor, $S_{RR}(Q)$, was measured for the first time for rare earth phosphate glasses containing the smaller ions Dy^{3+} and Ho^{3+}. Although severe contamination of this function from unwanted correlations was expected from the EPMA experiments, no compelling evidence for such correlations could be found in the measured $g'_{RR}(r)$.

When the measured $S_{RR}(Q)$ was used to form the $\Delta_{R\mu}(Q)$ and $\Delta_{\mu\mu}(Q)$ functions there was negligible structure in the differences $\Delta_{R\mu}^{(1)}(Q) - \frac{b_{Dy} - b_{Ho}}{b_{Dy} - b_{Dy/Ho}} \Delta_{R\mu}^{(2)}(Q)$, $\Delta_{R\mu}^{(1)}(Q) - \frac{b_{Dy} - b_{Ho}}{b_{Dy/Ho} - b_{Ho}} \Delta_{R\mu}^{(3)}(Q)$, $\Delta_{\mu\mu}^{(1)}(Q) - \Delta_{\mu\mu}^{(2)}(Q)$ and $\Delta_{\mu\mu}^{(1)}(Q) - \Delta_{\mu\mu}^{(3)}(Q)$ as expected for the completion of accurate experiments. Likewise, differences between the corresponding real space functions showed negligible structure. The neutron diffraction experiments therefore indicated that the composition of the DyC, DyHoE and HoG glasses was closer than indicated by the EPMA results.

Integrating the first peak in $g'_{RR}(r)$ over the range $5.1 \leq r$ (Å) ≤ 7.2 gave a R-R coordination number of 8.0(2) consistent with the distribution of eight R-R nearest neighbours for crystalline ErP_3O_9 (Dorokhova and Karpov 1984) extending over the range 5.37 – 6.97 Å. The large separation of the nearest neighbour R-R correlations means that an analysis of the low r region of $\Delta G'_R(r)$ and $\Delta G'_F(r)$ or of $\Delta G'_{R\mu}(r)$ and $\Delta G'_{\mu\mu}(r)$ yields Gaussians described by identical parameters.

10.4 THE STRUCTURE OF MOLTEN $TbCl_3$.

In Chapter 8 the total structure factor of molten $TbCl_3$ at 617 °C was measured using neutron diffraction. The data sets were in agreement with previous experimental work but the use of a diffractometer having an extended reciprocal-space measurement window resulted in an improved resolution in real-space. The new data showed that significant discrepancies occur between experiment and the polarisable ion model molecular dynamics simulations of Hutchinson *et al* (2001) for $TbCl_3$ in which the interaction potentials were refined to optimise agreement with the previous neutron diffraction results of Wasse and Salmon (1999). The oscillations in F(Q) at high-Q appear to be out of phase and in real-space the simulated first peak is too sharp. The agreement between the real-space experimental and simulation results reported by Hutchinson *et al* (2001) for liquid $TbCl_3$ is, therefore, largely an artefact of the limited measurement window of the diffractometer used in the previous neutron diffraction work. Thus for $TbCl_3$, as for most other MCl_3 (Hutchinson *et al* 1999, 2001) and MBr_3 (Wasse *et al* 2000, Hutchinson *et al* 2000) systems, notable discrepancies are observed between the simulation and experimental results. The present work therefore demonstrates a need to consider afresh issues such as the cation-anion repulsion and the anion compressibility in different environments if a truly transferable model for the interactions in trivalent metal halides is to be developed within the framework of the polarisable ion model across the entire range of ion size ratios.

10.5 FABRICATION OF RARE EARTH PHOSPHATE FIBRES AND FIBRE LASERS

In Chapter 9 optical fibres containing rare earth phosphate glasses were manufactured. The fibres were of good optical quality, free from defects, air bubbles and stress. The fibres possessed suitable mechanical properties to allow ease of handling. Lasing has been successfully demonstrated in these rare earth phosphate glasses, prepared at the University of Bath and described in detail in Chapter 2, for the first time. A laser was made to operate at a single wavelength and was tuneable by use of a diffraction grating. The laser appeared to have a high power density damage threshold.

10.6 FUTURE WORK.

Further areas worth investigating include the preparation of rare earth phosphate glasses in platinum or iridium crucibles. This would eliminate aluminium impurities and, therefore the $S_{Al\text{-}\alpha}(Q)$ correlations from the measured diffraction pattern, thus simplifying the structure by reducing the number of partial structure factors from ten to six. This would result in an overall simplification of the modelling process described in Chapters 6 and 7.

The glasses could also be prepared in sealed ampoules thereby eliminating the phosphorus pentoxide losses that occur during the manufacturing process. A range of glass compositions could then be formed, dependent only upon the starting ratio of P_2O_5 to R_2O_3. This would enable structural studies to be conducted on glasses with a range of compositions, providing information on how the network connectivity and R-R separation depend upon the rare earth concentration.

The ability to form phosphate glasses with predetermined and reproducible compositions would eliminate unwanted contamination correlations in the difference

functions formed when using the isomorphic substitution method and would thereby simplify the analysis procedure. It would also allow the method of isotopic substitution to be employed for neutron diffraction studies.

Once rare earth phosphate glasses can be prepared free from unwanted Al impurities a systematic study on the properties of Al within these glasses could be undertaken by adding known amounts of Al_2O_3 to the P_2O_5 and R_2O_3 starting chemicals. Hence it would be possible to determine the effect aluminium has on the glass hardness, density, susceptibility to water, elastic stiffness and fluorescence lifetimes, since these are all quantities that are likely to depend upon the aluminium concentration levels. Glasses could also be prepared by adding controlled quantities of pure water to understand the effect that water has on glass formation.

The structure of these rare earth phosphate glasses could also be studied using anomalous x-ray scattering. The effective scattering length of the rare earth ion changes with energy across an absorption edge. Therefore complementary information could be obtained on the R- α correlations.

The Faraday rotation and optical absorption and therefore the magneto-optical Figure-of-Merit could be measured over a wider range of wavelengths. This would overcome the limitations associated with measuring these values at single points. Also, to fully evaluate the potential of these rare earth phosphate glasses for use as optical isolators, the thermal stability, absorption at 1.06 μm and maximum power density damage threshold should be measured.

The fibre laser should be further characterised, the losses and the absorption of the pump and lasing wavelengths should be studied. The beam profile, polarisation, coherence length and maximum power density damage threshold should be studied.

The method of isomorphic substitution could be employed to separate the R-R, R-Cl and Cl-Cl correlations for molten trivalent metal halides. The Dy^{3+} ions in $DyCl_3$ could be substituted by pure Ho^{3+} or an equi-mixture of Ho^{3+} and Dy^{3+} ions in order to extract these correlations. The R-R distance provides information on the connectivity of the network. Short nearest neighbour R-R distances are associated with face

sharing coordination polyhedra, whilst corner sharing polyhedra are identified by larger R-R nearest neighbour distances. The present work also demonstrates a need to further develop the polarisable ion model for trivalent metal halides.

The fluorescence lifetimes of the rare earth ions could also be studied as a function of host environment to provide complementary information on the R-R separation. Diffraction studies find that the R-R distances in meta-phosphate crystals comprising larger rare earth ions (e.g. Nd^{3+}) are shorter than in meta-phosphate crystals comprising smaller rare earth ions (e.g. Er^{3+}) (Hong 1974a, Dorokhova and Karpov 1984). A study on crystalline meta-phosphates has reported a considerably longer fluorescence lifetime for Nd^{3+} ions in $Y_{0.9}Nd_{0.1}P_3O_9$ (490 μs) compared to Nd^{3+} ions in $La_{0.9}Nd_{0.1}P_3O_9$ (160 μs) (Hong 1974b). It should therefore be possible to repeat the above experiment for the corresponding glassy materials and extend it further by studying the fluorescence lifetime of smaller rare earth ions. If phosphate glasses comprising lanthanum or ytterbium ions are doped with sufficiently small amounts of Nd^{3+} or Er^{3+} ($\approx 1\%$), then the fluorescence lifetimes of these glasses could be studied. These results, coupled with information on the R-R separation from diffraction studies, would provide insight into the distance between large rare earth ions (Nd^{3+}) incorporated into both a large (La^{3+}) and small (Y^{3+}) rare earth phosphate host and conversely the distance between small rare earth ions (Er^{3+}) incorporated into both a large (La^{3+}) and small (Y^{3+}) rare earth phosphate host.

REFERENCES

Berger S.B, Rubinstein C.B, Kurkjian C.R and Treptow A.W. 1964. *Physical Review.* **133** (3A) A723.

Cole J.M, van Eck E.R.H, Mountjoy G, Newport R.J, Brennan T and Saunders G.A. 1999. *Journal of Physics: Condensed Matter.* **11**. p. 9165.

Cole J.M, van Eck E.R.H, Mountjoy G, Anderon R, Brennan T, Bushenell-Wye G, Newport R.J, and Saunders G.A. 2001. *Journal of Physics: Condensed Matter.* **13**. p.4105.

Dorokhova G.I and Karpov O.G. 1984. *Kristallografiya.* **29**. p. 677.

EOT. Electro-Optics Technology, Inc.1030 Hastings Street, Ste 140, Traverse City MI 49686. US.http://www.eotech.com/

Hong H.Y.P. 1974a. Acta Cryst. **B30**. p. 468.

Hong H.Y.P. 1974b. Acta Cryst. **B30**. p. 1857.

Hoppe U. 1996. *Journal of Non-Crystalline Solids.* **195**. p. 138.

Hoppe U, Kranold R, Stachel D, Barz A and Hannon A.C. 1998. *Journal of Non-Crystalline Solids.* **232-234**. p. 44.

Hoppe U, Ebendorff-Heidepriem H, Neuefeind J and Bowron D. 2001. Zeitschrift fur Naturforschung. **56a**. p. 237.

Hoppe U, Metwalli E, Brow R.K and Neuefeind J. 2002. *Journal of Non-Crystalline Solids.* **297**. p. 263.

Hutchinson F, Rowley A.J, Walters M.K, Wilson M, Madden P.A, Wasse J.C and Salmon P.S. 1999. *Journal of Chemical Physics.* **111.** p. 2028.

Hutchinson F, Wilson M and Madden P.A. 2000. *Journal of Physics: Condensed Matter.* **12.** p. 10389.

Hutchinson F, Wilson M. and Madden P.A. 2001. *Molecular Physics.* **99.** p. 811.

Wasse J.C and Salmon P.S. 1999. *Journal of Physics: Condensed. Matter.* **11.** p. 9293.

Wasse J.C, Salmon P.S and Delaplane R.G 2000. *Journal of Physics: Condensed. Matter.* **12.** p. 9539.

PUBLICATIONS

Structure of Molten $TbCl_3$ by Neutron Diffraction. R.A. Martin, P.S. Salmon, A.C. Barnes and G.J. Cuello. *Journal of Physics: Condensed Matter* **14**, L703, (2002).

Structure of lanthanum and cerium phosphate glasses by the method of isomorphic substitution in Neutron Diffraction. R.A. Martin, P.S. Salmon, H.E. Fischer, C.J. Benmore and G.J. Cuello. In-progress.

Structure of dysprosium and holmium phosphate glasses by the method of isomorphic substitution in Neutron Diffraction. R.A. Martin, P.S. Salmon, H.E. Fischer and G.J. Cuello. In-progress.